PIONEER AND INNOVATIVE STUDIES IN NATURAL SCIENCE AND MATHEMATICS

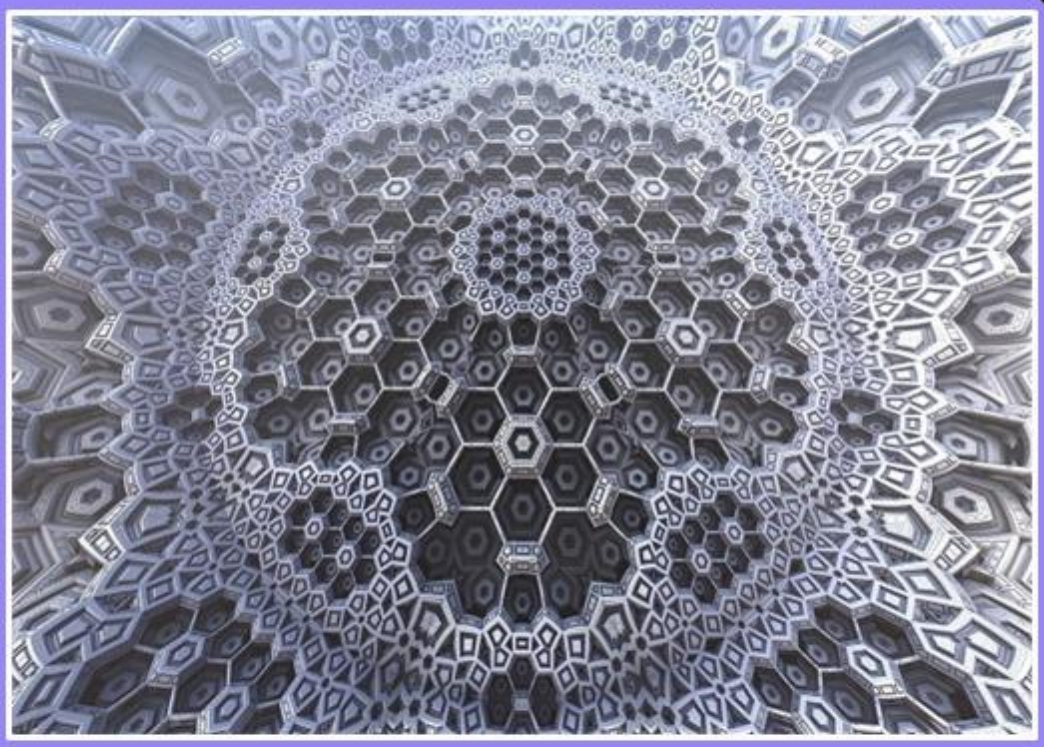

All Sciences Academy

PIONEER AND INNOVATIVE STUDIES IN NATURAL SCIENCE AND MATHEMATICS

Editor
Assoc. Prof. Dr. ALİ ÖZDEMİR

Pioneer and Innovative Studies In Natural Science and Mathematics
Editor: Assoc. Prof. Dr. ALİ ÖZDEMİR

Design: All Sciences Academy Design
Published Date: December 2024
Publisher's Certification Number: 72273
ISBN: 978-625-6314-95-5

www.allsciencesacademy.com
allsciencesacademy@gmail.com

CONTENT

The Impact of Climate Change on Macrozoobenthos

Ali MİROĞLU[1]
Ali SALUR[2]

1- Associate Professor; Ordu University, Fatsa Faculty of Marine Sciences, Department of Fisheries Technology Engineering. alimiroglu@gmail.com ORCID No: 0000-0001-8990-0766
2- Associate Professor; Hitit University, Faculty of Art and Science, Department of Molecular Biology and Genetic. alisalur@gmail.com ORCID No: 0000-0003-0761-3857

ABSTRACT

The impact of climate change on macrozoobenthos biodiversity is a critical area of research, as macrozoobenthos play a vital role in aquatic ecosystems, contributing to nutrient cycling, sediment stabilization, and serving as a food source for various organisms. Climate change, characterized by rising temperatures, altered precipitation patterns, and increased frequency of extreme weather events, poses significant threats to these benthic communities. This essay aims to explore the multifaceted impacts of climate change on macrozoobenthos biodiversity, drawing on a range of studies that highlight the complexities and interdependencies within aquatic ecosystems.

Keywords – Climate Change, Macrozoobenthos, Aquatic Ecosystem, Bentic Community,Biodiversity.

INTRODUCTION

The impact of climate change on macrozoobenthos, which encompasses the diverse assemblages of benthic organisms, is a pressing concern for marine and freshwater ecosystems globally. As climate change continues to alter environmental conditions, the responses of macrozoobenthic communities are becoming increasingly evident. This article synthesizes current research findings to elucidate the multifaceted effects of climate change on macrozoobenthos, highlighting changes in biodiversity, community structure, and ecosystem functioning.

Macrozoobenthos, which includes large invertebrates living on or in the sediment of aquatic environments, are particularly sensitive to changes in their environment, making them valuable indicators of ecosystem health (Adella, 2023; Ramadhaniaty et al., 2023; Al-Izhar et al., 2023). The literature highlights several key aspects of how climate change affects macrozoobenthos biodiversity, including shifts in species composition, changes in habitat conditions, and the implications for ecosystem functioning.

Climate change is primarily characterized by rising temperatures, altered precipitation patterns, and increased frequency of extreme weather events. These changes have profound implications for benthic habitats, particularly in freshwater and coastal ecosystems. For instance, Cohen et al. (2016) demonstrated that climate warming in Lake Tanganyika has led to significant reductions in fish production and benthic habitat, suggesting that rising temperatures and stratification are detrimental to both benthic and pelagic communities. Similarly, Pollack et al. (2011) observed long-term trends in the Lavaca-Colorado Estuary, Texas, where climate variability has influenced the stability and composition of benthic macrofauna, indicating

that certain species can dominate under changing conditions, thus reflecting the resilience of these ecosystems.

The implication of climate change is profound, as macrozoobenthos serve as critical components of aquatic food webs. Their decline can lead to cascading effects throughout the ecosystem, affecting fish populations and other species that rely on them for food (Bulling et al., 2010). Furthermore, the loss of biodiversity among macrozoobenthos can impair ecosystem functioning, reducing the resilience of these systems to further environmental changes (Rinawati et al., 2013). This is particularly concerning in light of predictions that climate change will continue to intensify, leading to more frequent and severe disturbances in aquatic environments (Bellard et al., 2012).

One of the primary effects of climate change on macrozoobenthos is the alteration of species composition and distribution. For instance, studies have documented that rising temperatures in Arctic regions are leading to a shift from cold-adapted species to more temperate species, which can disrupt existing ecological interactions and reduce the overall biodiversity of these habitats (Gebruk et al., 2019; Gebruk et al., 2023). This phenomenon is not limited to the Arctic; similar trends have been observed in various freshwater and marine environments, where temperature increases can favor invasive species over native ones, further threatening local biodiversity (Yan et al., 2015; Li et al., 2019). The introduction of new species can lead to competitive exclusion, where native species are outcompeted for resources, resulting in declines in their populations and, ultimately, biodiversity loss (Li et al., 2013).

Moreover, climate change exacerbates other stressors such as habitat degradation and pollution, which compound the challenges faced by macrozoobenthos. For example, coastal reclamation efforts, often driven by urban expansion and agricultural needs, have been shown to significantly impact macrozoobenthos communities by altering their habitats and reducing available resources (Yan et al., 2015). The degradation of habitats due to human activities, coupled with climate-induced changes such as increased salinity and altered sedimentation patterns, can lead to significant declines in macrozoobenthos diversity (Li et al., 2019). These changes not only affect the organisms themselves but also the broader ecosystem services they provide, such as water filtration and habitat structure for other aquatic life (Bulling et al., 2010).

Research also indicates that the impacts of climate change on macrozoobenthos are not uniform across different regions or ecosystems. Factors such as local hydrology, land use practices, and existing biodiversity levels can influence how these organisms respond to climate stressors (He et al., 2019). For instance, studies in freshwater ecosystems have shown that macrozoobenthos diversity is closely linked to water quality and habitat complexity, both of which can be adversely affected by climate change (Li et

al., 2019). In contrast, some studies suggest that certain macrozoobenthos species may exhibit resilience to temperature changes, potentially due to their adaptive capacities or ecological plasticity (Dewenter et al., 2023).

The effects of climate change on macrozoobenthos are not uniform across different environments. In coastal saltmarshes, Mely et al. (2023) reported that rising sea levels, increased salinity, and temperature fluctuations significantly affect the ecological dynamics of these habitats, leading to shifts in benthic community structure. These changes are compounded by the hydrological variability inherent in coastal ecosystems, which regulates benthic assemblages. Broman et al. (2019) further emphasized that salinity changes can drive meiofaunal community dynamics, suggesting that ongoing environmental changes may lead to decreased biodiversity and altered ecosystem functions.

The effects of climate change are not uniform across different ecosystems; rather, they manifest in various ways depending on local conditions and species interactions. For example, Yan et al. discuss how coastal reclamation efforts, exacerbated by climate change, can lead to intensified impacts on macrozoobenthos biodiversity, highlighting the role of human activities in compounding the effects of climate change (Yan et al., 2015). The introduction of invasive species, driven by changing climatic conditions, further complicates the dynamics within benthic communities, as these invaders can outcompete native species for resources, leading to declines in biodiversity (Firn et al., 2015). The interaction between climate change and anthropogenic stressors necessitates a holistic approach to conservation and management strategies.

Climate change has been shown to alter the structural characteristics and species composition of macrozoobenthos communities. For instance, Gladyshev et al. discuss how temperature variations across different river systems can lead to changes in the secondary production of highly unsaturated fatty acids by zoobenthos, which are crucial for the energy transfer within aquatic food webs (Gladyshev et al., 2015). This alteration in nutrient dynamics can have cascading effects on the entire ecosystem, as the availability of essential fatty acids influences the growth and reproduction of higher trophic levels. Furthermore, Dulić et al. highlight that macrozoobenthos metrics are closely linked to environmental conditions, such as fish biomass, which can be significantly affected by climate-induced changes in water supply (Dulić et al., 2014). The interplay between these factors underscores the complexity of managing aquatic ecosystems in the face of climate change.

In polar regions, where climate change is particularly pronounced, macrozoobenthos communities are experiencing notable shifts. Gebruk et al. observed changes in the composition of bivalve molluscs in the Pechora Bay, indicating a potential shift towards species that are more tolerant of warmer temperatures and altered salinity levels (Gebruk et al., 2023). This

shift not only reflects the immediate impacts of climate change but also raises concerns about the long-term viability of traditional species that may be outcompeted or unable to adapt to the changing conditions. Similarly, Gebruk et al. in their 2019 study emphasize that increasing temperatures in the Arctic will likely lead to changes in species distribution and interactions, allowing for the introduction of boreal species while diminishing the presence of native Arctic species (Gebruk et al., 2019). Such changes can disrupt established ecological relationships and lead to a decline in biodiversity. Blaen et al. (2013) highlighted that many insect populations in high-latitude areas are currently living in cooler conditions than their physiological optima, and future warming may push these species beyond their tolerance limits. This phenomenon is echoed by Link et al. (2013), who noted that climate change is altering the quality and quantity of food available to polar benthos, which could have cascading effects on community structure and ecosystem functioning.

The response of macrozoobenthos to climate change is also influenced by sediment characteristics and habitat structure. Dewenter et al. research indicate that macrozoobenthos species exhibit specific preferences for certain sediment types, which can affect their distribution and abundance in response to changing environmental conditions (Dewenter et al., 2023). As climate change alters sediment dynamics through increased erosion or sedimentation, the habitat suitability for various macrozoobenthos species may be compromised, leading to shifts in community composition and potential declines in species richness. This relationship underscores the importance of considering habitat structure in biodiversity assessments and management plans.

The interaction between climate change and eutrophication presents another layer of complexity for macrozoobenthic communities. Ehrnsten et al. (2020) found that while particulate organic carbon (POC) input drives macrofaunal biomass, the relationships are not linear, indicating that nutrient loading can have unpredictable effects on benthic fauna. This is particularly relevant in coastal regions where nutrient runoff from land exacerbates the impacts of climate change, leading to hypoxic conditions that further stress benthic organisms (Villnäs et al., 2012).

The role of macrozoobenthos in nutrient cycling and ecosystem functioning cannot be overstated. As primary producers in benthic environments, these organisms contribute significantly to biogeochemical cycles. For instance, Solan et al. (2020) discussed how benthic organisms can mitigate climate change impacts through their contributions to carbon cycling and nutrient recycling. However, the loss of biodiversity and functional redundancy within these communities, as highlighted by Meyer and Kröncke (2019), raises concerns about the resilience of benthic ecosystems to future environmental changes.

Moreover, the implications of climate change extend beyond immediate biodiversity loss; they also encompass broader ecological functions and services. As macrozoobenthos contribute to bioturbation and nutrient cycling, their decline can disrupt these processes, leading to decreased water quality and altered ecosystem functioning (Dulić et al., 2014). The interconnectedness of species within aquatic ecosystems means that the loss of even a few key species can have disproportionate effects on overall ecosystem health. This is particularly concerning in light of findings by Li et al., which illustrate how human activities and climate change have led to significant declines in macrozoobenthos biodiversity in regions such as the Poyang Lake Basin in China (Li et al., 2019). The degradation of such habitats not only threatens local biodiversity but also undermines the ecosystem services that communities rely on for their livelihoods.

In addition to direct impacts on biodiversity, climate change is also influencing the spatial distribution of macrozoobenthic species. For example, Renaud et al. (2019) noted that climate warming could facilitate the poleward expansion of boreal organisms, which may disrupt existing community structures and interactions. This shift in distribution patterns is critical for understanding the future dynamics of benthic ecosystems, particularly in the context of habitat loss and fragmentation.

Moreover, the interplay between climate change and anthropogenic stressors, such as pollution and habitat destruction, complicates the responses of macrozoobenthic communities. Hoppit and Schmidt (2022) emphasized that understanding regional variations in how benthic organisms respond to climate change is crucial for effective management and conservation strategies. This is particularly important in light of the increasing pressures faced by these ecosystems, which are often compounded by human activities.

The implications of these changes extend beyond ecological considerations; they also have significant socio-economic ramifications. Coastal and freshwater ecosystems provide essential services, including fisheries, water purification, and recreational opportunities. As highlighted by Gacheno and Amare (2021), the degradation of these ecosystems due to climate change can undermine their capacity to deliver these services, impacting human communities that rely on them.

In summary, the literature underscores the multifaceted impacts of climate change on macrozoobenthos biodiversity, highlighting the need for integrated management strategies that consider both climate and anthropogenic stressors. Effective conservation efforts must address the interconnectedness of these factors to mitigate the risks posed to macrozoobenthos and the ecosystems they inhabit. Future research should focus on long-term monitoring of macrozoobenthos communities, exploring their responses to climate change and identifying potential adaptive

strategies that could enhance their resilience (Pecl et al., 2017; Mantyka-Pringle et al., 2013).

CONCLUSION

The effects of climate change on macrozoobenthos biodiversity are multidimensional and complex according to the results of our research. First of all, temperature increase and changing precipitation patterns directly affect the distribution and abundance of macrozoobenthos species. These changes are especially clearly observed in coastal areas and freshwater ecosystems. The effect of sediment characteristics and habitat structure on macrozoobenthos communities is an important finding. Studies have shown how different species' preferences for certain sediment types affect their responses to changing environmental conditions. The alteration of sediment dynamics by climate change jeopardizes habitat suitability and causes potential decreases in species richness.

The interaction between eutrophication and climate change has yielded particularly striking results. The nonlinear effects of particulate organic carbon input on macrofaunal biomass have shown that nutrient loading can lead to unpredictable consequences on benthic fauna. This contributes to the formation of hypoxic conditions, especially in coastal areas. The role of macrozoobenthos in nutrient cycling and its contribution to ecosystem functioning is one of the important findings of our research. These organisms play a critical role in biogeochemical cycles and contribute significantly to the carbon cycle. However, the loss of biodiversity and the decrease in functional redundancy pose concerns about the future resilience of these ecosystems.

Changes in the spatial distribution of species are another important finding of this study. Climate warming is driving the expansion of boreal organisms, especially towards the poles, which significantly affects current community structures. These changes are critical for understanding the future dynamics of benthic ecosystems. The interaction of anthropogenic stressors and climate change further complicates the responses of macrozoobenthos communities. Understanding regional differences is fundamental for developing effective management and conservation strategies. These findings highlight the need to reduce the impacts of human activities.

Finally, this study highlights the importance of long-term monitoring programs and adaptive management strategies for the conservation of macrozoobenthos communities. The impacts of climate change have not only ecological but also socio-economic consequences. Therefore, future research and conservation efforts need to take these multifaceted impacts into account.

REFERENCES

Adella, C. (2023). Identification of macrozoobentos in the upstream of the brantas river, blitar. Jurnal Perikanan Pantura (Jpp), 6(2), 333-341.

Al-Izhar, M. Tanjung, A., & Elizal. (2023). Macrozoobenthos community structure in setan island, mandeh tourism area, pesisir selatan, west sumatra. Asian Journal of Aquatic Sciences, 6(2), 174-179.

Bellard, C., Bertelsmeier, C., Leadley, P., Thuiller, W., & Courchamp, F. (2012). Impacts of climate change on the future of biodiversity. Ecology Letters, 15(4), 365-377.

Blaen, P., Brown, L., Hannah, D., & Milner, A. (2013). Environmental drivers of macroinvertebrate communities in high arctic rivers (svalbard). Freshwater Biology, 59(2), 378-391.

Broman, E., Raymond, C., Sommer, C., Gunnarsson, J., Creer, S., & Nascimento, F. (2019). Salinity drives meiofaunal community structure dynamics across the baltic ecosystem. Molecular Ecology, 28(16), 3813-3829.

Bulling, M., Hicks, N., Murray, L., Paterson, D., Raffaelli, D., White, P., & Solan, M. (2010). Marine biodiversity–ecosystem functions under uncertain environmental futures. Philosophical Transactions of the Royal Society B Biological Sciences, 365(1549), 2107-2116.

Cohen, A., Gergurich, E., Kraemer, B., McGlue, M., McIntyre, P., Russell, J., Simmons, J.D., & Swarzenski, P. (2016). Climate warming reduces fish production and benthic habitat in lake tanganyika, one of the most biodiverse freshwater ecosystems. Proceedings of the National Academy of Sciences, 113(34), 9563-9568.

Dewenter, J., Yong, J., Schupp, P.J., Lõhmus, K., Kröncke, I., Moorthi, S., Pieck, D., Kuczynski, L., & Rohde, S. (2023). Abundance, biomass and species richness of macrozoobenthos along an intertidal elevation gradient. Ecology and Evolution, 13(12): e10815.

Dulić, Z., Marković, Z., Živić, M., Ćirić, M., Stanković, M., Simić, G., & Živić, I. (2014). The response of phytoplankton, zooplankton and macrozoobenthos communities to change in the water supply from surface to groundwater in aquaculture ponds. Annales De Limnologie - International Journal of Limnology, 50(2), 131-141.

Ehrnsten, E., Norkko, A., Müller-Karulis, B., Gustafsson, E., & Gustafsson, B. (2020). The meagre future of benthic fauna in a coastal sea—benthic responses to recovery from eutrophication in a changing climate. Global Change Biology, 26(4), 2235-2250.

Firn, J., Maggini, R., Chadès, I., Nicol, S., Walters, B., Reeson, A., Martin, T.G, Possingham, H.P., Pichancourt, J.B., Ponce-Reyes, R. & Carwardine, J. (2015). Priority threat management of invasive animals to protect biodiversity under climate change. Global Change Biology, 21(11), 3917-3930.

Gacheno, D., & Amare, G. (2021). Review of impact of climate change on ecosystem services—a review. International Journal of Food Science and Agriculture, 5(3), 363-369.

Gebruk, A. A., Borisova, P. B., Glebova, M. A., Basin, A. B., Simakov, M. I., Shabalin, N. V., & Mokievsky, V. O. (2019). Macrozoobenthos of the

shallow waters of pechora bay (se barents sea). Nature Conservation Research, 4(4), 1-11.
Gebruk, A., Dgebuadze, P., Rogozhin, V., Ermilova, Y., Shabalin, N., & Mokievsky, V. (2023). Macrozoobenthos of the pechora bay in 2020–2021 indicates a likely change of common bivalve molluscs in the arctic estuary. Polar Biology, 46(5), 473-487.
Gladyshev, M., Sushchik, N., Shulepina, S., Ageev, A., Dubovskaya, O., Kolmakova, A., … & Kalachova, G. (2015). Secondary production of highly unsaturated fatty acids by zoobenthos across rivers contrasting in temperature. River Research and Applications, 32(6), 1252-1263.
He, X., Liang, J., Zeng, G., Yuan, Y., & Li, X. (2019). The effects of interaction between climate change and land-use/cover change on biodiversity-related ecosystem services. Global Challenges, 3, 1800095.
Hoppit, G., & Schmidt, D.N. (2022). A regional view of the response to climate change: a meta-analysis of european benthic organisms' responses. Frontiers in Marine Science, 9, 896157.
Li, J., Lin, X., Chen, A., Peterson, A., Ma, K., Bertzky, M., Ciais, P., Kapos, V., Peng, C., & Poulter, B. (2013). Global priority conservation areas in the face of 21st century climate change. Plos One, 8(1), e54839.
Li, K., Liu, X., Zhou, Y., Yang, X., Lv, Q., Ouyang, S., & Wu, X. (2019). Temporal and spatial changes in macrozoobenthos diversity in poyang lake basin, china. Ecology and Evolution, 9(11), 6353-6365.
Link, H., Piepenburg, D., & Archambault, P. (2013). Are hotspots always hotspots? the relationship between diversity, resource and ecosystem functions in the arctic. Plos One, 8(9), e74077.
Mantyka-Pringle, C., Martin, T., & Rhodes, J. (2013). Interactions between climate and habitat loss effects on biodiversity: a systematic review and meta-analysis. Global Change Biology, 19(5), 1642-1644.
Mely, S., Hossain, M., Rahman, M., Albeshr, M., & Arai, T. (2023). Changes of macrobenthic diversity and functional groups in saltmarsh habitat under different seasons and climatic variables from a subtropical coast. Sustainability, 15(9), 7075.
Meyer, J., & Kröncke, I. (2019). Shifts in trait-based and taxonomic macrofauna community structure along a 27-year time-series in the south-eastern north sea. Plos One, 14(12), e0226410
Pecl, G., Araújo, M., Bell, J., Blanchard, J., Bonebrake, T., Chen, I., … & Williams, S. (2017). Biodiversity redistribution under climate change: impacts on ecosystems and human well-being. Science, 355(6332):eaai9214.
Pollack, J., Palmer, T., & Montagna, P. (2011). Long-term trends in the response of benthic macrofauna to climate variability in the lavaca-colorado estuary, texas. Marine Ecology Progress Series, 436, 67-80.
Ramadhaniaty, M., Ulfah, M., Nurfadillah, N., Amienatun, T., Syukran, M., Razi, N.M., Khalidin, K., & Muchlisin, Z.A. (2023). Macrozoobenthos diversity and heavy metal contamination in faunus ater in the rasian and asahan rivers in the southern coast of aceh, indonesia. Die Bodenkultur Journal of Land Management Food and Environment, 74(2), 81-89.
Renaud, P., Wallhead, P., Kotta, J., Włodarska-Kowalczuk, M., Bellerby, R., Rätsep, M., Slagstad, D., & Kukliński, P. (2019). Arctic sensitivity? suitable

habitat for benthic taxa is surprisingly robust to climate change. Frontiers in Marine Science, 6, 538.

Rinawati, F., Stein, K., & Lindner, A. (2013). Climate change impacts on biodiversity—the setting of a lingering global crisis. Diversity, 5(1), 114-123.

Solan, M., Bennett, E., Mumby, P., Leyland, J., & Godbold, J. (2020). Benthic-based contributions to climate change mitigation and adaptation. Philosophical Transactions of the Royal Society B Biological Sciences, 375(1794), 20190107.

Villnäs, A., Norkko, J., Lukkari, K., Hewitt, J., & Norkko, A. (2012). Consequences of increasing hypoxic disturbance on benthic communities and ecosystem functioning. Plos One, 7(10), e44920

Yan, J., Cui, B., Zheng, J., Xie, T., & Li, S. (2015). Quantification of intensive hybrid coastal reclamation for revealing its impacts on macrozoobenthos. Environmental Research Letters, 10(1), 014004.

Solar Energy and Solar Cells

Canan AYTUĞ AVA

Dr. Res. Asst. Canan Aytuğ Ava; Siirt University, Faculty of Engineering, Department of Electrical and Electronics, Siirt / Turkey.
cananaytug@hotmail.com, ORCID No: 0000-0003-4771-816X.

ABSTRACT

This study provides a detailed explanation of the historical development of solar energy and solar cells. The importance of solar energy and the advantages and disadvantages of renewable energy sources are also discussed. The development, characteristics, and types of solar energy, which is one of the renewable energy sources, and solar cells obtained by utilizing this energy, have been explained.

Keywords – Solar Energy, Solar Cells, Renewable Energy, Energy Sources.

SOLAR ENERGY

The presence of the sun, which is an indispensable element of the world of living beings and the most important factor ensuring the continuity of life, is crucial. The sun is the primary source of life, providing energy to both our planet and other planets, and is the only energy source with an almost infinite power. Humans and animals benefit from sunlight to feed, warm up, and simply survive, while plants use solar radiation to produce living tissue. As a result of the physical and chemical effects of solar radiation on materials, coal, oil, water potential, and wind energy emerge. The sun, being a thermonuclear reactor, emits energy at various wavelengths from each unit area per unit time. Only one-billionth of the energy filtered from the sun reaches the Earth's surface. Of the solar radiation that reaches the Earth's surface, 9.9% has a wavelength range between 0.2 and 3.0 mm. Outside the atmosphere, the average value of the solar radiation that hits a unit plane perpendicular to the sun's rays per unit time is 1353 W/m², and this is referred to as the "solar constant." After passing through the atmosphere, some of the solar radiation is reflected, while a certain amount is absorbed. The amount of solar radiation that reaches the Earth's surface can vary due to several reasons: it depends on the Earth's rotation around the sun (365 days, 6 hours) and its rotation around its own axis (24 hours), atmospheric conditions (cloudiness, humidity, visibility, etc.), and geographical factors (latitude, altitude).

The amount of solar radiation reaching a unit horizontal plane on the Earth's surface is typically between 400 and 800 W/m². The total solar radiation received by the Earth in one year is approximately 15,000 times the energy demand of the world. The amount of solar radiation that falls on a unit area varies depending on the seasons and latitude, particularly in the northern hemisphere. In countries with a latitude greater than 35° North, it is not very feasible to utilize solar energy during the winter months. In such cases, to maximize the use of solar radiation, the collector should be tilted at a specific angle relative to the horizontal by orienting it towards the south. If

the collectors are not facing south, both in our country and in countries further north, their efficiency is reduced.

Compared to fossil fuels and finite energy sources, solar energy has many advantages. Its most important feature is that it is the only inexhaustible energy source and the cleanest form of energy. It does not produce toxic waste such as smoke, gas, carbon monoxide, sulfur, or radiation, which are harmful to the environment. In local applications, the energy demand can be met with solar energy. For example, the energy needs of lighthouses, forest watchtowers, lighting for parks and gardens, street lamps, etc., can be met locally. This situation actually represents the freedom to produce energy without dependence on external sources. Thus, solar energy can be utilized with local technology and low operational costs without the need for complex technology. Despite these advantages of solar energy, the main reason for its limited application is the low amount of solar radiation that reaches a unit area, requiring large surfaces to capture enough energy. Since solar radiation is not continuous, it needs to be stored; however, storage options are limited. Additionally, during the winter months, when energy demand increases, solar radiation is lower, and there is almost no sunlight at night. Furthermore, solar energy systems need to have an unobstructed view of the sky to receive continuous solar radiation and avoid shading. For these reasons, solar energy cannot be applied everywhere.

In ancient times, famous scientists made use of solar energy in various ways. In the 5th century BC, Socrates increased the number of windows facing south in homes to allow more solar radiation to enter. In the 3rd century BC, Archimedes focused solar radiation using concave mirrors to burn enemy ships. In the 15th century, with Galileo's invention of the lens, there was an increase in solar energy research. In 1725, Belidor created the first water pump powered by solar energy. In 1839, French physicist Alexandre Edmond Becquerel discovered photovoltaic energy. In 1860, Mouchok focused solar radiation using parabolic mirrors to power a small steam engine, and in 1878, he succeeded in creating a cooling device based on solar energy, ultimately producing a block of ice. In 1913, Shuman and Boys created a steam generator using parabolic mirrors and successfully powered a 50 horsepower water pump that drew water from the Nile River. However, during and after World War I, with the growing importance of petroleum, studies on solar energy decreased. In 1939, Russell Ohl designed the solar cell and received the patent for his design in 1941. Later, the energy crisis, which progressed slowly, the powers controlling oil pipelines, and the potential for future wars made solar energy and the development of renewable energy sources a necessity. The major renewable energy sources include solar, wind, geothermal, biomass, fuel cells, wave (tidal), hydrogen, and nuclear energy.

Figure 1.

Turkey is a country with great diversity and potential in terms of renewable energy sources. Our country holds 8% of the world's geothermal energy potential and is in an advantageous position for solar energy. Additionally, due to its topography, Turkey has significant capacity for hydroelectric power generation and possesses considerable potential for wind energy as well.

Another prominent energy source among renewable resources is hydraulic energy. The most common method of utilizing this energy is by constructing dams on rivers to accumulate water, and then converting the potential energy of the stored water into electrical energy using turbines.

The accumulated water is released from a high point in the dam, and as it falls, the potential energy of the water is converted into kinetic energy. The falling water spins a machine called a turbine. The turbine converts the kinetic energy of the water into mechanical energy. The movement of the turbine drives a generator, which produces electricity. This electricity is then transmitted to the distribution network according to the plant’s production capacity.

The advantages of hydroelectric power plants that operate in this way are as follows: the water is naturally and cyclically replenished, there are almost no carbon emissions with low emissions, hydroelectric plants are a highly efficient energy source, and they provide a reliable and renewable form of energy. However, the disadvantages of hydroelectric plants include:

Ecological Impacts: Dams can have negative effects on river ecosystems and the surrounding fauna and flora.Displacement of Local Populations, The construction of dams can lead to the displacement of people from nearby villages.

High Initial Cost: The construction and maintenance of dams can be costly.

The future of hydroelectric energy could be brighter by developing more sustainable and environmentally friendly solutions to reduce these negative impacts.

One of the renewable energy sources, geothermal energy, is the Earth's natural heat and is defined as the thermal energy of pressurized hot fluids (steam, gas) and hot dry rocks accumulated in the Earth's crust. This energy is used for electricity generation and heating processes. Among renewable energy sources, solar energy can be considered a powerful and inexhaustible resource. Solar energy is a strong form of energy that results from the hydrogen-helium fusion reaction occurring in the core of the sun. This energy reaches Earth through sunlight and is directly converted into thermal energy or electrical energy using technologies such as solar collectors, solar power plants, and photovoltaic cells.

Biomass energy, one of the renewable energy sources, is a type of energy derived from the carbohydrate components found in plant and animal-based materials. Today, fuels such as bioethanol, biodiesel, and biogas are produced from these energy sources. Bioethanol and biodiesel are fuels obtained from various plants and animal fats. Biogas, on the other hand, is formed by the fermentation of organic materials (such as plant and animal waste, municipal and industrial waste) in an oxygen-free environment, mostly consisting of methane and carbon dioxide gases. In recent years, there has been an increased focus on cultivating plants for renewable energy production worldwide.

One of the renewable energy types is wind energy. This energy arises from the varying heating of the Earth's surface by sunlight. The different heating of the sea and air surfaces creates a pressure difference, and this difference causes the movement of air. Air moving from high pressure to low pressure generates wind. Systems such as Wind Energy Power Plants are used to produce electrical or mechanical energy from this source. Large areas covered by water, including seas and oceans, are the subject of various research aimed at utilizing their energy potential. Ocean energy production is derived from sources such as tidal movements, ocean heat, waves, currents, salinity, and methane gas.

Tidal energy is generated by the rise and fall of sea and ocean levels due to the Moon's gravitational pull. Calculations show that the tidal movements in the oceans have an energy capacity of about 3000 TWh per day. It is possible to convert 2% of this energy (60 TWh) into electrical energy. On Earth, there are 40 tidal regions with a level difference of more than 5 meters, and regions with high tidal energy include Europe, the Philippines, Indonesia, China, and Japan.

The wave energy potential generated by winds over the sea is quite high, and various technologies have been developed to harness this energy.

SOLAR CELLS

Solar cells are systems that directly convert light energy into electrical energy (photovoltaic). The main component of the photovoltaic systems found in solar panels is the solar cells. The structural foundation of solar cells is based on semiconductor technology, which plays a critical role in the electronic world. On the upper surface of solar cell modules, there are anti-reflective coatings and protective layers to prevent breakage and energy losses. In the lower layers, N-type and P-type semiconductor materials are present. These materials are obtained by processing semiconductor substances with specific additives while in a molten state. To explain in more detail: In the first layer, there is a surface coating that prevents light reflection and enhances light absorption. Beneath this, there is a protective front contact layer. In the lower layer, there is N-type silicon, which is created by displacing phosphorus atoms, resulting in the formation of negative charges. This layer is known as the N-type. In the layer beneath that, there is P-type silicon, where the displacement of atoms leads to the formation of positive charges. A solar cell typically generates a voltage between 0.5V and 0.6V. The current value varies depending on the size of the cell. As the surface area increases, the amount of electrons moving from the N-type layer to the P-type layer will increase, which causes the current to rise. In summary, the structure and operation of a solar cell are as follows: Solar light is absorbed by the photovoltaic cells on the solar cell. These cells contain P-type semiconductor material with an excess of electrons and N-type semiconductor material with a deficit of electrons. The sunlight frees electrons from the P-type semiconductor material. The freed electrons, due to their energy, move towards the N-type semiconductor material. This flow of electrons creates a steady one-way flow, generating direct current (DC). The electrons pass through the circuit and are used in applications such as charging batteries, and eventually return to the P-type semiconductor material.

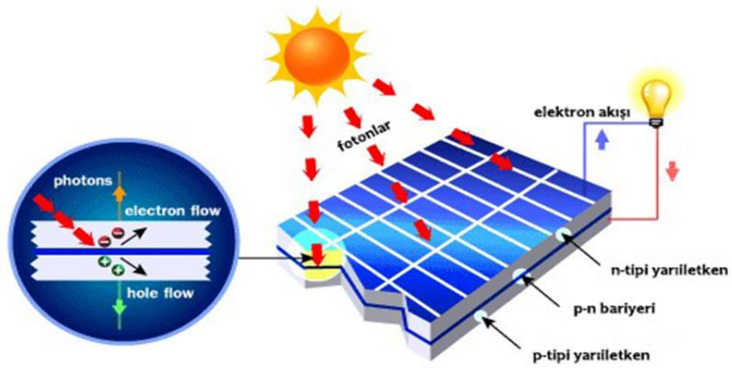

Figure 2. Solar Cell System

Solar cells are connected in series to form solar panels. For solar panels to generate electricity most efficiently, certain conditions must be at ideal levels. Some of the important conditions include system losses, the amount of solar radiation, wind speed and direction, temperature and humidity, panel cleanliness, air pollution, and the structure and efficiency of the solar panel. Solar cells are manufactured in different types based on the semiconductor materials and additives they contain. The efficiency and operating conditions of each type vary. The most commonly used types are inorganic solar cells. These cells are further divided into three main categories:

When solar cells are classified based on their production techniques, the categories are:

***MonocrystallineSolarCells**:*
The atomic structure of the material is homogeneous, meaning that the silicon atoms are arranged in a single, continuous crystal lattice. Monocrystalline solar cells have the highest efficiency compared to other types, typically around **20%**. They are known for their high performance but also tend to be more expensive due to the complex manufacturing process required to create them.

***PolycrystallineSolarCells**:*
Polycrystalline cells are made from silicon crystals that are not continuous but instead consist of multiple smaller crystals. As a result, the atomic structure is not as uniform as that of monocrystalline cells. These cells are less expensive to produce and typically have a lower efficiency compared to monocrystalline cells. However, their cost-to-efficiency ratio makes them the most common type of solar cells on the market.

AmorphousSiliconSolarCells:
These solar cells lack a crystalline structure entirely and are often referred to as thin-film solar cells. Because of the absence of a crystal lattice, they are less efficient, with efficiencies typically ranging from 5% to 8%**.** However, they are flexible and can be produced at a lower cost, which makes them suitable for applications where space and weight are important considerations, such as on curved surfaces or in portable devices.

CIS Solar Cells:
CIS (Copper-Indium-Diselenide) solar cells are thin-film solar cells with an efficiency of around 10%. Their thin structure provides several advantages, such as ease of installation, lower costs, and the ability to be applied easily over large surfaces. Additionally, the lightweight nature of CIS cells makes them suitable for various applications. These properties contribute to the growing interest in CIS solar cells, as they offer a cost-effective alternative to traditional solar cell technologies, while still maintaining a competitive level of efficiency.
Perovskite Solar Cells: Perovskite is a natural mineral structure that has been adapted for use in synthetic form to create perovskite solar cells.

REFERENCE

A. Kılıç. Günes Enerjisi ve Uygulamaları (1983).

Farber, E.A.; Solar energy, its conversion and utilization, solar Energy, 14, s.243-252(1973)

Gizlenci, Ş., Acar, M., Şahin, M. (2012). "Türkiye'de Yenilenebilir Enerji Kaynaklarının (Biyodizel, Biyoetanol ve Biyokütle) Projeksiyonu," Tarım Makinaları Bilimi Dergisi, sayı 8 (3), s. 337-344.

Güneş Enerjisi ve Teknolojisi. https://akademi.alarko-carrier.com.tr/sosyal-ogrenme/gunes-enerjisi-ve-teknolojisi

Koç, E., Kaya, K. (2015). "Enerji Kaynakları–Yenilenebilir Enerji Durumu," Mühendis ve Makina, cilt 56, sayı 668, s. 36-47.

Koltukçu, H. 2010. "Yenilenebilir Enerji Kaynaklarının Türkiye Açısından SWOT Analizi," Yüksek Lisans Tezi, Dumlupınar Üniversitesi Sosyal Bilimler Enstitüsü, Kütahya, 136 s.

McVeigh J.C.; Sun Power, an Introduction to thi Application of Solar Energy, Pergamon Press (1977)

Robotiksistem.com

Saliba, Michael; Correa-Baena, Juan-Pablo; Grätzel, Michael; Hagfeldt, Anders; Abate, Antonio 2017. "Perovskite Solar Cells: From the Atomic Level to Film Quality and Device Performance". A Journal of the German Chemical Society. doi:10.1002/anie.201703226

Yenilenebilir Enerji Araştırmaları Derneği. https://yenader.org/tr_tr/gunes-enerjisi-nedir.

Yılmaz, M. 2012. “Türkiye’nin Enerji Potansiyeli ve Yenilenebilir Enerji Kaynaklarının Elektrik Enerjisi Üretimi Açısından Önemi,” Ankara Üniversitesi Çevre Bilimleri Dergisi, sayı 4 (2), s. 33-54.
T.C. Enerji ve Tabii Kaynaklar Bakanlığı. https://enerji.gov.tr/bilgi-merkezi-enerji-gunes

Rare Earth Metals of CeO_2 Used in Supercapacıtors

Murat ATES[1, 2]

1- Prof. Dr..; Tekirdağ Namık Kemal Üniversitesi, Fen-Edebiyat Fakültesi, Kimya Bölümü. mates@nku.edu.tr ORCID No: 000-0002.-1806-0330
2- Nanochem Polymer Energy Company, Slihtaraga Mah., University 1st street, Number: 13/1, Z242/2, Tekirdag, Turkiye.

ABSTRACT

Rare earth metals are critical important in the preparation of electrode materials for supercapacitors. There are many different studies especially in Cerium oxide (CeO_2) in energy storage systems. In this review article, rare earth metal of CeO_2 nanoparticles were focused in the one of the significant components of electrode materials for supercapacitor applications. Cerium-based oxide nanomaterials have taken more interests because of more existence of cerium element in the world and good redox properties (Das et al., 2020). CeO_2 is an appropriate metal oxide as a rare-earth element sustainable future energy system due to its eco-friendly, low toxicity and the most existence of abundant element in the lanthanide series (Kim et al., 2019; Dahle and Anal, 2015; Castano et al., 2015). In this review study, CeO_2 is investigated as a component of electrode materials in supercapacitors. Electrode materials, electrolyte solution and binders / membranes of supercapacitors are also presented for this critical issue.

Keywords – Supercapacitor, Rare Earth Metals, Cerium Oxide, Electrode Material, Pseudocapacitance.

INTRODUCTION

Fossil fuels have been consumed for development of industrial area. So, supercapacitors have become a critical issue to solve this problem (Dincer and Abu-Rayash, 2020; Lerman et al., 2021).

Supercapacitors or electrochemical capacitors is a device to store electrical energy. They use in various applications, such as memory devices, mobile phones, digital cameras, etc. (Shayeh et al., 2015). The term of "supercapacitor" was firstly intrıduced by an electrical company in 1978 (Conway, 2013). In literature, there are three kinds of mechanisms for supercapacitors. These are electrochemical double layer capacitors (EDLCs), pseudocapacitors (PCs), and hybrid capacitors (HC).

Supercapacitors have more advantages, such as good charge/discharge capability, high power density, and rapid rate capability (Chen at al., 2014). In EDLCs mechanism, the electrode materials are made up of carbon materials, such as graphene, active carbon, carbon nanotube, etc. EDLCs system is a non-Faradic process.However, in PCs mechanism, the electrode material constitutes metal oxides, conductive polymers, and transtion metal oxides. PCs, where electroactive materials with strong charge interclating type compounds like CeO_2, RuO_2, NiO_2, etc. or conducting polymers (CPs). All of the PCs are Faradic process (Ambade et al., 2013; Miller and Simon, 2008).

Both EDLCs and PCs are used in a supercapacitor device that it can be called as hybrid capacitors (HC), which supplies higher electrochemical performances (higher power, higher energy, better charge/discharge stability (Kate et al., 2018).

Type of electrode materials mostly affecs the electrochemical performance of supercapacitor device. It can be controlled the surface area, pore size distribution, fast charge transfer and goos cyclic stability. An important strategy is to fabricate composite material, which can be affected by pore size, electrical conductivity and surface area. Pore size distribution in electrode material supply in the mobility, transport of ions, rate capability and electrochemical performance of supercapacitor (Hodaei et al., 2018).

Rare earth metals can be used as a critical component in supercapacitor electrode preparation. It is preferrable due to their low resistance results in high electrochemical performances (Gonzalez et al., 2016). Porous transtion metal oxide nano-materials have been used in supercapacitors due to their mesoporosity, good electrochemical study and large surface area. Therefore, they supply high energy storage performance (Ramulu et al., 2020).

CeO_2 based materials have good effects on electrochemical behavior of composite materials. It supplies a protective agent in supercapacitor applications. Due to its extra physochemical behavior, rare earth minerals such as CeO_2 has been mostly used in supercapacitor studies recently (Kowsuki et al., 2023). Moreover, CeO_2 materials have positive contribution of electrocatalytic activity (Li et al., 2011).

There are a few critical issue used in the performance of energy storage systems. In this review article, electrode materials, electrolyte solutions and membranes are presented to explain the effects of electrochemical performance of supercapacitors. There is an important strategy to improve the electrochemical performance of supercapacitors that the best choice of the electrode material (Li et al., 2019). CeO_2 nanoparticles have been critically investigated in this review article.

ELECTRODE MATERIALS

Nanoparticles in metal oxides have high redox properties. Therefore, they can be mostly used in supercapacitor electrode materials (Cui et al., 2016). In literature, there are many studies related to CeO_2 nanoparticles in supercapacitor applications. For example, Mazloum-Ardakani et al. have prepared a graphene aerogel/CeO_2 nanoparticles (Mazloum et al., 2019). Many techniques were presented to characterize the nanocomposite material, such as XRD, XPS, Raman, FTIR-ATR, BET, CV, GCD and EIS. The highest specific capacitances were obtained as C_{sp}= 365 F/g at 5 mV/s by CV method and C_{sp}= 376.2 F/g at 0.5 A/g by GCD method. It has also high capacitance protection of 92.4% after 4000 cycles using CV method.

Yari et al. have studied $CeMo_2O_8$/GO nanocomposites as the electrode material (Yari and Fathabad, 2020). $CeMo_2O_8$ nanoparticles and different dopants such as N and P together with rGO using heat-treatment process for electrode preparation enable high electrochemical performance of supercapacitive performance. CeO_2 can be used in different materials to enhance their electrochemical properties in supercapacitors such as CeO_2/graphene (Wang et al., 2011), CeO_2/NiO (Padmanathan and Seliadurais, 2014) and CeO_2/MnO_2 (Zhu et al., 2015).

Pakzad et al (Pakzad et al., 2023) have presented an electrocatalys including Ce element. CeO_2 has a ground state of $4f^15d^16s^2$ electronic configuration. Therefore, it can be obtained loosing of electrons in the electronic configuration. The low electrical conductivity causes the limitation of their energy storage applications. So, different types of materials such as graphene quantum dots solve this problem because of combination of a few materials (Nemati et al., 2022). Cerium-doped δ-MnO_2 (1.5%) microspheres have been presented a good electrochemical performance (C_{sp}=382.38 F/g) at 1 A/g. The addition of cerium dopant of material supply a good ion transport kinetics, decreasing the way and improve the ion transportation rate by adjusting the pore size, electrical conductivity of MnO_2 material and particle size (Wang et al., 2015). CeO_2/hydroxide-nickel hydroxide composite enables an easy transfer of ions and electrons during charge/discharge processes. Three-electrode was evaluated in 2 M KOH solution. The best electrode material shows good electrochemical performances (E=54 Wh/kg, P=1.28 kW/kg) (Wiston et al., 2023).

In recent years, CeO_2 is the high popularity among all rare earth metal oxides (Guo et al., 2021, Saravanakumar et al., 2012). Rhombus shaped CeO_2 sheets were prepared an easy, soft chemical approach in the literature (Talluri et al., 2022). It has a high capacitance (C_{sp}= 481 F/g at 5 mV/s) and capacitive protection of 92% of initial capacitance after 500 cycles. PANI was integrated to graphene/CeO_2 composite using in-situ polymerization technique and its electrochemical performances (C_{sp}= 454.8 F/g at 1 A/g and 70.23% after 10.000 cycles at 5 A/g) (Xie et al., 2018). In the other study, Ce doped MOF and rGO study shows a good electrochemical performances (C_{sp}= 556.3 F/g at 2 mV/s, E=60 Wh/kg, P=450 W/kg). It only decreases an initial capacitance of onyl 3.7% for 4000 cycles (Baizoki et al., 2022).

Asymmetric supercapacitor design supplies the large operating voltage (Tian et al., 2020). As a result, HC can be used to obtain a high capacitance, energy and power densities. So, both EDLC and PCs systems were combined to form electrode material (Selvamani et al., 2021). In addition, CeO_2 nanoparticles help to reduce defects of composite materials (Saravanan et al., 2015). In literature, cerium vanadate and polypyrrole ($CeVO_4$/PPy) composite was obtained by an easy heat-treatment method (Ponnaiah and Prakash, 2021). It has a high electrochemical performances (C_{sp}= 116 F/g,

E= 52.2 Wh/kg, P= 675.9 W/kg, and capacitance retention of 77.8% after 10.000 cycles).

CeO_2 and $LaMnO_3$ were mixed to form nanocomposite by hydrothermal method (Nagamutha et al., 2017). It has a good electrochemical performances (C_{sp}= 262 F/g at 1 A/g, E= 17,2 Wh/kg, P= 1015 W/kg). The CeO_2/$LaMnO_3$ nanocomposites have taken BET analysis and shoed a type IV hysteresis loop. Moreover, CNT@CeO_2 composite showed a good elecrtrochemical performances (70.7 Ah/cm^2 at 1 mA/cm^2, E=0.041 Wh/cm^2 at 1 A/cm^2 and good stability of 86.4%). SCs have limited energy density compared to batteries (El Kady et al., 2012; Pech et al., 2010).

ELECTROLYTE SOLUTIONS

CeO_2 has good surface morphologies due to porous structures and penetration of electrolyte ions. Pandit et al. have presented a paper including CeO_2 materials that it has a good electrochemical performances (C_{sp}=750 F/g and E= 61.4 Wh/kg) (Pandit et al., 2019).

In literature, CeO_2 has been reported extensively for supercapacitor applications (Mogensan et al., 2000). It has presented in various sectors, such as automotive exhaust cleaning (Masur et al., 2000), electro-chromic evaluations (Ozer, 2001), hybrid solar cells (Lira-Cantu and Krehs, 2006), and more recently for medicine evaluations (Mandal et al., 2010). Lee at al. have reported a highly pseudocapacitive performance and eco-friendly co-precipitated CeO_2 materials. It has a high electrochemical performances (C_{sp}=559 F/g) (Lee at al., 2021).

BINDERS / MEMBRANES

An electrolyte type and ionic conductivity plat a significant role on supercapacitors (Zhu et al., 2018). Especially, large porous materials and cavities, big surface areas and high electrical conductive materials supply extra ion transmission channels and minimize volume fkuctuations so they supply a good electrochemical perfromance of supercapacitors (Wei et al., 2022). A good choice electrolyte causes wider temperature, large voltage range, and good ionic conductivity, large cycle life, excellent biocompatibility usage, cheaper and eco-friendly (Jaiswal ey al., 2021).

RESULTS AND DISCUSSION

In this chapter, CeO_2 metal oxide was examined in supercapacitor applications. It can be used for the fabrication of SCs due to their good catalytic behavior, economic, fast redox properties, low toxicity and

adjastable pore size (Mazloum-Ardakani et al., 2020). In the world, Cerium (Ce) element exists more than tin and copper metals. It can be used one of the component to develop a capacity of cathode materials in hybrid supercapacitors on a large scale.

REFERENCE

Ambade RB, Ambade SB, Shrestha NK, Nah YC, Han SH, Lee W, Lee SH (2013). Polythiophene infiltrated TiO_2 nanotubes as high-performance supercapacitor electrodes. Chem. Commun., 49, 2308-2310.

Barzoki MF, Fatemi S, Ganjali MR (2022). Fabrication and comparison of composites of cerium metal-organic framework / reduced graphene oxide as the electrode in supercapacitor applications. J. Energy Storage, 55, Article number: 105545.

Castano CE, O'Keefe MI, Fahrenhoktz WG (2015). Cerium-based oxide coatings. Curr. Opin. Solid State Mater. Sci., 19, 69-76.

Chen Z, Yu D, Xiong W, Liu P, Liu Y, Dai L (2014). Graphene-based nanowire supercapacitors. Langmuir, 30, 3567-3571.

Cui C, Xu J, Wang L, Guo D, Mao M, Ma J, Wang T (2016). Growth of $NiCo_2O_4$@$MnMoO_4$ nano-column arrays with superior pseudocapacitors properties. ACS Appl. Mater. Interfaces, 8, 8568-8575.

Conway BE (2013). Electrochemical Supercapacitors: Scientific Fundamentals and Technological Applications, Springer Science & Business Media, 2013.

Dahle JT, Anal Y (2015). Environmental geochemistry of cerium applications and toxicity of cerium oxide nanoparticles. Int. J. Environ. Res. Publ. Health, 12, 1253-1278.

Das AK, Pan UN, Sharma V, Kim NH, Lee JH (2020). Nanostructured CeO_2/NiV-LDH composite for energy storage in asymmetric supercapacitor and as methanol oxidation electrocatalyst. Chem. Eng. J., Article number: 128019.

Dincer I, Abu-Rayash A. Chapter 2-energy sources, In Dincer I, Abu-Rayash A, editors. Energy Sustainability, Academic Press (2020), 19-58.

El Kady MF, Strong V, Dubin S, Kaner RB (2012). Laser scribing of high performance and flexible graphene based electrochemical capacitors. Science, 335, 1326-1330.

Guo D, Yuan J, Tang Y, Song C, Wang D (2021). Self-assembled PANI/CeO_2/$Ni(OH)_2$ hierarchical hybrid sphere with improved energy storage capacity for high-performance supercapacitors. Electrochim. Acta, 367, Article number: 137525.

Gonzalez A, Golkolea E, Barrena JA, Mysyk R (2016). Review on supercapacitors technologies and materials. Renewable Sustainable Energy Rev., 58, 1189-1206.

Hodaei A, Dezfuli AS, Naderi HR (2018). A high performance supercapacitor based on N-doped TiO2 nanoparticles. J. Mater. Sci., 29, 14596-14605.

Jaiswal KK, Dutta S, Pohrmen CB, Verma R, Kumar A, Ramaswamy AP (2021). Biowaste chicken eggshell-derived calcium oxide for photocatalytic application in methylene blue dye degradation under natural sunlight irradiation. Inorg. Nanometal Chem., 51, 995-1004.

Kate RS, Khalate SA, Deokate RJ (2018). Overview of nanostructured metal oxides and pure nickel oxide (NiO) electrodes for supercapacitors: a review, J. Alloys Compd. 734, 89-111.

Kowsuki K, Nirmala R, Ra YH, Navamathavan R (2023). Recent advances in cerium oxide-based nanocomposites in synthesis, characterization, and energy storage applications: A comprehensive review. Results in Chemistry, 5, Article number: 100877.

Kim SK, Pukird S, Chaiyo P, Inchidijui P, Bae G, Jung HK, Lee SS, An KS (2019). Superb pseudocapacitance observed from eco-friendly multi-dimensional quaternary composite electrode based on Ce and Cu oxides and sulfides. Ceram. Int., 45, 11114-11118.

Lee CE, Choi SH, Kim HY, Lee SS, Kim SK, An KS (2021). Enhanced pseudocapacitive performances of eco-friendly co-precipitated Fe-doped cerium oxide nanoparticles. Ceramics International, 47, 21988-21995.

Lerman LV, Benitez GB, Gerstiberger W, Rodriques GB, Frank AG (2021). Sustainable conditions for the development of renewable energy systems: a triple bottom line perspective sustain cities Soc., 75, Article number: 103362.

Li X, Liu X, Zheng T, Jiang D, Zhou Z, Liu C, Zhang X, Zhang Y, Losic D (2019). Tuning MnO_2 to FeOOH replicas with bio-template 3D morphology as electrodes for high performance asymmetric supercapacitors. Chem. Eng. J., 370, 136-147.

Li X, Zhang LH, Zhang C, Zhao M, Gong MC, Chen YQ (2011). Effects of La_2O_3 contents on the $Pd/Ce_{0.8}Zr_{0.2}O_2/La_2O_3$ catalysts for methanol decomposition. J. Rare Earths, 29, 544-549.

Lira-Cantu M, Kresh FC (2006). Hybrids solar cells based on MEH-PPV and thin film semiconductor oxides (TiO_2, Nb_2O_5, ZnO, CeO_2 and CeO_2-TiO_2) performance improvement during long-time irradiation. Sol. Energy Mater. Sol. Cells, 90, 2076-2086.

Mazloum-Ardakani M, Mohammadian-Sarcheshmeh H, Naderi H, Farbod F, Sabaghian F (2019). Fabrication of a high-performance hybrid supercapacitor using a modified graphene aerogel/cerium oxide nanoparticle composite. Journal of Energy Storage, 26, Article number: 100998.

Mazloum-Ardakani M, Sabaghian F, Yavari M, Ebady A, Sahraie N (2020). Enhance the performance of iron oxide nanoparticles in supercapacitor applications through internal contact of Fe_2O_3@CeO_2 core-shell. J. Alloys Compds. 819, Article number: 152949.

Mandal C, Pagliari F, Pagliari S, Forte G, Di Nordo P, Licoccia S, Travesa E (2010). Stem cell aligned growth induced by CeO_2 nanoparticles in PLGA scaffolds with improved bioactivity for regenerative medicine. Adv. Funct. Mater, 20, 1617-1624.

Masur T, Ozaki T, Machida KI, Adachi GY (2000). Preparation of ceria-zirconia sub-catalysts for automotive exhaust cleaning. J. Alloys Compd., 303-304, 49-55.

Miller JR, Simon P (2008). Materials Science-Electrochemical capacitors for energy management. Science, 321 (5889), 651-652.

Mogensen M, Sammes NM, Tompsett GA (2000). Physical, chemical and electrochemical properties of pure and doped ceria. Solid State Ionics, 129, 63-94.

Nagamutha S, Vijayakumar S, Ryu KS (2017). Cerium oxide mixed $LaMnO_3$ nanoparticles as the negative electrode mixed $LaMnO_3$ nanoparticles as the negative electrode for aqueous asymmetric supercapacitor devices. Mater. Chem. Phys., 199, 543-551.

Nemati F, Rezaie M, Tabesh H, Eid K, Xu G, Ganjali MR, Hosseini M, Karaman C, Erk N, Show PL, Zare N, Karimi-Maleh H (2022). Cerium functionalized graphene nanostructures and their applications, A review. Environmental Research, 208, Article number: 112685.

Ozer N (2001). Optical properties and electrochromic characterization of sol-gel deposited ceria films. Sol-Energy Mater. Sol. Cells, 66, 391-400.

Pakzad P, Mehrpooya M, Pourfayaz F, Ganjali MR (2023). Electrochemical aspects of Co_3O_4 nanorods supported on the cerium doped porous graphitic carbon nitride nanosheets as an efficient supercapacitor electrode and oxygen reduction reaction electrocatalyst. Int. J. Hydrogen Energy, 48, 16294-16319.

Padmanabhan N, Seliadurai S (2014). Electrochemical capacitance of porous NiO-CeO_2 binary oxide synthesized via sol-gel technique for supercapacitor. Ionics, 20(3), 409-420.

Pandit B, Kumar N, Koinkar PM, Sankapal BR (2019). Solution processed nanostructured cerium oxide electrode: Electrochemical engineering towards solid-state symmetric supercapacitor device. J. Electroanal. Chem., 839, 96-107.

Pech D, Bruret M, Durou H, Huang P, Mochalin V, Gogotsi Y, Taberna PL, Simon P (2010). Ultrahigh power micrometer-sized supercapacitors based on onion-like carbon. Nat. Nanotechnol., 5, 651-654.

Ponnaiah SK, Prakash P (2021). A new high performance supercapacitor electrode of strategically integrated cerium vanadium oxide and polypyrrole nanocomposite. Int. J. Hydrogen Energy, 46, 19323-19337.

Ramulu B, Nagaraju G, Sekhar SC, Yu JS (2020). Highly porous CNTs knotted cerium oxide hollow tubes with exalted energy storage performance for hybrid supercapacitors. J. Alloys Compd., 819, Article number: 152942.

Saravanakumar B, Purushothaman KK, Muralidharan G (2012). Interconnected V_2O_5 nanoporous network for high-performance supercapacitors. ACS Appl. Mater. Interfaces, 4, 4484-4490.

Saravanan T, Shanmugam M, Anandan P, Vanandhan M, Hayakawa Y, Jayavel R (2015). Facile synthesis of graphene-CeO_2 nanocomposites with enhanced electrochemical properties for supercapacitors. Dalton Trans., 44, 9901-9908.

Selvamani PS, Vijaya JJ, John Kennedy L, Saravanakumar B, Clament Sagaya Selvam N, Sophia PJ (2021). Facile microwave synthesis of cerium oxide@molybdenum disulfide @ reduced graphene oxide ternary composites as high performance supercapacitor electrode. J. Electroanal. Chem., 895, Article number: 115401.

Shayeh JS, Ehsani A, Gonjali MR, Norauzi P, Jaleh B (2015). Conductive polymer reduced graphene oxide / Au nanoparticles as efficient composite materials in electrochemical supercapacitors, Appl. Surf. Sci., 353, 594-599.

Talluri B, Yoo K, Kim J (2022). Novel rhombus-shaped cerium oxide sheets as a highly durable methanol oxidation electrocatalyst and high-performance supercapacitor electrode material. Ceramics Int., 48, 164-172.

Tian D, Song N, Zhang M, Lu X, Wang C (2020). Bimetallic MOF nanosheets decorated on electrospun nanofibers for high-performance asymmetric supercapacitors. ACS Appl. Mater. Interfaces, 12, 1280-1291.

Xie A, Tao F, Li T, Wang L, Chen S, Luo S, Yao C (2018). Graphene/Cerium oxide /porous polyaniline composite as a novel electrode material for supercapacitor. Electrochim. Acta, 261, 314-322.

Yari A, Fathabad SH (2020). A high-performance supercapacitor based on cerium molybdate nanoparticles anchored on N, P, co-doped reduced graphene oxide nanocomposite as the electrode. J. Mater. Sci.: Mater. Electronics, 31, 13051-13062.

Wang G, Ma Z, Zhang G, Li C, Shao G (2015). Cerium-doped porous K-birnessite manganese oxides microspheres as pseudocapacitor electrode material with improved electrochemical capacitance. Electrochim. Acta, 182, 1070-1077.

Wang Y, Guo CX, Liu JH, Chen T, Yang HB (2011). CeO_2 nanoparticles / graphene nanocomposite-based high performance supercapacitor. Dalton Trans., 40(24), 6388-6391.

Wei C, Sun J, Zhang Y, Liu Y, Guo Z, Du W, Liu L, Zhang Y (2022). Hierarchical $Ni(OH)_2$-MnO_2 hollow spheres as an electrode material for high-performance supercapacitors. Inorg. Chem. Front., 9, 3542-3551.

Wiston BR, Tewatia S, Ashok M (2023). Insights into co-precipitated cerium oxide / hydroxide-nickel hydroxide composite for high efficacy supercapacitors. Materials Today Sustainability, 21, Article number: 100291.

Zhu SJ, Jia JQ, Wang T, Zhao D, Yang J, Dang F, Shang ZG, Zhang YX (2015). Rational design of octahedron and nanowire CeO_2@MnO_2 core-shell heterostructures with outstanding rate capability for symmetric supercapacitors. Chem. Commun., 51(80), 14840-14843.

Zhu Y, Li N, Lv T, Yao Y, Peng H, Shi J, Cao S, Chen T (2018). Ag-doped PEDOT: PSS/CNT composites for thin film all solid state supercapacitors with a stretchability of 480%. J. Mater. Chem. A. 6, 941-947.

Green Chemıstry Applıcatıons in Nanopartıcle Synthesıs

Nurhan GÜMRÜKÇÜOĞLU[1]

1. Prof. Dr. Nurhan GÜMRÜKÇÜOĞLU, Karadeniz Technical University, Vocational School of Health Sciences, Department of Medical Services and Techniques, 61080, Trabzon, TURKEY, ngumrukcuoglu@ktu.edu.tr, ORCID No: 0000-0002-9669-6318

INTRODUCTION

Many chemical products such as medical products, plastics, cosmetic products, fabrics, pesticides, liquid crystals and artificial organs make our lives easier; However, there is a problem of waste generated both during production and after use. As a result, treatment technologies are needed in the production sector to eliminate these growths, which increase in amount and diversity. It is not affected by the structure of the green chemistry that will be used to eliminate these negativities that may arise from traditional chemistry methods at their source.

Basic principles of green chemistry; aiming to avoid pollution without obstructing the cleaning site, consumption of maximum atom economy, amount of toxic substances, use and properties of safe chemicals, classification of additives (solvents, separation elements), supported by synthetic methods at appropriate temperature and pressure, the raw material used, whenever possible, even if technically or economically to be extended instead of being thrown away, to minimize unnecessary derivatization if possible or not to do it at all, to design catalytic reagents in a better working condition than stoichiometric reagents, to not turn into harmful products for a long time and not to persist in the environment, to operate the production process continuously and control it before the formation of hazardous parts.

It is the choice of analytical methods to provide options and to minimize the risks of chemical accidents, including the use of chemical methods and maddening explosion or deflagration.

GREEN CHEMISTRY

Economic development is a more pronounced climate change. It has caused environmental degradation, manifested by increased depletion in the ozone layer and accumulation of organic pollutants in all parts of the biosphere. Deterioration and environmental risk factors include the use of natural resources. It has revealed the need to seek solutions to balance economic growth and environmental protection.

As a result of these; the need to seek solutions to protect the environment. It also increased awareness about environmental protection. Technologies called “green” have gained great importance. With green technologies, chemicals are subjected to green processes. In this context, the concept of sustainable or green chemistry constitutes a concept associated with chemical products and processes that reduce or eliminate the use and production of harmful substances. Green chemistry has an ecological approach; As a new branch of chemistry, it refers to reducing or eliminating the use of harmful substances in chemical processes and also reducing the formation of toxic and harmful intermediate products (Ivanković et al., 2017).

The concept of green chemistry was introduced in the workshop "IUPAC Synthetic Pathways and Processes in Green Chemistry. Green chemistry is the study of chemical science and chemical production that is sustainable, safe and non-polluting, and produces little or no waste materials; It is an application that consumes minimum energy and resources. As a rapidly developing sub-discipline in the field of chemistry, it has a wide range of chemical knowledge.

Thanks to this knowledge, it implements practices in a way that minimizes the production, use, final disposal of chemicals, material consumption, and the exposure of other living organisms, including humans, to toxic substances and chemicals. While performing the application, it provides the most economical cost; chooses the most efficient chemistry application possible (Stanley and Manahan, 2006). The idea of green chemistry was first developed in the 1990s under the "Pollution Prevention Act" as a solution to prevent pollution instead of treatment and disposal. As a result, the main goals of green chemistry used and developed to date are as follows (Ivanković et al., 2017).

- Conducting research in the field of catalytics and biocatalytics to obtain highly selective, pure compounds without the formation of toxic by-products,
- Finding new harmless and renewable raw materials such as biomass,
- Designing less toxic and eco-compatible chemicals,
- Discovery and testing of new alternative reaction conditions such as microwave, ultrasound and light reaction,
- Researching alternative ways to purify toxic air and water.

With the realization of these determined goals, green chemistry is constantly making changes in industrial practices; produces new applications; It cleans pollution and becomes the heart and soul of industrial ecology. The benefits of green chemistry can be generally listed as follows:

- Provides competitive advantage.
- It ensures the protection of the environment and human health.
- It makes the working environment safer.
- It helps to create safer final products.
- It reduces the risk of accidents by ensuring that reactions proceed in safer ways.
- It reduces waste material generation.
- It reduces regulatory and production costs.
- It is intended to save energy.
- Economical by providing new reactions that will reduce production costs provides benefits.

In line with these benefits, green chemistry aims to reduce and eliminate hazard by rejecting the need for exposure control, rather than limiting risk by controlling exposure to harmful chemicals. 12 basic principles of green

chemistry function in achieving these goals. These are as follows (Ivanković et al., 2017).

1. Prevention: Preventing the formation of waste materials and/or by-products; It states that it is better than processing or cleaning.
2. Atomic economy: It refers to designing methods to maximize the inclusion of all products participating in the reaction process in the final product. Logically, atomic economics and the principle of prevention are interconnected. Because both ultimately aim to reduce the amount of waste. In order to reduce and prevent waste, product inclusion in the final product must be maximized.
3. Less harmful chemical syntheses: It refers to using and producing substances that have less or no toxicity to human health and the environment wherever applicable. Redesigning these processes and reducing these risks is an important task of green chemistry. In this context, replacing harmful chemicals with biological enzymes makes industrial processes both cleaner and cheaper.
4. Designing safer chemical substances: It means that the product design should be safe in terms of human health and the environment, and in this way, safer chemical substance design is designed to minimize the toxicity of chemical products. Maintaining both product functionality and effectiveness and minimizing toxicity can be one of the most challenging aspects of designing safer products and processes; For this, it is necessary to understand both chemistry and the principles of toxicology and environmental sciences very well.
5. Safer solvents: The solvent chosen for a particular reaction should not pollute the environment or pose a danger to human health. Applications that use large amounts of solvents are problematic due to environmental pollution. Safer solvents and auxiliaries suggest minimizing the synthesis process to the maximum extent and avoiding the use of auxiliary chemicals (e.g. solvents, separators) whenever possible.
6. Energy efficiency design: Principle of energy efficiency design; It refers to taking into account the effects of the energy requirements required in chemical processes on the environment and economic balance and reducing energy requirements.
7. Use of renewable materials: This principle advocates the use of renewable raw materials in every application where it is technically and economically acceptable. It is very important that raw materials and intermediate materials are renewable in order to be advantageous both technically and economically.
8. Reduction of derivatives: One of the main principles of green chemistry refers to avoiding the use of chemical derivatives in the synthesis of target molecules.

9. Catalyst: Catalyst principle to protect the environment; It promotes the use of biodegradable catalysts, which means less energy use, avoids the use of organochlorine compounds, and reduces water use or produces less wastewater.
10. Degradation design: This principle states that chemical products should be designed in such a way that they turn into harmless degradation products as a result of their functions and do not remain in the environment.
11. Real-time analysis for pollution prevention: This requires further development of analytical methodology; In each case, it states that the production process must be constantly monitored. In traditional analytical chemistry, analysis requires large amounts of sample, solvent and energy. However, with green chemistry applications, it is possible to make the analysis sample smaller and use less solvents.
12. Safe chemistry to prevent accidents: The principle states that reagents used to carry out chemical processes should be carefully selected to prevent accidents such as re-release of toxic substances into the atmosphere, explosion and fire.

NANOPARTICLE

As a result of efforts to use technology and information effectively, its use in production and product processes has become widespread; new application areas have been discovered and new technologies have become more common day by day (Dahlman, 2007). One of these new technologies, and perhaps the most important today, is nanotechnology. The word nano constitutes the unit of measurement accepted as one billionth of a meter (10-9). This measurement it corresponds to a very small range (Miller et al., 2004). In this context, very small objects are studied in nanotechnology.

In the synthesis of nanoparticles produced using chemical methods, toxic chemicals cause serious damage to the environment and living beings (Erdogan et al., 2019). Many studies are being conducted involving nanoparticle synthesis using various extracts and metals (transition metals such as Ag, Fe, Cu, Zn, Au, Ti) (Youssef et al., 2019). When the studies are considered, green synthesis is an application method that is human-centered, especially targets the economy and the environment, and meets this in the most appropriate way. For example, the usability of a natural resource such as honey in both the economy and food and health fields, its rich content, its non-toxicity due to its physical and chemical structure, its easy accessibility, its fructose-glucose structures in its components, and its biocompatibility as an agent have led to detailed research worldwide and have attracted interest as a research topic (Rasouli et al., 2018; Karadal and Yildirim, 2012). For this reason, it is used in research as a reducing agent in the green synthesis of nanoparticles (Jeyageetha, Geetha and Packiam, 2019).

Nanotechnology, in its most general definition, has applications in many fields, including engineering, materials science, physics, biology and chemistry; It constitutes an area where very small materials are used. In other words, nanotechnology refers to the field of atomic, molecular and macromolecular study at the level of approximately 1-100 nanometers, which enables understanding substances and their behavior at the nanoscale and allows the creation of structures, devices and systems with unique properties and functions.

Nanotechnology means controlling matter at the molecular and atomic level; It is an application area that aims to create new structures at the nanoscale and to provide new functions and features through changes in the structures. Working limit at nanoscale level in nanotechnology; This causes the application area to have a very wide freedom. For this reason, it is used in many application areas; It is considered as an interdisciplinary dimension (Perez and Sandgren, 2008).

Nanotechnologies are called general-purpose technologies with their interdisciplinary dimension and use in many application areas. Since substances between 1 and 100 nanometers in size constitute the field of nanotechnology, this technology is frequently used in advanced and new application areas. Today, nanotechnology applications can be seen in the fields of agriculture, space, informatics, electronics, materials, energy, medicine, physics, biology, chemistry and environment. General application areas and uses of nanotechnology can be listed as follows (Kaounides et al., 2007); (Hunt and Mehta, 2013):

- Nanomaterials: Such as nanodot, nano polymer, nano crystal, nano tube and nano wire,
-Nanobiotechnology: Such as nanomedicines, cellular biology, biomolecular fabrics, molecular machines, biosensors, biomolecular devices,
- Defense technologies: Air vehicles, rockets, steel vests, camouflage clothing, such as bomb disposal robots, nano sensors, laser,
- Photonics: High-capacity data storage devices, fast CD readers, laser technology, fast information transmission and the internet,
-Computer: High storage memories, DNA computer, quantum nanocomputer, mechanical nanocomputer, biochemical and chemical nanocomputers and electronic computers,
-Automotive: Hydrogen cars, water-repellent and non-reflective glasses, energy-saving fuels, reducing wear and friction, etc.
- Electronics: Nano, semiconductor, electron and microelectronic devices, CDs and DVDs, chip technology, OLED and LED vehicles, etc.
- Energy: Such as nano magnet, hydrogen cells, fuel cells, solar cells, solar and hydrogen energy storage and battery technology,
- Textile: Nanofibers, water-repellent fabrics, smart clothes, odor-repellent fabrics, heat-retaining fabrics, etc.
- Medicine and Biology: Nano devices that carry drugs, nano sensors that can move in the blood, heart valves, harmless and durable platinum orthopedic

devices, healing of hereditary diseases by interfering with DNA, early diagnosis, DNA chips, nano structures that bind to tumors and prevent them from spreading, such as artificial organs, nano tissues that can combine with living tissues, tissue and stem cell production, nano robots that treat only the diseased area, nano machines that can move easily within the human body.

-Environment: Heavy metals, dyes, organic matter, etc. From environmental environments, such as removal of pollutants.

New ones are constantly being added to these usage areas and applications; Nanotechnology, as a multidisciplinary technology, is becoming more important day by day. Nanotechnology generally offers the following

opportunities as a technology that causes less harm to nature and enables lighter and more durable production in every field (Ozdoğan et al., 2006):

- Possibility of producing substances at the atomic level with the rules of chemistry and physics,
- Possibility to place each atom where desired.

Nanotechnology generally aims to:

- Less energy and material usage,
- Faster, lighter and more durable structures,
- Obtaining superior and different production processes and material properties than known,
- Establishing a connection between the macroscopic and nanoscopic World with appropriate methods,
- Development of nanoscale and precision devices,
- Analysis of nanometer scale structures.

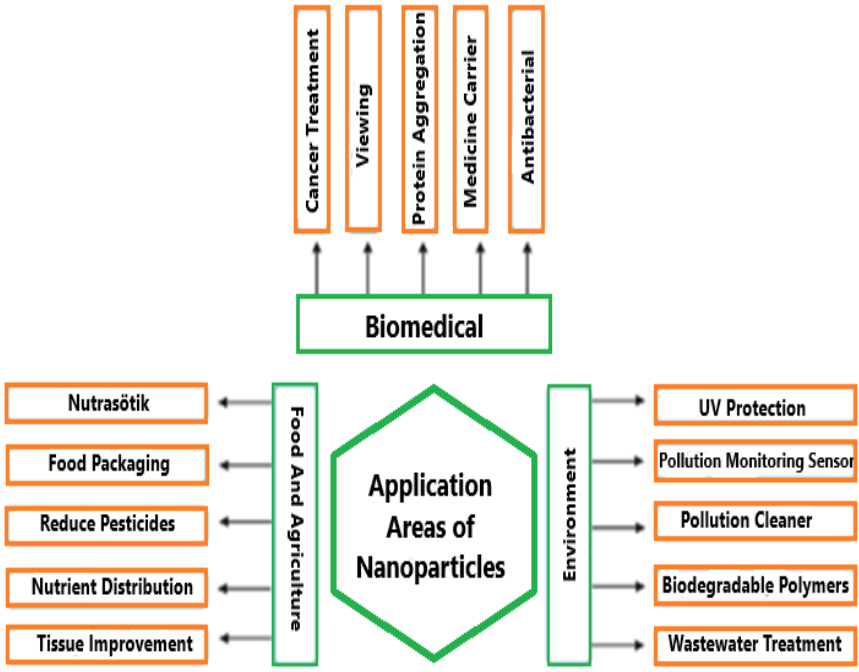

Figure (1): Applications of nanoparticles in different fields (Koul et al., 2021).

Nanoparticles have larger surface areas compared to microparticles and are particles smaller than 1 micrometer in size. It is possible to encapsulate bioactive molecules in nanoparticles or to immobilize bioactive molecules onto the particle surface.

Nanoparticles enable specific interactions for the application and have functional groups on their surface. It allows the creation of data (Orive et al., 2003). Nanoparticles have unique morphological (such as quantum effects, surface mass ratio, nano size) and physicochemical properties due to their small size. Nanoparticles, which are not simple molecules, generally consist of three layers (Shin et al., 2016):

a) With various small molecules, metal ions, surfactants and polymers functionalizable surface layer,

b) The shell layer, which is chemically different from the core in all aspects, c) It is essentially the central part of the nanoparticle and is usually the core that expresses itself.

With these features, nanoparticles are considered more important than other commercial materials. By applying external energy to any substance, chemically or mechanically, the substances can be broken down into nano-size and nanoparticles can be synthesized. In general, the following methods are used to synthesize nanoparticles: (Tunca, 2015):

- Ultrasonic spray pyrolysis method,

- Chemical vapor condensation method,

- Noble gas condensation method,

- Mechanical etching method,

- Flame synthesis method,

- Hydrogen reduction method,

- Laser cutting method.

Based on physical and chemical properties, some of the well-known types of nanoparticles are as follows (Khan et al., 2019):

- Carbon-based nanoparticles: Fullerenes and carbon nanotubes represent the two main classes of carbon-based nanoparticles. Carbon-based nanoparticles have attracted much commercial attention due to their electrical conductivity, high strength, structure, electron affinity and versatility.
- Metal nanoparticles: Metal nanoparticles are produced entirely from metal precursors. Due to their well-known localized surface plasmon resonance characteristics, these nanoparticles have unique optoelectric properties. Nanoparticles of alkali and noble metals, namely Cu, Ag and Au nanoparticles, have a broad absorption band in the visible region of the electromagnetic solar spectrum.
- Ceramic nanoparticles: Ceramic nanoparticles are inorganic and non-metallic solids synthesized through heat and successive cooling. They have been used in many applications such as catalysis, photocatalysis, photodegradation of dyes, and imaging. It is used in many applications and attracts great attention from researchers.
- Semiconductor nanoparticles: Semiconductor properties exist between metals and non-metals and are used in various applications in the literature due to this feature. Semiconductor nanoparticles have wide band gaps and with these properties, they consist of important components of photocatalysis, photo optics and electronic components.
- Polymeric nanoparticles: Organic based polymeric nanoparticles; mostly in the form of nanospheres or nanocapsules. Polymeric nanoparticles can be easily functionalized and are used in a wide range of applications with these properties.

GREEN CHEMISTRY APPLICATIONS

In this context, green nanotechnology aims to apply green chemistry theories in the development of nanoscale materials, reduce hazardous waste generation, and design production techniques with safer practices (Dahl et al., 2007).

Using examples from nature, the conversion of living organisms into inorganic materials through bio-driven processes forms the basis of green chemistry and green chemistry in nanoparticles. Nanoparticles are synthesized from organisms such as bacteria, actinomycetes, fungi and plants in the green chemistry process (Figure 2).

Studies show that using plant extracts from various parts of plants such as tissues, leaves, seeds, oils and roots is simpler and more useful for nanoparticle synthesis. While nanoparticles are synthesized with green chemistry, first reducing agents, then solvent and finally stabilizing reagents are selected. For these reasons, plant extracts appear to play a role in nanoparticle formation during synthesis.

Plant extract stands out because it takes less time and is easier than difficult and time-consuming applications such as microbial cell growth and cell culture preparation. Other reasons why plant extracts are advantageous over other biomaterials in nanoparticle synthesis with green chemistry can be listed as follows (Babu Maddinedi et al., 2017):

Suitable for large-scale syntheses, more stable nanoparticles can be obtained, environmentally friendly, fast synthesis possibility, elimination of detailed maintenance of cell cultures, contains various metabolites as reductants, can be synthesized in a single step and simple process, cost effective, safe to use, easy to use.

Ehrampoush et al. (2015) in their study, to examine the cadmium removal of green synthesis iron oxide nanoparticles from tangerine peel extract from aqueous solution; stated that metal oxide nanoparticles are effective substances in the removal of organic and inorganic pollutants from water and wastewater.

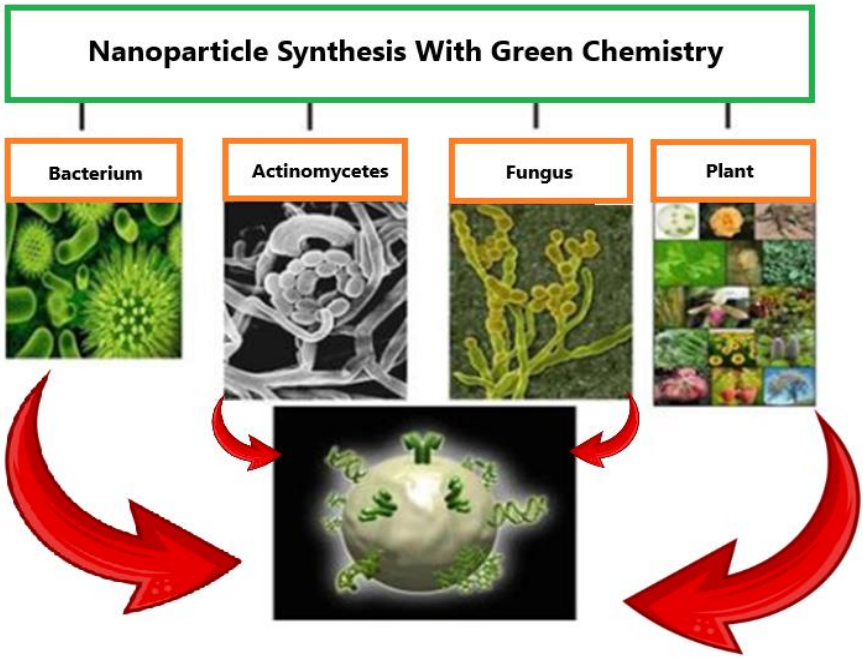

Figure (2): Nanoparticle synthesis with green chemistry (Razavi et al., 2015).

They synthesized iron oxide nanoparticles from tangerine peel extract to remove cadmium ions from contaminated water. In the study, tangerine peel extract was used to prevent accumulation of iron oxide nanoparticles prepared by the co-precipitation method and to reduce the diameter of the particles. It has been determined that iron oxide nanoparticles are good absorbents in the removal of cadmium ions from wastewater.

In another study, Pandian et al. (2015), biosynthesized nickel nanoparticles using Ocimum sanctum leaf extract as an environmentally friendly adsorbent. Nanoparticles produced as adsorbents have been used to remove dyes such as crystal violet, eosin Y, orange II, anionic pollutants nitrate and sulfate from aqueous solution. Adsorption capacity of nickel nanoparticles depends on different pH, contact time, dosage and concentration of different dyes and pollutants were examined. As a result of the study, it was determined that the adsorption process was dependent on pH, and while the adsorption capacity increased according to the contact time and nickel nanoparticle dosage, the adsorption capacity decreased at higher dye and pollutant concentrations. It has been found to be an effective adsorbent in removing it from solution and it has been stated that it can be applied for the treatment of textile and tannery wastewater.

Saif et al. (2016) in their review on the green synthesis and environmental applications of iron nanoparticles, stated that recent developments in nanoscience and nanotechnology have led to the development of new nanomaterials that increase health and environmental hazards; Therefore, environmentally friendly methods are used in the synthesis of metallic and magnetic nanoparticles. They stated that one of the areas of use of nanoparticles obtained by green synthesis is the removal of heavy metals from wastewater.

Weng et al. (2016) studied the removal of mixed pollutants Cr(IV) and Cu(II) with green synthesized iron-based nanoparticles using eucalyptus leaf extracts and iron-based nanoparticles (FeNPs).

In the study conducted by Es'haghi et al. (2016), a new method to be used in the analysis of nickel ions in soil, potatoes, red tea, white tea, mushrooms, lettuce, cabbage, apples, domestic water, and drinking water purified with a home water purification device.

To optimize the important parameters affecting the extraction procedure, analyte concentration, pH, dispersive solvent type, absorption time, ionic strength effect, desorption solvent type and desorption time were examined. The techniques used in the characterization of synthesized magnetic nanoparticles are SEM and FT-IR. Measurements were made under optimized conditions. The effectiveness and accuracy of the matrices were examined by determining the relative recovery (%RR) of real samples (Es'haghi et al., 2016).

Ali et al. (2017), phytogenic magnetic field for wastewater treatment in their compilations on nanoparticles; The research trend regarding the use of phytogenic magnetic nanoparticles in wastewater treatment due to their dynamic morphology, desired size, superparamagnetic behavior and high saturation magnetization value. He stated that it was quite new; They suggested that these nanoparticles constitute a promising wastewater treatment technology due to their clean, non-toxic, fast, environmentally friendly and economical green production. It has been mentioned that other aspects of these particles, such as reusability, biomass separation, metal recovery and regeneration, need to be further investigated.

Goutam et al. (2018) carried out the green synthesis of TiO_2 nanoparticles using Jatropha curcas leaf extract for the photocatalytic degradation of tannery wastewater; stated that green synthesis is a simple, environmentally friendly and evolving approach to synthesize nanoparticles; green titanium dioxide synthesized nanoparticles and evaluated the photocatalytic degradation of tannery wastewater after biological treatment. The results revealed the presence of phytochemicals in spherical TiO_2 nanoparticles. TiO_2 nanoparticles have been determined to be effective in purifying tannery water as an alternative clean green purification solution.

Sebastian and his colleagues (2018) examined the purification of heavy metal in contaminated water using magnetite nanoparticles produced phenolically from coconut shell extract. In the study, semi-crystalline magnetite nanoparticles were synthesized by mixing equal volumes of 10.0 mM ferric

chloride solution and coconut shell extract at room temperature. Kinetic studies have shown that metal adsorption is a combined effect of both physical and chemical processes.

Acar et al (2023) reported that selenium nanoparticles (SeNP) synthesized using biological resources have unique physical, chemical properties and biological activity compared to inorganic and organic Se.

RESULTS AND DISCUSSION

Environmentally friendly, eco-sustainable technologies always attract attention. In this context, we come across concepts such as “green chemistry” and “environmentally friendly”. By adapting these concepts to today’s technology, a synthesis method called “green synthesis”, which is both technological and environmentally friendly, has emerged.

Green chemistry has a very important place today in reducing the production of hazardous waste worldwide and developing energy-efficient synthesis methods. In order to implement the basic standards of green chemistry, the production of nanoparticles using biocompatible and non-toxic solvents and environmentally reducing substances is also a very important issue today.

Additionally, due to the high specificity of biocatalysts, biochemical processes can occur at low temperatures; accordingly using a synthetic method comprising one or more biological steps; It causes less energy use and less environmental impact compared to traditional methods. To optimize safer nanoparticle production, using bio-based techniques that minimize hazardous material production forms is very popular today.

The essence of green synthesis is the use of completely organic structures that are easily found in nature as an alternative to traditional chemical solvents. Nanomaterials are used in many different engineering fields, but it should not be forgotten that the environment should not be harmed while these materials are being produced. In environmental engineering, green nanomaterials are used in water treatment, soil pollution, air quality improvement, and groundwater treatment. The high efficiency achieved with the use of these materials suggests that it will be an alternative to the use of traditional nanomaterials. Thus, both treatment will be carried out and no burden will be created for the environment. In addition, being economical and easily applicable is one of its biggest advantages. By using organic substances instead of harmful solvents, the health of people working in the synthesis phase will not be negatively affected.

REFERENCES

Acar, B. Ç.,Yüksekdağ, Z., Şahin, T., Açar, E., KaraBerat, F. (2023). Selenium Nanoparticle (SeNP) Synthesis Through Green Synthesis, Gazi Üniversitesi Fen Fakültesi Dergisi, 4 (1), 32-50.

Ali, I., Peng, C., Naz, I., Khan, Z. M., Sultan, M., Islam, T. and Abbasi, I. A. (2017). Phytogenic magnetic nanoparticles for wastewater treatment: a review, RSC Advances, 7 (64), 40158-40178.

Anastas, P. T. and Evan, S. (2009). Beach, Green Chemistry Education ACS Symposium Series; American Chemical Society: Washington, DC.

Babu, M. S., Mandal, B. K. and Maddili, S. K. (2017). Biofabrication of size controllable silver nanoparticles–a green approach, Journal of Photochemistry Photobiology B: Biology, 167, 236-241.

Dahl, J. A., Maddux, B. L. and Hutchison, J. E. (2007). Toward greener nanosynthesis, Chemical reviews, 107 (6), 2228-2269.

Dahlman, C. (2007). Technology, Globalization, and International Competitiveness: Challenges for Developing Countries. In: United Nations Department of Economic and Social Affairs, Ed., Industrial Development in the 21st Century: Sustainable Development Perspectives, United Nations, New York, 29-83. http://www.un.org/esa/sustdev/publications/industrial_development/1_2.pdf

Ehrampoush, M. H., Miria, M., Salmani, M. H. and Mahvi A. H. (2015). Cadmium removal from aqueous solution by green synthesis iron oxide nanoparticles with tangerine peel extract. Journal of Environmental Health Science & Engineering, 13, 84. https://doi.org/10.1186/s40201-015-0237-4

Erdoğan, Ö., Birtekocak, F., Oryaşın, E., Abbak, M., Demirbolat, G. M.et al. (2019). Enginar yaprağı sulu ekstraktı kullanılarak çinko oksit nanopartiküllerinin yeşil sentezi, karakterizasyonu, anti-bakteriyel ve sitotoksik etkileri. Duzce Medical Journal, 21 (1), 19–26.

Es'haghi, Z., Vafaeinezhad, F. and Hooshmand, S. (2016). Green synthesis of magnetic iron nanoparticles coated by olive oil and verifying its efficiency in extraction of nickel from environmental samples via UV–vis spectrophotometry, Process Safety Environmental Protection, 102, 403-409.

Goutam, S. P., Saxena, G., Singh, V., Yadav, A. K., Bharagava, R. N. et al. (2018). Green synthesis of TiO_2 nanoparticles using leaf extract of Jatropha curcas L. for photocatalytic degradation of tannery wastewater, Chemical Engineering Journal, 336, 386-396.

Hunt, G. and Mehta, M. (2013). Nanotechnology: Risk, Ethics and Law, Routledge.

Ivanković, A., Dronjić, A., Bevanda, A. M., Talić, S. and Energy, G. (2017). Review of 12 Principles of Green Chemistry in Practice, International Journal of Sustainable, 6 (3), 39-48.

Jeyageetha, J., Geetha, M., and Packiam (2019). Synthesis of honey mediated biogenic zinc oxide nanoparticles and structural parameters ınvestigations. Jetir, 6(2), 882-888.

Kaounides, L., Yu, H. and Harper, T. (2007). Nanotechnology innovation and applications in textiles industry: current markets and future growth trends, Materials Technology, 22 (4), 209-237.

Karadal, F., and Yildirim, Y. (2012). Balın kalite nitelikleri, beslenme ve sağlık açısından önemi. Erciyes Üniversitesi Veteriner Fakültesi Dergisi, 9(3), 197-209.

Khan, I., Saeed, K., Khan I. (2019). Nanoparticles: Properties, applications and toxicities Arabian Journal of Chemistry, 12 (7), 908-931.

Koul, B., Poonia, A. K., Yadav, D., Jin, J. O. (2021). Microbe-mediated biosynthesis of nanoparticles: Applications and future prospects. Biomolecules, 11(6), 886.

Miller, J. C., Serrato, R., Represas-Cardenas, J. M. and Kundahl, G. (2004). The handbook of nanotechnology: Business, policy, and intellectual property law, John Wiley & Sons.

Orive, G., Hernandez, R., Gascon, A., Igartua, M. and Pedraz, J. (2003). Survival of different cell lines in alginate-agarose microcapsules, European journal of pharmaceutical sciences, 18 (1), 23-30.

Özdoğan, E., Demir, A. and Seventekin, N. (2006). Nanotechnology and Its Applications In Textıle Industry, Tekstil ve Konfeksiyon, 16 (3), 159-168.

Pandian, C. J., Palanivel, R. and Dhananasekaran, S. (2015). Green synthesis of nickel nanoparticles using Ocimum sanctum and their application in dye and pollutant adsorption, Chinese journal of Chemical engineering, 23 (8), 1307-1315.

Perez, E. and Sandgren, P. (2008). Nanotechnology in Sweden: An innovation system approach to an emerging area, VINNOVA Stockholm.

Rasouli, E., Basirun, W.J., Rezayi, M., Shameli, K., Nourmuhammadi, E., Khandanlou, R. et al. (2018). Ultrasmall superparamagnetic Fe_3O_4 nanoparticles: Honey-based green and facile synthesis and in vitro viability assay," International Journal of Nanomedicine, 13, 6903-6911.

Razavi, S., and H. V. Gupta (2015), What do we mean by sensitivity analysis? The need for comprehensive characterization of ''global'' sensitivity in Earth and Environmental systems models, Water Resources Research, 51, 3070–3092, doi:10.1002/2014WR016527.

Saif, S., Tahir, A. and Chen, Y. (2016). Green synthesis of iron nanoparticles and their environmental applications and implications, Nanomaterials, 6 (11), 209.

Sebastian, A., Nangia, A. and Prasad, M. (2018). A green synthetic route to phenolics fabricated magnetite nanoparticles from coconut husk extract: Implications to treat metal contaminated water and heavy metal stress in Oryza sativa L, Journal of cleaner production, 174, 355-366.

Shin, W.-K., Cho, J., Kannan, A. G., Lee, Y.-S. and Kim, D.-W. (2016). Cross-linked composite gel polymer electrolyte using mesoporousmethacrylate-functionalized SiO_2 nanoparticles for lithium-ion polymer batteries, Scientific reports, 6, 26332.

Stanley, E., Manahan, A. (2006). Sustainable Approach to Green Science and Technology, Second Edition, Environmental Science and Technology.

Tunca, E. Ü. (2015). Nanoteknolojinin Temeli Nanopartiküller ve Nanopartiküllerin Fitoremediasyonu, Ordu Üniversitesi Bilim ve Teknoloji Dergisi, 5 (2), 23-34.

Türkoğlu, S., Kepekçi, R. A., & Keskinkan, O. (2023). Diospyros kaki L.

Weng, X., Jin, X., Lin, J., Naidu, R. and Chen, Z. (2016). Removal of mixed contaminants Cr (VI) and Cu (II) by green synthesized iron based nanoparticles, Ecological Engineering, 97, 32-39.

Youssef, G. A., El-Boraey, A. M., and Abdel-Tawab, M. M. (2019). Eco-friendly green synthesis of silver nanoparticles from egyptian honey: Evaluating its antibacterial activities. Egyptian Journal of Botany, 59(3), 709–721.

Some Ecological Relationships of Aquatic Plants

Seher DİRİCAN[1]

1- Assoc. Prof. Dr. Seher Dirican; Sivas Cumhuriyet University, Faculty of Science, Department of Biology Sivas, Turkey. sdirican@cumhuriyet.edu.tr ORCID No: 0000-0001-9130-5114

ABSTRACT

In the ecosystems, living and nonliving things are in constant interaction. This interaction occurs through energy flow and material cycles. Each living and nonliving component in ecosystems has its own unique role. Therefore, the structure of ecosystems is quite complex. Aquatic ecosystems are very important in terms of their physical, chemical and biological functions. Aquatic ecosystems with such important functions should be protected and used sustainably. In recent years, aquatic ecosystems have been under various threats. The natural structures of aquatic ecosystems should be protected for ecological sustainability. For this, the natural ecological relationships of all aquatic ecosystems should be protected. Aquatic plants show many differences when compared to plants living on land. Aquatic plants have direct relationships and interactions with the aquatic ecosystems they live in. Ecological relationships are interconnected and can directly or indirectly affect each other. For this reason, aquatic plants are critical for the conservation and sustainable management of aquatic ecosystems. The protection of aquatic plants is a fundamental step to prevent the degradation of aquatic ecosystems. In this study, the physical and chemical environments of aquatic plants in aquatic ecosystems and their ecological relationships with animal organisms they share their environments with were generally examined.

Keywords – Aquatic Plants, Ecology, Relationships, Interaction, Sustainability.

INTRODUCTION

The inanimate factors around organisms do not exist independently of each other in ecosystems. They also have an interaction with each other. Therefore, the effects of two or more environmental factors on organisms are different than their effects on themselves. This effect can develop in a positive way as well as a negative way (Kocataş, 2003). An organism is a functional whole composed of parts that coordinate with many intertwined processes. There are several separate subsystems in humans, such as the respiratory system and the circulatory system, and these somehow continue their interactions with the environment in a coordinated manner and provide life. There are other states of coordination in other species. Plants are modular organisms. Each module contains meristem tissue that has the capacity to form the entire plant. Parts of plants such as roots, stems, and leaves work as a whole for the continuation of plant life. The parts are dynamically and actively in communication with each other and the environment through the transportation of various molecules and other signal transmission pathways. The entire plant body is coordinated through these interactions. The organism exists through a continuous environment-

organism interaction. The organism actively decides which gene fragments to turn on through its interaction with its environment and in what quantities to produce the proteins it will produce from these. An organism's environment includes both inanimate objects and other organisms. Organisms continue their lives through very close and indispensable interactions with each other and their environment (Yılmaz, 2022). This is necessary for life.

Natural resources such as water, air and soil, which ensure the continuity of life on Earth, are being polluted or depleted at alarming rates. With the rapid increase in population, water, agricultural lands, forests, which are the basic components of the ecological balance, and main biological systems are rapidly disappearing. The amount of toxic gases and waste that threaten future generations and the world is rapidly increasing all over the world. As a result of climate change and global warming, glaciers are melting and many land areas are in danger of being flooded. With the rapid development of technology, global warming and the increasing mixing of pollutants into environmental environments seriously affect the existence of organisms (Kılçık, 2020).

While the amount of carbon-dioxide in the atmosphere was 250 ppm before the industrial revolution, this rate has reached 410 ppm in recent years. It is predicted that the carbon-dioxide rate in the atmosphere will increase to 500-600 ppm towards the middle of the twenty-first century. All these changes indicate that drought severity will increase with global warming. In addition, the conversion of forests and pastures to agricultural areas accelerates erosion and causes the fertile topsoil to be transferred to aquatic ecosystems, thus leading to decreases in net terrestrial production and a decrease in the amount of carbon sequestered from the atmosphere. The conversion of forest areas to agricultural areas reduces the amount of precipitation falling on land and increases the severity of drought (Tüfekçioğlu and Tüfekçioğlu, 2018). All these reveal the necessity of protecting the natural environment.

Aquatic ecosystems worldwide attract attention in terms of their economic importance and natural functions. Aquatic ecosystems have usage values such as their effect on the climate conditions of the region they are located in, feeding underground water resources, and creating an environment for biodiversity. Aquatic ecosystems are also areas that allow social activities to be carried out with their landscape value and view from a socio-cultural perspective. The protection of aquatic ecosystems, which have important functions, is very important (Kocataş, 2003). Aquatic plants living in aquatic ecosystems have very important functions and benefits ecologically. As the primary producers of the aquatic ecosystem, aquatic plants produce nutrients and dissolved oxygen. Aquatic plants provide protection, nutrition and reproduction environments for aquatic organisms. Aquatic plants increase the biological diversity of aquatic ecosystems and

improve water quality. Aquatic plants create a connection between the lower and upper levels of the food web in aquatic ecosystems. Some aquatic plants keep lime in their structure and make the water alkaline. Aquatic plants in non-acidic aquatic environments prevent the formation of aquatic pathogenic microorganisms. Aquatic plants provide water retention in aquatic ecosystems. Aquatic plants provide benefits by preventing coastal erosion and sediment mixing. In addition, aquatic plants create food, reproduction and protection habitats for aquatic organisms and clean water through bioremediation. In addition, aquatic plants have the potential to be used in the treatment of diseases. Products obtained from aquatic plants are safe. Phytochemicals such as carotenoids, alkaloids, terpenoids, flavonoids, minerals, steroids and proteins in the structure of aquatic plants are preferred in the field of health (Topaldemir and Taş, 2024). In this study, the physical and chemical environments of aquatic plants living in aquatic ecosystems and their ecological relationships with animal organisms they share their environments with were generally examined.

ECOLOGICAL RELATIONSHIPS IN AQUATIC PLANTS

Aquatic ecosystems include animals, plants and microorganisms living in biological communities, interacting with each other and their chemical and physical environments. Aquatic ecosystems must be ecologically healthy and their ecosystem functions must be sustained. Recently, aquatic ecosystems have been under various threats due to global warming, climate change, changing land uses in the water basin, water pollution and interference with the hydrological cycle of streams. For ecological sustainability, the natural structures of aquatic ecosystems must be protected, water level and water flow must be maintained. Erosion of aquatic ecosystem shores and beds must be prevented. Land, air, geology, physicochemical properties, fauna and flora of aquatic ecosystems must be known and protected. The natural ecological relationships of all aquatic ecosystems must be protected. The basis of ecology is the relationships of organisms with their living and non-living environments. Organisms can affect their environments as well as being affected by them. Organisms are exposed to the simultaneous effects of the highly variable physical, chemical and biological elements of the environment in which they live. This effect can be direct or indirect (Kocataş, 2003).

Aquatic plants show various morphological, cytological, anatomical and ecological differences when compared to plants living on land. Various aquatic plants have direct relationships and therefore interactions with the aquatic ecosystems they live in. Each ecological relationship is interconnected and can affect each other directly or indirectly (Cirik et al. 2011). Here are some ecological relationships of aquatic plants such as

nutrient, nitrogen fixation, temperature, light, oxygen, carbon-dioxide and pH value, respectively.

Food Relations

All animals, including fish, aquatic invertebrates and other aquatic animals, depend on green plants for food. In all aquatic ecosystems, the vast majority of nutrients consumed by animals are again created in those aquatic ecosystems. It is inevitable that there will be some exchange between water and the surrounding terrestrial ecosystem in terms of nutrients (Cirik et al. 2011). Food abundance and diversity determine the composition of species and the size of fish populations. The key chemical factors and nutrients in the first link of the fish food chain include carbon-dioxide for photosynthesis and hydrogen, nitrogen, phosphorus, potassium, calcium, magnesium and trace elements. There are relationships such as competition, predation, symbiosis, commensalism and parasitism between individuals of the same or different species. There is competition between organisms for survival. Some survive while others die due to competition. Predation ensures that the best of prey and predator survive (Timur, 1985). The stunted, underdeveloped, weak and sick individuals are the first to disappear.

Natural food chains are inefficient in transferring energy from one trophic level to another. Due to this inefficiency, a large amount of plant material is needed for the production of a relatively small amount of fish. This situation is expressed as a food pyramid (Cirik et al. 2011). Ecologists compare the groups of organisms in nature to a pyramid consisting of steps in which the number and types of organisms in it decrease. The producers at the base of the pyramid are rich in both number and variety. Primary, secondary, tertiary and similar consumers are located in various intermediate steps of the pyramid. Each organism listed in this pyramid feeds on the organisms in the previous step. The energy that plants receive from the sun is transferred from animals to animals on various levels of the pyramid. The base of this food pyramid must be wide and strong. The base of the pyramid consists of productive plants. This base level must be wide enough to support all the remaining biological groups. Because it will support the weight of the entire remaining pyramid. The second level of the food pyramid is represented by the numerous small animals that feed on the plants at the base, namely herbivores. The total mass of the small herbivores must be smaller than the plants at the base. Otherwise, if the total mass of the animals is greater than the existing plants, all the plants will be eaten immediately and the level that holds the pyramid up will be destroyed. This herbivore level supports the smaller, meat-eating small animal level. As a result, the upper end of the pyramid is formed by a small number of large animals. The volume of each organism on this level is large, but the number of animals it contains is less than the level below (Timur, 1985). In this case, it is important for the continuity and sustainability of the ecosystem.

Nitrogen Fixation Relations

The main protein source of the biosphere is atmospheric nitrogen. In aquatic ecosystems, molecular nitrogen is retained by cyanobacteria. The retained nitrogen or the nitrogen assimilated by green plants in the form of nitrates and ammonium compounds is used in the synthesis of plant proteins. Plant proteins are a source of amino acids for animal organisms. Animal organisms digest plant proteins and convert them into animal proteins. The waste of all animal organisms in the form of urea and uric acid contains nitrogen. When plant and animal organisms die, their bodies are decomposed with the help of bacteria and fungi. The nitrogen of proteins and amino acids returns to water in the form of ammonia. Ammonia can be converted back into nitrates with the help of nitrifying bacteria. These last nitrogen compounds return to water as molecular nitrogen (Timur, 1985). Nitrogen is an important factor that can limit or increase algal growth. Nitrogen is in the structure of plant and animal proteins. Plants cannot develop if there are no nitrogenous substances in the environment, even if they receive light. Nitrogen is an indispensable element for the intensive development of plants. Nitrogen gas, which is very dense in the atmosphere, is found in significant amounts in aquatic ecosystems. On the other hand, many living organisms cannot benefit from nitrogen directly (Cirik and Cirik, 2008).

It is of great importance to convert nitrogen gas in the air into chemical compounds that plants can use, both naturally and artificially. Because nitrogen has a great effect on the efficiency of the environment. Lack of nitrogen in the environment means protein deficiency. This brings with it the problem of nutrition and hunger (Kocataş, 2003).

Nitrogen in elemental form cannot be used by plants without being fixed in nitrate or ammonia forms. While different species of cyanobacteria have the capacity to fix nitrogen, none of the higher plants have this feature. However, *Azolla*, an aquatic fern, has established a symbiotic relationship with *Anabaena azollae*, a cyanobacteria that can fix nitrogen. *Azolla* is an aquatic fern in the group of seedless plants. *Azolla* provides nutrients and protection to algae. Under suitable conditions, *Azolla* can double its weight every 3-5 days and can fix 2-4 kg of nitrogen per hectare per day. Nitrogen can also be used by other plants with the death and decomposition of the fern (Cirik et al. 2011). With these features, *Azolla* is a freshwater fern that grows exponentially and moves freely under optimum conditions and is of great importance for the future.

Temperature Relations

Temperature is an important ecological factor primarily responsible for air movements in the atmosphere, the formation of climatic changes and the emergence of seasons. Therefore, it has an active role in the life of organisms and their distribution on earth. Organisms localize in the most

suitable area for them in their distribution regions (Kocataş, 2003). Temperature is an important ecological factor for the growth and development of plants. When we compare the vegetation at the equator and the poles and the rapid growth and development in plants in the summer months and the stagnation in the winter months, the importance of temperature becomes apparent. With the sunrise, the temperature begins to increase rapidly on earth (Eser and Geçit, 2007).

The temperature of aquatic ecosystems varies depending on the geographical location, seasons, depth, area, amount of dissolved matter in it and the solar energy it absorbs. In natural waters, heat is provided by solar energy (Tanyolaç, 2009). Water temperature has a direct effect on other physical, chemical and biological parameters. Organisms can be divided into two groups as stenotherm and eurytherm according to their tolerance to heat. The density of fresh water increases with the decrease in temperature. The density of water reaches its highest value when the temperature of the water drops to +4 ^{0}C. This feature ensures that water freezes from the top in places where the air temperature drops below 0 ^{0}C in the winter season. Surface water, which comes into contact with cold air and loses heat, condenses and sinks to the bottom. The warm water at the bottom rises to the surface and cools. When the density of the entire water mass reaches +4 ^{0}C, circulation stops. Thus, the ice formed during freezing remains on the surface (Egemen, 2011). This feature is necessary and important for the survival of both plant and animal organisms in the water.

Temperature is one of the most important ecological factors that allows plants to start growing in the spring and enter a dormant period in the fall, limiting their growth rates. Although some underwater plants can grow at temperatures as low as 2 ^{0}C, weed problems can generally reach significant levels at high temperatures between 20 and 35 ^{0}C (Anonymous, 2009). Therefore, attention should generally be paid to high temperatures.

Light Relations

Light has important effects ecologically with its duration, intensity and structure. The intensity and structure of light are generally not constant and can change depending on environmental factors. The duration of light, which has much more important effects on organisms, shows a regular change only depending on latitudes and seasons. Therefore, most of the biological rhythms observed in organisms develop depending on the light and dark periods (Kocataş, 2003). Light is one of the most important climate factors that provide the energy necessary for life to continue in all organisms. The natural source of light is the sun. The amount of light reaching the earth and the duration of light change significantly according to latitude degrees, seasons and hours of the day due to the rotation of the earth around itself (Eser and Geçit, 2007).

The capacity of a natural aquatic ecosystem to sustain organisms is a result of the mutual effects of physical, chemical and biological events and all are affected by solar energy. Light in natural waters is provided by solar energy. Not all of the rays coming to the surface of the water are absorbed by the water, some of them are reflected. The amount of reflection varies depending on whether the water surface is flat, turbulent or wavy. Light is very effective on biological events in water. The effect of light on aquatic organisms is either direct or related to photosynthesis. Most aquatic organisms are sensitive to high intensity sunlight. Organisms exposed to too much light escape to the lower layers of the water or take shelter in the shadows of aquatic plants to protect themselves from the light. Phytoplanktonic organisms live on the surface where the light is at its maximum in order to photosynthesize. The effect of sunlight on chlorophyllous plants in water is quite high. Aquatic plants, like terrestrial plants, provide the carbohydrates and proteins of aquatic ecosystems. Light intensity and wavelength are effective in photosynthesis. As light intensity increases, the rate of photosynthesis increases. As light wavelength decreases, photosynthesis also decreases (Tanyolaç, 2009).

Even if the surface of aquatic ecosystems freezes in winter, the light required for photosynthesis continues to pass into the water at certain rates depending on the structure of the ice. If this surface is completely covered with snow, photosynthesis is largely prevented (Cirik and Cirik, 2008). In such cases, the amount of oxygen in the water decreases significantly, and organisms are negatively affected by this.

The light transmittance of water is of great importance in terms of the amount of light energy used by aquatic plants, especially phytoplankton. This feature indirectly determines the amount of fish present in a certain habitat (Timur, 1985). In other words, the light transmittance of water is very effective on the productivity of aquatic ecosystems.

Oxygen Relations

Oxygen is an inevitable factor for life in aquatic ecosystems as well as in terrestrial ecosystems. Therefore, oxygen is the most important dissolved gas. There are factors that increase and decrease the amount of oxygen dissolved in water. The main factors that increase the amount of oxygen are photosynthesis, the relationship of oxygen-poor surface waters with the atmosphere, and the effects of currents and winds. The main factors that decrease the amount of oxygen are respiration and oxidation. The amount of oxygen in aquatic ecosystems is lower than in air. Because the solubility of oxygen in water is weak and directly depends on the temperature and salinity of the water. The solubility of oxygen in water decreases in parallel with the increase in both factors in the environment (Kocataş, 2003). The superiority of oxygen produced by photosynthesis in aquatic ecosystems compared to dissolved atmospheric oxygen is largely related to the degree of mixing that

occurs in the water. The dissolution of oxygen in the atmosphere in aquatic ecosystems occurs at the surface and its downward movement in the water mass requires a mechanical force or mass movement. On the other hand, photosynthetic oxygen in still waters with slight mixing is sufficient for animals in deeper waters to sustain their lives (Cirik et al. 2011).

The most important chemical substance found in natural aquatic ecosystems is oxygen. This importance of oxygen is both a regulator of metabolic events in water and an indicator of the condition of water. The oxygen in aquatic ecosystems is less than in air. Because the solubility of oxygen in water is low. The amount of oxygen detected in water at any given time depends on the temperature of the water at that moment, the partial pressure of the gas in the atmosphere touching the water surface, the concentration of dissolved salt in the water and biological events. Dissolved oxygen is provided to water either by diffusion from the atmosphere or by photosynthetic aquatic plants. Photosynthesis is an important source of oxygen in aquatic ecosystems, but it is specific to certain regions where sunlight can enter. The main consumption of oxygen in water is through the respiration of plants and animals and the decay of organic matter (Tanyolaç, 2009).

When light intensity falls below the equilibrium level, respiratory photosynthesis stops and plants begin to consume more oxygen than they produce. This happens every night and on some dark days. Plants that cover the water surface, such as water lettuce, duckweed and various cyanobacteria species, can reduce the level of dissolved oxygen. The reasons for this are that these plants shade the water column below them, preventing submerged species from photosynthesizing and preventing contact between the water and the atmosphere, reducing the oxygen coming from this source. In addition, these plants constantly release dead thallus, leaves, roots and other organic residues into the water. The oxygen in the water decreases during the decomposition and decay of these plants (Cirik et al. 2011). The death of vegetation in aquatic ecosystems due to reasons such as weather conditions, disease or herbicide applications results in the suppression of dissolved organic matter and oxygen levels in the environment.

Carbon-dioxide Relations

Carbon-dioxide, which is very important for aquatic organisms, is very high in water due to its high solubility, although it is found in very low density in the atmosphere. Carbon-dioxide has some important features in creating a suitable environment for natural water organisms. The first of these is the buffering effect of carbon-dioxide on the aquatic ecosystem from becoming acidic and basic very quickly. The other is its role in regulating the biological events of aquatic organisms. In this context, events such as seed development and growth of some aquatic plants vary depending on the carbon-dioxide density (Tanyolaç, 2009). Carbon-dioxide is more soluble in

water than oxygen. In addition, natural conditions such as carbon-dioxide temperature and pressure, photosynthesis and respiration are effective in the dissolution of carbon-dioxide in water. Since aquatic plants use carbon-dioxide in photosynthesis, they are effective in the distribution of carbon-dioxide in aquatic ecosystems. Carbon-dioxide is used in the assimilation of plants and oxygen is given. Especially during the temperature stratification in the summer season, the amount of carbon-dioxide decreases significantly in this region due to the intensive use of carbon-dioxide due to the intense photosynthesis event in the epilimnion (Cirik and Cirik, 2008).

Green plants produce organic carbon compounds, namely carbohydrates, fats and proteins, by using solar energy to combine carbon-dioxide with water during photosynthesis. During photosynthesis, carbon atoms enter the skeleton of complex organic compounds as carbon-dioxide. Since animals feed on plants and their products, the same carbon atoms are transferred to the carbohydrates, fats and proteins in the animals' bodies and remain locked there. Carbon atoms remain locked in the bodies of plant and animal organisms until they die. When plant and animal organisms die, they break down into carbon-dioxide. The carbon atoms in carbon-dioxide return to the air and water to be used in photosynthesis again (Timur, 1985). Chlorophyllous aquatic plants use carbon-dioxide in photosynthesis by taking it from the water and thus the carbon taken from the water is combined in the organic molecules of the dry matter made. Living plant cells use compounds containing organic carbon in their respiration and as a result of this physiological event, carbon is given back to the water in the form of carbon-dioxide. When chlorophyllous plants are eaten by animals, some of the carbon compounds pass into the animals' bodies. The rest remains in the water as inanimate organic residue when the plant loses its vitality. Some of the carbon compounds found in the bodies of animals pass into the water as carbon-dioxide through respiration, while the other part is given to the water as organic residues with their feces or death (Eser and Geçit, 2007). Carbon-dioxide, which is the building block of photosynthesis in particular, is quite effective in the development of aquatic plants. Carbon-dioxide is necessary for photosynthesis and therefore carbon-dioxide is essential for aquatic plants to be able to photosynthesize.

The pH Relations

The pH value is a measure that shows the acidity or alkalinity level of water. Neutral waters have a pH value of 7. Acidic waters have pH values lower than 7, while alkaline waters have pH values higher than 7. Waters in nature show great differences in terms of acidity and alkalinity properties. Some waters are acidic and some are alkaline. Alkalinity of waters comes from hydroxide, carbonate and bicarbonate ions. Acidity in waters depends on free carbon-dioxide, organic acids and acidic salts in water. The pH value of the aquatic ecosystem affects the metabolic activities of organisms. An

increase in pH value generally accelerates respiration in aquatic plants. A decrease in pH value slows down respiration in aquatic plants (Timur, 1985). So, there is a proportion between the pH value and the respiration and metabolism components of aquatic plants.

The relationship between pH value of water and the distribution of aquatic plants is complex. It is difficult to distinguish the effects of pH value on submersible plants from calcium and magnesium and carbonate and bicarbonate. However, aquatic plants have an effect on the pH value of water. With the consumption of carbon-dioxide during photosynthesis, the amount of carbonic acid in the water decreases and the pH value of the water increases. When respiration passes to photosynthesis, free carbon-dioxide is added to the water and the amount of carbonic acid in the ecosystem increases. Thus, the pH value of the water decreases. As a result, aquatic plants tend to reduce the pH value of the water body during the night and increase the pH value of the water body during the day. The decreases and increases in the pH value depend on the plant concentration and the buffering capacity of the water. In poorly buffered waters, aquatic plants can cause a significant pH value change between sunrise and sunset. This can negatively affect the organisms in the environment (Cirik et al. 2011). The pH value of aquatic ecosystems causes a series of indirect effects on submersible plants. The pH value causes phosphate ions to form mixed compounds with metal cations, which negatively affects the uptake of phosphate ions and, to some extent, metal ions by plants. Therefore, the solubility of trivalent iron phosphates in water is at its lowest level in waters where the pH value is less than 6 and makes it difficult to uptake phosphate in acidic waters. The pH value also affects the uptake of nitrogen and the types of nitrogen compounds. In acidic environments where the pH value is low, the conversion of ammonium to nitrate ions or nitrification decreases significantly. Surface weeds and floating weeds are tolerant to pH value changes (Anonymous, 2009).

It is interesting that benthic water plants are tolerant to pH changes that will occur in the environment they live in. In the experiments, it was observed that *Ulva* genus from Chlorophyceae continued photosynthesis in a pH environment of 9.4. Similarly, it has been observed that freshwater pterophytes *Salvina auriculata* can withstand pH levels ranging from 6.8 to 9.5 and bryophytes *Fontinalis decarlica* can withstand pH levels ranging from 3 to 10.5. *Desmarestia* species from marine algae have been detected in environments with pH levels of 1.13 and even lower (Kocataş, 2003). For these reasons, the pH value of water plays a critical role in the growth and development of aquatic plants. The optimum pH value ensures that nutrients are absorbed most easily by aquatic plants. Different aquatic plants have different pH tolerances. Some aquatic plants grow and develop better in acidic waters, while others grow and develop better in alkaline waters.

Therefore, monitoring pH values in aquatic ecosystems at regular intervals is very important for the health of aquatic plants.

CONCLUSION

No organism can live alone, all organisms live together in the ecosystem and dependent on each other. Organisms interact with each other and with many different species. This interaction is of vital importance for organisms. Some organisms produce their own food, while others have to get their food by eating other organisms. Depending on the food chain, predators can also become prey. Organisms such as plants, algae and phytoplankton are producers and have incredible photosynthesis abilities. Thus, autotrophs have the ability to feed themselves. Thus, they can perform functions such as growth, movement and reproduction. If a consumer eats a producer, the consumer takes the building block molecules and chemical energy in the producer's body. The lives of consumer organisms depend on producer organisms. Death is inevitable for all organisms. This is where decomposers come into play. The work done by decomposers is sometimes unnoticed, but it is of vital importance. These organisms break down organic matter and waste products, ensuring that the nutrients and minerals in them are returned to the ecosystem. This interaction is very important for the health of humans and the entire world. As a result, there are many interactions between organisms and the inanimate environment in an aquatic ecosystem. Interactions between organisms are inherent in life and are necessary for the health and proper functioning of ecosystems.

REFERENCES

Anonymous, (2009). *Aquatic weeds - distribution areas, lifestyles, environmental relations, problems and control methods*. Republic of Turkey, Ministry of Environment and Forestry, General Directorate of State Hydraulic Works, Department of Operation and Maintenance, Ankara, Turkey, pp. 374.

Cirik, S., Cirik, Ş. (2008). *Limnology* (Textbook). Ege University, Faculty of Fisheries Publications, İzmir, Turkey, pp. 166.

Cirik, S., Cirik, Ş., Dalay, M.C. (2011). *Aquatic plants II - biology, ecology and cultivation techniques of inland water plants*. Ege University Faculty of Fisheries Publications No: 61, Textbook Index No: 28, pp. 160.

Egemen, Ö. (2011). *Water quality* (Textbook). Ege University, Faculty of Fisheries Publications No: 14, pp. 150.

Eser, D., Geçit, H.H. (2007). *Ecology* (Textbook). Ankara University, Faculty of Agriculture Publications No: 1559, pp. 178.

Kılçık, F. (2020). Aquatic ecosystems and biomonitoring in the framework of environmental ethics. Tabula Rasa: Philosophy and Theology, 36, 53-60.

Kocataş, A. (2003). *Ecology and environmental biology*. Ege University, Faculty of Fisheries Publications No: 51, pp. 597.

Tanyolaç, J. (2009). *Limnology* (Freshwater Science). Hatipoğlu Printing and Publishing Industry Trade Limited Company, pp. 237.
Timur, G. (1985). *Ecology* (Textbook). Akdeniz University, Faculty of Isparta Engineering, Eğirdir Fisheries Highschool Publication No: 7, pp. 86.
Topaldemir, H., Taş, B. (2024). Common macrophytes with potential for ethnobotany and medicinal in the Terme wetlands of the Yeşilırmak delta. Aquatic Research, 7(2), 51-73.
Tüfekçioğlu, A., Tüfekçioğlu, M. (2018). Forest ecosystems and drought interactions. Turkish Journal of Forestry, 19(1), 103-108.
Yılmaz, Ö. (2022). The Concept of Organism in Philosophy of Biology. Kilikya Journal of Philosophy, 1, 78-86.

Effects of Atmospheric Microplastics on the Epidermal System in Plants: Example, Spinach (*Spinacea oleracea* L.)

Sümeyye Ezgi BARUT[1]

Tahir ATICI[2*]

Gutes DOĞAN[3]

Ayşe Rümeysa KARACASOY[4]

1- Student, Millî Eğitim Bakanlığı, Ankara-Türkiye. E-mail: sezgibarut19@gmail.com OrcID:0009-0007-4036-9397

2- Prof. Dr. *Sorumlu Yazar, Gazi Üniversitesi Gazi Eğitim Fakültesi, Biyoloji Eğitimi ABD. Ankara-Türkiye. E-mail: tahir@gazi.edu.tr OrcID: 0000-0002-3396-3407

3- Student, Millî Eğitim Bakanlığı, Ankara-Türkiye. E-mail: gutesdogan@gmail.com OrcID:0009-0000-6655-7109

4- Res. Asst., Gazi Üniversitesi Gazi Eğitim Fakültesi, Biyoloji Eğitimi ABD. Ankara-Türkiye E-mail: karacasoy.ak@gmail.com OrcID: 0000-0001-7244-1081

ABSTRACT

Plastic production worldwide has increased significantly in recent years and reached 368 million tons in 2019. Recycling only 10% of the plastics produced turns the remaining 90% into waste. Since these wastes are not stored under appropriate conditions and their use cannot be controlled, microplastic rates in ecosystems are increasing and microplastics are becoming a serious threat to the ecosystem. In order to obtain comprehensive data, plants at the bottom of the food pyramid were studied. Spinach (*Spinacea oleracea* L.), a vascular and annual herbaceous plant, was chosen as the model organism. "Atmospheric microplastics precipitate on the leaves of plants, which disrupts plant photosynthesis and development" the hypothesis has been established. To prove the hypothesis, a controlled experimental setup was established, consisting of two experimental groups: microplastic-treated and filtered air, and a control group under normal outdoor air conditions. As a result of the carbon dioxide and oxygen measurements, the oxygen rate in the plant treated with microplastic was measured to be 3% less than the system with filtered air. The amount of carbon dioxide was measured to be approximately 11.6% higher in the microplastic-treated experimental group than in the other experimental group. In line with these data, it was concluded that photosynthesis was disrupted. It has also been observed that microplastics affect the transpiration process and create stress in the plant. In line with the data obtained, it is possible to say that atmospheric microplastics pose a serious danger to plants, which are the basic unit of the ecosystem. Ignoring biological riches and allowing them to disappear for some short-term benefits is the same as destroying a great economic potential that we can leave as a legacy to future generations. It is desired to raise awareness on this issue and it is recommended to investigate the effects of atmospheric microplastics on different plants.

Keywords: Atmospheric Microplastic, Vascular Plant, Photosynthesis, Stoma, Spinach (Spinacia Oleracea L.).

INTRODUCTION

Ecosystems behave like living organisms. They are in constant interaction with the living beings they host. Similar hierarchies of cell-tissue-organ in organisms exist in ecosystems in the form of prey-predator and trophic levels (Reece et al., 2015). Just as life in organisms depends on the preservation of this hierarchy, ecosystems depend on the interaction between living beings and the environment. The most important life factor that maintains this order for both organisms and ecosystems is balance. Any disruption of the balance for any reason poses a vital risk to both systems. It should also be remembered that both systems are interdependent. Considering

that organisms live in ecosystems and are in constant interaction with ecosystems, it is possible that threats to organisms directly affect the ecosystem, and threats to ecosystems directly affect organisms (Reece et al., 2015).

Today, human activities are one of the main factors that disrupt the balance in ecosystems. In particular, human-created pollution threatens the ecological balance. One of these, plastic pollution, has come to the fore as an ecological threat due to the rapid increase in plastic consumption worldwide. Plastics are preferred in almost all sectors because they are easy to process, lightweight, durable and cheap (Esmeray and Armutcu, 2020). The data obtained showed that 368 million tons of plastic were produced worldwide in 2019 (Yao et al., 2022), and the fact that only 10% to 20% of this amount is recyclable (Yurtsever, 2015) has increased concerns on this issue. This situation led to the first studies being conducted on macro-sized plastics, which constitute a large part of primary waste. Later, microplastics and nanoplastics smaller than 5 mm in size, formed by the abrasion of macro-sized plastic pieces by various external factors (Yurtsever, 2015), were detected. The fact that microplastics and nanoplastics are harder to control due to their size has intensified studies in this area. Microplastics have been detected in all ecosystems and in the bodies of many organisms living in these ecosystems today. This has made microplastics an ecological threat and has caused scientific research to focus on microplastics. Studies have focused on the characteristics, types and effects of microplastics on the ecosystems they are located in. The fact that microplastics found in aquatic and terrestrial ecosystems are easier to detect and study has concentrated research on these ecosystems. However, studies on microplastics in the atmosphere have mostly failed to go beyond detection and prediction. Apart from aquatic and terrestrial ecosystems, microplastics found in the atmosphere also negatively affect organisms.

After the research on the definition and properties of microplastics, their effects on human health and different ecosystems have been studied (Yurtsever, 2019; Yao et al., 2022). It is possible to classify these ecosystems as terrestrial, aquatic and atmospheric ecosystems. The fact that microplastics are easier to detect and monitor in terrestrial and aquatic ecosystems than in atmospheric ecosystems has shaped the research in this direction (Horton and Dixon, 2017). Various studies have been conducted on living things in these ecosystems. The possible effects of microplastics found in terrestrial ecosystems on the ecosystem have been examined (Akça and Ok, 2021). There are studies on algae (Bhattacharya et al., 2010) and other aquatic creatures in aquatic ecosystems (Shukur et al., 2023). It is known that microplastics absorb heavy metals and various pollutants due to their hydrophobic surfaces, especially in aquatic ecosystems, and pose a threat to living things (Yurtsever, 2015). In terrestrial ecosystems, there are studies in

which plants such as lettuce, wheat, corn, and rice are exposed to microplastics through soil and water (Campanale et al., 2021). In the studies, plants were exposed to MPs and NPs, especially through rhizomes and roots, and it was proven that they had negative effects on agricultural plants. It has been mentioned that many other living things can be negatively affected by the consumption of agricultural products contaminated by MPs (Li et al., 2019; Qi et al., 2018).

When current studies on microplastics are examined, it is seen that the focus is on photoautotrophic organisms, which are the basic unit of the ecosystem, in order to obtain more comprehensive data and make predictions. The photosynthesis processes carried out by photoautotrophic organisms are effective in the formation of this situation. Photosynthesis is an interface between inanimate matter and living organisms and provides the flow of energy and matter within the ecosystem. Therefore, organisms at all trophic levels need photosynthesis. Studies have shown that photoautotrophic organisms convert 200 billion tons of carbon dioxide into complex organic compounds every year and produce 140 billion tons of oxygen for the atmosphere. (Li et al., 2021) In line with these data, it is expected that the ecosystem will be directly threatened in a process where photoautotrophic organisms and therefore photosynthesis are negatively affected.

There are many studies proving that photosynthesis is disrupted by microplastics. For example, in a study on algae in aquatic ecosystems, it was proven that microplastics accumulate on the algae and disrupt photosynthesis (Rillig et al., 2019). Plants in terrestrial and aquatic ecosystems have also been studied as photoautotrophs (Ge et al., 2021). In subsequent comprehensive studies, it was determined that microplastics and nanoplastics applied to plants in terrestrial ecosystems can enter the cells through stomata and are transported to various parts of the plant in this way, disrupting photosynthesis and development (Azeem et al., 2021; Lian et al., 2021; Sun et al., 2021; Yao et al., 2022). MPs and NPs, especially applied to leaves, which are the photosynthetic organs of plants, have serious side effects for plants. Lian et al. In a study conducted by (2021), it was observed that polystyrene nanoplastics applied to the leaves of lettuce (Lactuga sativa var. capitata L.) plants entered the leaf through the stomata, reached the roots and disrupted the development of lettuce. Again, in the application of modified (PS-COOH) and amino group modified (PS-NH_2) polystyrene nanoplastics to corn (Zea mays L.) plants through the leaves, it was observed that nanoplastics could reach the roots as a result of entering through the stomata and it was also proven that they negatively affected photosynthesis (Sun et al., 2021). At the same time, it was determined that nanoplastics could also travel between cells via apoplasts due to their small size, and it was observed that MPs could not pass the epidermis and remained on the leaf surface (Sun et al., 2021). Based on the obtained data, it is possible to say that nanoplastics are more advantageous than

microplastics in terms of transport at the cellular level. This makes nanoplastics a much more serious threat to plants and other organisms.

It is known that microplastics in the atmosphere can be transported due to the more dynamic structure of the atmosphere compared to other ecosystems and can also contribute to MP contamination in terrestrial and aquatic ecosystems through dry and wet deposition (Bi, He, & Chen, 2023; Horton & Dixon, 2017). This situation increases concerns about atmospheric ecosystems and creates a need for new studies. When existing studies on plant and atmospheric microplastics were examined, it was concluded that microplastics can cause dry and wet deposition on plant leaves (Yao et al., 2022). It was also mentioned that plant leaves can serve as bowls for atmospheric microplastics (Bi et al., 2023; Yin et al., 2021). As a result of the compilation of studies on the effects of microplastics on vascular plants, which constitute a large part of terrestrial plants, it has been seen that there are not enough studies on plants and more research is needed to fully understand the effects of microplastics on their complex internal structures (Li et al., 2019).

As a result of the literature study, it was determined that there were not enough studies on atmospheric microplastics and their effects on plants. It was thought that even if microplastics could not pass-through stomata, they would block them and disrupt CO_2 and O_2 transfer between plant and environment, and thus photosynthesis. The hypothesis "Atmospheric microplastics sediment on plant leaves, which disrupts plant photosynthesis and development" was established and a controlled experiment was conducted.

MATERYAL AND METHOD

To prove the hypothesis that "Atmospheric microplastics settle on plant leaves, which disrupts plant photosynthesis and development." a controlled experimental setup consisting of two experimental groups and one control group was established and a controlled experiment was conducted within the scope of the experimental model (Büyüköztürk et al., 2008).

Establishment of the Experimental Setup and Experimental Process

Spinach plants grouped in pairs were placed in glass bowls and a setup was created with serum sets to continuously supply air to the experimental setup. Air hoses, transparent drip chambers and spikes were placed in the holes so that they would remain inside the bowls and 0.8 g of microplastic was placed in the transparent drip chamber of the air hose of the 1st experimental group and filter paper (Cellulose Nitrate Filter, Pore size = 8µ) was placed in the drip chamber of the air hose placed in the 2nd experimental group to ensure that the air was filtered. No intervention was made to the air hose placed in the control group. In order to best observe the photosynthesis processes of the plants, the setups were placed in a way that they could benefit from sunlight.

In the established setup, in the 1st Experimental Group, spinach plants were treated with air contaminated with microplastic (Figure 1-a), in the 2nd Experimental Group, the ambient air was filtered (Figure 1-b), and in the control group, the plants were observed in ambient air without any treatment (Figure 1-c).

Figure 1-a

Figure 1-b

Figure 1-c

Figure 1. Preparation of experimental setups

The plants were carefully weighed and grouped (Figure 2 a-b-c) and the microplastics to be used in the experiment were produced in a laboratory environment. For this purpose, the most commonly used plastic materials today, such as pet bottle caps, old bags and plastic parts of daily used items, were used. The materials that were broken down with microdisintegrators and made air-soluble were passed through a micro mesh and their dimensions were reduced to a size accepted as microplastic (<1 mm).

Figure 2-a

Figure 2-b

Figure 2-c

Figure 2. Weighing the spinach plant before the experiment

The spinach plants that were physically closest to each other were selected and grouped in pairs. Three of these groups were used in the experimental setup. The weights of the groups were measured individually (Table 1-a), the number of leaves was determined (Table 1-b) and noted as the initial values. At the beginning of the experiment, the carbon dioxide measurement of the ambient air was also made (Table 1-c), and the measured value was determined as the initial CO_2 amount for all setups.

Table 1. Initial measurement values of the experimental setups

Experimental Setups	Weight (a)	Number of Leaves (b)	Initial CO_2 Amount (c)
1. Experimental Group (MP Added Air)	165,9 g (Figure 2-a)	13	374 ppm
2. Experimental Group (Filtered Air)	182,2 g (Figure 2-b)	12	374 ppm
Control Group	185,6 g (Figure 2-c)	13	374 ppm

After the first day of the experiment, the devices were observed every two days and each device was given air for five minutes in turn. In this way, both the accumulation of microplastics in certain areas was prevented and the amount of filtered air in the device that was given filtered air was increased. In order to meet the water needs of the spinach plants, water vapor was injected into the air in the experimental devices with a syringe on the 8^{th} and 15^{th} days of the experiment. The environment on which the devices were located was punctured with syringe needles and the subjects were given ten milliliters of water on the 8^{th} day and twenty milliliters of water on the 15^{th} day without any air exchange with the outside. The duration of the experiment was determined as 17 days, considering that air would be given every two days for both the adaptation period of the plants to their new environment and the accuracy of our observations, and the data was noted.

FINDINGS

Observations were made during the experiment and the obtained data were reported. In order to obtain meaningful and consistent results from the experiment with the hypothesis, data were collected on 5 different parameters. These are:

- Change and difference in CO_2 amounts in the bowls
- Difference in O_2 rates in the bowls
- Change in the weight of the plants
- Change in the number of leaves of the plants
- Change in the physical properties of the plants

Changes in CO_2 (Table 2) and O_2 (Table 3) Amounts in the Bowls

The amount of carbon dioxide in the experimental group treated with microplastic showed a greater increase than the other setups (Table 2). When the oxygen rates were compared, the amount of oxygen was measured the highest in the setup with filtered air (Table 3. This value is 3% higher than the lowest measured microplastic treated air.

Table 2. Changes in CO_2 amounts of experimental setups

Experimental Setups	Initial CO_2	Final CO_2	Difference
1. Experimental Group (MP Added Air)	374 ppm	968 ppm	594 ppm
2. Experimental Group (Filtered Air)	374 ppm	947 ppm	573 ppm
Control Group	374 ppm	867 ppm	493 ppm

Table 3. Final O_2 Ratios of Experimental Setups

Experimental Setups	Rate of final O_2
1. Experimental Group (MP Added Air)	%47
2. Experimental Group (Filtered Air)	%50
Control Group	%48

Changes in Plant Weights

When the initial and final weights of the plants were compared, a decrease in plant weights was observed in all groups. This situation was evaluated as the plants not being able to adapt to their new environment and the insufficient water given. A comparison was made based on the amount of decrease in weights. Accordingly, it was seen that the least decrease in weight was in the experimental group treated with microplastic. The greatest decrease was observed in the control group, and the decrease in weight in the experimental group with filtered air was between the values of the other experimental setups (Table 4)**.**

Table 4. Weight changes of the experimental setups

Experimental Setups	İnitial weight	Final weight	Difference
1. Experimental Group (MP Added Air)	165.9g	161g	4.9g
2. Experimental Group (Filtered Air)	182.2g	175g	7.2g
Control Group	185.6g	176g	9.4g

Change in the Number of Leaves in Plants

At the beginning of the experiment, the groups were determined in such a way that the number of leaves in the groups would not differ greatly from each other. When the number of leaves was determined at the end of the experiment, significant differences were detected between the groups. In the experimental group treated with microplastic, 5 new leaves were observed. In the experimental group with filtered air, an increase of 4 was observed, while in the control group, no new leaves were observed, but there was an increase in leaf thickness (Table 5).

Table 5. Change in leaf number of experimental setups

Experimental Setups	Starts leaf count	Final leaf Count	Difference
1. Experimental Group (MP Added Air)	13	18	5 new leaves
2. Experimental Group (Filtered Air)	12	16	4 new leaves
Control Group	13	15	-

Changes in the Physical Properties of Plants

Due to the long duration of the experiment and the inability to provide sufficient water for spinach plants that love water, a slight discoloration was observed in all experimental groups. This situation was neglected because it

was observed in all groups. The final conditions of the plants were compared to understand which group of plants could cope better with thirst.

It was observed that the plants in the filtered air experimental group were more vibrant and greener than the other subjects. It was determined that the condition of the plants in the control group was approximately similar to the microplastic-treated experimental group. Newly formed leaves were not observed in the control group, unlike the microplastic-treated experimental group.

DISCUSSION AND CONCLUSION

When the findings were evaluated, microplastics were found in the leaves of the plants in the microplastic-contaminated setup, and it was observed that photosynthesis and development were disrupted. This situation proves the hypothesis that "Atmospheric microplastics settle on plant leaves, which disrupts plant photosynthesis and development." According to the findings, the study was evaluated under the subheadings of;

- Photosynthesis
- Plant development
- Transpiration.

Photosynthesis; in order to comment on the photosynthesis processes of plants, the increase in CO^2 amounts and final oxygen rates in the setups were compared. As a result, it was observed that the microplastic-treated setup had the greatest increase with 594 ppm. The final oxygen rate (47%) was also measured lower than the other setups in the same subject. This situation shows that the most inefficient photosynthesis occurred in the setup. The highest final oxygen rate (50%) was also measured in the filtered air experimental group. When the carbon dioxide change was examined, a similar but lesser increase was observed in the microplastic experimental group. Considering the balance in the photosynthesis process, it is an expected result that the carbon dioxide amount is measured more in proportion to the oxygen rate. The establishment of balance shows that the most efficient and healthy photosynthesis occurs in this setup.

When the experimental groups were compared with the control group, it was seen that the carbon dioxide increase was the least in the control group. However, the low oxygen rate also shows that photosynthesis in this system is constantly performing metabolic respiration for new leaf formation and other similar growth and development activities and is at a level between the two experimental groups. Based on this situation, it is possible to say that there is a certain amount of microplastic in the atmosphere right now and that it affects photosynthesis.

Plant development; In order to make inferences about the development of plants, the initial and final weights and leaf numbers were compared. When the weight changes were examined, a decrease was observed in all experimental groups. This situation was interpreted as the plant not being able to adapt to the environment and the insufficient water given, and was neglected because it was observed in all setups. In order to make a comparison, the decrease in weights was determined**.**

An increase in the number of leaves was also observed in the plants in the experimental group treated with microplastics. When this situation was evaluated together with the other data obtained, it was concluded that it was caused by microplastics. Microplastics were found on the leaves in the microscope observations. Guo et al. (2023) concluded that microplastics reached the vascular bundles through symplastic and apoplastic pathways in their study on corn and soybean plants. Similarly, in this study, it was concluded that the microplastics observed on the leaves caused stress in the plant by rendering the plant leaves unusable. The stress in the plant directed the plant to form new leaves in order to survive. As a result, the decrease in weight was the least in the plants in this arrangement.

In the filtered air setup, an increase of 4 leaves was observed. When evaluated together with the photosynthesis data obtained, it is possible to interpret the leaf increase as the normal growth and development of the plant. The decrease in weight was also greater than in the microplastic-treated setup due to the lower leaf increase.

The increase in the number of new leaves observed in the control group is remarkable and the amount of weight decrease was greater than in the other groups. When the findings obtained in terms of development are evaluated, it is possible to say that the development of the filtered air experimental group was better than in the other setups.

Transpiration; when the qualitative physical properties in plants are focused on, regional and color fading are observed in the leaves of all plants due to dehydration. However, it was concluded that the amount of fading was not similar and there were differences between the experimental groups. It was observed that the leaves in the experimental group with filtered air were livelier and turgorous. On the contrary, the amount of fading in the leaves in the microplastic treated and control groups was much higher. In addition, the leaves were more lifeless. It is possible to explain this situation with the disruption of the transpiration process in the plants.

Microplastics have been observed in abundance on plant leaves in microscope images. Considering that there are stomata on leaves that are smaller than the size of microplastics, it is possible that microplastics on the leaf block the stomata. Stomata create osmotic pressure potential in plants through transpiration and play a role in the transfer of water taken from the roots to the leaves. In some plants adapted to dry environments, closing the

stomata prevents transpiration due to internal balance. However, this situation is often observed as an adaptive feature in plants that do not have a large leaf area. This situation is also used to provide a short-term solution in plants with large leaf areas.

When the roles of stomata on the plant are evaluated, the blockage of stomata due to microplastics, independent of the internal balance, will reduce transpiration and will not be enough to meet the osmotic pressure potential required for transpiration. As a result, the plant will lose water, but will not be able to deliver it to the leaves despite taking water from the roots. This will cause wilting in the leaves. The situation mentioned in the microplastic-treated setup and the control group is the case. All setups were given water by spraying equal amounts of air into the environment. The experimental group with filtered air was able to easily take water from its leaves and deliver water to its leaves through transpiration. However, the opposite occurred in the microplastic experimental group. Microplastics prevented both water intake from the leaves and the water absorbed from the roots from reaching the leaves. The same situation was observed in the control group. From the other data obtained, it was concluded that there is a certain amount of microplastic in the atmosphere right now and that microplastics have an effect on the plant. Therefore, it is an expected result that microplastics disrupt transpiration in the control group, similar to the experimental group treated with microplastics.

When the control group and the experimental setups were compared as a whole, it was observed that the control group followed a process closer to microplastics. Studies indicate that the amount of microplastics currently in the atmosphere is not high, and the possible negative effects of atmospheric microplastics are ignored. However, the data obtained from the experiment prove that even a small amount of microplastics currently in the atmosphere causes quite negative effects on plant photosynthesis and development. In a study conducted on climate change adaptation modeling of crop plants (Azeem et al. 2021), it was stated that crop plants (wheat, canola and sunflower) showed different responses in order to cope with similar problems arising from the effect of climate change. The geographical distribution and future existence of the species should be modeled by modeling the results of climate change and microplastic effects in spinach-like plants. In this respect, the study is a pioneer for the literature.

Conflict of Interest Statement

As the authors of the article, we declare that there is no conflict of interest between us.

Ethics Committee Approval

This study does not require approval from the ethics committee.

Authorship Contribution Statement

The authors contributed 30%, 30%, 25% and 15%, respectively, to the planning of the study, development of materials and methods, data collection and processing, writing of the article, review and editing of data, and literature review stages.

REFERENCE

Akça, M. ve Ok, S. (2021). Toprak ekosistemi üzerine mikroplastiklerin etkileri, *Toprak Bilimi ve Bitki Besleme Dergisi*, 9(2), 79-91. doi: 10.33409/tbbbd.997807

Azeem, I., Adeel, M., Ahmad, M. A., Shakoor, N., Jiangcuo, G. D., Azeem, K., Ishfaq, M., Shakoor , A., Ayaz, M., Xu, M. ve Rui, Y. (2021). Uptake and accumulation of nano/microplastics in plants: A critical review, *Nanomaterials Journal*, 11(2935), 1-22. https://doi.org/10.3390/nano11112935

Bhattacharya, P., Lin, S., Turner, J. P. ve Ke, P. C. (2010). Physical adsorption of charged plastic nanoparticles affects algal photosynthesis, *The Journal of Physical Chemistry C*, 114(2010),16556–16561. https://doi.org/10.1021/jp1054759

Bi, M., He, Q. ve Chen, Y. (2023). What Roles Are Terrestrial Plants Playing in Global Microplastic Cycling? *Environ. Sci. Technol*. 2020, 54, 5325−5327. https://dx.doi.org/10.1021/acs.est.0c01009

Büyüköztürk, Ş., Çakmak E.K., Akgün, Ö.E., Karadeniz, Ş. ve Demirel, F. (2008). Bilimsel Araştırma Yöntemleri. Pegem Yayınları, Ankara.

Campanale, C., Galafassi, S., Savino, I., Massarelli, C., Ancona, V., Volta, P. & Uricchio, V. F. (2021). Microplastics pollution in the terrestrial environments: Poorly known diffuse sources and implications for plants, *Science of the Total Environment*, 805 (2022). https://doi.org/10.1016/j.scitotenv.2021.150431

Esmeray, E. ve Armutcu, C. (2020). Mikroplastikler, çevre-insan sağlığı üzerine etkileri ve analiz yöntemleri, *Düzce Üniversitesi Bilim ve Teknoloji Dergisi*, 8(2020), 839-868. https://doi.org/10.29130/dubited.586453

Ge, J., Li, H., Liu, P., Zhang, Z., Ouyang, Z. ve Guo, X. (2021). Review of the toxic effect of microplastics on terrestrial and aquatic plants, *Science of the Total Environment*, 791(2021), 1-9. https://doi.org/10.1016/j.scitotenv.2021.148333

Guo, S., Wang, J., Sun, H., Wu, J., Xu, J. ve Sun, J. (2023). Foliar uptake and in-leaf translocation of micro(nano)plastics and their interaction with epicuticular wax, *Environ. Science.* 10,1126-1137. https://doi.org/10.1039/D2EN00975G

Horton, A.A. ve Dixon, S.J. (2017). Microplastics: An introduction to environmental transport processes, *WIREs Water*, 2017- 1268. https://doi.org/10.1002/wat2.1268

Lian, J., Liu, W., Meng, L., Wu, J., Chao, L., Zeb, A. ve Sun, Y. (2021). Foliar-applied polystyrene nanoplastics (PSNPs) reduce the growth and nutritional quality of lettuce (Lactuca sativa L.), Environmental Pollution, 280. https://doi.org/10.1016/j.envpol.2021.116978

Li, L., Zhou, Q., Yin, N., Tu, C. ve Luo, Y. (2019). Uptake and accumulation of microplastics in an edible plant, *Chinese Science Bulletin*, 64(9), 928-934. https://doi.org/10.1360/ N972018-00845

Li, Y., Liu, X., Shinde, S., Wang, J. ve Zhang, P. (2021). Impacts of Microand Nanoplastics on Photosynthesis Activities of Photoautotrophs: A Mini-Review. *Front. Microbiol*. 12:773226. https://doi.org/10.3389/fmicb.2021.773226

Qi, Y., Yang, X., Pelaez, A. M., Lwanga, E. H., Beriot, N., Gertsen, H., Garbeva, P. ve Geissen, V. (2018). Macro- and micro- plastics in soil-plant system: Effects of plastic mulch film residues on wheat (Triticum aestivum) growth, *Science of the Total Environment*, 645(2018), 1048-1056. https://doi.org/10.1016/j.scitotenv.2018.07.229

Reece, J. B., Urry, L. A., Cain, M. L., Wasserman, S. A., Minorsky, P. V. ve Jackson, R. B. (2015). Ekoloji, Campbell Biology Ninth Edition. (Çev. Editörler: Gündüz, E. ve Türkan, İ.) Palme Yayıncılık, 1142-1261.

Rillig, M. C., Lehmann, A. de Souza Machado, A.A. ve Yang, G. (2019). Microplastic effects on plants, *New Phytologist*, 223(2019), 1066-1070. https://doi.org/10.1111/nph.15794

Shukur, S.A., Hassan, F.M., Fakhry, S.S., Ameen, F. ve Stephenson, S.L. (2023) Evaluation of microplastic pollution in a lotic ecosystem and its ecological risk. *Marine Pollution Bulletin*, Volume 194, Part A,115401. https://doi.org/10.1016/j.marpolbul.2023.115401

Sun, H., Lei, C., Xu, J. ve Li, R. (2021). Foliar uptake and leaf-to-root translocation of nanoplastics with different coating charge in maize plants. *Journal of Hazardous Materials*, 416(2021). Erişim adresi: https://doi.org/10.1016/j.jhazmat.2021.125854

Yao, X., Luo, X.-S., Fan, J., Zhang, T., Li, H. ve Wei, Y. (2022). Ecological and human health risks of atmospheric microplastics (MPs): a review, Environmental Science: Atmospheres, 2(2022), 921-942. https://doi.org/10.1039/d2ea00041e

Yin, L., Wen, X., Huang, D., Du, C., Deng, R., Zhou, Z., Tao, J., Li, R., Zhou, W., Wang, Z.ve Chen, H. (2021). Interactions between microplastics/nanoplastics and vascular plants, Environmental Pollution, 290. https://doi.org/10.1016/j.envpol.2021.117999

Yurtsever, M. (2015). Mikroplastiklere Genel Bir Bakış, *Dokuz Eylül Üniversitesi Mühendislik Fakültesi Fen ve Mühendislik Dergisi,* 17(50), 68-83.

Yurtsever, M. (2019). Nano- ve mikroplastik' lerin insan sağlığı ve ekosistem üzerindeki olası etkileri, *Menba Kastamonu Üniversitesi Su Ürünleri Fakültesi Dergisi*, 5(2), 17-24.

Comparison of Physical Properties, Antioxidant Capacity, Total Flavonoid and Total Phenolic Contents of Naturally Fermented Vinegar from Apple Pulp

Zuhal SAHİN[*1]

Fatih SONMEZ[2]

ABSTRACT

Apple is one of the most consumed and most traded pome fruit. It is consumed both fresh and processed. With the processing of these products, a waste product with rich phenolic content. In this study, Apple pulp vinegar was obtained by applying slow method with apple pulp. TPC, TFC and antioxidant activity for apple pulp vinegar was determined. In addition, TFC, TPC and antioxidant activities of apple pulp, apple pulp wine, apple pulp vinegar and apple fruit vinegar were investigated. Total flavonoid and phenolic contents of apple pulp vinegar were determined as 373.81 mg GAE/L and 200.23 mg catechin/L, respectively. Although the DPPH activity of apple pulp vinegar is 19.05 mM trolox/mL, the ABTS activity is 22.94 m trolox/mL. The results showed that vinegar produced from apple pulp has a bioactive content similar to apple fruit vinegar. It is seen that vinegar production can be accepted as an alternative to add value to apple pulp.

Keywords: Apple Pulp, Antioxidant Activity, TFC, TPC, Vinegar.

INTRODUCTION

Vinegar is a product that comes out as a result of fermentation of ethanol by acetic acid bacteria under aerobic conditions after ethanol fermentation of sugars in fresh and/or dried fruits (Vilela, 2023). In addition, this product, which is produced as a result of acetic acid fermentation of wines, takes the color of the raw material from which it is produced (Al-Dalali et al., 2023). Vinegar production occurs as a result of two-stage fermentation. In the first step, sugars are broken down into ethanol by *Saccharomyces cerevisiae* in an anaerobic environment. In the second stage, ethyl alcohol formed by yeasts under aerobic conditions is converted into acetic acid by bacteria such as *Acetobacter* and *Gluconobacter* (Bayram et al., 2018). Apple cider vinegar is very rich in polyphenols (catechin, epicatechin, gallic acid, chlorogenic acid, etc.) (Budak et al., 2011). They reported that vinegar rich in bioactive content can be produced from apple pulp (Du et al., 2019).

In this study, it was aimed to recycle industrial waste apple pulp by using it in vinegar production. Vinegar production from waste apple pulp and its phytochemical properties were investigated by natural method. The antioxidant activity, TFC and TPC were determined. All properties of vinegar obtained from apple pulp were compared with naturally fermented apple fruit vinegar.

MATERIALS AND METHODS

Vinegar Production

Vinegar production was made by modifying according to Karataş (2022). Vinegar production process was carried out by natural method. The first stage of the vinegar production process is alcohol fermentation. At this stage, apple

pulp (50 g), sterile water and 0.25 g/L *Saccharomyces cerevisiae* were combined in a jar. The SÇKM was adjusted to 13 brix. It was incubated at 20±2 °C under anaerobic conditions for 8 weeks The alcohol content reaches approximately 7-8% and alcoholic fermentation ends.. The second stage of the vinegar process is acetic acid fermentation. At this stage, the apple pulp is filtered. 5% mother vinegar was added to the remaining part. The mouth of the jars was covered with a thin cheesecloth. It was incubated for 11 weeks under aerobic conditions. Acetic acid fermentation ends when the alcohol content reaches approximately 0.5% (Akbaş, 2008).Apple pulp vinegar production flow chart is given in Figure 1.

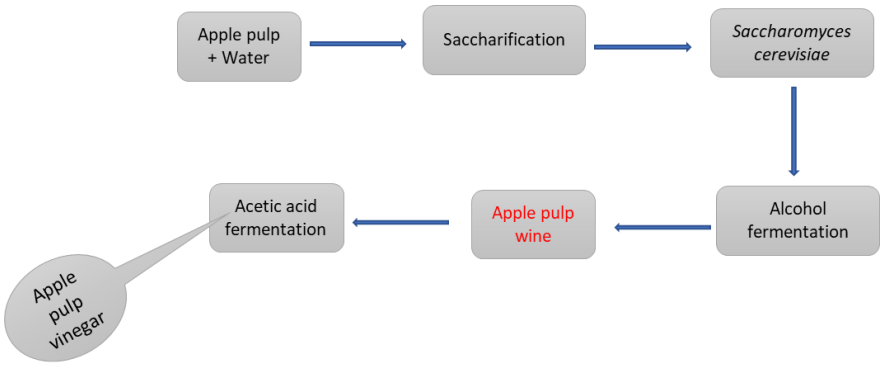

Figure 1: Apple pulp vinegar production flow chart

Extraction

Apple pulp sample was thoroughly mixed with methanol and then the methanolic extracts were filtered. The filtrates were stored at 4^0C for 2 days to be analyzed later.

Total Phenolic Content

While determining the total phenolic substance content, the method reported by Sönmez et al. (2023) was applied. Diluted Folin-Ciocalteu reagent was added to 100 µl of apple pulp, apple pulp wine and apple pulp vinegar and waited for 3 minutes. 20% aqueous Na_2SO_3 solution was added. Samples were incubated for 60 minutes and absorbance values were measured on a UV-vıs at 765 nm. The standard graph was created using gallic acid (GAE).

TFC (Total Flavonoid Content)

The method applied by Chlopicka et al. (2012) was used to determine total flavonoid content.

DPPH assay

DPPH radical scavenging activities were measured according to Guldane et al., (2022). Apple pulp, apple pulp wine and apple pulp vinegar were mixed with of 3 mL DPPH. The sample and DPPH mixture was incubated for 30 min. After the incubation period, the absorbance value was measured at 517 nm.

ABTS activity

To determine the ABTS activity of the extracts, it was measured by the method specified by Sonmez et al. (2019). Firstly, ABTS radical solution is prepared. For this, ABTS and $K_2S_2O_3$ are dissolved in water, mixed and left for 24 hours. The prepared samples are mixed with ABTS radical and after 6 minutes the absorbance values are measured at 734 nm in a UV-VIS spectrophotometer. Trolox standard graph is prepared and results are calculated according to this graph.

Sensory analysis

Consumer preference test of vinegar samples was carried out with 20 semi-trained volunteer panelists consisting of academic staff and students of Pamukova Vocational School. Examples are presented in random order. Water was served before analysis and between tastings. Panelists were asked to rate the color, taste, and smell of the samples using a 9-point scale (1 = disliked at all and 9 = liked very much).

RESULTS AND DISCUSSION

In vinegar production, raw materials directly affect the quality of vinegar. The total phenolic content (TPC), DPPH, ABTS and TFC of apple pulp, apple pulp wine, apple pulp vinegar and apple fruit vinegar are given in Table 1. The TPC of apple pulp, apple pulp wine, apple pulp vinegar and apple fruit vinegar were determined as 189.64±13.71 mg GAE/L, 79.22±3.66 mg GAE/L, 373.81±28.89 mg GAE/L and 427.14±15.36 mg GAE/L, respectively. It is seen that the TPC of the raw material decreased in the alcohol fermentation (Apple pulp wine) part and then increased in the vinegar part. The total flavonoid content of apple pulp, apple pulp wine, apple pulp vinegar and apple fruit vinegar were determined as 135.94±0.54 mg catechin/L, 30.12±0.54 mg catechin/L, 200.23±6.25 mg catechin/ L and 68.09±8.77 mg catechin/ L, respectively. The total flavonoid content (TFC) also showed a significant increase in vinegar formation. It was determined that there was a decrease in the TPC and TFC during the alcohol fermentation stage.

DPPH antioxidant activities of apple pulp, apple pulp wine, apple pulp vinegar and apple fruit vinegar were calculated as 3.42±0.02 mM trolox/mL,

5.21±0.06 mM trolox/mL, 19.05±0.27 mM trolox/mL and 22.59±0.07 mM trolox/mL, respectively. At the same time, ABTS antioxidant activity capacities of them were 135.86±6.15 mM trolox/mL, 41.96±0.38 mM trolox/mL, 22.94±0.58 mM trolox/mL and 53.57±0.12 mM trolox/mL, respectively. DPPH activity of apple pulp, which was low, increased considerably in vinegar formation. The apple pulp vinegar and apple fruit vinegar have similar DPPH activities. However, it was determined that the high ABTS activity of apple pulp decreased in vinegar form.

Table 1: Total phenolic content (TPC), mM trolox/mL of DPPH, ABTS and TFC of apple pulp, apple pulp wine, apple pulp vinegar and apple fruit vinegar

Sample	TPC (mg GAE/L)	DPPH (mM trolox/mL)	ABTS (mM trolox/mL)	TFC (mg catechin/L)
Apple Pulp	189.64±13.71	3.42±0.02	135.86±6.15	135.94±0.54
Apple Pulp Wine	79.22±3.66	5.21±0.06	41.96±0.38	30.12±0.54
Apple Pulp Vinegar	373.81±28.89	19.05±0.27	22.94±0.58	200.23±6.25
Apple Fruit Vinegar	427.14±15.36	22.59±0.07	53.57±0.12	68.09±8.77

Graphical representation of TPC (mg GAE/L), DPPH, ABTS (mM trolox/mL) and TFC (mg catechin/L) results for apple pulp, apple pulp wine, apple pulp vinegar and apple fruit vinegar are given in Figure 2.

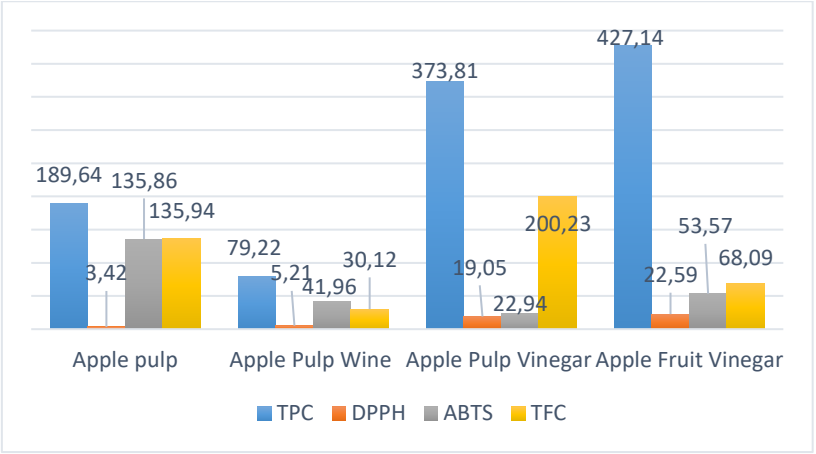

Figure 2: Graphical representation of TPC, DPPH, ABTS, and TFC results for apple pulp, apple pulp wine, apple pulp vinegar and apple fruit vinegar

Sensory scoring results of apple pulp vinegar and apple fruit vinegar are presented in Figure 3. Apple pulp vinegar and apple fruit vinegar were scored for color, smell and taste. Apple pulp vinegar was rated 5.75, 5.8 and 7.15 respectively. Additionally, apple cider vinegar was evaluated as 7, 5.65 and 5.8, respectively.

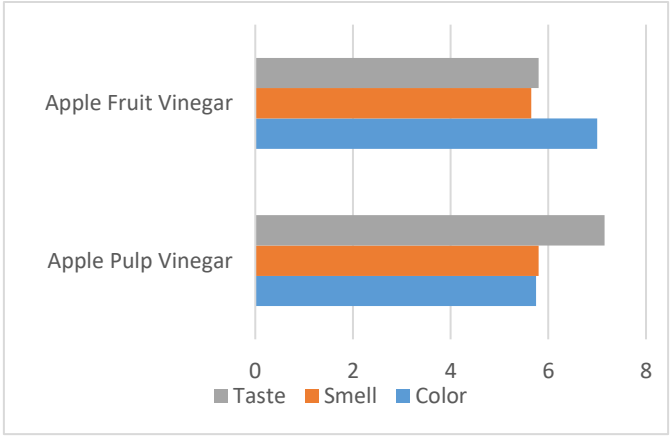

Figure 3: Sensory score results for apple pulp vinegar and apple fruit vinegar

CONCLUSIONS

It was determined that the TPC and TFC of apple pulp vinegar was significantly higher than that of apple pulp and apple pulp wine. The flavonoid content of apple pulp vinegar was determined higher than natural apple

vinegar. Moreover, the apple pulp vinegar showed higher DPPH activity than the apple pulp and apple pulp wine. In addition, apple pulp vinegar showed lower ABTS activity than apple pulp and apple pulp wine. The apple pulp vinegar has high TPC and TFC (respectively, 373.81 mg GAE/L and 200.23 mg catechin/L). The apple pulp vinegar has strong DPPH (19.05 mM trolox/mL) activities as antioxidant property while low ABTS (22.94 mM trolox/mL) inhibitory activity. The L* value of apple pulp vinegar (41.178±0.35) is very close to the L* value of apple fruit vinegar (40.152±1.00). Sensory analysis results show that; it was seen that apple pulp vinegar received better scores than apple fruit vinegar in terms of taste, while it also received similar scores in terms of smell. As a result, it was determined that the TPC, TFC and DPPH antioxidant activity of apple pulp vinegar were higher than apple pulp and apple pulp wine. Based on the results obtained, the production of apple pulp vinegar is recommended.

Apple pulp vinegar, which is not produced in our country, can be used as an alternative product for the use of food industry wastes with its rich phenolic and flavonoid compound content. As a result, this study is very important in terms of being the scientific study conducted with apple pulp vinegar in Turkey, and it will help further detailed studies and contribute to the literature. It is also important in terms of recycling and evaluation of industrial waste apple pulp. It is considered that apple pulp, which has rich bioactive content, can be used in vinegar production instead of apple fruit.

REFERENCES

Akbas M (2008) A research on the determination of composition of grape vinegars produced in turkey and their conformity to food legislation. MSc Thesis, Cukurova University

Al-Dalali S, Zheng F, Xu B, Abughoush M, Li L, Sun B (2023) Processing Technologies and Flavor Analysis of Chinese Cereal Vinegar: a Comprehensive Review. Food Anal Methods 16:1–28. https://doi.org/10.1007/s12161-022-02328-w

Bayram M, Kaya C, Esin Y, Er B, Gülmez E, Terzioğlu E, Yücel EE (2018) Some Quality Properties of Rice Vinegar and Various Commercial Vinegar Samples. Akademik Gıda 16(3):293-300. https://doi.org/10.24323/akademik-gida.475357

Budak HN, Kumbul-Doguç D, Savaş CM, Seydi, AC, Kök-Taş T, Ciriş IM, Güzel-Seydim ZB (2011) Effects of apple cider vinegars produced with different techniques on blood lipids in highcholesterol-fed rats. Journal of Agricultural and Food Chemistry, 59:6638–44

Chlopicka J, Pasko P, Gorinstein S, Jedryas A, Zagrodzki P (2012) Total phenolic and total flavonoid content, antioxidant activity and sensory evaluation of

pseudocereal breads. Food Sci Technol 46:548-555. https://doi.org/10.1016/j.lwt.2011.11.009

Du G, Zhu Y, Wang X, Zhang J, Tian C, Liu L, Meng Y, Guo Y (2019) Phenolic composition of apple products and by-products based on cold pressing technology. Journal of Food Science and Technology, 56:1389–1397. https://doi.org/10.1007/s13197-019-03614-y

Guldane M, Yagmur T, Cetin H, (2023) Doğal Biyoaktif Sebze Özütlerinin Beze Özelliklerine Etkisi. Gıda 48(5): 1047-1059. https://doi.org/10.15237/gida.GD23085

Karatas D (2022) Vinegar production from red beet (*beta vulgaris l.*) and some physicochemical and sensory properties in red beet vinegars. M.Sc. Thesis, Afyon Kocatepe University

Sonmez F, Gunesli Z, Kurt BZ, Gazioglu I, Avci D, Kucukislamoglu M (2019) Synthesis, antioxidant activity and SAR study of novel spiro-isatin-based Schiff bases. Mol Diversity 23:829-844. https://doi.org/10.1007/s11030-018-09910-7

Sonmez F, Sahın Z (2023) Comparative Study of Total Phenolic Content, Antioxidant Activities, and Polyphenol Oxidase Enzyme Inhibition of Quince Leaf, Peel, and Seed Extracts. Erwerbs-Obstbau 65: 745-750. https://doi.org/10.1007/s10341-022-00696-5

Vilela A. (2023) Microbial Dynamics in Sour–Sweet Wine Vinegar: Impacts on Chemical and Sensory Composition. Appl Sci 13(13); 7366. https://doi.org/10.3390/app13137366

Clustering the Number of People According to Employment Branches in Türkiye Between 1960-2009

Cengiz GAZELOGLU [1]
Ece OZGOREN UNLU[2*]

1-Department of Statistics/Suleyman Demirel University, Türkiye
2-Department of Statistics/Suleyman Demirel University, Türkiye
[*](eceozgoren@sdu.edu.tr)

ABSTRACT

In order to explain the social and economic processes of a country, economic activity branches have great importance. In this study, in order to explain the above-mentioned situation, it was aimed to cluster the relevant years with hierarchical cluster analysis, which is a statistical analysis of employment in economic activity branches in Türkiye between 1960-2009. According to the results obtained, 4 different clusters were formed. Cluster 1 was formed by clustering in the years 1960-1973. These years correspond to the years when the agricultural sector was dominant. The second cluster consists of the years 1974-1992. These years correspond to the years when the industrial sector came to the forefront. The third cluster, the years 1993-2003, shows the period when the weight of the service sector increased in economic activities under the influence of neoliberal policy and structural transformations accelerated. Finally, the fourth cluster, the years 2004-2009, shows the period when the service sector peaked and the effect of the agricultural sector decreased on the economy. As a result, the clusters formed indicate important periods in Türkiye. In this case, it shows how accurate the analysis results are.

Keywords – Hierarchical Cluster Analysis, Economy, Employment, Türkiye.

INTRODUCTION

In a country, the branches of activity in the economy are considered as one of the basic indicators of transformation in the development process of the economy. These branches of activity are classified under 3 main headings. The first of these is the agricultural sector, the second is the industrial sector and the third is the service sector. The weights of these branches of activity in the total economy change over time [1]. As in the rest of the world, economic waves occurred in Türkiye between 1960 and 2009 and these waves resulted in significant structural changes. Examining this period is of critical importance in terms of understanding the impact of economic development strategies, global economic conditions and local policies on economic branches of activity ([2]- [3]).

In the 1960s, Türkiye attempted to produce some of the goods it imported from abroad domestically, thus attempting to get rid of dependency abroad, which was a policy called import substitution industrialization. During these years, employment and income generation capacity increased in the agricultural sector. In addition, state-supported industrial policies were also given importance [4]. These years can be expressed as a period when industrialization efforts were carried out under the leadership of the state. In addition, it is seen that the main theme of economic activities was agricultural activities in these years. The main purpose of these years was the import substitution policy, which was a policy that reduced external dependency [5].

Again, during these years, a large portion of citizens living in rural areas were employed in the agricultural sector. However, when the technological conditions at that time were considered, the contribution of agriculture to the economy was low. In other words, in a sense, the contribution of agriculture to the economy remained limited [6].

The 1980s were a turning point for Türkiye in economic terms. During these years, neoliberal policies were adopted, which aimed to increase free trade, reduce trade barriers, reduce industrial regulation, privatize some state-owned enterprises and reduce government spending. With this transition, foreign trade became free thanks to the flexibility in exchange rates By determining such policies that Türkiye implemented in these years, new reforms were made, industrial production accelerated in international markets and the volume of economic activities in the service sector increased [7]. It became the locomotive of the economy in some areas in particular. Examples of these areas are manufacturing industry, banking, trade and finance (Balassa, 1981). However, some problems also emerged during this process. The most important of these problems are unemployment and inequalities in income distribution [8]. The economic crisis experienced in the early 2000s led to some structural reforms. These reforms led to changes in many areas, especially agriculture. For example, while the share of total employment in agricultural activities decreased, the service sector and industry in particular became an important driving force of the Turkish economy. In addition, as a result of rapid integration into the world economy and the development of technology, the service sector grew. All of these affected the country's internal balances as well as global economic conditions [9].

In this study, structural changes in Türkiye's economic activity branches are discussed specifically for the period 1960-2009. The main purpose is to cluster similar years by bringing them together in employment according to economic activity branches. In this way, it will be clearly determined which years are similar to each other.

I. MATERIALS AND METHOD

A. Cluster Analysis

Cluster analysis is a multivariate statistical analysis method used in numerous scientific disciplines such as medicine, social sciences, and engineering. This method allows summary information to be obtained and interpreted more easily by combining the obtained data sets and variables with similar characteristics to create a complex structure. [11].

The term 'bibliometrics' was first used by Tryon in 1939. Subsequently, in 1963, the seminal work, "The Foundations of Numerical Classification" by Sokal and Sneath, made significant contributions to this field. [11].

The main purpose of cluster analysis is to classify ungrouped data according to their similarities and to allow the researcher to obtain appropriate

summative information for interpretation. Although the number of clusters is unknown in cluster analysis, it cannot be used in prediction since only results related to the current state of the data are obtained. Although there is an assumption of normality in cluster analysis, as in multivariate statistical analyses, the normality of distance values is considered sufficient even if classical normality is not achieved [12].

Clustering methods can be classified into two principal categories: The two main categories of clustering methods are hierarchical and non-hierarchical. In contrast to hierarchical clustering methods, which perform analyses based on both similarity and distance criteria, non-hierarchical clustering methods are not required to utilize these criteria and can instead operate with raw data. Non-hierarchical clustering analysis is typically employed when preliminary information is available regarding the number of clusters that the data set will be divided into. [10].

In this study, Euclidean Distance measure was used as the distance measure. In addition, the intergroup connection method was used as the clustering method.

Euclid Distance,

$$d(x_i, x_j) = \sqrt{\sum_{k=1}^{p} (x_{ik} - x_{jk})^2} \qquad (1)$$

While xi and x_i in Equation 1 show the observation vectors, d (x_i, x_j) shows the distance value.

B. Intergroup Connection Method

It is the most commonly used clustering method among hierarchical clustering analyses. The method basically starts by merging the units that are closest to each other and then creates clusters by merging the next unit that is closest to the units it has combined. In this way, by continuing the operations one after the other, the clusters created at each stage are expanded.

$$d_{k(ij)} = Min(d_{ki}, d_{kj}) \qquad (2)$$

In the method i. and j. assuming units are merged, k of the merged cluster. The distance measure to the cluster is calculated by the formula given in Equation 2.

$dk_{(i,\,j)}$: k. previously formed i of the cluster. and j. distance from clusters
dkj: k. j of the cluster. distance to the cluster,
dki: It refers to the distance of the kth cluster from the ith. cluster.

RESULTS

The data set used in this study covers the period 1960-2009. In these years, analysis were carried out on the number of employed people over the age of 15 according to the field of economic activity [13]. In addition, the number of people subject to analysis was processed in a 1/1000 ratio. Readers who want to get more detailed information about the data set. They can look at internet resources 1 in the resources section.

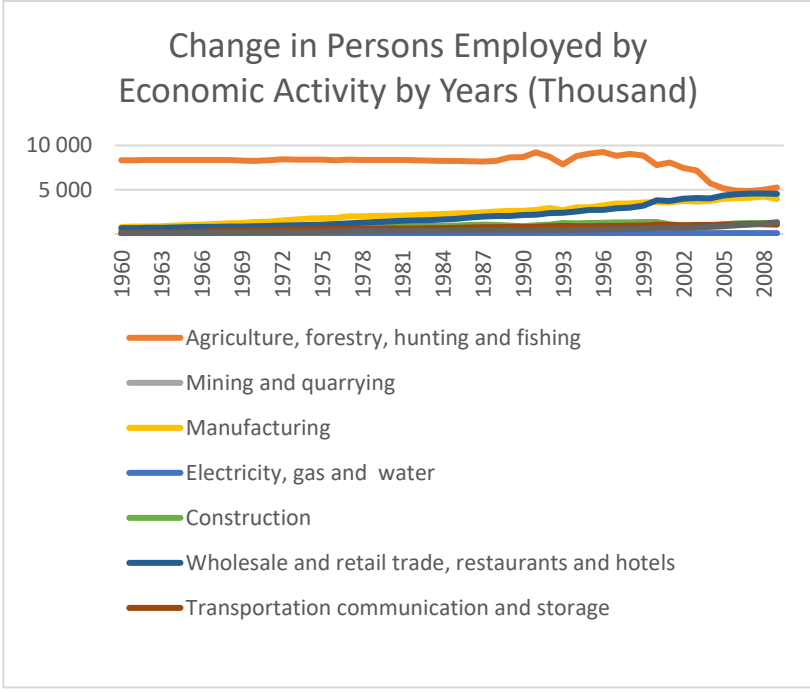

Fig. 1. Numbers of Employment by Branch of Activity Between 1960-2009

Fig. 1. shows year-based changes in the number of employed people over the age of 15 according to economic activity areas in Türkiye between 1960 and 2009. The data graphed was made by dividing the year-based values of all variables by 1000 for the sake of display and convenience in some calculations. In other words, the values seen on the screen should be deducted as the actual situation x 1000. When the figure 2. is examined in detail, it is seen that there is a general increase in the number of people employed between 1960 and 1991, except in the fields of "Agriculture, Forestry, Hunting and Fishing". It is clearly visible that the fastest increase among these years was in the manufacturing industry. While it was observed that the increases were not as rapid in other areas, it was found to remain almost constant in the fields of Agriculture, Forestry, Hunting and Fishing. In fact, in some years (1970,

1976) there was a slight decrease. Although there appear to have been some decreases and increases in this area after 1991, the remaining decreases between 1998 and 2007 are noteworthy. Although there have been small declines in other areas of activity in some years, it can be said that there is a general increase.

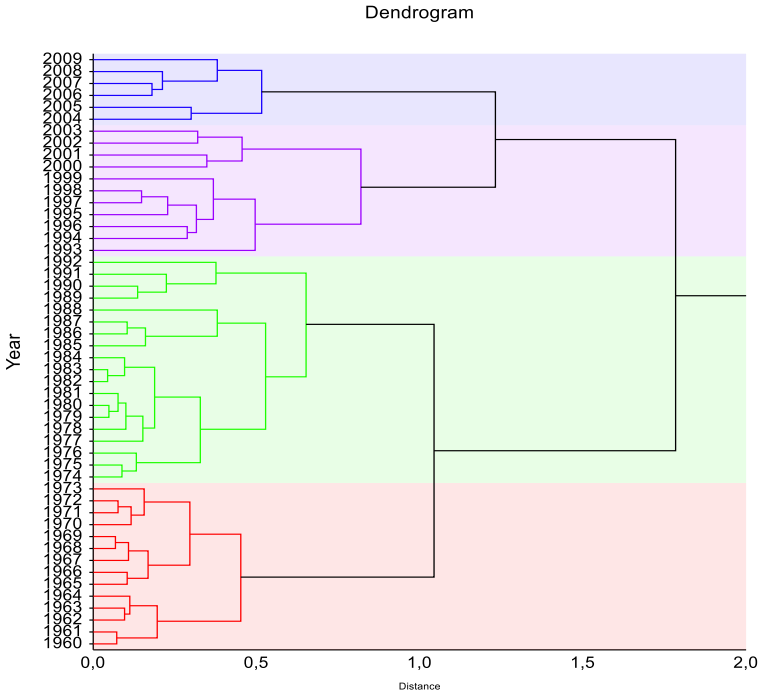

Fig. 2. Cluster Analysis Results of Employed Persons

In Figure 2 Agriculture, forestry, hunting and fishing, Mining and quarrying, Manufacturing industry, Electricity, gas and water, Construction and public works, Wholesale and retail trade, restaurants and hotels, Transportation, in Türkiye between 1960-2009. The hierarchical clustering analysis of those employed in areas of economic activity such as communication and storage, financial institutions, insurance, real estate affairs and auxiliary business services to institutions, community services, social and personal services, and clustering results by year are included. According to the results of the analysis, it was concluded that similar years showed 4 different clusters. While the 1st Cluster covers the years 2004-2009, the 2nd Cluster covers the years 1993-2003, the 3rd Cluster covers the years 1974-1992 and finally the remaining years 1960-1973. It has been determined that they are similar in terms of the number of people employed in these years.

DISCUSSION AND CONCLUSION

In this study, employment dynamics in economic activity branches of Türkiye were examined between 1960-2009 and significant structural changes in these periods were evaluated by hierarchical cluster analysis. The analysis results obtained showed that economic activities experienced significant changes in different periods and these changes were affected by economic policies, global conditions and technological advances.

Between 1960 and 1970, Türkiye had an economic structure dominated by agricultural production, and during this period, industrialization efforts began under the influence of policies such as import substitution. However, the technological deprivation in the agricultural sector limited its contribution to the country's economy. In the 1980s, the industrial and service sectors came to the fore with neoliberal reforms, and integration into international markets accelerated, especially with the adoption of flexible policies in foreign trade. This situation increased the share of the industrial and service sectors in the economy, but it also brought with it some social problems such as income inequality and unemployment.

The 2000s represent a critical period in terms of both global economic conditions and Türkiye's adaptation process with structural reforms. During this period, the service sector grew rapidly, while the share of the agricultural sector in the economy decreased. Technological advances and global integration were the main factors that accelerated the expansion of the service sector.

According to the cluster analysis results, the period 1960-2009 is divided into four different clusters in terms of employment dynamics:

• Cluster 1 (1960-1973): Years when the agricultural sector was dominant and industrialization efforts were in their early stages.

• Cluster 2 (1974-1992): Years when the pace of industrialization increased, but the service sector still had a limited role.

• Cluster 3 (1993-2003): The period when the effects of neoliberal policies were felt and the service sector came to the fore.

• Cluster 4 (2004-2009): Years when the service sector increased its dominance in the economy and the agricultural sector significantly declined in employment.

These results are an important guide to understand the structural transformations that the Turkish economy has undergone and the changing roles of different sectors in this process. In future studies, it is recommended to examine the regional effects of these changes, to evaluate the effects of the decline in the agricultural sector on rural development, and to analyze the social and economic consequences of the growth in the service sector in more detail.

ACKNOWLEDGMENT

In this study, 'chatGPT-4o' programs were used in the literature review section, and 'Google Translate' and 'DeepL Translate' programs were used for translation and grammar editing.

REFERENCES

[1] World Economic Forum, *Global Competitiveness Report 2007–2008.* Geneva, Switzerland: World Economic Forum, 2007.
[2] W. A. Lewis, "Economic development with unlimited supplies of labour," *The Manchester School*, vol. 22, no. 2, pp. 139–191, 1954.
[3] S. Kuznets, "Modern economic growth: Findings and reflections," *The American Economic Review*, vol. 63, no. 3, pp. 247–258, 1973.
[4] A. O. Krueger, "The political economy of the rent-seeking society," *The American Economic Review*, vol. 64, no. 3, pp. 291–303, 1974.
[5] B. Balassa, The Newly Industrializing Countries in the World Economy. Oxford, U.K.: Pergamon Press, 1981.
[6] H. P. Binswanger and J. McIntire, "Behavioral and material determinants of production relations in land-abundant tropical agriculture," *Economic Development and Cultural Change*, vol. 36, no. 1, pp. 73–99, 1987.
[7] D. Rodrik, "Premature liberalization and Turkish economic performance in the 1980s," *World Development*, vol. 18, no. 5, pp. 757–770, 1990.
[8] World Bank, *Turkey: Economic Reforms and the Role of the World Bank.* Washington, D.C.: World Bank Publications, 2001.
[9] OECD, *OECD Economic Surveys: Turkey 2009.* Paris, France: OECD Publishing, 2009.
[10] S. Yavan and C. Gazeloğlu, "Yerel yönetimlerde cinsiyete duyarlı bütçelemenin hiyerarşik kümeleme analizi ile incelenmesi: Aydın ilçe belediyeleri örneği," *Çağdaş Yerel Yönetimler Dergisi,* vol. 31, no. 1, pp. 165–200, 2022.
[11] M. R. Anderberg, *Cluster Analysis for Applications.* New York, NY: Academic Press, 1973.
[12] H. Tatlıdil, *Uygulamalı Çok Değişkenli İstatistiksel Analiz.* Ankara, Turkey: Akademi Matbaası, 2002.
[13] Türkiye İstatistik Kurumu (TÜİK), *Data Set.* [Online]. Available: https://data.tuik.gov.tr/

A Comprehensive Review of Fuzzy Numbers and Linear Operators

Sevilay KIRCI SERENBAY

Mathematics, Harran University, Türkiye
*(sevilaykirci@gmail.com)

ABSTRACT

Traditional mathematical models often fall short in effectively representing uncertainty, while classical logic lacks the necessary flexibility to address this challenge. As a solution, fuzzy logic, introduced by Lotfi Zadeh in 1965, has emerged as a pivotal approach for modeling uncertain and nonlinear systems. Within this framework, uncertain or ambiguously defined data are represented using fuzzy numbers, which are manipulated according to established rules and various operators applied to fuzzy sets. In particular, linear operators facilitate the integration of fuzzy logic into linear systems by allowing for the establishment of linear relationships among variables.

Keywords – Fuzzy Logic, Linear Operators, Sample, Approximation, Fuzzy Numbers.

INTRODUCTION

In many real-world scenarios, traditional mathematical models often struggle to effectively represent uncertainty, especially when dealing with ambiguous or imprecise information. Classical logic, which relies on rigid true/false propositions, lacks the flexibility needed to model such uncertainty. To address this limitation, fuzzy logic, introduced by Lotfi Zadeh in 1965, has become a fundamental tool for handling uncertain and nonlinear systems. Fuzzy logic allows for the representation of uncertain data through fuzzy numbers, which capture the inherent imprecision in real-world phenomena.

Within this framework, fuzzy numbers are manipulated according to a set of rules, applying various operators to fuzzy sets. Among these operators, linear operators play a crucial role by enabling the integration of fuzzy logic into linear systems. They facilitate the establishment of linear relationships among variables, even when the data are uncertain or imprecise. This paper explores the relationship between fuzzy numbers and linear operators, offering a comprehensive overview of the theoretical underpinnings of this approach and demonstrating its practical application through a case study. The aim is to show how fuzzy logic and linear operators can be utilized together to enhance decision-making processes in uncertain environments.

FUZZY NUMBERS

Unlike classical numbers, fuzzy numbers do not have a fixed value but include an interval or uncertainty. They are commonly represented by triangular, trapezoidal, or Gaussian membership functions. Each fuzzy

number is defined by a membership function, determining membership degrees at various values.

For instance, a triangular fuzzy number $A = (a, b, c)$ is represented by the following membership function:

Function description here:

$$\mu_A(x) = \begin{cases} 0 & , \quad x \leq a \\ \dfrac{x-a}{b-a} & , \quad a < x \leq b \\ \dfrac{c-x}{c-b} & , \quad b < x \leq c \\ 0 & , \quad c \leq x \end{cases}$$

This function determines the membership degree for values between a and c, with b as the peak point [3].

Operations with Fuzzy Numbers

Operations with fuzzy numbers differ from classical arithmetic:

- **Addition and Subtraction:** Summing two fuzzy numbers A and B yields a new fuzzy number C

$$C = A + B = (a1 + b1, a2 + b2, a3 + b3)$$

- **Multiplication and Division:** Multiplying or dividing two fuzzy numbers is calculated based on membership functions, resulting in a fuzzy number.

Through these operations, mathematical relationships between fuzzy numbers can be modeled.

LINEAR OPERATORS

Linear operators establish a linear relationship between two vectors or functions, making them useful in fuzzy logic systems for modeling linear relationships between fuzzy numbers. The main properties of linear operators include:

1. **Additivity (Linearity):** For a linear operator L and functions f and g,

$$L(f + g) = L(f) + L(g)$$

2. **Scalar Multiplication:** For a scalar c and operator L,

$$L(cf) = cL(f)$$

These properties allow linear operators to be used in modeling linear systems, enabling predictions based on linear relationships in fuzzy systems.

Fuzzy Numbers and Linear Operators

In operations with fuzzy numbers, linear operators play a significant role, especially in prediction and optimization, by providing linear relationships in calculations. For instance, when building a prediction model with fuzzy input variables, linear operators allow us to estimate outputs**.**

APPLICATION: A FUZZY DECISION MODEL

This section presents an application example using fuzzy numbers and linear operators to determine the risk level in an investment project. In investment projects, decisions often need to be made based on uncertain factors like cost, return, and risk. These uncertain values can be represented by fuzzy numbers and analyzed with linear operators.

1. Problem Definition

An investor is evaluating three potential projects, each characterized by fuzzy values:

- Project A: Cost (80,120,160), Expected Return (200,240,380)
- Project B: Cost (90,110,130], Expected Return (180,220,260)
- Project C: Cost (120,180,240), Expected Return (210,280,290)

Given the uncertain nature of costs and returns, they are represented by triangular fuzzy numbers. The investor seeks to select the project with the highest return-to-cost ratio.

2. Fuzzy Return-Cost Ratio

The expected return-cost ratio for each project can be calculated using fuzzy numbers. This ratio is obtained by dividing the project's return by its cost. For returns and costs expressed as triangular fuzzy numbers, the ratio is calculated as follows:

$$\text{Ratio} = \left(\frac{\text{Cost1}}{\text{Return1}}, \frac{\text{Cost2}}{\text{Retur2}}, \frac{\text{Cost3}}{\text{Return3}}\right)$$

For example, the return-cost ratio for Project A is calculated as follows:

- Return: (200, 240, 380)
- Cost: (80, 120, 160)
-

RatioA=(2.5,2.0,1.875)

Similarly, calculations can be made for Projects B and C.

3. Comparison Using Linear Operators

Projects are compared based on these ratios, and the project with the highest return-cost ratio is selected. By ranking these ratios using linear operators, the most profitable project for the investor can be identified.

We can proceed with the following steps:

3.1. Ratio Calculations: Calculate the return/cost ratios for each project.
3.2. Ranking: Sort the ratios for each project from highest to lowest and compare based on the average or the highest ratio.
3.3. Decision Making: Identify the most profitable project as the one with the highest average or maximum ratio.

If you provide the data for Projects B and C, we can complete the calculations and determine the most profitable project together.

It is possible to estimate profitability ratios and identify the most profitable project using Bernstein operators. Bernstein operators are a method used to approximate the average of a continuous function over a specific interval. Here, we can apply Bernstein polynomials to the return/cost ratios of each project.

Calculation Steps with Bernstein Operator

Bernstein operators $B_n(f;x)$ are generally used to approximately evaluate a function (here, the ratios for each project) and are defined as follows [1]:

$$B_n(f;x)k = \sum_{k=0}^{n} f\left(\frac{k}{n}\right)\binom{n}{k}x^k(1-x)^{n-k}$$

Using this method, we can approximately calculate the average return/cost ratios for the projects.

1. **Data Preparation**: Determine the return/cost ratios for each project (either the average or a specific value for each set of ratios). In this case, we will find the average ratio for each project.
2. **Approximation with Bernstein Polynomials**: By applying the Bernstein polynomial to the calculated average ratios for each project, we can obtain a more general estimate. This will allow us to rank the projects based on profitability according to their average ratios.

Example Application: Bernstein Operator for Project A

Ratios for Project A:

$$\text{RatioA} = (2.5, 2.0, 1.875)$$

Let's proceed with calculating the approximate profitability using Bernstein operators for each project's return-cost ratios.

Given:

- **Ratio A** = (2.5, 2.0, 2.375)
- **Ratio B** = (2.0, 2.0, 2.0)
- **Ratio C** ≈ (1.75, 1.56, 1.21)

Step 1: Average Ratios Using Bernstein Operator (with n=2)

For a simple Bernstein polynomial approximation with $n = 2$, the formula is:

$$B_2(f; x) = f(0) \cdot (1 - x)^2 + 2 \cdot f(0.5) \cdot x \cdot (1 - x) + f(1) \cdot x$$

Here, we can treat the points $f(0), f(0.5)$, and $f(1)$ as the three ratios for each project, and we'll calculate for $x = 0.5$ to obtain an approximation of each project's average profitability.

Let's perform these calculations for each project to determine which has the highest profitability.

The Bernstein polynomial approximations for the average return-cost ratios of each project are as follows:

Calculation Steps with the Favard-Szász-Mirakyan Operator

Favard-Szász-Mirakyan operators fall under the class of positive linear operators and are specifically used to approximate monotonic functions. Using this method, we can calculate the profitability ratios of the projects.

The Favard-Szász operator $S_n(f, x)$ estimates the average of a function over a specific interval and is generally defined as follows [2]:

$$S_n(f, x) = e^{-(nx)} \sum \frac{(nx)^k}{k!} f\left(\frac{k}{n}\right).$$

However, since we only have three ratios for our projects, we will perform a calculation limited to a finite number of terms. Let's calculate this for Projects A, B, and C.

First, I will calculate the values obtained from the Favard-Szász operator using the return/cost ratios for each project.

To calculate the average ratios using the **Favard-Szász operator** with n=2, we can apply the following formula for approximating a function f(x) based on the given points. For n=2, the operator is generally defined as:

$$S_2(f,x) = \frac{1}{2}(f(0) + 2f(\frac{1}{2}) + f(1))$$

Where: $f(0), f(0.5)$, and $f(1)$ represent the three ratios for each project.

Let's now calculate the Favard-Szász operator for each project (A, B, and C) using this formula with the given ratios:

- **Project A**: (2.5, 2.0, 2.375)
- **Project B**: (2.0, 2.0, 2.0)
- **Project C** ≈ (1.75, 1.56, 1.21)

I'll now perform the calculations for the average ratios using the Favard-Szász operator.

The average return/cost ratios calculated using the **Favard-Szász operator** for each project are as follows:

- **Project A**: 4.4375
- **Project B**: 4.0
- **Project C**: 3.04

Based on these values, **Project A** has the highest average profitability, followed by **Project B** and **Project C**

CONCLUSION

In this paper, fuzzy numbers and linear operators were discussed, explaining how linear relationships can be modeled on uncertain data. Fuzzy numbers are an effective tool in data analysis and decision-making processes, especially when uncertainty is high. The use of linear operators allows for establishing linear relationships and making inferences on these uncertain systems. Particularly in decision-making processes for uncertain and nonlinear systems, the combination of fuzzy numbers and linear operators makes the decision process more flexible and reliable.

The example provided in this study demonstrated the effect of linear operators on uncertain data, and it is anticipated that in future research, they can be applied to more complex and nonlinear systems.

REFERENCES

[1] Bernstein, S. N., 1912-1913. Demonstration du theoreme de weierstrass fondee surle calcul des probabilites. Commun. Soc. Math. Kharkow, 13(2): 1-2.

[2] Favard, J., 1944. Sur les multiplicateurs d'interpolation. J. Math. Pures Appl.23(9), 219--247.

[3] Majeed, S.Y., Serenbay Kırcı, S. 2023. "Analyzing Convergence of Fuzzy Numbers Using Generalized Max-Product Bernstein-Chlodowsky Operators on Compact Intervals". *Rare Metal Materials and Engineering*, *52*(9), 38-52.

In silico Study on Zn(II) Complex as α-Glucosidase Inhibitor

Merve ŞİMŞEK[1]
Davut AVCI[1]
Fatih SONMEZ[2]

1- Graduate student; Sakarya University Faculty of Science Department of Physics. merve.simsek9@ogr.sakarya.edu.tr ORCID No: 0009-0008-6276-0976; Prof. Dr.; Sakarya University Faculty of Science Department of Physics. davci@sakarya.edu.tr ORCID No: 0000-0002-9011-6191
2- Prof. Dr.; Sakarya University of Applied Sciences Pamukova Vocational High School. fsonmez@subu.edu.tr ORCID No: 0000-0001-7486-6374

ABSTRACT

One of the illnesses with the fastest global growth rates of the 21st century is type 2 diabetes. Effective new inhibitors of its treatment, including inhibition of carbohydrate hydrolysing enzymes such as α-glucosidase, are needed. In this regard, *in silico* study of the synthesized Zn(II) complex [Zn(6-MePyAld)$_2$(Cl)] was carried out. According to the molecular docking results, the K_i value for the Zn(II) complex was calculated as 22.06 μM and the binding energy was -6.29 kcal/mol. The docking study was performed to illustrate the target protein interactions with the Zn(II) complex. In addition, a docking study was fulfilled to investigate the structure-activity relationships in order to reveal its potential as a new α-glucosidase inhibitor.

Keywords – Glucosidase; Inhibition Constant; Molecular Docking; Type-2 Diabetes; Zinc Complex.

INTRODUCTION

6-Methylpyridine-2-carboxaldehyde, also known as 6-methylpicolinaldehyde, is a remarkable organic compound characterized by its unique molecular structure. The coordination versatility of aldehyde complexes of zinc halides appears to enable complex formation with a variety of transition metal ions, leading to a wide variety of structural motifs and coordination geometries. In general, metal complexes derived from such ligands possess an abundance of interesting physicochemical properties that make them subjects of research in many disciplines, and these are not limited to diametrical properties such as electronic structure, optical behaviour, and enzyme activity. One of the top five causes of mortality worldwide is diabetes, a chronic metabolic, non-communicable illness (Wild et al., 2004; Balan et al., 2017). Hyperglycemia brought on by an absolute or relative insulin shortage is the hallmark of this condition, a clinical ailment of socioeconomic significance (Aguwa, 2004; Alam, 2012). Type 2 diabetes, which is usually seen in people aged 40 and above, is a complex type of diabetes due to impaired insulin secretion, although insulin resistance, genetic and environmental factors are stated to be linked to this type of diabetes (Iwahashi et al., 1998; Kumari and Jain, 2012; Tripath et al., 2014). Inhibiting the gastrointestinal tract's carbohydrate-digesting enzymes, such as α-amylase and α-glucosidase, is one method used to treat diabetes. This slows down the intestine's breakdown of carbohydrates and delays the absorption of glucose (Rhabasa-Lhoret and Chiasson, 2004). Research has demonstrated that α-glucosidase activity modulation or control can avert metabolic illness (e.g., diabetes, tumor metastasis) (Bertozzi and Kiessling, 2001; Horii et al., 1986; Floris et al., 2005; Fernandes et al., 1991; Ogawa et

al., 2001). The Zn(II) complexes of some heterocyclic compounds, which have the potential to be a new α-glucosidase inhibitor that forms the basis of type 2 diabetes treatment, is a remarkable organic compound characterized by its unique molecular structure (Müller et al., 1994, 1999a, 1999b, 1999c).

The synthesis and detailed electronic structure calculations of the Zn(II) complex of 6-methylpyridine-2-carboxaldehyde, which has the potential to be a new α-glucosidase inhibitor that forms the basis of type 2 diabetes treatment, were reported (Şimşek et al., 2024). In this chapter, the investigation of structure-activity relationships was carried out by molecular docking study to reveal its potential as a new α-glucosidase inhibitor.

RESULTS AND DISCUSSION

The synthesis of Zn(II) complex was carried out according to previous study (Şimşek et al., 2024) (Figure 1).

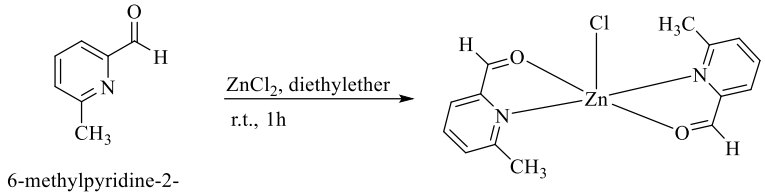

6-methylpyridine-2-carboxaldehyde (6-MePyAld)

$Zn(6\text{-}MePyAld)_2(Cl)$

Figure 1: Synthesis of Zn(II) complex

To investigate the protein-ligand interactions of the Zn(II) complex, the target protein (*Saccharomyces cerevisiae* isomaltase (PDB ID: 3A4A)) provided from the Protein Data Bank was selected as the solid and the molecular docking study was performed with the AutoDock4 (Morris et al., 2009) program implemented through the graphical user interface AutoDockTools (ADT1.5.7). PDB files were generated for the Zn(II) complex and genistein optimized by the DFT/CAM-B3LYP level. The program ADT1.5.7 (Sanner, 1999) was used to select Kollman charges, spend rotatable bonds, and combine nonpolar hydrogen atoms to carbon atoms. The Lamarckian genetic algorithm (LGA) was used for all complex-target flexible docking computations (Morris et al., 1998). Molecular docking parameter files in PDBQT format were prepared for target and ligand using AutoDock4.2. AutoGrid4 enabled the determination of the molecular docking area. Different points were determined to cover the target binding site and allow the Zn(II) complex to move freely with genistein. Other fitting parameters used are as follows: population size: 150, mutation rate: 0.02, exclusivity: 1, crossover rate: 0.8, local search rate: 0.06, and energy considerations: 2,500,000. The final docked conformations were

obtained within a root mean square deviation (RMSD) tolerance of 2 Å. The points on xyz: 126, 126, 126 and center on xyz: 21.276, -0.752, 18.634. The molecular docking results obtained here were used to clarify the relative effectiveness of the complexes' binding energy and stability. 2-D and 3-D structures showing the interactions between amino acid residues and ligands of the Zn(II) complex were visualized with the Discovery Studio 4.0 program (Systèmes, 2016).

Ligand-protein interactions of the complexes were determined using the AutoDock (Morris et al., 1998, Morris et al., 2009) software and the AutoDockTools (ADT1.5.7) graphical user interface, and *S. cerevisiae* isomaltase (PDB ID: 3A4A) was accepted as the target protein. The binding energy and estimated inhibition constant (Ki) were determined from the molecular docking results. The Discovery Studio 4.0 program (Systèmes, 2016) was used to display the 2D and 3D structures of the interactions between ligands and amino acid residues (Table 1). Considering to the molecular docking results, the Ki value for the Zn(II) complex was calculated as 22.06 μM and the binding energy was -6.29 kcal/mol. Direct/indirect interactions with the enzyme active site vary depending on the coordination environment of the complex. The interactions of some parts of the complex with amino acid residues are given in Table 1 and Figures 2-4. These interactions can be listed as pi-cation, pi-sigma, pi-alkyl and charge-charge, conventional hydrogen bonding, pi-donor H-bonding, pi-pi T-shape, amide-pi stacking, pi-alkyl. In this study, the calculated charge-charge interaction distances between ring(C)/ring(N)/aldehyde(C)/carbonyl(C=O)/methyl(C)/Zn and GLU-271(OE2)/GLU-11(OE2) amino acid residues in the Zn(II) complex vary in the range of 3.13-5.59 Å. The distances of conventional hydrogen bond and amide-pi stacking interactions between the carbonyl (C=O)/ring and LEU-297 (C, O)/LEU-297(O) amino acid residues are on the order of 3.25 Å and 4.19 Å. The pi-alkyl interaction distance between the ring and the LYS-13 (pi orbitals) amino acid residue was found to be 5.30 Å. From the genistein data, the conventional hydrogen bond interaction distance between the carbonyl (C=O) and the LEU-297 (O) amino acid residue was found to be 3.29 Å, while the same interaction distance in the Zn(II) complex was found to be 3.25 Å.

Table 1: Docking results for Zn(II) complex

Substrate	Receptor	Interaction	Distance (Å)	K_i (μM)	Binding energy (kcal/mol)
Zn(II) complex				24.42	−6.29
Ring (C)	GLU-271 (OE2)	Charge-Charge	5.03		
Ring (N)	GLU-271 (OE2)	Charge-Charge	5.37		
Ring (N)	GLU-271 (OE2)	Charge-Charge	5.48		
Ring (C)	GLU-271 (OE2)	Charge-Charge	4.64		
Ring (C)	GLU-271 (OE2)	Charge-Charge	5.36		
Aldehyde (C)	GLU-271 (OE2)	Charge-Charge	3.29		
Oxygen (C=O)	GLU-271 (OE2)	Charge-Charge	3.13		
Methyl (C)	GLU-271 (OE2)	Charge-Charge	4.25		
Zn	GLU-271 (OE2)	Charge-Charge	5.17		
Ring (C)	GLU-11 (OE2)	Charge-Charge	5.59		
Ring (C)	GLU-11 (OE2)	Charge-Charge	4.84		
Ring (C)	GLU-11 (OE2)	Charge-Charge	5.58		
Methyl (C)	GLU-11 (OE2)	Charge-Charge	5.41		
Oxygen (C=O)	LEU-297 (O)	Conventional H-Bond	3.25		
Ring	SER-298 (OG)	Pi-Donor H-Bond	3.51		
Ring	ALA-292 (CB)	Pi-Sigma	3.43		
Ring	TRP-15 (pi orbitals)	Pi-Pi T-shaped	4.68		
Ring	LEU-297 (C, O)	Amide-Pi Stacked	4.19		
Ring	LYS-13 (pi orbitals)	Pi-Alkyl	5.30		
Genistein (Özge et al., 2023)				22.06	-6.35
C=O (benzopyran-4-one)	ILE-272	Conventional H-Bond	2.73		
CO (5-hydroxy-benzopyran-4-one)	SER-298	Conventional H-Bond	2.45		
CO (7-hydroxy-benzopyran-4-one)	LEU-297	Conventional H-Bond	3.29		
CO (7-hydroxy-benzopyran-4-one)	SER-291	Conventional H-Bond	2.88		
CO (7-hydroxy-benzopyran-4-one)	ALA-292	Conventional H-Bond	3.14		
Phenyl	ARG-263	Pi-Alkyl	4.19		
Phenyl	ILE-272	Pi-Alkyl	5.25		

In another study, for example, the calculated conventional hydrogen bond interaction distances between azide-containing Schiff base Zn complex [$Zn_2(L_1)(N_3)2Cl_2 \cdot 4H_2O$; L_1: N-(pyridine-2-ylmethylene)methanamine]

Nitrogen (N) and VAL404 (O)/TYR407 (O) amino acid residues are between 3.03 Å and 3.13 Å. The amide-pi stacking interaction distance is 5.57 Å. The pi-alkyl interaction distance between L_1 and VAL404 amino acid residue was calculated as 5.50 Å. The K_i value was found to be 358.10 (Avcı et al., 2024).

In a previously reported study, the convective hydrogen bond interaction distance between the synthesized isothiocyanate-containing Schiff base Zn complex [$Zn(L_1)(NCS)_2$; L_1: N-(pyridine-2-ylmethylene)methanamine] NCS and the amino acid residue SER-490 was found to be in the order of 3.13 Å. The distance of the pi-alkyl interaction between L_1 and PRO-488 amino acid residue was determined as 5.39 Å. The Ki value was found to be 531.4 µM (Özge et al., 2023).

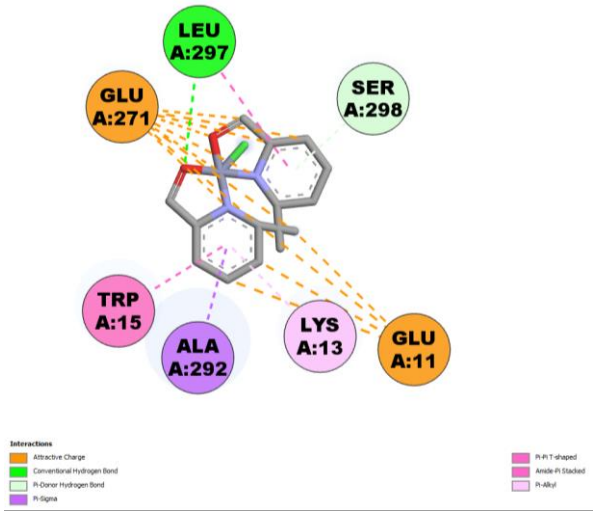

Figure 2: 2D view of the most active interactions for Zn(II) complex

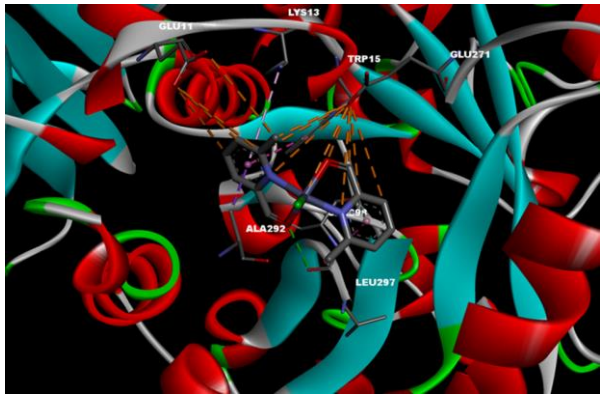

Figure 3: 3D view of the most active interactions between ligands and amino acid residues of the Zn(II) complex located in the active site of α-glucosidase

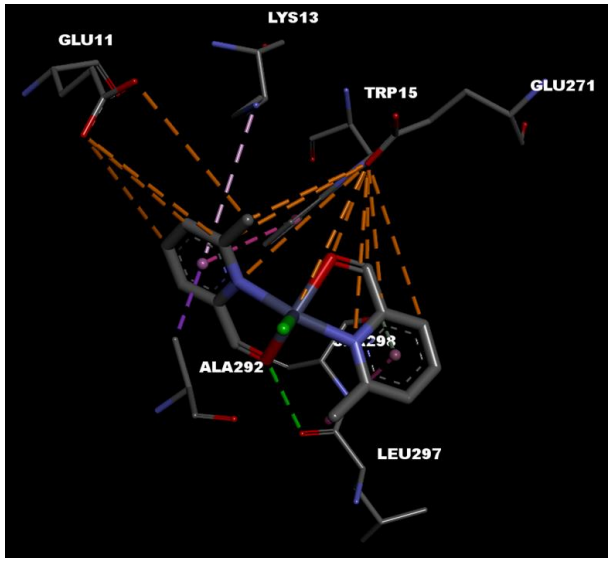

Figure 4: 3D view of the most active interactions between the amino acid residues of the Zn(II) complex and the ligands

In summary, molecular docking data indicate that, depending on the coordination environment, the contact with the enzyme active site influences the α-glucosidase inhibitory activity either directly or indirectly. The abundance of molecular interactions, especially conventional hydrogen bonding interactions, for the Zn(II) complex contributes to its ability to be a good inhibitor. It has been predicted that the hydrogen bond is a strong bond and that it interacts with genistein on the same protein residue may support its good inhibitory properties.

ACKNOWLEDGMENTS

This work was supported by the Scientific and Technological Research Council of Turkey (TÜBİTAK), Grant/Award Number: 1919B012305969 (2209-A 2023/1).

REFERENCE

Aguwa, C.N. (2004). *Therapeutic Basis for Clinical Pharmacy in the Tropics*. (pp. 125–230). 3rd ed. SNAAP Press Ltd:Enugu.

Alam, E. A. (2012). Initiation of Pharmaceutical Factories depending on more Application of Biotechnology on some Medicinal Plants Review Article (In Vitro Production of some Antioxidant, Analgesic, Antibacterial, Antidiabetic agents). *Research Journal of Recent Sciences*, 1(ISC-2011), 398-404.

Avcı, D., Özge, Ö., Sönmez, F., Tamer, Ö., Başoğlu, A., Atalay, Y., Zengin Kurt, B. (2024). In vitro α-glucosidase, docking and density functional theory studies on novel azide metal complexes. *Future Medicinal Chemistry*, 16, 1109–1125.

Balan, K. Ratha, P., Prakash, G., Viswanathamurthi, P., Adisakwattana, S., Palvannan, T. (2017). Evaluation of invitro a-amylase and a-glucosidase inhibitory potential of N_2O_2 schiff base Zn complex. *Arabian Journal of Chemistry*, 10, 732–738.

Bertozzi, C.R., Kiessling, L.L. (2001). Chemical glycobiology. *Science*, 291, 2357-2364.

Fernandes, B., Sagman, U., Auger, N., Demetrio, M., Dennis, J.W. (1991). β1–6 branched oligosaccharides as a marker of tumor progression in human breast and colon neoplasia. *Cancer Research*, 51(2), 718–723.

Floris, A.L., Peter, L.L., Reinier, P., Eloy, H.L., Guy, E.R., Chris, W. (2005). α-Glucosidase inhibitors for patients with type 2 diabetes: results from a Cochrane systematic review and meta-analysis. *Diabetes Care*, 28, 154–163.

Horii, S., Fukase, H., Matsuo, T., Kameda, Y., Asano, N., Matsui, K. (1986). Synthesis and. alpha-D-glucosidase inhibitory activity of N-substituted valiolamine derivatives as potential oral antidiabetic agents. *Journal of Medicinal Chemistry*, 29(6), 1038–1046.

Iwahashi, H., Itoh, N., Yamagata, K., Imagawa, A., Nakajima, H., Tomita, K., Moriwaki, M., Waguri, M., Yamamoto, K., Miyagawa, J., Namba, M., Hanafusa, T., Matsuzawa, Y. (1998). Molecular mechanisms of pancreatic

beta-cell destruction in autoimmune diabetes: potential targets for preventive therapy. *Cytokines, Cellular & Molecular Therapy*, 4(1), 45–51.

Kumari, M., Jain, S. (2012). Tannins: An Antinutrient with Positive Effect to Manage Diabetes. *Research Journal of Recent Sciences*, 1(12), 70–73.

Morris, G.M., Goodsell, D. S., Halliday, R. S., Huey, R., Hart, W. E., Belew, R.K., Olson, A.J. (1998). Automated Docking Using a Lamarckian Genetic Algorithm and and Empirical Binding Free Energy Function. *Journal of Computational Chemistry*, 19(14), 1639–1662.

Morris, G. M., Huey, R., Lindstrom, W., Sanner, M.F., Belew, R.K., Goodsell, D.S., Olson, A.J. (2009). AutoDock4 and AutoDockTools4: Automated docking with selective receptor flexibility. *Journal of Computational Chemistry*, 30, 2785–2791.

Müller, B., Ruf, M., Vahrenkamp, H. (1994). On the Nature of Zinc Chloride–Aldehyde Interactions. *Angewandte Chemie International Edition in English*, 33, 2089–2090.

Müller, B., Vahrenkamp, H. (1999a). Zinc-Aldehyde Complexes with Weakly Coordinating Anions. *European Journal of Inorganic Chemistry*, 117–127.

Müller, B., Vahrenkamp, H. (1999b). Aldehyde Complexes of Zinc Halides. *European Journal of Inorganic Chemistry*, 129–135.

Müller, B., Vahrenkamp, H. (1999c). Zinc Complexes of Chelating Aldehydes. *European Journal of Inorganic Chemistry*, 137–144.

Ogawa, S., Maruyama, A., Odagiri, T., Yuasa, H., Hashimoto, H. (2001). Synthesis and Biological Evaluation of α-L-Fucosidase Inhibitors: 5a-Carba-α-L-fucopyranosylamine and Related Compounds. *European Journal of Organic Chemistry*, 2001(5), 967–974.

Özge, Ö., Avcı, D., Sönmez, F., Tamer, Ö., Dege, N., Başoğlu, A., Atalay, Y., Zengin Kurt, B. (2023). Synthesis DFT calculations α-glucosidase inhibitor activity and docking studies on Schiff base metal complexes containing isothiocyanate. *Applied Organometallic Chemistry*, 37: e7084.

Sanner, M.F. (1999). Python: a programming language for software integration and development. *Journal of Molecular Graphics and Modelling*, 17, 57–61.

Systèmes D. (2016). *Biovia, discovery studio modeling environment*. Dassault Systèmes Biovia:San Diego, CA, USA.

Şimşek, M., Avcı, D., Sönmez, F., Başoğlu, A., Tamer, Ö., Atalay, Y. (2024). Unveiling the NLO potential of new Zn(II) complex of 6−methylpyridine−2−carboxaldehyde: Experimental/DFT study on spectral,

static and frequency–dependent linear/nonlinear optical parameters, *Applied Organometallic Chemistry*, e7798.

Rhabasa-Lhoret, R., Chiasson, J.L. (2004). *Alpha-glucosidase inhibitors*. In: Defronzo, R.A., Ferrannini, E., Keen, H., Zimmet, P. (Eds.), International Textbook of Diabetes Mellitus, 3rd Ed., vol. John Wiley, UK.

Tripath, I.P., Kumar, M. M., Ruchita, T., Chinmayi, M., Arti, K., Laxmikant, S., Atul, D., Kumar, S.U., Bhihari, P.K. (2014). Synthesis, Spectral, Electrochemical analysis and Screening for a-Glucosidase inhibition of some complexes of Cobalt (II) and Ethylenediamine. *Research Journal of Chemical Sciences*, 4(6), 13–17.

Wild, S., Roglic, K., Green, A., Sicree, R. and King, H. (2004). Global prevalence of diabetes, Estimation for the year 2000 and projections for 2030. *Diabetes Care*, 27, 1047–1053.

Investigation of The Molecular Properties of Acoramidis Using Quantum Chemical Calculations

Güvenç GÖRGÜLÜ[1]
Bülent DEDE[2]

1- Assoc. Prof. Dr.; Burdur Mehmet Akif Ersoy University, Faculty of Education, Department of Science Education, 15030, Burdur, Türkiye. guvencgorgulu@mehmetakif.edu.tr ORCID No: 0000-0003-4740-7265
2- Prof. Dr.; Süleyman Demirel University, Faculty of Engineering & Natural Sciences, Department of Chemistry, 32260, Isparta, Türkiye. bulentdede@sdu.edu.tr ORCID No: 0000-0003-1416-7373

ABSTRACT

Acoramidis is an important drug used in the treatment of heart muscle diseases known as cardiomyopathy. In this study, the molecular structure, electronic characteristics, and chemical reactivity of acoramidis were examined using quantum chemical computations. in more detail. The DFT method was used to calculate the optimized molecular geometry of acoramidis using the 6-311G(d,p) basis set and the B3LYP functional. The molecular electrostatic potential (MEP) diagram and frontier molecular orbitals (HOMO/LUMO) of the molecule were also obtained using the same method and basis set. By using the optimized geometry of acoramidis in the ground state, significant geometrical parameters such as bond length, bond angle, and dihedral angle were achieved. The molecular electrostatic potential diagram of acoramidis revealed regions of high and low electrostatic potential in its structure. Calculations revealed that the HOMO-LUMO band gap energy of the molecule was 4.727 eV. The intramolecular non-covalent interactions (NCI) of acoramidis were also calculated and the regions containing hydrogen bonds, Van der Waals interactions, and steric effects in the structure of the compound were determined.

Keywords – Cardiomyopathy, Quantum Chemical Calculation, DFT, MEP, NCI.

INTRODUCTION

Amyloid diseases are serious pathological conditions that result from disruption of the normal structure of proteins and lead to organ damage. Transthyretin amyloidosis (ATTR) is a rare but important amyloid disease caused by misfolding of the transthyretin protein. ATTR causes a variety of clinical symptoms, including cardiomyopathy and peripheral neuropathy, and effective treatment options are limited (Muchtar, et. al. 2021:268). Acoramidis is a novel pharmaceutical agent approved by the FDA for the treatment of ATTR and inhibits amyloid deposition through stabilization of the transthyretin protein (Ma, et al., 2024:17172).

Quantum chemical calculations are a powerful tool for evaluating properties of molecules such as geometric, electronic, and reactivity. The purpose of this study was to use density functional theory (DFT)-based calculations to examine the acoramidis molecule's geometry, electronic properties, and reactivity.

MATERIALS AND METHOD

The Gaussian 09 program package was used for all quantum chemical calculations of acoramidis (Frisch, et al., 2016). Molecular visualization was performed using the GaussView 5.0.9 program (Dennington, 2016). For the title molecule, the 6-311G(d,p) basis set and the DFT method with B3LYP functional were employed to determine its optimized molecular geometry. (Becke, 1988:3098; Lee, et al. 1988:785). At the previously mentioned theoretical level, the acoramidis' HOMOs-LUMOs and molecular electrostatic potential diagram were also computed. Multiwfn 3.8 software was used to examine the molecule's reduced density gradient (RDG) and intramolecular non-covalent interactions (NCI) (Lu and Chen, 2012:580). The VMD 1.9.4a53 tool was used to show the results (Humphrey et al. 1996:33).

RESULT AND DISCUSSION

Optimized Molecular Geometry

The DFT/B3LYP/6-311G(d,p) level was used to calculate the acoramidis' optimized molecular geometry (Figure 1). Some selected geometrical parameters obtained from this optimized geometry are given in Table 1.

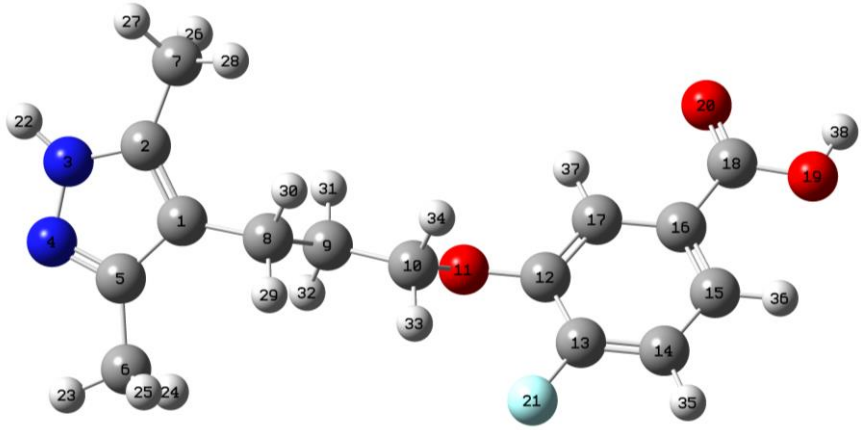

Figure 1. Calculated optimized molecular geometry of the acoramidis

Table 1. Geometric parameters of the optimized molecular geometry of the acoramidis

Bond Length (Å)	
N3-N4	1.351
N3-C2	1.361
N4-C5	1.329
C2-C7	1.495
C1-C8	1.502
C9-C10	1.519
C10-O11	1.445
O11-C12	1.363
C16-C17	1.398
C13-F21	1.351
C16-C18	1.486
C18-O20	1.208
C18-O19	1.357
O19-H38	0.968
Bond Angle (º)	
C2-N3-N4	113.5
N3-C2-C7	122.5
C5-C1-C8	127.4
C9-C10-O11	107.5
O11-C12-C17	119.2
C12-C13-F21	119.1
C16-C18-O20	
Dihedral Angle (º)	
N4-N3-C2-C7	179.4
C5-C1-C8-C9	88.6
C8-C9-C10-O11	179.3
C10-O11-C12-C13	60.1
C17-C16-C18-O19	179.9

The N3-N4, N3-C2, and N4-C5 bond lengths in the pyrazole ring of acoramidis were calculated as 1.351, 1.361, and 1.329 Å, respectively. The C9-C10 bond was among the longest bonds in the molecule, with a bond length of 1.519 Å. The C13-F21 bond in the molecule was calculated as 1.351 Å and the C18-O20 bond length in the carbonyl group was found to be 1.208 Å. The O19-H38 bond in the carboxyl group in acoramidis was one of the shortest bonds with a length of 0.968 Å. On average, the bond angles between the atoms of acoramidis were close to 120º. In general, the geometry surrounding the atoms was close to a trigonal planar, according to

the computed bond angle values. On the other hand, the dihedral angles of N4-N3-C2-C7, C8-C9-C10-O11, and C17-C16-C18-O19 were close to 180º, revealing that these atoms lie in the same plane. The calculation of the C5-C1-C8-C9 and C10-O11-C12-C13 dihedral angles of 88.6º and 60.1º, respectively, indicated that the pyrazole ring, the phenyl ring, and the aliphatic region between these two rings in the molecule do not lie in the same plane.

Molecular Electrostatic Potential Diagram

A Molecular Electrostatic Potential (MEP) diagram is a map that visualizes the electrostatic properties of a molecule and shows the electrostatic potential in different regions along the surface of the molecule in color. Green areas have a neutral electrostatic potential. At the DFT/B3LYP/6-311G(d,p) level of theory, acoramidis' MEP diagram was computed and given in Figure 2.

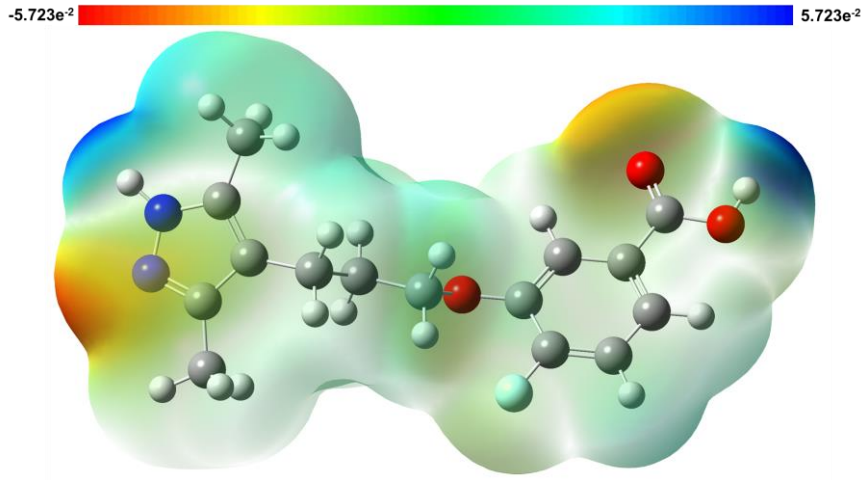

Figure 2. Calculated MEP diagram of the acoramidis

Both the double-bonded nitrogen atom in the pyrazole moiety of the acoramidis and the oxygen atom of the carbonyl group had reddish zones, indicating that the negative electrostatic potential was high in these areas. These calculated electron-dense regions were the points where the molecule could show nucleophilic effect. On the other hand, blue-colored areas were observed on the proton atoms bound to the nitrogen atom in the pyrazole ring and located in the carboxylic acid unit of the title molecule. These blue regions on acoramidis had a positive electrostatic potential and were electron-poor. Moreover, these electron-poor regions were considered to behave electrophilically in the reactions of the molecule.

Frontier Molecular Orbitals and DOS Analyses

HOMO (Highest Occupied Molecular Orbital) is the highest energy occupied orbital in a molecule that contains electrons.

The highest energy occupied orbital in a molecule where electrons can be found is called HOMO (Highest Occupied Molecular Orbital) and the lowest energy unoccupied orbital to which electrons can be transferred is called LUMO (Lowest Unoccupied Molecular Orbital). The energy gap between the HOMO and LUMO orbitals provides important information about the reactivity and electronic properties of a molecule. Figure 3 displays the HOMO and LUMO of acoramidis as calculated by the DFT method using the B3LYP functional and the 6-311G(d,p) basis set. The calculated HOMO of acoramidis was mainly located on the pyrazole ring and the methyl group bound to this ring. The LUMO of the title molecule was on the phenyl ring and the carboxyl group was attached to moiety.

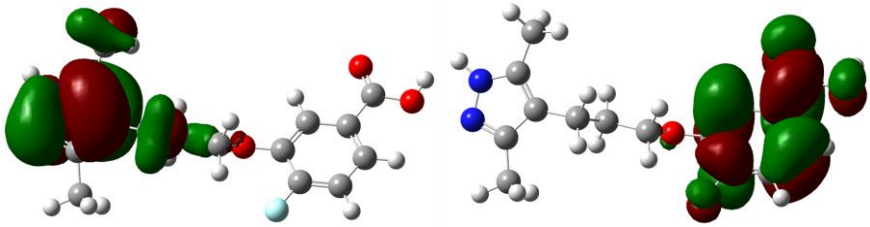

Figure 3. Calculated HOMO (left) and LUMO (right) of the acoramidis

The calculated DOS diagram of acoramidis at the mentioned level is shown in Figure 4. The energy gap between HOMO and LUMO of the title molecule was obtained as 4.727 eV. This calculated value revealed that high energy is required for the excitation of acoramidis' electrons from HOMO to LUMO, meaning that its thermal stability is high. Moreover, the electronic conductivity and chemical reactivity of acoramidis were considered to be low. On the other hand, based on the DOS diagram of the molecule, it was determined that its electrons were mostly located in orbitals with energies between -15 and -10 eV.

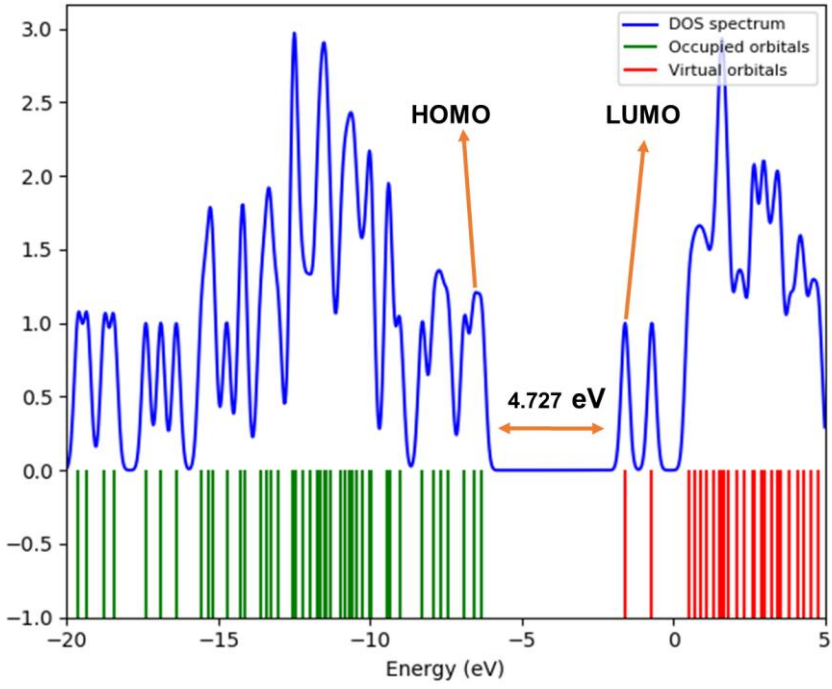

Figure 4. Calculated DOS diagram of the acoramidis

Non-covalent Interactions

Non-covalent interaction (NCI) diagrams are used to visualize the presence and placement of weak bonds (e.g. Van der Waals forces, hydrogen bonds, steric effects) in a molecule or in intermolecular interactions. In these diagrams, green regions usually represent weak Van der Waals interactions, blue regions indicate strong and stabilizing interactions such as hydrogen bonds, and red regions usually represent steric repulsion or destabilizing interactions. An image showing the intramolecular non-covalent interactions of acoramidis is given in Figure 5. In the NCI diagram of the molecule, steric repulsion was found to be effective inside the pyrazole and phenyl rings. Furthermore, it was observed that the methyl groups attached to the pyrazole ring have a sterile effect in the regions close to the main skeleton, while the Van der Waals effect is more dominant in slightly more distant regions. Similarly, the presence of steric effect in the regions close to the carbon atoms in the phenyl ring of the oxygen atom in the carboxyl group and the Van der Waals effect in the distant regions was determined.

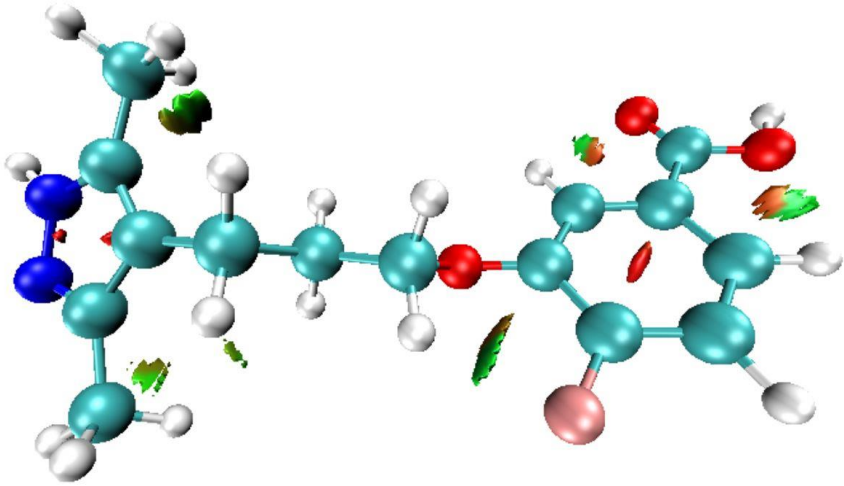

Figure 5. Calculated NCI of the acoramidis

Reduced Density Gradient (RDG) plot of the acoramidis is presented in Figure 6. The blue colored regions due to hydrogen bonds were found to have point scattering between -0.05 and -0.02 au. The green regions resulting from Van der Waals interactions in the molecule had point scattering between -0.02 and 0 au. Moreover, the point dispersions that appeared in the RDG plot of the molecule between 0 and 0.05 au were attributed to steric repulsion effects in the compound.

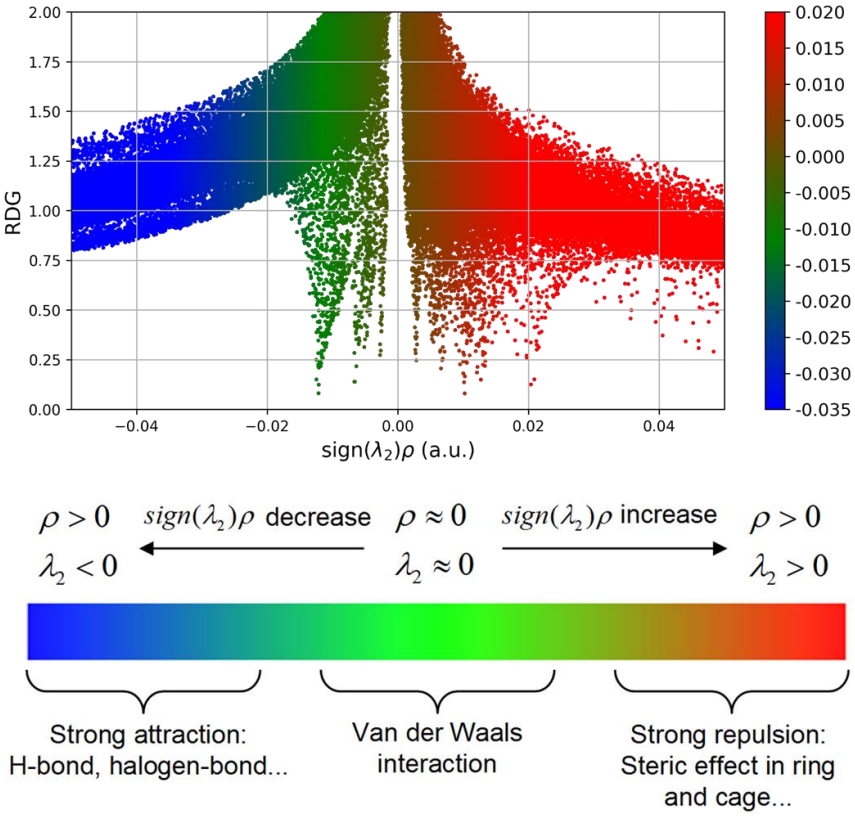

Figure 6. Calculated RDG plot of the acoramidis

CONCLUSION

The findings of this study on the quantum chemical properties of acoramidis revealed the electronic, structural, and reactivity properties of the molecule. As a result of the geometrical optimization significant geometrical parameters of the molecule were calculated and the effects of these parameters on the overall stability and planarity of the molecule were discussed. The calculation of the energy gap between the HOMO and LUMO as 4.727 eV indicated that acoramidis has low chemical reactivity and high thermal stability. The MEP diagram of the molecule clearly demonstrated the distribution of the electrostatic potential in various zones and the possible nucleophilic and electrophilic sites. Furthermore, non-covalent interaction analyses identified the locations of Van der Waals, hydrogen bonds, and steric effects within the molecule. These results provided important insights into understanding the chemical behavior of acoramidis. The results of the study will contribute to the understanding of

the role of acoramidis in the stabilization of transthyretin and the prevention of amyloid deposition at the molecular level.

REFERENCE

Becke, A. D. (1988). Density-functional exchange-energy approximation with correct asymptotic behavior. *Physical Review A*, *38*(6), 3098-3100.

Dennington, R., Todd, K., John, M. (2009). GaussView Revision 5.0.9, Semichem. Inc. Shawnee Mission, KS.

Frisch, M.J. et al. (2016). Gaussian 09, Revision E.01, Gaussian, Inc., Wallingford CT.

Humphrey, W., Dalke, A., Schulten, K. (1996). VMD: visual molecular dynamics. *Journal of Molecular Graphics*, *14*(1), 33-38.

Lee, C., Yang, W., Parr, R. G. (1988). Development of the Colle-Salvetti correlation-energy formula into a functional of the electron density. *Physical Review B*, *37*(2), 785-789.

Lu, T., Chen, F. (2012). Multiwfn: A multifunctional wavefunction analyzer. *Journal of Computational Chemistry*, 33(5), 580-592.

Ma, S., Jiang, M., Wang, X., Li, B. (2024). Clinically Approved Representative Small-Molecule Drugs for Cardiopathy Therapy. *European Journal of Medicinal Chemistry*, 117172.

Muchtar, E., et. al. (2021). Systemic amyloidosis from A (AA) to T (ATTR): a review. *Journal of Internal Medicine*, *289*(3), 268-292.

Schiff Bases and Their Metal Complexes: Use and Application

Güvenç GÖRGÜLÜ[1]
Bülent DEDE[2]

1- Assoc. Prof. Dr.; Burdur Mehmet Akif Ersoy University, Faculty of Education, Department of Science Education, 15030, Burdur, Türkiye. guvencgorgulu@mehmetakif.edu.tr ORCID No: 0000-0003-4740-7265
2- Prof. Dr.; Süleyman Demirel University, Faculty of Engineering and Natural Sciences, Department of Chemistry, 32260, Isparta, Türkiye. bulentdede@sdu.edu.tr ORCID No: 0000-0003-1416-7373

ABSTRACT

Schiff bases are organic compounds formed by the condensation of primary amines with carbonyl compounds. These compounds have a wide range of uses in fields such as chemistry, biochemistry and materials science. Metal complexes of Schiff bases attract attention, especially due to their important role in coordination chemistry. In addition to exhibiting various biological activities (antibacterial, antifungal, antioxidant and anticancer), these complexes are also widely used in catalyst, sensor and optical material applications.

In this section, the basic chemical properties, synthesis methods and structural properties of Schiff bases are explained in detail. The studied structural and electronic properties of metal complexes characterized by spectroscopic analysis techniques were described. The applications of Schiff bases and metal complexes as antimicrobial, anticancer and industrial catalysis were emphasized. This review also aims to shed light on the chemical and biological significance of Schiff bases and their metal complexes.

In this context, the current literature on the design and synthesis of Schiff bases and metal complexes was reviewed, and the obtained information was evaluated from a scientific and practical point of view. It is thought that these studies will serve as an important guide for future applications.

Keywords – Schiff Bases, Metal Complexes, Azomethine, Imine, Industrial Applications.

INTRODUCTION

Schiff bases and their metal complexes are compounds of great importance in terms of both theoretical and applied research which is located at the intersection of organic and inorganic chemistry. These compounds exhibit special reactivity and selectivity in both chemical reactions and biological processes due to the imine group containing the double bond between carbon and nitrogen. Schiff bases can easily be synthesized, their structures can be customized by adding various functional groups, and they can form strong coordination bonds with metal ions. These properties make these compounds very versatile and ideal research materials for many disciplines such as catalysis, biomedicine, materials science and environmental chemistry. Further improvement of the chemical and physical properties of Schiff bases with metal complexes enables their use possible in different industrial and technological areas. In this context, Schiff bases and metal complexes are beyond being merely an academic curiosity in modern

chemistry and are leading to innovative solutions in real-world applications (Meena, R., et al., 2023)

1. SCHIFF BASES

Compounds that occur as a result of condensation of aldehydes and ketones with primary amines under appropriate reaction conditions and have C=N in their structure are called “Schiff bases”. In general, compounds with C=N in their structure are called “azomethine or imine compounds”. Schiff bases were first synthesized in 1864 by the German chemist H. Schiff (Schiff, 1869). Later in 1933, Schiff bases were used as a ligand by Pfeiffer (Pfeiffer, 1933). Metal complexes of N-alkyl salicylaldimines (Figure 1) have been obtained by heating under a backcooler with transition metals in the presence of a small amount of sodium hydroxide or sodium acetate in an alcoholic or aqueous-alcoholic medium with any aliphatic primary amine taken slightly more than the stoichiometric ratio with salicylaldehyde (Schiff, 1869).

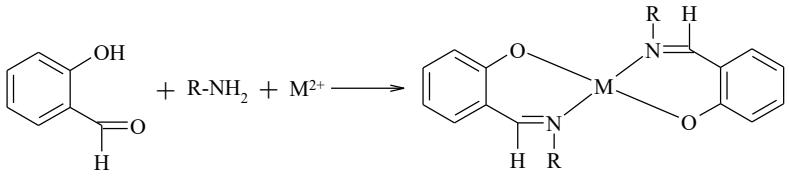

Figure 1. Metal complexes of N-alkyl salicylaldimines

1.1. The properties of Schiff bases

The stability of the azomethine compound increases by the attachment of an electron-releasing alkyl or aryl group to the nitrogen atom. In the nitrogen atom, –OH-bearing oximes, -NH-bearing phenylhydrazone and semicarbazones are much more resistant to hydrolysis than Schiff bases carrying alkyl or aryl substituent.

Schiff bases in the structure of N-alkyl or N-aryl substituted imine, consisting of condensation of primary amines with carbonyl compounds, are not very resistant to hydrolysis. Especially at low pHs, it is divided into its constituents; carbonyl and amine groups.

The reaction is twofold and the equilibrium generally takes place with a perceptible rapidity. If the reaction occur with amines containing at least one unpaired electron bearing an electronegative atom in its nitrogen (hydroxylamine, semicarbazide, hydrazine, etc.), the reaction becomes one-way. By this procedure, the reaction product can be isolated with a high efficiency, due to not going an easy hydrolysis.

Due to their predisposition to hydrolysis, Schiff bases are studied more in an anhydrous environment to obtain. The water that occurs as a

result of the reaction is removed with an azeotrope-forming solvent. If the Schiff base synthesis is from aldehyde and dialkyl ketones, water removal is not necessary. But, if the synthesis is from diaryl and alkyl-aryl ketones it is still important to remove the reaction water. Therefore, it can be concluded that diaryl and alkylaryl ketimines are less resistant to hydrolysis than aldimines and dialkyl ketimines (Pratt Pratt and Kamlet, 1961).

Aromatic aldehydes react with amines at low temperature in a suitable solvent environment. In the condensation of aromatic aldehydes with aromatic amines, the reaction rate increases if an electron-attractive substituent in the para position is present in the aldehyde, and the reaction rate decreases if it is present in the amine (Pratt and Kamlet, 1961).

Although, aldehydes can easily give Schiff base with primary amines, it is quite difficult to obtain Schiff base from ketones. There are numerous factors must be taken into account, such as the selection of an azeotropic solvent with water released during the reaction, the choice of catalyst, the appropriate pH range and the selection of the appropriate reaction temperature, in order to obtain Schiff base from ketones. Besides, to obtain Schiff bases, especially from aromatic ketones, high temperature, long reaction time and catalyst are required (Patai, 1970].

In Table 1, frequencies of C=N bonds of some Schiff bases from their IR spectra are given. Frequencies of aniline compounds were seen at range of 1631-1613 cm^{-1}. Also, there is an increasing interest to Ar-CH=N-Ar type compounds which give bands at 1627-1626 cm^{-1} (Patai, 1970).

Table 1. Frequencies of C=N bonds of some Schiff bases

Compounds	**Frequency (cm^{-1})**
N-benzyldinaniline	1631
N-(2-hydroxy)benzyldinaniline	1622
N-(4-hydroxy)benzyldinaniline	1629
N-(4-methoxy)benzyldinaniline	1630
N-(2-nitro)benzyldinaniline	1621
N-(4-acetylamino)benzyldinaniline	1629
N-(4-dimethylamino)benzyldinaniline	1626
N-benzyldinaniline-2-aminophenol	1629
N-benzyldin-N'-dimethyl-4-phenyldiamine	1627
N-(2-hydroxy)benzyldine-2-aminophenol	1624
N-(4-dimethylamino)benzyldine-2-aminophenol	1613
N-N'-dibenzyldin-4-phenyldiamine	1628

The intramolecular hydrogen bonds found in Schiff bases can be formed and broken reversibly in polar solvents (Figure 2), where naphthalene and phenanthroline derivatives are mainly exemplified for. The

NH/OH tautomeric balance of these molecules can be significantly affected by temperature and solvent changes (Patai, 1970).

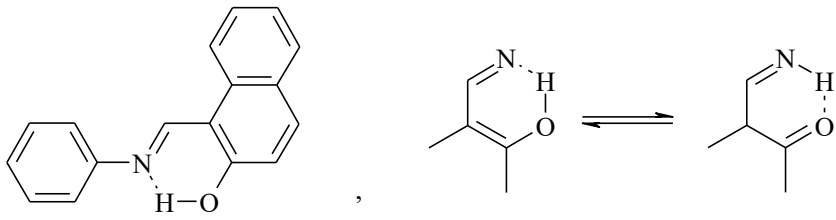

Figure 2. Intramolecular hydrogen bonding seen in some Schiff bases

1.2. The formation mechanism of Schiff bases

Imine formation is slow at very low and very high pH and optimum pH is 4.5. If the proposed mechanism for imine formation is considered, it is clear why an acid catalyst is needed. The critical step is the one in which the protonated alcohol loses a water molecule to become the iminium ion. The protonation of the alcohol group by the acid, converts a poor leaving group (-OH) into a good leaving group (H_2O). If the hydronium ion concentration is too high, the reaction proceeds more slowly because the amine itself is also significantly protonated, reducing the concentration of the nucleophile required in the first step. If the hydronium ion concentration is too low, the reaction is still slow because the concentration of the protonated aminoalcohol decreases. The fastest formation occurs at a pH between 4 and 5 (Figure 3) (Solomons and Fryhle, 2002).

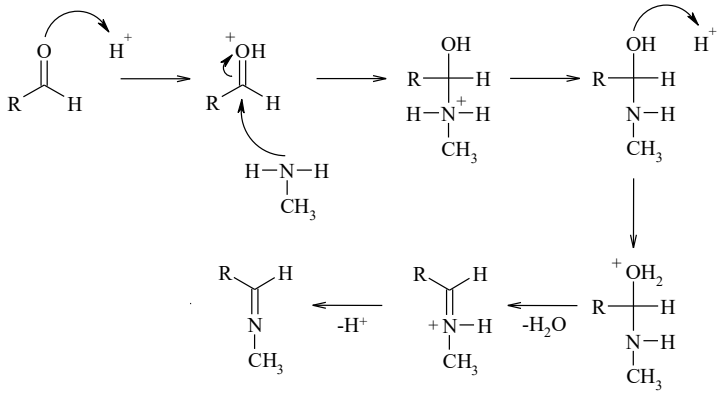

Figure 3. Proposed reaction mechanism for imine formation

2. METAL COMPLEXES OF SCHIFF BASES

Ligands are Lewis bases that can donate electron pairs to the central atom. The nitrogen atom in the imine bond is an electron donor and has a basic character since it has an unpaired electron. This atom, which can also be defined as the azomethine nitrogen, is the primary coordination point for a Schiff base.

The azomethine system, where the nitrogen atom is bonded with a double bond, can also be a coordination site for d-metal ions suitable for back-bonding by the π-orbitals. Therefore, this nitrogen bearing group may show both σ- and π-donor acceptor functions. This is one of the most important factors for which the Schiff bases formed metal complexes have a higher stability (Canpolat, 2003).

The second important factor in the ability of the azomethine group to form stable complexes as a ligand is the presence of a functional group (preferably the phenolic -OH group) close to the azomethine bond from which the hydrogen atom can be easily removed. Depending on this characteristic feature, five- or six-membered chelate ring structures are formed to which the metal can quantitatively bound (Öztürk, 1998).

2.1. The classification of Schiff bases

The classification of metal complexes of Schiff bases is made by taking into account the donor atoms of the compound. Accordingly, the most common metal complexes are those with the donor atom system: N-O, O-N-O, O-N-S, N-N-O, O-N-N-O, N-N-N-N. Examples of metal complexes formed by such Schiff bases are as follows:

2.1.1. N-O Type Schiff bases

The N-O type Schiff bases are formed by salicylaldehyde and p-N,N'-dimethylaniline which is bidentate and forms a 1:1 complex with Ag+ ion (Figure 4) (Erk and Baran, 1990).

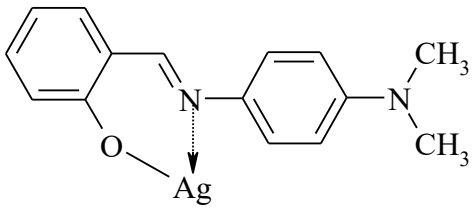

Figure 4. N-O Type Schiff bases

2.1.2. O-N-O Type Schiff bases

The Schiff bases derived from *o*-hydroxyaniline and salicylaldehyde has a tridentate coordination property. It reacts with zirconium metal in a 2:1 ratio to form a complex. The predicted geometry of the zirconium complex is given in Figure 5 (Nath and Yadav, 1995).

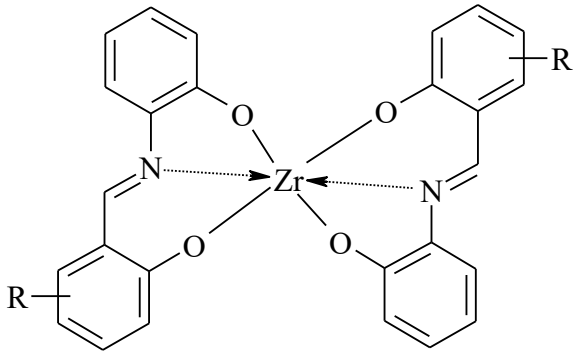

Figure 5. Predicted geometry of Zirconium complex

2.1.3. O-N-S Type Schiff bases

The tridentate and dibasic Schiff base, consisting of 2-hydroxy-1-naphthaldehyde and 2-aminoethanethiol (Figure 6), can be given as an example for O-N-S type Schiff Bases (Syamal and Singhal, 1981).

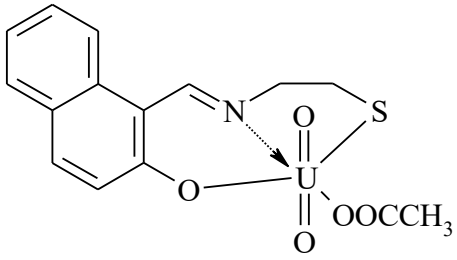

Figure 6. O-N-S Type Schiff Base

2.1.4. N-N-O O-N-S Type Schiff bases

The chelation of the compound N-(salicylidenemiminoacet)-α-picolyl with a Zn^{2+} salt, which is formed from N-(glycyl)-α-picolylamine and salicylaldehyde (Figure 7), is an example of N-N-O type Schiff base complexes (Yüksel and Bekaroğlu 1982).

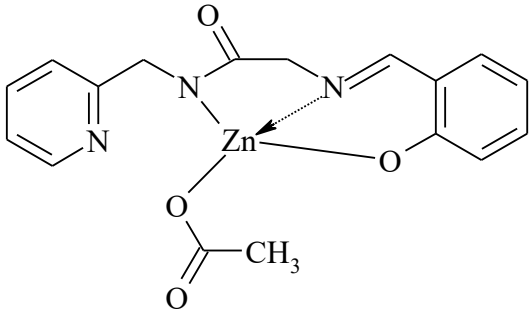

Figure 7. N-N-O type Schiff base complex

2.1.5. O-N-N-O Type Schiff bases

This group of Schiff bases is derived from substituted salicylaldehyde. The most well-known member is salen which is the condensation product of ethylenediamine and salicylaldehyde (Figure 8). Salen gives the acetohydrato-N,N'-ethylenebis(salicylideneminato)cobalt(III) complex with Co^{2+}. Almost all of these compounds exhibit tetradentate properties and can form complexes with some metals other than *d*-elements.

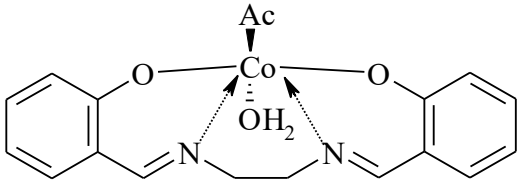

Figure 8. O-N-N-O Type Schiff base

2.1.6. N-N-N-N Type Schiff bases

An example of this group is the Fe^{2+} complex of N,N'-bis(2-salicylideneminobenzoyl)ethylenediamine (Figure 9), which is formed from N,N'-bis(2-aminobenzoyl)ethylenediamine and salicylaldehyde (Okur and Bekaroğlu, 1981).

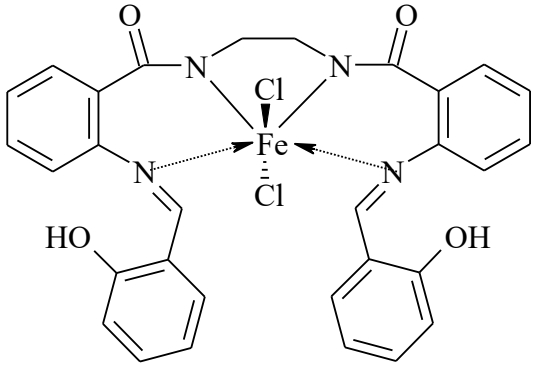

Figure 9. N-N-N-N Type Schiff Bases

2.1.7. Compartmental Type Schiff bases

Schiff base ligands can also hold two metals together, such as Mn(II)-Mn(II) or Mn(II)-Mn(III). Ligand types that can hold metals side by side are called "compartmental" (Figure 10). These types of ligands can be obtained by condensation of 1,3,5-triketones with α,ω-ethylenediamines (Koç, 2006).

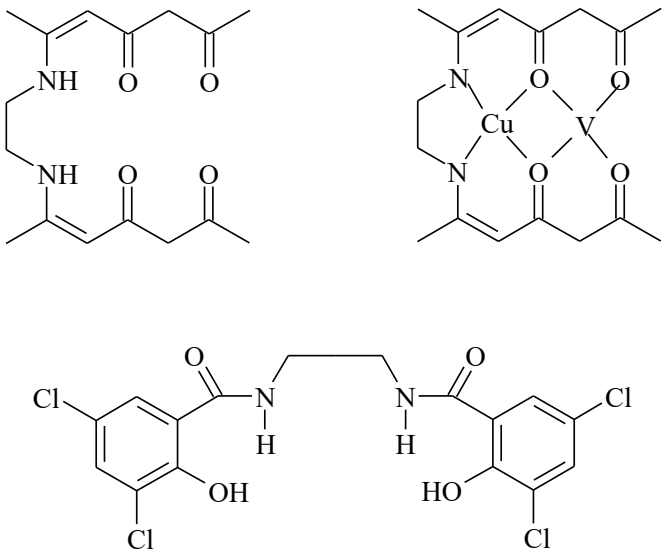

Figure 10. Compartmental ligands holding metals aside

3. SOME APPLICATIONS OF SCHIFF BASES AND THEIR METAL COMPLEXES

3.1 Biological applications

3.1.1. Antibacterial and antifungal activities

Schiff bases and metal complexes attract attention as effective agents in combating bacterial and fungal infections. Metal complexes generally act by mechanisms that disrupt cell membranes and inhibit cellular processes. In particular, Cu(II), Ni(II) and Zn(II) complexes of Schiff bases have shown broad-spectrum antimicrobial activity. The high bioavailability of these complexes and their potential to reduce cellular toxicity play an important role in the development of new antibiotics. Cu(II)-Schiff base complexes were reported to exhibit strong inhibitory effects against *E. coli* and *S. aureus*. Similarly, Zn(II) complexes were observed to exhibit high antifungal activity against *Candida albicans*, a pathogenic fungi (Diab, M. A. *et al*., 2017).

3.1.2. Anticancer activities

Schiff bases and metal complexes are considered promising candidates in the field of cancer treatment. These compounds usually target cancer cells by intercalating into DNA or producing reactive oxygen species (ROS). Their ability to interact strongly with DNA can stop the proliferation of cancer cells and trigger the apoptosis process. For example, Palladium(II)-Schiff base complexes have been reported to exhibit high cytotoxicity in breast and lung cancer cell lines (MCF-7 and A549) (Canovic, P., et al. 2017). It is aimed to develop such complexes as alternatives to chemotherapy drugs in cancer treatment.

3.1.3. Enzyme inhibition

Schiff bases and their metal complexes exhibit significant potential in enzyme inhibition and are of particular interest in medical and biotechnological applications. Molecular docking studies have shown that Schiff bases exhibit strong binding to tyrosinase enzyme via residues such as HIS, GLY and ASN (Peng, Z. et al 2021). In particular, tyrosinase enzyme inhibitors are used as skin-whitening agents in the cosmetics. Schiff bases can suppress the activity of tyrosinase enzyme and reduce melanin production, which is particularly valuable in skin-whitening cosmetic products and in the treatment of hyperpigmentation. These compounds are often designed to form specific interactions with biological targets. In

addition, electron donor groups (e.g. nitrogen and oxygen) make contribution to Schiff bases' effectiveness in binding to the active sites of enzymes.

3.2. Catalytic applications

3.2.1. Oxidation-Reduction reactions

Schiff bases and metal complexes have a wide range of usage in catalytic applications. Efficiency as catalysts in oxidation and reduction reactions, are critical for increasing efficiency in organic synthesis. Mn(III)-Schiff base complexes have been used as effective catalysts in the oxidation of phenol derivatives (Chaudhary et al. 2021). Such catalysts provide great advantages in the synthesis of valuable intermediates, especially those used in the pharmaceutical and polymer industries. High selectivity, stability and environmental compatibility make these compounds attractive for industrial-scale applications.

3.3. Polymerization reactions

Metal complexes of Schiff bases are also used as catalysts in polymer production. For example, Ni(II)-Schiff base complexes have been effectively used in the polymerization of olefins. Such complexes provide high efficiency and product quality in the polymerization process.

3.4. Metallurgical applications

3.4.1. Optoelectronic materials

Metal complexes of Schiff bases are used in optoelectronic devices due to their light emitting properties. Zn(II)-Schiff base complexes have attracted attention by exhibiting high quantum efficiency in light emitting diodes (LEDs) (Kagatikar, S. and Sunil, D. 2021). Such materials have potential for application in energy efficient lighting and display technologies.

3.4.2. Magnetic materials

Schiff base metal complexes exhibiting magnetic properties are used in data storage and superconductor technologies. Cobalt and manganese complexes can be used as magnetic resonance imaging (MRI) contrast agents (Kahn, 2021).

3.5. Environmental applications

3.5.1. Heavy metal removal

Schiff bases are effectively used in water treatment for the removal of heavy metals due to their ability to bind metal ions. For example, the effectiveness of Schiff base complexes in removing Pb(II) and Cd(II) ions from water has been reported (Liaquat, S et al, 2024). These applications provide sustainable solutions for reducing environmental pollution.

3.5.2. Photocatalytic applications

Schiff bases and metal complexes are used in photocatalytic degradation of organic pollutants. Environmental applications of such compounds contribute to the development of green energy and environmental friendly Technologies (Awad, A.A.A., et al, 2023).

3.6. Medical and pharmaceutical applications

Schiff bases and their metal complexes play an important role in pharmaceutical chemistry, both in drug delivery systems and in the development of new drug molecules. Anticancer, antimicrobial and antioxidant properties make these compounds attractive for a wide range of biological applications. For example, Schiff base complexes have been shown to have neuroprotective and cardiovascular effects, finding a place in multidisciplinary research.

CONCLUSION

Schiff bases and metal complexes have potential applications in many areas due to their versatile chemical and biological properties. The advantages provided by these compounds in a wide range of areas such as catalysis, medicine, analytical chemistry, materials science, electrochemistry, sensor technology and agriculture have caused them to become the focus of research and industry. The environmental friendly, biologically active and highly efficient structures of Schiff bases and metal complexes will allow these compounds to be used in more scientific and industrial fields in the future.

REFERENCE

Awad, A. A. A., Moustafa Ali, O. A., and Fattah Nassar, D. A. (2023). Degradation of dye wastewater by using cobalt, copper and nickel Schiff base complexes as catalysts: spectral, molecular modelling, catalytic activity and metal removal from aqueous solution. *International Journal of Environmental Analytical Chemistry*, 103(20), 9562-9581.

Canovic, P., Bogojeski, J., Kosaric, J., Markovic, S., and Zivanovic, M. (2017). Pt (IV), Pd (II), and Rh (III) complexes induced oxidative stress and cytotoxicity in the HCT-116 colon cancer cell line. *Turkish Journal of Biology*, 41(1), 141-147.

Canpolat, E., 2003. İmin ve Oksim İçeren Ligandların Sentezi, Karakterizasyonu ve Bu Ligandların Bazı Metal Komplekslerinin İncelenmesi. F.Ü. Fen Bilimleri Enstitüsü, Doktora Tezi, 128 sayfa, Elazığ.

Chaudhary, V., and Sharma, S. (2021). Study of ethylbenzene oxidation over polymer-silica hybrid supported Co (II) and Cu (II) complexes. *Catalysis Today*, 375, 601-613.

Diab, M. A., El-Sonbati, A. Z., Shoair, A. F., Eldesoky, A. M., and El-Far, N. M. (2017). Synthesis, structural, spectroscopic and biological studies of Schiff base complexes. *Journal of Molecular Structure*, 1141, 710-739.

Erk, B., Baran, Y. (1990). Kinetict of Complexation of The Schiff Base (DMAPS) with Copper (II) and Silver (II) in Methanol, *Chim. Acta. Turc, 18.*

Kagatikar, S., and Sunil, D. (2021). Schiff bases and their complexes in organic light emitting diode application. *Journal of Electronic Materials*, 1-16.

Kahn, O. (2021). *Molecular magnetism*. Courier Dover Publications.

Koç, Z.E., 2006. Tripodal Schiff Bazlı Ligandların Sentezi ve Metal Komplekslerinin İncelenmesi. S.Ü. Fen Bilimleri Enstitüsü, Doktora Tezi, 196 sayfa, Konya.

Liaquat, S., Farrukh, S., Ahmad, N., Karim, S. S., Pervaiz, E., Sultan, A., and Ali, S. (2024). Fabrication of Fe 3 O 4 based cellulose acetate mixed matrix membranes for As (iii) removal from wastewater. *Environmental Science: Water Research and Technology* 10, 1637-1652.

Meena, R., Meena, P., Kumari, A., Sharma, N., and Fahmi, N. (2023). Schiff bases and their metal complexes: Synthesis, structural characteristics and applications. In Schiff Base in Organic, *Inorganic and Physical Chemistry*. IntechOpen.

Nath, M., Yadav, R., 1995. Synthesis, Spectral and Thermal Studies of Fe(III), Co(II), Ni(II), Cu(II) and Zn(II) Complexes of Schiff-Bases Derived from o-Aminobenzyl Alcohol. *Synt. React. Inorg. Met.-Org. Chem*., 25(9), 1529-1547.

Okur, A.İ., Bekaroğlu, Ö., 1981. *Bull. Tech. Univ. İstanbul*, 34(2). 34(C.A.96:14544z).

Öztürk, N.S., 1998. Değişik Piridin Aldehitler ile Çeşitli Anilinlerden Türeyen Schiff Bazlarının Sentezi ve Bazı Geçiş Metal Komplekslerinin Hazırlanması, İ.Ü. Fen Bilimleri Enstitüsü, Doktora Tezi, İstanbul.

Patai, S., 1970. *The Chemistry of Carbon-Nitrogen Double Bond*. Interscience Publisher, 360, London.

Peng, Z., Wang, G., Zeng, Q. H., Li, Y., Wu, Y., Liu, H., and Zhao, Y. (2021). Synthesis, antioxidant and anti-tyrosinase activity of 1, 2, 4-triazole hydrazones as antibrowning agents. *Food Chemistry*, 341, 128265.

Pfeiffer, P, Breith, E., Lubbe, E., Tsumaki, T., 1933. Tricyclische Orthokondensierte Nebenvalenzringe. *Annalen der Chemie*, 503, 84.

Pratt, E.F., Kamlet, M.J., 1961. Reaction Rates by Distillation. IX. The Condensation of Anilines with Benzaldehydes. *J. Org. Chem*., 26(10), 4029-4031.

Schiff, H., 1869. Untersuchungen über salicinderivate. *Annalen der Chemie*, 150, 193-200.

Singh, B., Wang, Z., Park, S., Gautam, G. S., Chotard, J. N., Croguennec, L., and Canepa, P. (2021). A chemical map of NaSICON electrode materials for sodium-ion batteries. *Journal of Materials Chemistry A*, 9(1), 281-292.

Solomons, T.W.G. ve Fryhle, C.B., 2002. *Organik Kimya*, Literatür Yayıncılık Dağıtım, 1350, İstanbul.

Syamal, A., Singhal, O.P., 1981. Synthesis and Characterization of New Dioxouranium(VI) Complexes with Tridentate Sulfur Donor Ligands. *J. Inorg. Nucl. Chem*., 43(11), 2821-2825.

Yüksel, M., Bekaroğlu, Ö. (1982). Some Transition Metal Complexes of N-(Glycyl)-α-Picolylamine and Its Schiff Base. *Synthesis and Reactivity in Inorganic and Metal-Organic Chemistry*, *12*(7), 911-922.

Performance Results of Commercıal Energy Storage Systems

Murat ATES[1, 2]

1- Prof. Dr.; Tekirdag Namik Kemal University, Faculty of Arts and Sciences, Department of Chemistry, mates@nku.edu.tr ORCID No: 000-0002.-1806-0330
2- Nanochem Polymer Energy Company, Slihtaraga Mah., University 1st street, Number: 13/1, Z242/2, Tekirdag, Turkiye.

ABSTRACT

Batteries including lithium and sodium rechargeable batteries and supercapacitors are mostly used as energy storage systems in different electrical devices. Researchers concentrate on enhancing the capacity and long-term stability.

In this study, three different electrode materials (rGO/MnO_2/PTTh, rGO/RuO_2/PVK and rGO/TiO_2/PEDOT) were used in the supercapacitor device which connected a real circuit with charging, discharging and burning lamp process. So, the best performance of supercapacitor device was presented in this study. It has also taken for commercial supercapacitor performances with amount of voltage in commercial supercapacitors, charging time, discharging time and commercial supercapacitors amount of obtained voltage (V). As a result, rGO/MnO_2/PTTh electrode burned brighter and for a longer time period than the other supercapacitor electrodes.

Keywords – Supercapacitor, Real Circuit, Hybrid Nanocomposite, LED Lamp, Charging Process.

INTRODUCTION

Our study is compared in harmony with the literature studies. For example, Chien et al. show that charging in the potential of 3.8 V in 600 s turned on the 1.6 V red LED, the 2V green LED and the 2.4 V blue LED lamp (Chien et al., 2015). In the study of NF/$CuCo_2S_4$@$Ni_2(CO_3)(OH)_2$ electrode hybrid supercapacitors conducted by Zhou et al. It was seen that the series circuit consisting of double hybrid electrodes turns on the 3V yellow LED lamp after being charged to 3.0 V (Zou et al., 2019). It was shown that a 1.6 V red LED lamp turned on by charging an amorphous titanium dioxide supercapacitor with 10 V^{-1} mA (Fukuhara et al., 2016).

Commercial Supercapacitors

Supercapacitors have mostly used for many electric and electronic devices because of their high power density and long time stability performances (Kaempgen et al., 2009). Three different mechanisms were evaluated in supercapacitors.

1- Carbanous materials such as graphene, fullerene, active carbon (AC), etc. shows electrical double layer capacitance (EDLC) from electrostatic separation of charges at the Helmholtz plane.
2- Conducting polymers (PANI, PTh, PCz, PPy, etc.) and metal oxides (NiO, MnO_2, RuO_2, etc.) show pseudocapacitance (PCs) by the

redox reaction processes constituting in the electrode material (Naveen et al., 2015).

3- Both EDLC and PCs system show a hybrid supercapacitor (Miller and Simon, 2008).

In literature, there are different kinds of electrode materials for supercapacitor applications. For example, rGO/TiO_2/PEDOT nanocomposite was used in supercapacitor applications in different feed ratios of $[rGO]_o/[TiO_2]_o$. The highest specific capacitance at $[rGO]_o/[TiO_2]_o$=1/5 shows as C_{sp}= 652 F/g 1 mV/s (Ates et al., 2019). rGO/Co_3O_4/nickel foam (NF) was presented as electrode system for supercapacitors. The highest specific capacitance was measured as C_{sp}= 1016.4 F/g at 1 A/g. In addition, the stability test shows that it preserves 95.5% of the first capacitance after 3000 cycles at 7A/g (Yao et al., 2017).

In literature, there is an economically viable and innovative method for fabricating binder-free electrode materials including the Ru: alpha-Fe_2O_3 nanocomposite for supercapacitor application (Pujar et al., 2024). Graphene/PANI/Co_3O_4 composite was chemically synthesized using hydrothermal method (Wang et al., 2017). The highest specific capacitance was calculated as C_{sp}=789.7 F/g at 1 A/g. In addition, the initial capacitance was remained 81.8% at 10 A/g for 1000 charge-discharge cycles.

Xiang et al. have been reported PANI-nanofibers (NFs)/rGO nanocomposites. It shows the highest specific capacitance of C_{sp}= 942 F/g at 1 A/g (Xiang et al., 2019). In literature, the synthesis of PANI/graphene nanocomposites have improved the electrochemical performances of the SCs. Wang et al. have studied Cu_2O/CuO/RGO nanocomposite, which was controllably synthesized through hydrothermal method (Wang et al., 2015). PANI/TiO_2/graphene (GN) hybrid electrode was synthesized an easy methodology for supercapacitor applications (Parveen et al., 2017). The highest specific capacitance was calculated as C_{sp}= 403.2 F/g at 2 A/g.

Calculation of electrochemical parameters

The specific capacitances were obtained from the GCD measurements using Eq.1.

$$C_s = 4I / m \times dV/dt \qquad (1)$$

In this formula, I is the constant current (A), m is the total mass of the two electrodes and dV/dt (V/s) is the slope of the discharge curve (Stoller et al., 2010).

The electrical series resistance (ESR) was calculated in Eq.2. (Sudhakar et al., 2017).

$$ESR = I \times R_{drop} / 2I \quad (2)$$

The coulombic efficiency (η) was given in Fig.3. (Wang et al., 2015).

$$\eta\ (\%) = t_d/t_c \times 100 \quad (3)$$

where t_c and t_d are charge and discharge times, respectively. The relaxation time (ζ) was obtained from phase angle (θ) (Bode-phase plot) using Eq.4. (Yuan et al., 2011).

$$\zeta = 1 / f_o \quad (4)$$

where f_o is the significant frequency resposnsible for $\theta = -45^o$.
The energy density (E, Wh/kg) was given in Fig.5 (Lin et al., 2016).

$$E = 1/2 \times C_s \times (\Delta V)^2 \quad (5)$$

where C_s is the specific capacitance (F/g), ΔV is the potential window (V) and Δt is the discharge time (s). The power density (P) was calculated using Eq.6.

$$P = E / \Delta t \quad (6)$$

where E is the energy density and Δt is the discharge time in s.

Commercial batteries

Rechargeable system works to understand ion transfer process at the anode side, where anode materials include carbanous materials and metal alloys etc. (Chen et al., 2016; Jiang et al., 2020). Moreover, polyaniline (PANI) has been used as electrode materials in rechargeable batteries due to its easy and economic synthesis compared to other conducting polymers (Zhang et al., 2012).

In literature, Na_2O@Ru@G//$NaLi_{0.05}Mn_{0.5}Ni_{0.30}Cu_{0.10}Mg_{0.05}]O_2$//hard carbon pouch cell can be obtained to 90% and energy density of E= 295 Wh/kg (Zhang et al., 2021). In literature, lithium ion batteries (LIBs) are used in battery technologies due to high voltage, long stability and good electrochemical performances (Kovalenko et al., 2011). In recent years, graphene material was used as LIBs anode side and measured as capacity of 200 mAh/g after 14 cycles (Bhardwaj et al., 2010). Wu et al. have presented some important issues related to commercial production of 1-D nano-PANI (Wu et al., 2019). In the last years, sodium ion batteries (SIBs) are mostly

studied for development of energy density and long time stability (Cao et al., 2020; Meng et al., 2019).

Commercial separators

In literature, there are mostly used two types of commercial organic separators (nonwoven and cellulose) for supercapacitor applications. However, they show flammable and large thermal shrinkage. So, they supply a restricted ionic conductivity (Qin et al., 2018). Metal oxide separators have better fire resistance and higher ionic conductivity compared with organic polymers such as polypropylene (PP) and polyethylene (PE) (He et al., 2017). In addition, there is different types of separators obtained from MOF and doped Cu nanoparticles, which enable electroactive sides to improve electrochemical performance of energy storage systems (Ngo et al., 2025). Moreover, new type of electrolytes develop to enlarge the cell voltage of energy storage system (Dou et al., 2018).

MATERIALS AND METHOD

In this study, power supply, SC in cover, three types of resistances (R_1= 10 Ω, R_2= 330 Ω and R_3= 1 kΩ) and LED (red light) were used for demonstration of the installation in the real circuit system as shown in Fig.1.

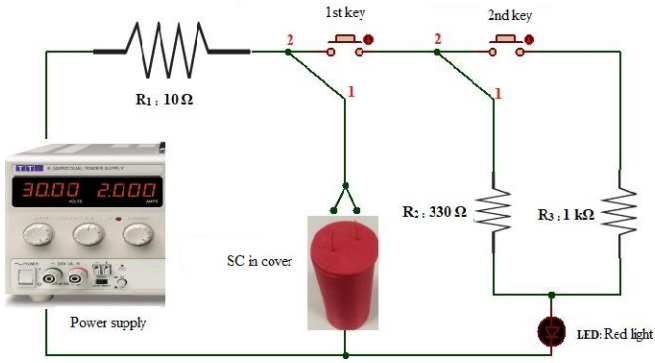

Fig. 1. Demonstration of the installation of our supercapacitor in the real circuit system.

A. Charging results

In this study, we have tested charging performance of commercial supercapacitors in Table 1.

Table 1. Charging results of commercial supercapacitors.

Amount of voltage in commercial supercapacitors	Amount of voltage (V) in commercial supercapacitors	Charging time (h-min.)	Commercial supercapacitors amount of obtained voltage (V)
0.47 F	3.17	1	5.5
0.1 F	1.58	2	5.5
15 F	1.27	1	1.4
25 F	0.22	1 h- 16 min	2.5
50 F	1.45	12	2.7
100 F	1.67	2 h-18 min	2.7
500 F	1.40 – 1.69	4 h-25 min -3h- 4 min	2.54 -2.60

B. Discharge process results

In this study, we have tested discharging performance of commercial supercapacitors in Table 2.

Table 2. Discharge process results of commercial supercapacitors.

Amount of voltage in commercial supercapacitors	Amount of voltage (V) in commercial supercapacitors	Discharging time (h-min.)	Commercial supercapacitors of voltage (V)
0.47 F	5.5	8	1.64
0.1 F	5.5	10	1.64
15 F	1.4	The lamp did not turn on	1.4
25 F	2.5	1 h 48 min.	1.34
50 F	2.7	1 h 21 min.	1.40
100 F	2.7	3 h 38 min.	1.76
500 F	2.7	7 h 43 min.	1.74

C. Charge-discharge process results of the supercapacitors

In this study, we have tested charge-discharge performance of our fabricated supercapacitors in Table 3.

Table 3. Charge-discharge results of the supercapacitors used in this study.

Materials	Charging voltage/V	Lamp burning time/s	Discharge voltage/V
rGO/MnO_2/PTTh	3.12	5	1.64
rGO/RuO_2/PVK	3.18	6	1.47
rGO/TiO_2/PEDOT	3.12	10	1.61

Charging time is 1 h.

D. Real circuit applications of rGO/TiO_2/PEDOT, rGO/RuO_2/PVK and rGO/MnO_2/PTTh nanocomposites

Real circuit applications of rGO/TiO_2/PEDOT, rGO/RuO_2/PVK and rGO/MnO_2/PTTh nanocomposites were presented in Fig.2 & 3.

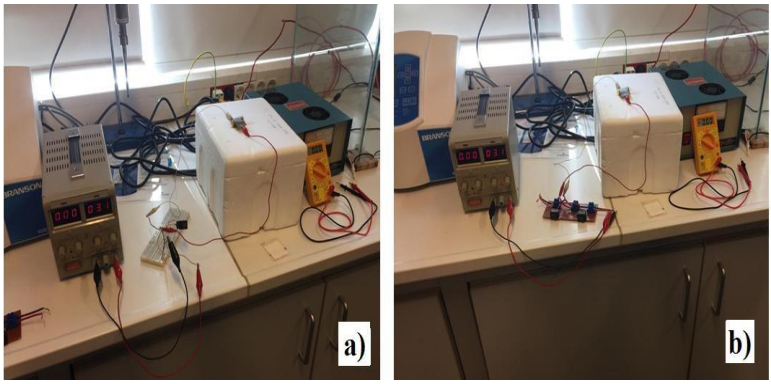

Fig. 2 Circuit model with a) no resistance, b) low and high resistance, established for real circuit applications.

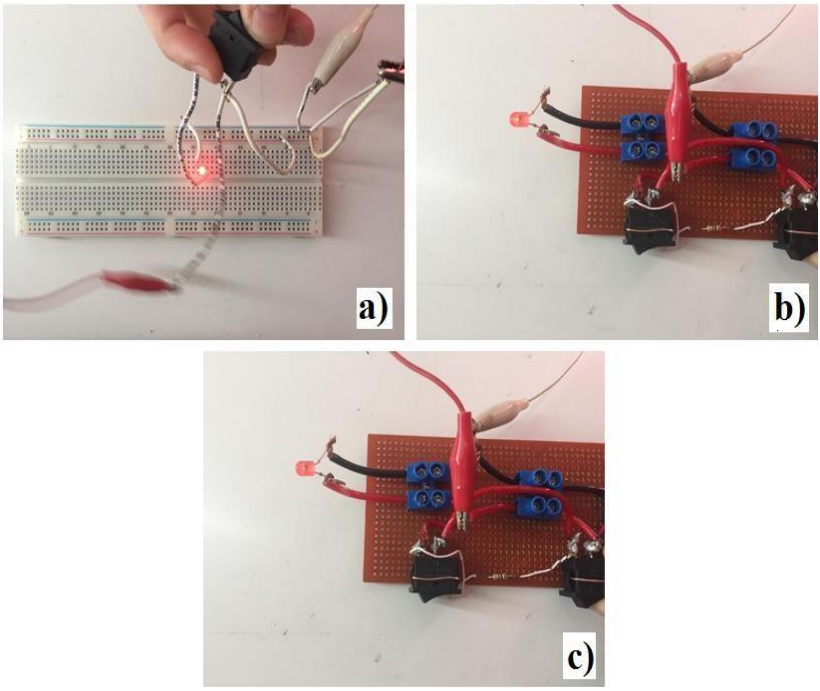

Fig. 3 Visuals of the lamps lit with a) no resistance, b) low resistance, c) high resistance at the end of the charging process.

In this chapter, our supercapacitors were designed as a hybrid supercapacitor containing reduced graphene oxide, ruthenium dioxide, titanium dioxide, manganese oxide, and polyterthiophene, polyvinylcarbazole, PEDOT, a carbon based pseudocapacitors and also EDLC electrodes, rGO, MnO_2, and PTTh were designed symmetrically. By using two different resistors in the circuit, we have built, we show how brightly LED lamp glow through the charging and discharging processes of our supercapacitors. Additionally, the cover was made with the help of a 3D printer.

In the current we built, the charging of our supercapacitor was done first. Charging is done by turning the number 1 and giving 4V energy from our supercapacitor. The reason why we give energy at 4V here is the use of 1-Butyl-3-methyl imidazolium tetra fluoro borate ionic liquid electrolyte. Since ionic liquid has a wider potential range than the decomposition of water, we can go up to 3.5-4.0 V and therefore, our LED lamp can burn for a longer time and also provides a larger discharge time in circuit systems.

Then, by moving our switch number 1 to position 2 and our switch number 2 to position 1, current is passed over the low resistance of 330 Ω, and our LED iodine will glow brighter since its light intensity is higher. It provides a larger discharge time due to its brighter light intensity and the gradual decrease in voltage during the discharge process.

Finally, by turning our switch number 2 to position 2 and passing current over the high resistance of 1 kΩ, the light intensity four LED diode will decrease slightly, so the brightness of our light is less bright compared to the low resistance 330 Ω. The light intensity of our LED iodine decreases with the discharge process of our supercapacitor. The discharge process is slower than commercial supercapacitors.

When we applied this process to our rGO/MnO_2/PTTh, rGO/RuO_2/PVK and rGO/TiO_2/PEDOT supercapacitors one by one, it was observed that rGO/MnO_2/PTTh burned brighter and for a longer time.

RESULTS AND DISCUSSION

In this review article, commercial energy storage systems such as batteries and supercapacitors were given from literature. In addition, our designed and fabricated 3 different SC's were presented in a real circuit system. When we applied it one by one to our rGO/MnO_2/PTTh, rGO/RuO_2/PVK and rGO/TiO_2/PEDOT supercapacitors, it was observed that rGO/MnO_2/PTTh burned brighter and for a longer time. For supercapacitor design and real circuit applications, ionic liquid (1-Butyl-3-methyl imidazolium tetra fluoro borate) was used in the 1.8 V red LED lamp in the supercapacitor of rGO/MnO_2/PTTh nanocomposite, which burns brightest and for the longest time. Instant LED burning was observed with 1 M H_2SO_4 solution. As a suggestion, it is thought that ionic liquid synthesis can be carried out in future studies. Such supercapacitors can be applied in more economical and various devices with organic structure. Another suggestion is to package the supercapacitors that we produce individually with 5 or 10 units in series or parallel connection, aiming to produce higher electrochemical performance so that they can be commercial products.

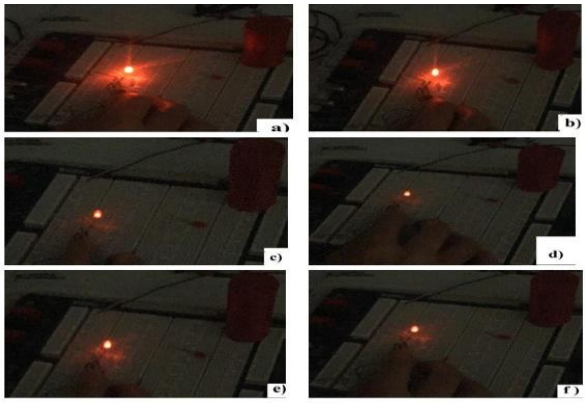

Fig.4. At the end of the charging process, rGO/MnO_2/PTTh, a) low resistance, b) high resistance burning lamp, At the end of the charging process, rGO/RuO_2/PVK, c) low resistance, d) high resistance burning lamp, At the end of the charging process, rGO/TiO_2/PEDOT visuals of burning lamp with e) low resistance, f) high resistance.

ACKNOWLEDGMENT

I would like to thank Prof.Dr. Haydar Ozkan, Selin Aktas and Fatih Sultan Mehmet Vakıf Uni. Electronics Eng. Lab. During the TUBITAK 117M042 project. I also thank to TUBITAK for supporting for this project.

REFERENCE

Ates M, Bayrak Y, Ozkan H, Yoruk O, Yildirim M, Kuzgun O (2019). Synthesis of rGO/TiO_2/PEDOT nanocomposites, supercapacitor device performances and equivalent electrical circuit models. J. Polymer Research, 26, Article number: 49.

Bhardwaj T, Antic A, Pavan B, Barone V, Fahlman BD (2010). Enhanced electrochemical lithium storage by graphene nanoribbons. J Am Chem Soc., 132(36), 12556-12558.

Cao L, Gao X, Zhang B, Qu X, Zhang J, Luo WB (2020). Bimetallic sulfide Sb_2S_3@FeS_2 hollow nanorods as high-performance anode materials for sodium-ion batteries. ACS Nano, 14, 3610-3620.

Chien CT, Hiralal P, Wang DY, Huang IS, Chen CC, Chen CW, Amaratunga GAJ (2015). Graphene-based ıntegrated photovoltaic energy harvesting/storage device. Small Nano Micro., 24, 2929-2937.

Chen D, Zhu C, Yang P, Xia X, Liu J, Wang J, Fan X, Savilov SV, Lin J, Fan HJ, et al. (2016). Array of nanosheets render ultrafast and high-capacity Na-ion storage by tunable pseudocapacitance. Nat. Commun., 7, Article number: 12122.

Dou Q, Lei S, Wang DW, Zhang Q, Xiao D, Guo H, Wang AP, Yang H, Li HYL, Shif SQ, Yan XB (2018). Safe and high rate supercapacitors based on an "acetonitrile/water in salt" hybrid electrolyte. Energy Environ. Sci., 11(11), 3212-3219.

Fukuhara M, Kuroda T, Hasegawa F (2016). Amorphous titanium-oxide supercapacitors. Scientific Reports, 6, 35870.

He T, Jia R, Lang X, et al., (2017). Preparation and electrochemical performance of PVdF ultrafine porous fiber separator-cum electrolyte for supercapacitor. J. Electrochem. Soc., 164 (13), E379-E384.

Jiang Y, Song D, Wu J, Wang Z, Huang S, Xu Y, Chen Z, Zhao B, Zhang J (2019). Sandwich-like SnS_2/graphene/SnS_2 with expanded interlayer distance as high-rate lithium/sodium ion battery anode materials. ACS Nano, 13, Article number: 9100-9111.

Kaempgen M, Chan CR, Ma J, Cui Y, Gruner G (2009). Printable thin film supercapacitors using single-walled carbon nanotubes: Nano Lett., 9(5), 1872-1876.

Kovalenko I, Zdyrko B, Magasinski A, Hertzberg B, Milicev Z, Burtovyy R, Kuzinov I, Yushin G (2011). A major constituent of brown algae for use in high-capacity Li-ion batteries. Science, 334 (6052) 75-79.

Lin H, Huang Q, Wang J, Jiang J, Liu F, Chen Y, Wang C, Lu D, Han S (2016). Self-assembled graphene / polyaniline/Co_3O_4 ternary hybrid aerogels for supercapacitors. Electrochim. Acta, 191, 444-451.

Miller JR, Simon P (2008). Materials science: Electrochemical capacitors for energy management. Science, 321 (5889), 651-652.

Meng QS, Lu YX, Ding FX, Zhang QQ, Chen LQ, Hu YS (2019). Tuning the closed pore structure of hard carbons with the highest Na storage capacity. ACS Energy Lett., 4, 2608-2612.

Naveen AN, Manimaran P, Selladurai S (2015). Cobalt oxide (Co_3O_4)/graphene nanosheets (GNS) composite prepared by novel route for supercapacitor application. J. Mater. Sci. Mater. Electron., 26, 8988-9000.

Ngo NM, Nguyen MH, Song SW, Park S (2025). Bimetallic metal organic framework-modified glass fiber as composite separator for lithium sulfur batteries. Materials Letters, 382, Article number: 137835.

Pujar SS, Bobade RG, Shaikh SF, Al-Enizi AM, Ambare RC, Lokhande BJ (2024). A binderless Ru: α-Fe_2O_3 binary nanocomposite electrode for supercapacitor applications. J. Mater. Sci. Mater. Electronics, 35(34), Article number: 2162.

Parveen N, Ansari MO, Han TH, Cho MH (2017). Simple and rapid synthesis of ternary polyaniline / titanium oxide / graphene by simultaneous TiO2 generation and aniline oxidation as hybrid materials for supercapacitor applications. J. Solid State Electrochem., 21, 57-68.

Sudhakar YN, Hemant H, Nitinkumar SS, Poornesh P, Selvakumar M (2017). Green synthesis and electrochemical characterization of rGO-CuO nanocomposites for supercapacitor applications. Ionics, 23, 1267-1276.

Stoller MD, Ruoff RS (2010). Best practice methods for determining and electrode materials performance for ultracapacitors. Energy Environ. Sci., 3, 1294.

Qin B, Han Y, Ren Y, et al. (2018). A ceramic-based separator for high-temperature supercapacitors. Energy Technol., 6(2), 306-311.

Wang H, Guo Z, Yao S, Li Z, Zhang W (2017). Design and synthesis of ternary graphene/polyaniline/Co_3O_4 hierarchical nanocomposites for supercapacitors. Int. J. Electrochem. Sci., 12, 3721-3731.

Wang Q, Zhu L, Sun L, Liu Y, Jiao L (2015). Facile synthesis of hierarchical porous $ZnCo_2O_4$ microspheres for high-performance supercapacitors. J. Mater. Chem. A., 3, 982-985.

Wang K, Dong X, Zhao C, Qian X, Xu Y (2015). Facile synthesis of Cu_2O/CuO/RGO nanocomposite and its superior cyclability in supercapacitor. Electrochim. Acta, 152, 433-442.

Wu Y, Wang J, Qu B, Zhao S, Wang Z (2019). Some important issues of the commercial production of 1-D nano-PANI. Polymers, 11, 681-705.

Xiang S, Wang Y, Chu J, Wang X, Zhang R, Gang M, Wu B, Li Z (2019). One-pot hydrothermal synthesis of polyaniline nanofibers/reduced graphene oxide nanocomposites and their supercapacitive properties. High Performance Polymers, 31(9-10), 1238-1247.

Yao T, Guo X, Qin S, Xia F, Li Q, Li Y, Chen Q, Li J, He D (2017). Effect of GO coating on interconnected Co_3O_4 / rGO / NF architecture. Nano-Micro Lett., 9, Article number: 38.

Yuan L, Lu X, Xiao X, Zhai T, Dai J, Zhang F, Hu B, Wang X (2011). Flexible solid-state supercapacitors based on carbon nanoparticles / MnO_2 nanorods hybrid structure. ACS Nano, 6, 656-661.

Zhang Q, Gao XW, Shi Y, Luo WB, Li Y, Gu QF, Fan HN, Li F, Liu HK (2021). Electrocatalytic-driven compensation for sodium-ion pouch with high energy density and long life span. Energy Storage Materials, 39, 54-59.

Zhang F, Cao H, Yue D, Zhang J, Qu M (2012). Enhanced anode performances of polyaniline TiO_2-reduced graphene oxide nanocomposites for lithium ion batteries. Inorg. Chem., 51, 9541-9551.

Zou Q, Huang J, Li C, Lv Z, Zhu H, Gang H (2019). Wrapping $CuCO_2S_4$ arrays on nickel foam with $Ni_2(CO_3)(OH)_2$ nanosheets as a high-performance faradaic electrode. New Journal of Chemistry, 43, 5904-5913.

Eco-Friendly Extraction Techniques: An Overview of Ultrasonic, Maceration, and Soxhlet Methods

Ebru KONDOLOT SOLAK

Prof. Dr. Ebru Kondolot Solak; Gazi University, Vocational School of Technical Sciences, Department of Chemistry and Chemical Processing Technologies, ebrukondolot@gazi.edu.tr ORCID No: 0000-0002-6260-9247

ABSTRACT

Ultrasonic extraction, maceration, and Soxhlet extraction methods, frequently used in green synthesis, are commonly preferred for extracting compounds from plant-based and natural materials. Ultrasonic extraction enables the efficient and energy-saving recovery of bioactive compounds by breaking cell walls through cavitation caused by ultrasonic waves in a liquid medium. This method finds widespread use in cosmetics, pharmaceuticals, and environmental applications. Maceration, a traditional method involving the soaking of plant material in a solvent, is favored for extracting temperature-sensitive compounds and is often employed in producing medicinal plant extracts, natural cosmetics, liqueurs, and essential oils. Soxhlet extraction ensures complete compound recovery through a continuous solvent recycling system. This high-yield method is effective in the pharmaceutical industry, natural dye production, environmental analyses, and R&D. However, it is unsuitable for heat-sensitive compounds. The choice of method depends on the properties of the compound to be extracted, thermal stability, environmental factors, and economic requirements. Each method offers unique advantages and applications, particularly within the context of green synthesis, where they are evaluated as eco-friendly, sustainable, and energy-efficient processes.

Keywords: Green Synthesis, Ultrasonic Extraction, Maceration, Soxhlet Extraction, Natural Compounds, Bioactive Materials.

INTRODUCTION

Extraction methods play a fundamental role in isolating active compounds from natural and plant-based sources. These methods enable the isolation of bioactive substances for use in pharmaceuticals, cosmetics, food, and environmental industries. Green synthesis approaches aim to make these processes more efficient and environmentally friendly in line with the principles of environmental sustainability and energy conservation.

Ultrasonic extraction, maceration, and Soxhlet extraction are three commonly used methods, each offering unique advantages and applications. Ultrasonic extraction, leveraging the high energy of ultrasonic waves, provides a fast and effective process. Maceration, a more traditional method, is preferred for obtaining compounds sensitive to heat. Soxhlet extraction ensures high efficiency through a continuous recycling system and is extensively used in pharmaceutical and chemical industries.

This study examines the fundamental characteristics, applications, and advantages of each extraction method. It highlights the effectiveness of ultrasonic extraction in cosmetics, pharmaceuticals, and environmental analyses, the traditional use of maceration in natural cosmetics and food

production, and the high efficiency of Soxhlet extraction in isolating pharmaceutical compounds and natural dyes. The study also compares these methods, offering guidance for selecting the most suitable techniques for various applications.

ULTRASONIC EXTRACTION

Ultrasonic extraction is a method that applies high-frequency ultrasonic waves to a liquid medium, facilitating the extraction of desired compounds from plant materials. These waves create cavitation (the implosion of microbubbles) in the liquid, generating energy that breaks cell walls and releases compounds into the solution (Shen et al., 2023:101). This method is widely used for extracting bioactive compounds such as polyphenols and alkaloids.

Applications:

- ***Cosmetics Industry:*** Effective for extracting natural compounds (e.g., aloe vera, ginseng, chamomile) used in skin care products with antioxidant and anti-aging properties, such as collagen and elastin (Zhang et al., 2023:100).
- ***Pharmaceuticals****:* Frequently employed for extracting alkaloids, terpenoids, flavonoids, and other bioactive materials from medicinal plants. It enables the rapid and efficient isolation of ingredients for drug formulations (Naidu et al., 2022:86).
- ***Environmental Applications****:* Utilized for analyzing pollutants (e.g., pesticides, heavy metals) in soil, water, and air samples. Also used for biofuel production and the separation of chemical substances.
- ***Chemistry and Materials Science****:* Applied in the green synthesis of nanoparticles from plant sources and in integrating natural compounds into polymeric matrices (Jiao et al., 2017:98).

The speed, energy efficiency, and eco-friendly nature of ultrasonic extraction make it a valuable method for both research and commercial applications, depending on the type of compound to be extracted and its intended use.

MACERATION EXTRACTION

Maceration involves soaking plant material in a solvent to facilitate the extraction of compounds through diffusion (Gori et al., 2021:148). Plant material, whether fresh or dry, is immersed in a solvent (e.g., water, ethanol) for a specified period, allowing the solvent to penetrate the plant cells and release the contents. This method is particularly suitable for temperature-sensitive compounds, although it may be time-consuming and limited for compounds with low solubility.

Applications:

- ***Medicinal Plants and Phytotherapy***: Widely used to extract active compounds such as alkaloids, flavonoids, phenolic compounds, and essential oils from plants like chamomile, echinacea, and nettle.
- ***Food and Beverage Industry***: Utilized for extracting natural flavors and aromas from fruits, herbs, or spices into solvents for liqueurs (e.g., limoncello), flavored oils, and vinegars.
- ***Dermatological Products****:* Commonly used in natural cosmetics to derive plant extracts for skin care products, such as serums, creams, and hair care formulations.
- ***Perfumes and Essential Oils***: Applied for extracting natural fragrances from flowers and herbs.
- ***Dye Industry***: Employed to extract natural pigments for use in textiles, art, and handmade products.

Due to its simplicity and effectiveness, maceration remains a preferred method for obtaining natural products from plant materials in various industries.

SOXHLET EXTRACTION

Soxhlet extraction employs a continuous reflux system to achieve complete extraction of compounds into a solvent (Vieira et al., 2020:9(11)). Plant material is placed in a Soxhlet apparatus, where the solvent is heated, vaporized, and then condensed back onto the plant material. This cycle is repeated until the desired compounds are fully extracted. While the method ensures high efficiency and reduced solvent use, it is unsuitable for heat-sensitive compounds due to the heating involved.

Applications:

- ***Pharmaceutical Industry***: Used for extracting pharmacologically active compounds such as alkaloids, flavonoids, and phenolics from medicinal plants.
- ***Chemical Industry***: Commonly applied in isolating natural dyes from plants for use in textiles and food coloring.
- ***Environmental Analyses***: Helps extract and analyze pollutants (e.g., pesticides, heavy metals) from soil and water samples.
- ***Research and Development***: Facilitates the discovery and isolation of compounds from new natural sources, particularly in botany, biochemistry, and pharmacology.

Soxhlet extraction is particularly suitable for obtaining high-purity compounds when the substances are non-volatile and thermally stable.

The choice of extraction method (Table 1) depends on the chemical structure, thermal stability, environmental concerns, and economic factors associated with the compound being extracted.

Table 1: Comparative Analysis of Extraction Methods

Feature	**Ultrasonic**	**Maceration**	**Soxhlet**
Speed	Very fast	Slow	Moderate
Eco-Friendliness	Yes	Yes (low energy)	Relative
Technology Requirement	Medium-high	Low	Medium
Suitability	Thermally stable	Thermally sensitive	Thermally stable

STATE OF THE ART

Modern extraction techniques are evolving through innovative approaches and advanced technologies. Ultrasonic extraction devices have optimized the application of cavitation to biological and plant materials, promoting sustainable production through reduced solvent use and energy efficiency. The integration of ultrasonic extraction with micro and nanotechnologies enables the isolation of high-purity compounds and nanoparticles.

Traditional maceration methods have been refined with automated systems offering temperature and solvent ratio controls, enhancing efficiency and sustainability through eco-friendly solvent choices. Soxhlet extraction, with next-generation solvents and integrated heating systems, is advancing through the use of supercritical fluids and green solvents. These improvements ensure environmentally friendly and effective extraction processes.

CONCLUSION

This study thoroughly examines ultrasonic, maceration, and Soxhlet extraction methods for isolating bioactive compounds from natural and plant-based sources. Each method is distinguished by specific advantages and applications:

- Ultrasonic extraction offers speed, energy efficiency, and eco-friendliness, making it ideal for various applications.
- Maceration remains a traditional method suitable for temperature-sensitive compounds.
- Soxhlet extraction ensures high yields and solvent efficiency, particularly in pharmaceutical, chemical, and environmental analyses.

The selection of an appropriate method depends on the compound's characteristics, process duration, energy consumption, and environmental impacts. Employing these techniques under green synthesis principles contributes to achieving sustainability goals while addressing industrial needs. The development and optimal combination of these methods promise enhanced efficiency and sustainability in future extraction processes.

REFERENCES

Shen, L., Pang, S., Zhong, M., Sun, Y., Qayum, A., Liu, Y., Rashid, A., Xu, B., Liang, Q., Ma, H., Ren, X. (2023). A comprehensive review of ultrasonic assisted extraction (UAE) for bioactive components: Principles, advantages, equipment, and combined technologies. Ultrasonics Sonochemistry, 101, 106646.

Saborirad, S., Baghaei, H., Hashemi-Moghaddam, H. (2024). Optimizing the ultrasonic extraction of polyphenols from mango peel and investigating the characteristics, antioxidant activity and storage stability of extract nanocapsules in maltodextrin/whey protein isolate, Ultrasonics Sonochemistry, 103, 106778.

Zhang, Y., Liu, Y., Cai, Y., Tian, Y., Xu, L., Zhang, A., Zhang, C., Zhang, S. (2023) Ultrasonic-assisted extraction brings high-yield polysaccharides from Kangxian flowers with cosmetic potential, Ultrasonics Sonochemistry, 100, 106626

Naidu, H., Kahraman, O., Feng, H.(2022) Novel applications of ultrasonic atomization in the manufacturing of fine chemicals, pharmaceuticals, and medical devices, Ultrasonics Sonochemistry, 86, 105984

Jiao, F., Wang, X., Song, X., Jing, H., Li, S., Ren, Z., Gao, Z., Zhang, J., Jia, L. (2017). Processing optimization and anti-oxidative activity of enzymatic extractable polysaccharides from Pleurotus djamor. International Journal of Biological Macromolecules, 98, 469–478.

Gori, A., Boucherle, B., Rey, A., Rome, M., Fuzzati, N., Peuchmaur, M. (2021). Development of an innovative maceration technique to optimize extraction and phase partition of natural products, Fitoterapia, 148, 104798

Bréard, D., Esselin, H., Bugeia, L., Boisard, S., Guilet, D., Richomme, P., Le Ray, A. -M., & Ripoll, C. (2023). Influence of Maceration Solvent on Chemical Composition of Gemmotherapy Macerates—A Case Study on *Olea europaea* Young Shoots. Nutraceuticals, 3(4), 574-590

Vieira, S. F., Ferreira, H., & Neves, N. M. (2020). Antioxidant and Anti-Inflammatory Activities of Cytocompatible *Salvia officinalis* Extracts: A Comparison between Traditional and Soxhlet Extraction. Antioxidants, 9(11), 1157.

The Role of Xenograft Zebrafish in Personalized Cancer Therapies

Melek ACAR[1]

Yağmur ÜNVER[2]

1- PhD Student; Atatürk University, Graduate School of Natural and Applied Sciences, Department of Molecular Biology and Genetics. mlkacar@yahoo.com ORCID No: 0000-0001-5931-7799

2- Assoc. Prof. Dr.; Atatürk University, Faculty of Science, Department of Molecular Biology and Genetics. yagmurunver@yahoo.com ORCID No: 0000-0003-1497-081X

ABSTRACT

Personalized medicine aims to optimize healthcare services based on clinical, genetic, genomic, and environmental information of individuals. Since cancer is a disease that affects each person differently, the most effective method of treatment must be chosen for each patient. The tumor microenvironment should be considered while evaluating cancer. Patient-derived xenografts (PDXs) are created by placing primary tumor cells obtained from a patient individual into a host animal. Although mouse PDXs are the most frequently utilized, zebrafish PDXs offer a more affordable and rapid option. Because of their rapid development, simplicity of genetic modification, inexpensive care, and production costs, and physiological and genetic parallels to humans, zebrafish have gained popularity as model organisms. In cancer research, zebrafish are used to study angiogenesis, gene function alterations, molecular pathways, and anticancer medications. Three methods are used to establish cancer models in zebrafish: chemical, xenograft, and genetic models. One major benefit of using xenograft zebrafish is that there are fewer patient-related cells or tissues. Furthermore, since zebrafish are small in size, all organs can be analyzed simultaneously after application. The most widely utilized analyses include morphological observations, histopathology, immunohistochemistry, metabolome analysis, RNA sequencing analysis, and real-time polymerase chain reaction. Zebrafish PDXs are currently becoming a popular fast model that enables the quick testing of several medications at once.

Keywords – Cancer, Personalized Therapies, Zebrafish, Tumor, Xenograft Model.

PERSONALIZED CANCER THERAPY

Personalized medicine aims to optimize healthcare services based on clinical, genetic, genomic, and environmental information of individuals (Chan & Ginsburg, 2011:217). Increasing cancer mortality proves that there are differences in individual patient responses to treatments and that cancer is a highly personalized disease (Xiao et al., 2020:569). Therefore, the most appropriate chemotherapeutic and the most effective treatment method for each patient need to be determined before clinical application (Acar & Unver, 2023:21). For this purpose, personalized medicine in oncology develops treatment and prevention strategies by considering the genetic and intratumoral variability of each cancer patient, the tumor environment, and lifestyle. This approach aims to optimize treatment responses and reduce treatment-related toxicities (Gambardella et al., 2020:1009; Hoeben et al., 2021:242).

In cancer evaluation, the tumor microenvironment should be considered. 2D cultures cannot fully mimic the tumor region. For this reason, 3D models with cell-cell and cell-extracellular matrix (ECM) interactions are used (Costa et al., 2020:293). Patient-derived xenografts (PDXs), which are used in the development of personalized treatment strategies, are created by placing primary tumor cells obtained from a patient individual into a host animal. Thus, the tumor microenvironment structure is preserved with the tumor created in a living organism. In addition, cell migration, metastasis, and angiogenesis can be observed (Abdolahi et al., 2022:206; Costa et al., 2020:293). PDX models are ideal for biomarker evaluation and preclinical studies by preserving the structure of the tumor microenvironment. These models are used to evaluate drug sensitivity and treatment responses of tumor cells in real time (Costa et al., 2020:293; Xiao et al., 2020:569). The results obtained can be directly transferred to the clinic.

Although mouse PDXs are the most frequently utilized, zebrafish PDXs offer a more affordable and rapid option. Therefore, zebrafish xenografts offer a rapid and effective model for personalized medicine.

XENOGRAFT ZEBRAFISH MODEL

Mice and rats are frequently used model animals for tumor model creation. However, these model organisms have disadvantages such as difficulty and cost of maintenance, ethical problems in the number of animals required, and long tumor formation time (Al-Thani et al., 2021:625; Casey & Stewart, 2020:407). In the past two decades, the zebrafish (*Danio rerio*) model has gained popularity for studying human diseases, particularly cancers, because of the ease of tumor creation and the delayed development of the adaptive immune system (which typically develops 28 days post-fertilization) (Lam et al., 2004:9). Additionally, zebrafish have been extensively utilized in medical and biological research for many years (Al-Thani et al., 2021:625; Rahman Khan & Sulaiman Alhewairini, 2019:13). The reasons that make this model organism so popular and important are as follows:

- It has low maintenance and production costs, has a rapid development process, is transparent in embryonic and early larval stages, and can be genetically manipulated.
- The organism exhibits physiological and genetic similarities to humans, such as the digestive, vascular, brain, and immune systems.
- An experienced researcher can inject up to 500 embryos per day. Therefore, many active substances can be tested at the same time, especially in dose experiments.

- A zebrafish facility is much cheaper than a mammalian facility, and the logistics of the facility are much simpler.
- Due to the transparency of the zebrafish, labeled tumor cells (cells expressing GFP/RFP or loaded with fluorescent dye) can be easily seen in the embryo. Thus, tumor cells and metastasis can be followed.
- The adaptive immune system of zebrafish embryos develops late. Therefore, the proliferation, metastasis, and persistence of cancer cells can be achieved in zebrafish without the need for an immunosuppressive application at the beginning. This feature has made them an important model, especially in cancer studies.
- The transparency of the zebrafish embryo enables the dynamic observation of nanomaterials in the body of the fish.
- It can allow the identification of genes involved in angiogenesis in tumor angiogenesis studies. In particular, the effect of inhibitors added to water on vessel formation can be monitored dynamically in angiogenesis inhibition studies.
- Owing to the rapid development of zebrafish embryos relative to other animal models, the experiment duration and the observation of changes in fish morphology and behavior are reduced.
- Its small size allows for the simultaneous analysis of all organs in the analyses to be performed after the application (Al-Thani et al., 2021:625; Evensen et al., 2016:862; Lam et al., 2004:9; Nicoli & Presta, 2007:2918).

Due to these features, zebrafish have taken their place in the scientific world as a popular model organism in cancer studies in recent years. Zebrafish are used to study molecular pathways, changes in gene functions, angiogenesis, and anticancer drugs.

Three different cancer models are created in zebrafish: genetic, xenograft, and chemical models. Xenograft zebrafish embryos are created by transferring human cancer cells to the animal model (Al-Thani et al., 2021:625) (**Figure 1**).

Figure 1: Tumor creating summary figure

Zebrafish has been used as a model organism to create xenograft models for many types of cancer (Table 1).

Table 1: Zebrafish tumor models

Cell line used to create tumor	Injection area	Injection time (hpf)	Purpose	Reference
Tumorigenic FGF2-T-MAE Cells	Perivitelline space	48	Investigating tumor angiogenesis	(Nicoli & Presta, 2007:2918)
Human Breast Cancer BT-474	Yolk sac	48	A new approach for drug screening of cancer stem cells	(Eguiara et al., 2011:3751)
Human Glioma Cells (U87)	Perivitelline space	48	Investigating the molecular mechanisms of tumor angiogenesis	(D. Li et al., 2012:937)
Human Metastatic Melanoma Cell Line Melmet 5	Ducts of Cuvier	48	Screening for new anti-cancer NPs	(Evensen et al., 2016:862)
Human Breast Cancer (MDA-MB-231)	Perivitelline space or Ducts of Cuvier	48	Investigating the invasive behavior of cancer cells	(Ren, Liu, Cui, & Ten Dijke, 2017:1)
Glioblastoma Multiforme (GBM) Tumor Cells (U87 and U251)	Brain	72	Identifying a small compound that can efficiently cross the blood-brain barrier and inhibit tumor growth	(Zeng et al., 2017:14372)
Liver Cancer Cell Lines (Hep3B and SKHep1)	Yolk sac	48	Developing a new xenograft model in zebrafish embryos and using this system for drug screening studies	(Avci et al., 2018:1570)
Human Lung Cancer (A549), Stomach Cancer (SGC-7901), Liver Cancer (HepG2), Pancreatic Cancer (JF 305), and Breast Cancer (MCF-7)	Yolk sac	48	Investigating the anticancer effect of furanodiene, a natural terpenoid	(X. Y. Zhu et al., 2019:4541)
MDA-MB-231_eGFP	Ducts of Cuvier	48	Treatment with drug-loaded nanoparticles	(Nadar et al., 2020:13582)
Human Pancreatic Cancer Cell Line (Mia Paca-2)	Yolk sac	48	Chemotherapy-hyperthermia treatment	(d'Amora et al., 2020:666)
MC38 Murine Colon Cancer Cell Line	Perivitelline space	48	Oncolytic virotherapy	(Mealiea et al., 2021:769)
Chronic myelogenous leukemia (CML) K562 cells	Yolk sac	48	Investigating the effect of anti-leukemic agents	(Somasagara et al., 2021:5715)

KB Human Cervical Cancer Cells	Yolk sac	48	Developing nanoplatform that can enhance anti-angiogenic activity and targeting cancer cells	(Moret et al., 2022:2488)

* hpf (hours post fertilization)

Another advantage of using xenograft zebrafish in personalized cancer treatment is the use of 100-400 cells per animal (Asokan et al., 2020:13254; Kocere et al., 2020:102902; Konantz et al., 2012:124; McKeown et al., 2022:1065; Nadar et al., 2020:13582; Xiao et al., 2020:569). This provides a great advantage in terms of less patient-related cells or tissue.

ZEBRAFISH XENOGRAFTS AND CANCER RESEARCH

Somasagara et al. (2021:5715) stated that mice are generally used as a model organism for *in vivo* screening of the effects of cancer drugs, but these creatures are not suitable for large-scale and rapid screening. Instead, they tested the suitability of zebrafish, which has optical transparency, allows fluorescence imaging, lacks adaptive immunity in its early stages, and can respond quickly to any drug application. Another factor for selecting zebrafish is their genetic and protein similarity to humans (70-80%), with numerous molecular and cellular components involved in tumor formation being conserved in both species. In their study, they injected fluorescently labeled chronic myelogenous leukemia (CML) K562 cells into SCID (severe combined immunodeficiency) zebrafish embryos and examined the effects of anti-leukemic agents. They observed that cancer cell proliferation decreased as a result of the treatment and that they performed an effective treatment. On the other hand, they planned to develop a system that would complete screening and testing drug efficacy at high throughput for personalized medicine in the shortest time. By using zebrafish, tumor formation will be achieved in this organism in a short time with cancer cells taken from the patient, and tumor-drug sensitivity tests can be completed within 3-7 days. For this purpose, they injected primary human $CD34^+$ and T cells into zebrafish and showed that they can survive in the embryo for at least 15 days. Thus, they confirmed that the *in vivo* zebrafish model is a suitable model for the inoculation of both human primary cells and leukemia cell lines. This shows that the use of xenograft zebrafish may be suitable for the development of a high-yield and superior model for preclinical research.

Gatzweiler et al. (2022:849) used different cultures and environments to compare the drug screening results obtained from functional assays of patient-derived cell models. 3D-cultured tumor cells demonstrate increased

resistance to drug therapy, better reflecting the *in vivo* conditions. For a more clinically relevant and reliable prediction of individual patient responses, patient-derived tumor cells and the tumor microenvironment (TME) surrounding the tumor should also be tested. Consequently, patient-derived xenograft (PDX) models are more accurate predictors than cell culture studies, as they reconstruct cell-cell and cell-extracellular matrix (ECM) interactions, allowing for cell polarization, differentiation, and migration. Although mouse PDXs remain the most utilized model, zebrafish PDXs are emerging as a less expensive and much faster option, allowing for the concurrent testing of various drugs and combinations. In addition, the yolk sac, one of the primary injection sites in early zebrafish larvae, also supplies a nutrient-rich environment for the transplanted cells. In this study, Gatzweiler et al. (2022:849) performed drug sensitivity profiling of different culture models against 76 anticancer drugs. Later, some of these drugs (methotrexate, panobinostat, tazemetostat, idasanutlin, etc.) were tested in different pediatric tumors established as xenografts in zebrafish and it was observed that tumor volume was reduced. As a result, *in vivo* zPDX drug screening represents a hopeful method for functional drug screening on precision medicine platforms.

d'Amora et al. (2020:666) conducted a study on zebrafish in which they injected human pancreatic cancer cell line Mia Paca-2 into 48 hpf embryos and then injected doxorubicin-loaded folic acid-conjugated polyacrylamide nanoparticles (DOX:PAA-NP-FA) 2 hours after injecting them. They then incubated the embryos at 41 °C for 5 minutes to induce doxorubicin release from the nanoparticles. They determined that exposing the embryos to heat did not cause embryo death or malformations. In addition, when the tumor area was examined after 24 and 48 hours of incubation, it was stated that no increase in tumor size was observed in the embryos injected with DOX:PAA-NP-FA, and a significant increase in apoptosis was observed in this treatment group. As seen in this study, chemotherapy and hyperthermia treatments were applied together to the zebrafish, which is the model organism used for cancer studies, and the effectiveness of targeted dual therapy in the organism was tested.

Kong et al. (2020:1901489) created a different nanocarrier system for targetability. In this system, they used folate receptor and UV light to target liposomes (nanocarriers) to the tumor region created in xenograft zebrafish. The MDA-MB-231 cell line was used to create a xenograft model. They added folate receptors to liposomes to target liposomes to cancer cells and thus improve the uptake of drug-loaded liposomes by cancer cells. At the same time, they applied a strategy called PEGylation of nanoparticles to extend the circulation life of drug-loaded liposomes and to start drug release after all of them accumulate in the tumor region. However, since it is stated

in the literature that the cellular uptake of PEGylated nanoparticles is limited (Mishra et al., 2004:97), they performed dePEGylation of nanoparticles to achieve effective intracellular drug delivery. dePEGylation can be triggered by an external stimulus (light, pH, etc.), and thus drug release can be achieved after the nanocarrier reaches the target site. In this study, UV light was used for the dePEGylation of nanoparticles. Thus, doxorubicin-loaded liposomes were targeted to breast cancer cells with the folate receptor, and a targeted drug release was achieved by dePEGylation. In the xenograft groups where doxorubicin-loaded EPEG-liposomes (fusogenic peptide E was added to the liposomes for more specific binding) were applied, tumor volume remained the same as the control group in the absence of light activation, while it was significantly reduced in the groups with UV light.

In another study, high-efficiency drug screening using zebrafish xenografts was conducted to find novel combination therapies for Ewing sarcoma. As a pediatric cancer affecting bones and soft tissues, Ewing sarcoma necessitates the urgent development of new treatments. Phenotypic drug screening is a powerful method to identify effective drugs for preclinical Ewing sarcoma treatment. However, the yield that can be obtained from mouse xenografts used for this purpose is limited. Therefore, Grissenberger et al. (2023:216028) tested zebrafish xenografts for high-throughput drug screening. Because the analysis time is short, and the cost is low in zebrafish. It was also stated that the pharmacological responses among zebrafish and humans are relatively well preserved. They screened different drug combinations (A-1331852, S63845, YK-4-279, and irinotecan) that exhibited strong efficacy against Ewing sarcoma cells in the established zebrafish xenograft models. They found that the most specific and sensitive activity was identified in the simultaneous inhibition of MCL-1 and BCL-XL, both of which are anti-apoptotic proteins. Compared to most healthy cells, cancer cells appear to be more prone to apoptosis and frequently depend on anti-apoptotic proteins to survive. Therefore, inhibiting anti-apoptotic proteins is becoming a promising approach for cancer treatment.

ANALYSES USED IN THE ZEBRAFISH MODEL

Since zebrafish are small, all organs can be analyzed at the same time after the application. This is the biggest advantage of using xenograft zebrafish. The most frequently applied analyses after therapy are given in **Figure 2**.

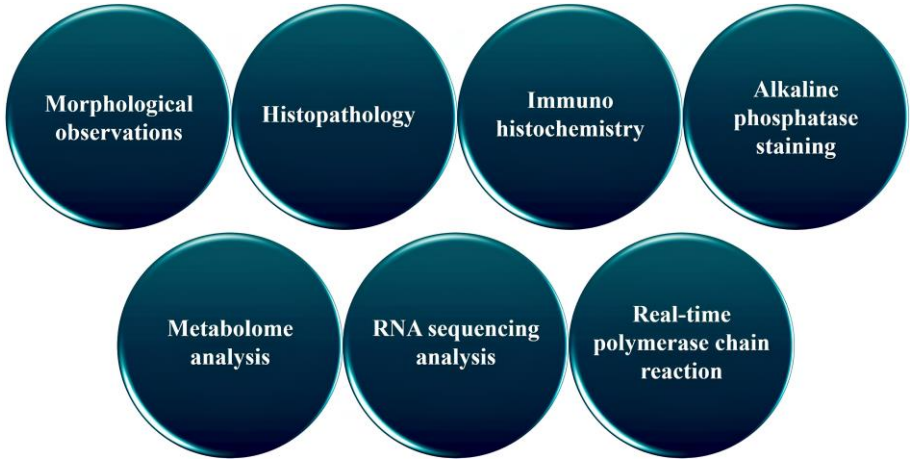

Figure 2: Analysis methods for zebrafish

Morphological observations

In the analyses performed on the zebrafish model, morphological abnormalities such as edema, tail and spine deformations, curved body axis, and tumor formations observed in zebrafish larvae after the application, as well as hatching rate and survival data, are important indicators. In addition, if cells expressing fluorescent protein are used, the tumor area can be visualized with a confocal microscope (Letrado et al., 2018:6048; Martinez-Lopez et al., 2021; Ren et al., 2017:1)

Histopathology

Histopathology is the histological examination of tissues and is frequently used in the diagnosis of diseases such as cancer. The most used stain for histopathological evaluation is hematoxylin-eosin (HE) staining. In HE staining, hematoxylin is dark blue-purple and stains nucleic acids. Eosin is a pink dye that non-specifically stains proteins. In typical tissue samples, the nuclei appear blue-black, and the cytoplasm and extracellular components are stained in varying shades of pink. With this staining, sufficient general information about cells and tissues can be provided (Nacar & Nacar, 2017:46; Sulukan et al., 2022:156391).

Immunohistochemistry

The use of specific fluorescently labeled antibodies is common for post-application metastasis, prognosis, determination of apoptotic cells and

oxidative stress, and cancer pathology. VEGF, Ki-67, CEA, and Caspase-3, as well as 8-OHdG antibodies, are frequently used. The process of angiogenesis, forming new blood vessels from the existing vascular network, is crucial for the continued growth and spread of tumors. Vascular endothelial growth factor (VEGF), one of the most potent and specific angiogenic factors, is associated with metastasis. Ki-67 expression is utilized as a predictive biomarker and is closely linked to aggressive carcinoma biology and tumor growth in the development of breast cancer (Davey et al., 2021:4455). In addition, carcinoembryonic antigen (CEA) is a tumor-associated antigen and one of the most widely used important prognostic markers in breast cancer (Fan et al., 2020:2889; Li et al., 2022:114598). It provides information about the presence and prognosis of the tumor. Since Bcl-2 family proteins regulate apoptosis, it's critical to maintain a balance between Bax and Bcl-2 expression (Sogwagwa et al., 2016:163). In addition to low expressions of anti-apoptotic genes such as Bcl-2, high p53 and Bax expressions are stated to play a key role in apoptosis induction (Mortezaee et al., 2019:228). The effector caspase that has been investigated the most is Caspase-3. It has a significant function in the mitochondrial route involving Caspase-9 as well as the death receptor pathway started by Caspase-8 (O'Donovan et al., 2003:738). 8-OHdG is the best biomarker to determine DNA damage and is used to evaluate oxidative stress (Plasay et al., 2022:979; Valavanidis et al., 2009:120).

Alkaline phosphatase staining

Since angiogenesis is a mechanism that is essential to the growth of tumors, it is a primary target for cancer treatment (Marques et al., 2009:128; Serbedzija et al., 1999:353; Zhang et al., 2018:2423). The arrangement of blood vessels in the growing zebrafish embryo is very distinctive. To assess angiogenesis, subintestinal vessels (SIVs) can be stained and observed under a microscope. Alkaline phosphatase staining has been used to visualize angiogenesis in zebrafish (Nicoli & Presta, 2007:2918).

Metabolome analysis

When there is any change in the body (such as drug administration, stress conditions), a rapid change is observed in metabolite levels. Metabolites (amino acids, fats, etc.) are the end products of biochemical changes in the body, and quantitative changes in the body are an important tool in elucidating the mechanisms (Şenol et al., 2023:164682; Sulukan et al., 2023:160086). Changes in cancer cells play an important role in defining cancer metabolism (Schmidt et al., 2021:333). Since cancer cells cannot

meet their nutritional needs normally, their metabolism changes (Ada et al., 2021:66). As a result of the disruption of metabolic balance and uncontrolled cell proliferation, a characteristic metabolic phenotype occurs in these cells. For example, the conversion of pyruvate (tricarboxylic acid) to lactate instead of acetyl CoA in the TCA cycle (Warburg effect) is one of the oldest known cancer-based metabolic changes (Warburg, 1956:309). Cancer has recently been defined not only as a genetic disease but also as a metabolic disorder in which metabolism is reprogrammed. Therefore, monitoring the metabolic changes that occur plays an important role in determining the general characteristics of cancer and in its diagnosis.

The primary tumor microenvironment (TME) is intimately linked to the sequential, multi-step process of tumor metastasis. As a result of changes in the TME during cancer progression, tumor cells separate from the primary site and begin to migrate to the extracellular matrix. Furthermore, these modifications may alter the distant microenvironment to promote metastasis. Also, the tumor and healthy tissues, such as the circulatory system, interact closely at the metabolic level. Therefore, metabolomic profiling can reflect small changes within the TME (Dai et al., 2019:2883; Echeverria et al., 2018:5079; Elia & Haigis, 2021:21; W. Zhu et al., 2022:5589). W. Zhu et al. (2022:5589) used metabolomic profiling to enable real-time monitoring of the extent of breast cancer metastasis and TME to establish a connection between metabolomic characteristics and tumor metastatic status. On the other hand, when metabolome analyses are examined, it is seen that many biomarkers related to cancer can be analyzed. Thanks to this analysis, the changes in all metabolites in a living creature (zebrafish) can be monitored and compared with cancer biomarkers in the literature (Aboud & Weiss, 2013:138; Silva et al., 2019:102). In addition, new prognostic markers can be determined and new therapeutic targets can be discovered (Denkert et al., 2012:37).

RNA sequencing analysis

RNA sequencing is used to determine the sequence of genes, which genes are transcribed (expressed as mRNA), and the expression levels of specific genes under dissimilar conditions. This technique is used to understand the molecular mechanisms of diseases, to diagnose them, and to identify potential therapeutic targets. RNA sequencing analysis is used to collect large amounts of data and determine gene expression profiles. This analysis evaluates multiple gene expression to determine which genes are expressed, at what level they are expressed, and which genes are potentially regulated (Ding et al., 2024:175; Ozsolak & Milos, 2011:87).

Real-time polymerase chain reaction

RNA sequencing analysis alone is not sufficient for quantitative analysis of a specific gene or gene expression. Therefore, to confirm the data obtained by RNA sequencing analysis, a few transcripts that show statistically significant increases or decreases are selected and analyzed by real-time PCR. For example, it can be used to examine in more detail the expression of genes such as P53, BAX, BCL-2, Caspase-7, and Caspase-9, which are related to the apoptotic pathway, or IL6, CSF2, CCL5, VEGFA, and VEGFC, which are related to metastasis (Yamashita, 2003:731; Yang et al., 2024:e35200; Yuan et al., 2024:116789).

CONCLUSION

It is critically necessary to develop new personalized medicine strategies that are specific to each tumor to enhance cancer treatment methods. The xenograft zebrafish is a suitable system for high-content screening of small compounds. Zebrafish PDXs (zPDX, patient-derived xenograft model) are now emerging as a rapid model that allows several medications to be examined simultaneously in a short time frame in clinical practice.

REFERENCE

Abdolahi, S., Ghazvinian, Z., Muhammadnejad, S., Saleh, M., Asadzadeh Aghdaei, H., & Baghaei, K. (2022). Patient-derived xenograft (PDX) models, applications and challenges in cancer research. *Journal of Translational Medicine*, *20*(1), 206. https://doi.org/10.1186/s12967-022-03405-8

Aboud, O. A., & Weiss, R. H. (2013). New Opportunities from the Cancer Metabolome. *Clinical Chemistry*, *59*(1), 138–146. https://doi.org/10.1373/clinchem.2012.184598

Acar, M., & Unver, Y. (2023). Kanser tedavisinde ısıyla indüklenebilir sistemler ve gen terapisinde kullanımı. In *Doğa Bilimleri ve Matematikte İleri ve Çağdaş Çalışmalar* (pp. 21–38). Duvar Yayınları.

Ada, S., Ertürk, C., Uçar, A., Akyüz, S., Doğan, F., & Yücel, B. (2021). Kanser Hücre Metabolizması. *Türkiye Sağlık Enstitüleri Başkanlığı Dergisi*, *4*(3), 66–75. https://doi.org/10.54537/tusebdergisi.981144

Al-Thani, H. F., Shurbaji, S., & Yalcin, H. C. (2021). Zebrafish as a Model for Anticancer Nanomedicine Studies. *Pharmaceuticals*, *14*(7), 625. https://doi.org/10.3390/ph14070625

Asokan, N., Daetwyler, S., Bernas, S. N., Schmied, C., Vogler, S., Lambert, K., Wobus, M., Wermke, M., Kempermann, G., Huisken, J., Brand, M., & Bornhäuser, M. (2020). Long-term in vivo imaging reveals tumor-specific dissemination and captures host tumor interaction in zebrafish xenografts. *Scientific Reports*, *10*(1), 13254. https://doi.org/10.1038/s41598-020-69956-2

Avci, M. E., Keskus, A. G., Targen, S., Isilak, M. E., Ozturk, M., Atalay, R. C., Adams, M. M., & Konu, O. (2018). Development of a novel zebrafish xenograft model in ache mutants using liver cancer cell lines. *Scientific Reports*, *8*(1), 1570. https://doi.org/10.1038/s41598-018-19817-w

Casey, M. J., & Stewart, R. A. (2020). Pediatric Cancer Models in Zebrafish. *Trends in Cancer*, *6*(5), 407–418. https://doi.org/10.1016/j.trecan.2020.02.006

Chan, I. S., & Ginsburg, G. S. (2011). Personalized Medicine: Progress and Promise. *Annual Review of Genomics and Human Genetics*, *12*(1), 217–244. https://doi.org/10.1146/annurev-genom-082410-101446

Costa, B., Estrada, M. F., Mendes, R. V., & Fior, R. (2020). Zebrafish Avatars towards Personalized Medicine—A Comparative Review between Avatar Models. *Cells*, *9*(2), 293. https://doi.org/10.3390/cells9020293

d'Amora, M., Colucci, P., Usai, A., Landi, E., Deleye, L., Dente, L., De Angelis, F., Raffa, V., & Tantussi, F. (2020). Heat-sensitive poly-acrylamide nanoparticle for cancer treatment. *Precision Nanomedicine*, *3*(4). https://doi.org/10.33218/001c.17629

Dai, J., Escara-Wilke, J., Keller, J. M., Jung, Y., Taichman, R. S., Pienta, K. J., & Keller, E. T. (2019). Primary prostate cancer educates bone stroma through exosomal pyruvate kinase M2 to promote bone metastasis. *Journal of Experimental Medicine*, *216*(12), 2883–2899. https://doi.org/10.1084/jem.20190158

Davey, M. G., Hynes, S. O., Kerin, M. J., Miller, N., & Lowery, A. J. (2021). Ki-67 as a Prognostic Biomarker in Invasive Breast Cancer. *Cancers*, *13*(17), 4455. https://doi.org/10.3390/cancers13174455

Denkert, C., Bucher, E., Hilvo, M., Salek, R., Orešič, M., Griffin, J., Brockmöller, S., Klauschen, F., Loibl, S., Barupal, D. K., Budczies, J., Iljin, K., Nekljudova, V., & Fiehn, O. (2012). Metabolomics of human breast cancer: new approaches for tumor typing and biomarker discovery. *Genome Medicine*, *4*(4), 37. https://doi.org/10.1186/gm336

Ding, Z., Jia, H., Yang, Z., Yao, N., & Wang, Y. (2024). The cardiovascular toxicity of clozapine in embryonic zebrafish and RNA sequencing-based transcriptome analysis. *Journal of Applied Toxicology*, *44*(2), 175–183. https://doi.org/10.1002/jat.4530

Echeverria, G. V., Powell, E., Seth, S., Ge, Z., Carugo, A., Bristow, C., Peoples, M., Robinson, F., Qiu, H., Shao, J., Jeter-Jones, S. L., Zhang, X., Ramamoorthy, V., Cai, S., Wu, W., Draetta, G., Moulder, S. L., Symmans, W. F., Chang, J. T., … Piwnica-Worms, H. (2018). High-resolution clonal mapping of multi-organ metastasis in triple negative breast cancer. *Nature Communications*, *9*(1), 5079. https://doi.org/10.1038/s41467-018-07406-4

Eguiara, A., Holgado, O., Beloqui, I., Abalde, L., Sanchez, Y., Callol, C., & Martin, A. G. (2011). Xenografts in zebrafish embryos as a rapid functional assay for breast cancer stem-like cell identification. *Cell Cycle*, *10*(21), 3751–3757. https://doi.org/10.4161/cc.10.21.17921

Elia, I., & Haigis, M. C. (2021). Metabolites and the tumour microenvironment: from cellular mechanisms to systemic metabolism. *Nature Metabolism*, *3*(1), 21–32. https://doi.org/10.1038/s42255-020-00317-z

Evensen, L., Johansen, P. L., Koster, G., Zhu, K., Herfindal, L., Speth, M., Fenaroli,

F., Hildahl, J., Bagherifam, S., Tulotta, C., Prasmickaite, L., Mælandsmo, G. M., Snaar-Jagalska, E., & Griffiths, G. (2016). Zebrafish as a model system for characterization of nanoparticles against cancer. *Nanoscale*, *8*(2), 862–877. https://doi.org/10.1039/C5NR07289A

Fan, Y., Chen, X., & Li, H. (2020). Clinical value of serum biomarkers CA153, CEA, and white blood cells in predicting sentinel lymph node metastasis of breast cancer. *International Journal of Clinical and Experimental Pathology*, *13*(11), 2889. /pmc/articles/PMC7716139/

Gambardella, V., Tarazona, N., Cejalvo, J. M., Lombardi, P., Huerta, M., Roselló, S., Fleitas, T., Roda, D., & Cervantes, A. (2020). Personalized Medicine: Recent Progress in Cancer Therapy. *Cancers*, *12*(4), 1009. https://doi.org/10.3390/cancers12041009

Gatzweiler, C., Ridinger, J., Herter, S., Gerloff, X. F., ElHarouni, D., Berker, Y., Imle, R., Schmitt, L., Kreth, S., Stainczyk, S., Ayhan, S., Najafi, S., Krunic, D., Frese, K., Meder, B., Reuss, D., Fiesel, P., Schramm, K., Blattner-Johnson, M., … Oehme, I. (2022). Functional Therapeutic Target Validation Using Pediatric Zebrafish Xenograft Models. *Cancers*, *14*(3), 849. https://doi.org/10.3390/cancers14030849

Grissenberger, S., Sturtzel, C., Wenninger-Weinzierl, A., Radic-Sarikas, B., Scheuringer, E., Bierbaumer, L., Etienne, V., Némati, F., Pascoal, S., Tötzl, M., Tomazou, E. M., Metzelder, M., Putz, E. M., Decaudin, D., Delattre, O., Surdez, D., Kovar, H., Halbritter, F., & Distel, M. (2023). High-content drug screening in zebrafish xenografts reveals high efficacy of dual MCL-1/BCL-XL inhibition against Ewing sarcoma. *Cancer Letters*, *554*(November 2022), 216028. https://doi.org/10.1016/j.canlet.2022.216028

Hoeben, A., Joosten, E. A. J., & van den Beuken-van Everdingen, M. H. J. (2021). Personalized Medicine: Recent Progress in Cancer Therapy. *Cancers*, *13*(2), 242. https://doi.org/10.3390/cancers13020242

Kocere, A., Resseguier, J., Wohlmann, J., Skjeldal, F. M., Khan, S., Speth, M., Dal, N.-J. K., Ng, M. Y. W., Alonso-Rodriguez, N., Scarpa, E., Rizzello, L., Battaglia, G., Griffiths, G., & Fenaroli, F. (2020). Real-time imaging of polymersome nanoparticles in zebrafish embryos engrafted with melanoma cancer cells: Localization, toxicity and treatment analysis. *EBioMedicine*, *58*, 102902. https://doi.org/10.1016/j.ebiom.2020.102902

Konantz, M., Balci, T. B., Hartwig, U. F., Dellaire, G., André, M. C., Berman, J. N., & Lengerke, C. (2012). Zebrafish xenografts as a tool for in vivo studies on human cancer. *Annals of the New York Academy of Sciences*, *1266*(1), 124–137. https://doi.org/10.1111/j.1749-6632.2012.06575.x

Kong, L., Chen, Q., Campbell, F., Snaar-Jagalska, E., & Kros, A. (2020). Light-Triggered Cancer Cell Specific Targeting and Liposomal Drug Delivery in a Zebrafish Xenograft Model. *Advanced Healthcare Materials*, *9*(6), 1901489. https://doi.org/10.1002/adhm.201901489

Lam, S. ., Chua, H. ., Gong, Z., Lam, T. ., & Sin, Y. . (2004). Development and maturation of the immune system in zebrafish, Danio rerio: a gene expression profiling, in situ hybridization and immunological study. *Developmental & Comparative Immunology*, *28*(1), 9–28. https://doi.org/10.1016/S0145-305X(03)00103-4

Letrado, P., de Miguel, I., Lamberto, I., Díez-Martínez, R., & Oyarzabal, J. (2018). Zebrafish: Speeding Up the Cancer Drug Discovery Process. *Cancer Research*, *78*(21), 6048–6058. https://doi.org/10.1158/0008-5472.CAN-18-1029

LI, D., LI, X.-P., WANG, H.-X., SHEN, Q.-Y., LI, X.-P., WEN, L., QIN, X.-J., JIA, Q.-L., KUNG, H.-F., & PENG, Y. (2012). VEGF induces angiogenesis in a zebrafish embryo glioma model established by transplantation of human glioma cells. *Oncology Reports*, *28*(3), 937–942. https://doi.org/10.3892/or.2012.1861

Li, N., Jiang, Y., Lv, T., Li, G., & Yang, F. (2022). Immunofluorescence analysis of breast cancer biomarkers using antibody-conjugated microbeads embedded in a microfluidic-based liquid biopsy chip. *Biosensors and Bioelectronics*, *216*, 114598. https://doi.org/10.1016/j.bios.2022.114598

Marques, I. J., Weiss, F. U., Vlecken, D. H., Nitsche, C., Bakkers, J., Lagendijk, A. K., Partecke, L. I., Heidecke, C.-D., Lerch, M. M., & Bagowski, C. P. (2009). Metastatic behaviour of primary human tumours in a zebrafish xenotransplantation model. *BMC Cancer*, *9*(1), 128. https://doi.org/10.1186/1471-2407-9-128

Martinez-Lopez, M., Póvoa, V., & Fior, R. (2021). Generation of Zebrafish Larval Xenografts and Tumor Behavior Analysis. *Journal of Visualized Experiments*, *172*. https://doi.org/10.3791/62373

McKeown, B. T., Relja, N. J., Hall, S. R., Gebremeskel, S., MacLeod, J. M., Veinotte, C. J., Bennett, L. G., Ohlund, L. B., Sleno, L., Jakeman, D. L., Berman, J. N., Johnston, B., & Goralski, K. B. (2022). Pilot study of jadomycin B pharmacokinetics and anti-tumoral effects in zebrafish larvae and mouse breast cancer xenograft models. *Canadian Journal of Physiology and Pharmacology*, *100*(11), 1065–1076. https://doi.org/10.1139/cjpp-2022-0152

Mealiea, D., Boudreau, E., De Silva, N., Okamoto, L., Ho, T., Fish, J. E., & McCart, J. A. (2021). Modeling oncolytic virus dynamics in the tumor microenvironment using zebrafish. *Cancer Gene Therapy*, *28*(7–8), 769–784. https://doi.org/10.1038/s41417-020-0194-7

Mishra, S., Webster, P., & Davis, M. E. (2004). PEGylation significantly affects cellular uptake and intracellular trafficking of non-viral gene delivery particles. *European Journal of Cell Biology*, *83*(3), 97–111. https://doi.org/10.1078/0171-9335-00363

Moret, F., Conte, C., Esposito, D., Dal Poggetto, G., Avitabile, C., Ungaro, F., Tiso, N., Romanelli, A., Laurienzo, P., Reddi, E., & Quaglia, F. (2022). Biodegradable nanoparticles combining cancer cell targeting and anti-angiogenic activity for synergistic chemotherapy in epithelial cancer. *Drug Delivery and Translational Research*, *12*(10), 2488–2500. https://doi.org/10.1007/s13346-021-01090-6

Mortezaee, K., Najafi, M., Farhood, B., Ahmadi, A., Potes, Y., Shabeeb, D., & Musa, A. E. (2019). Modulation of apoptosis by melatonin for improving cancer treatment efficiency: An updated review. *Life Sciences*, *228*, 228–241. https://doi.org/10.1016/j.lfs.2019.05.009

Nacar, E., & Nacar, A. (2017). Hematoksilen ve Eozin: Histopatologların Eskimeyen Dostları. *Mustafa Kemal Üniversitesi Tıp Dergisi*, *8*(29), 46–46.

https://doi.org/10.17944/mkutfd.209597
Nadar, R. A., Asokan, N., Degli Esposti, L., Curci, A., Barbanente, A., Schlatt, L., Karst, U., Iafisco, M., Margiotta, N., Brand, M., van den Beucken, J. J. J. P., Bornhäuser, M., & Leeuwenburgh, S. C. G. (2020). Preclinical evaluation of platinum-loaded hydroxyapatite nanoparticles in an embryonic zebrafish xenograft model. *Nanoscale*, *12*(25), 13582–13594. https://doi.org/10.1039/D0NR04064A
Nicoli, S., & Presta, M. (2007). The zebrafish/tumor xenograft angiogenesis assay. *Nature Protocols*, *2*(11), 2918–2923. https://doi.org/10.1038/nprot.2007.412
O'Donovan, N., Crown, J., Stunell, H., Hill, A. D. K., McDermott, E., O'Higgins, N., & Duffy, M. J. (2003). Caspase 3 in breast cancer. *Clinical Cancer Research*, *9*(2), 738–742.
Ozsolak, F., & Milos, P. M. (2011). RNA sequencing: advances, challenges and opportunities. *Nature Reviews Genetics*, *12*(2), 87–98. https://doi.org/10.1038/nrg2934
Plasay, M., Natzir, R., Cangara, M. H., Hardjo, M., Syahrijuita, S., & Soraya, G. V. (2022). Melittin-Induced Cell Death Through p53 and 8-OHdG in Breast Cell Cancer MCF-7. *Biomedical and Pharmacology Journal*, *15*(2), 979–983. https://doi.org/10.13005/bpj/2433
Rahman Khan, F., & Sulaiman Alhewairini, S. (2019). Zebrafish (Danio rerio) as a Model Organism. In *Current Trends in Cancer Management* (p. 13). IntechOpen. https://doi.org/10.5772/intechopen.81517
Ren, J., Liu, S., Cui, C., & ten Dijke, P. (2017). Invasive Behavior of Human Breast Cancer Cells in Embryonic Zebrafish. *Journal of Visualized Experiments*, *2017*(122), 1–9. https://doi.org/10.3791/55459
Schmidt, D. R., Patel, R., Kirsch, D. G., Lewis, C. A., Vander Heiden, M. G., & Locasale, J. W. (2021). Metabolomics in cancer research and emerging applications in clinical oncology. *CA: A Cancer Journal for Clinicians*, *71*(4), 333–358. https://doi.org/10.3322/caac.21670
Şenol, O., Sulukan, E., Baran, A., Bolat, İ., Toraman, E., Alak, G., Yildirim, S., Bilgin, G., & Ceyhun, S. B. (2023). Global warming and nanoplastic toxicity; small temperature increases can make gill and liver toxicity more dramatic, which affects fillet quality caused by polystyrene nanoplastics in the adult zebrafish model. *Science of The Total Environment*, *892*, 164682. https://doi.org/10.1016/j.scitotenv.2023.164682
Serbedzija, G. N., Flynn, E., & Willett, C. E. (1999). Zebrafish angiogenesis: A new model for drug screening. *Angiogenesis*. https://doi.org/10.1023/A:1026598300052
Silva, C., Perestrelo, R., Silva, P., Tomás, H., & Câmara, J. S. (2019). Breast Cancer Metabolomics: From Analytical Platforms to Multivariate Data Analysis. A Review. *Metabolites*, *9*(5), 102. https://doi.org/10.3390/metabo9050102
Sogwagwa, N., Davison, G., Khan, S., & Solomon, W. (2016). P9. Correlation of radiation induced apoptosis with Bax and Bcl-2 protein expression. *Physica Medica*, *32*, 163. https://doi.org/10.1016/j.ejmp.2016.07.076
Somasagara, R. R., Huang, X., Xu, C., Haider, J., Serody, J. S., Armistead, P. M., & Leung, T. (2021). Targeted therapy of human leukemia xenografts in immunodeficient zebrafish. *Scientific Reports*, *11*(1), 5715.

https://doi.org/10.1038/s41598-021-85141-5
Sulukan, E., Baran, A., Şenol, O., Kankaynar, M., Yıldırım, S., Bolat, İ., Ceyhun, H. A., Toraman, E., & Ceyhun, S. B. (2023). Global warming and glyphosate toxicity (I): Adult zebrafish modelling with behavioural, immunohistochemical and metabolomic approaches. *Science of The Total Environment*, *858*, 160086. https://doi.org/10.1016/j.scitotenv.2022.160086
Sulukan, E., Şenol, O., Baran, A., Kankaynar, M., Yıldırım, S., Kızıltan, T., Bolat, İ., & Ceyhun, S. B. (2022). Nano-sized polystyrene plastic particles affect many cancer-related biological processes even in the next generations; zebrafish modeling. *Science of The Total Environment*, *838*, 156391. https://doi.org/10.1016/j.scitotenv.2022.156391
Valavanidis, A., Vlachogianni, T., & Fiotakis, C. (2009). 8-hydroxy-2′ -deoxyguanosine (8-OHdG): A Critical Biomarker of Oxidative Stress and Carcinogenesis. *Journal of Environmental Science and Health, Part C*, *27*(2), 120–139. https://doi.org/10.1080/10590500902885684
Warburg, O. (1956). On the Origin of Cancer Cells. *Science*, *123*(3191), 309–314. https://doi.org/10.1126/science.123.3191.309
Xiao, J., Glasgow, E., & Agarwal, S. (2020). Zebrafish Xenografts for Drug Discovery and Personalized Medicine. *Trends in Cancer*, *6*(7), 569–579. https://doi.org/10.1016/j.trecan.2020.03.012
Yamashita, M. (2003). Apoptosis in zebrafish development. *Comparative Biochemistry and Physiology Part B: Biochemistry and Molecular Biology*, *136*(4), 731–742. https://doi.org/10.1016/j.cbpc.2003.08.013
Yang, Z., Zeng, H., Li, J., Zeng, N., Zhang, Q., Hou, K., Li, J., Yu, J., & Wu, Y. (2024). Dissecting the emerging role of cancer-associated adipocyte-derived cytokines in remodeling breast cancer progression. *Heliyon*, *10*(15), e35200. https://doi.org/10.1016/j.heliyon.2024.e35200
Yuan, W., Xiao, Y., Zhang, Y., Xiang, K., Huang, T., Diaby, M., & Gao, J. (2024). Apoptotic mechanism of development inhibition in zebrafish induced by esketamine. *Toxicology and Applied Pharmacology*, *482*, 116789. https://doi.org/10.1016/j.taap.2023.116789
Zeng, A., Ye, T., Cao, D., Huang, X., Yang, Y., Chen, X., Xie, Y., Yao, S., & Zhao, C. (2017). Identify a Blood-Brain Barrier Penetrating Drug-TNB using Zebrafish Orthotopic Glioblastoma Xenograft Model. *Scientific Reports*, *7*(1), 14372. https://doi.org/10.1038/s41598-017-14766-2
Zhang, J., Gao, B., Zhang, W., Qian, Z., & Xiang, Y. (2018). Monitoring antiangiogenesis of bevacizumab in zebrafish. *Drug Design, Development and Therapy*, *Volume 12*, 2423–2430. https://doi.org/10.2147/DDDT.S166330
Zhu, W., Qian, W., Liao, W., Huang, X., Xu, J., Qu, W., Xue, J., Feng, F., Liu, W., Liu, F., & Han, L. (2022). Non-Invasive and Real-Time Monitoring of the Breast Cancer Metastasis Degree via Metabolomics. *Cancers*, *14*(22), 5589. https://doi.org/10.3390/cancers14225589
Zhu, X.-Y., Guo, D.-W., Lao, Q.-C., Xu, Y.-Q., Meng, Z.-K., Xia, B., Yang, H., Li, C.-Q., & Li, P. (2019). Sensitization and synergistic anti-cancer effects of Furanodiene identified in zebrafish models. *Scientific Reports*, *9*(1), 4541. https://doi.org/10.1038/s41598-019-40866-2

A Note on Taxicab Incircles and Taxicab Excircles of Triangles

Süheyla EKMEKÇİ[1]

1- Prof. Dr.; Eskişehir Osmangazi University, Department of Mathematics and Computer Science, Faculty of Science,. sekmekci@ogu.edu.tr ORCID No: 0000-0003-2820-2096

ABSTRACT

In this study, the taxicab midsets of two lines were first defined and subsequently analyzed based on the classifications of the lines. In the taxicab plane, the concepts of incircles and excircles are introduced using taxicab midsets, which are sets of points equidistant from the sides of a triangle. A taxicab incircle lies inside the triangle, tangent to all three sides, with its center, called the incenter, located at the intersection of the internal taxicab midsets. And, a taxicab excircle lies outside the triangle, tangent to one side and the extensions of the other two, with its center determined by the intersection of an internal and two external taxicab midsets.

In the taxicab plane, a line can be tangent to a taxicab circle in two distinct ways: either at a vertex or along a side. Based on these tangency cases, taxicab circles tangent to all sides of a triangle are classified into two types. First, a taxicab circle is classified as *tangent at vertex* to the triangle if each side (or its extended line) of the triangle is tangent at a vertex to the circle. Second, a taxicab circle is classified as *tangent along side and at vertex* to the triangle if at least one side (or its extended line) of the triangle is tangent along a side, while the remaining sides are tangent at vertex to the circle.

Subsequently, the taxicab incircle and taxicab excircles of a given triangle were identified and classified based on the triangle's side configurations. It was observed that when all sides of the triangle lie on gradual lines or steep lines, the triangle possesses one taxicab incircle and two taxicab excircles. If the sides of the triangle lie on a combination of gradual and steep lines, one taxicab incircle and three taxicab excircles were identified. All these circles were found to be *tangent at vertex* to the triangle. Additionally, when one or two sides of the triangle lie on separator lines, the resulting taxicab incircle and taxicab excircles were observed to be *tangent along side and at vertex* to the triangle.

Keywords – Taxicab Distance, Incircle, Excircle, Tangent.

INTRODUCTION

Taxicab geometry, a non-Euclidean metric geometry, has garnered significant interest for its distinct mathematical properties and practical applications. Taxicab geometry, also referred to as Manhattan geometry, is based on the concept of the taxicab distance or metric, providing an alternative to Euclidean distance measurement. The distance in the taxicab geometry is determined using only horizontal and vertical paths between two points.

Hermann Minkowski played a significant role in the advancement of taxicab geometry. Building on Minkowski's foundation, Karl Menger and E. F.

Krause further developed taxicab geometry, with Krause making significant contributions in his work. Menger and Krause explored numerous properties and theorems in this geometric structure, developing taxicab geometry. Over time, extensive research on various aspects of the taxicab plane and the taxicab space has further enriched and expanded this field. Some notable contributions include: (Akça and Kaya, 1997:151), (Kaya et al, 2000:135), (Özcan et al, 2002: 381), (Akça and Kaya, 2004:521), (Akça and Kaya, 2004:491), (Bayar and Kaya, 2005:41), (Bayar et. al., 2009:17), (Bayar and Ekmekçi, 2014: 33), (Bayar and Ekmekçi, 2015: 58) and (Akça and Çalış, 2021:175).

In this study, the taxicab midsets of two lines were first defined and subsequently analyzed based on the classifications of the lines. In the taxicab plane, the concepts of incircles and excircles are introduced using taxicab midsets, which are sets of points equidistant from the sides of a triangle. A taxicab incircle lies inside the triangle, tangent to all three sides, with its center, called the incenter, located at the intersection of the internal taxicab midsets. And, a taxicab excircle lies outside the triangle, tangent to one side and the extensions of the other two, with its center determined by the intersection of an internal and two external taxicab midsets.

In the taxicab plane, a line can be tangent to a taxicab circle in two distinct ways: either at a vertex or along a side. Based on these tangency cases, taxicab circles tangent to all sides of a triangle are classified into two types. First, a taxicab circle is classified as *tangent at vertex* to the triangle if each side (or its extended line) of the triangle is tangent at a vertex to the circle. Second, a taxicab circle is classified as *tangent along side and at vertex* to the triangle if at least one side (or its extended line) of the triangle is tangent along a side, while the remaining sides are tangent at vertex to the circle.

Subsequently, the taxicab incircle and taxicab excircles of a given triangle were identified and classified based on the triangle's side configurations. It was observed that when all sides of the triangle lie on gradual lines or steep lines, the triangle possesses one taxicab incircle and two taxicab excircles. If the sides of the triangle lie on a combination of gradual and steep lines, one taxicab incircle and three taxicab excircles were identified. All these circles were found to be *tangent at vertex* to the triangle. Additionally, when one or two sides of the triangle lie on separator lines, the resulting taxicab incircle and taxicab excircles were observed to be *tangent along side and at vertex* to the triangle.

PRELIMINARIES

In this section, some definitions, concepts and theorems used throughout this work are mentioned.

Definition 2.1. The taxicab distance between two points $A=(a_1,a_2)$ and $B=(b_1,b_2)$ in the analytical plane is $d_T(A,B)=|a_1-b_1|+|a_2-b_2|$.

It is seen from the definition that the taxicab distance between the points *A* and *B* is equal to the sum of the Euclidean lengths of the sides parallel to the coordinates axes in the right triangle with the hypotenuse *AB.*

The taxicab plane is the analytical plane equipped with the taxicab distance d_T and symbolized by R_T^2.

Theorem 2.2. Let a point $P(x_0,y_0)$ be given in the taxicab plane. The taxicab distance from the point P to the line l with the equation $ax+by+c=0$ is

$$d_T(P,l)=\frac{|ax_0+by_0+c|}{\max\{|a|,|b|\}},$$

(Kaya, Akça, Günaltılı and Özcan,2000:136).

Krause classified lines depending on their slope as the following definition:

Definition2.3. Let m be the slope of the line l in taxicab plane. The line l is referred to as *the steep line*, *the gradual line* and *the separator line* in the cases where $|m|>1$, $|m|<1$ and $|m|=1$, respectively. In the special cases that the line l is parallel to x-axis or y-axis, it is called *the horizontal line* or *the vertical line*, respectively, (Krause, 1975:31).

Every Euclidean translation preserves the taxicab distance. So, it is an isometry in R_T^2. Reflections in the coordinate axes and the separator lines through the origin are isometries in R_T^2. The set of axes of isometric reflections is $\{x=0, y=0, y=x, y=-x\}$. The rotations by θ-angle in the set $\left\{\theta \mid \theta=k\frac{\pi}{2}, k=0,1,2,3\right\}$ are isometries in R_T^2.

THE TAXICAB MIDSET OF TWO LINES

Definition 3.1. The set of points that are at equal taxicab distance from any two lines l_1 and l_2 in the taxicab plane is called the taxicab midset of the lines l_1 and l_2, and this set

$$\left\{ X \in \mathbf{R}_T^2 \mid \ d_T(X,l_1) = d_T(X,l_2) \right\},$$

(Ekmekçi,2001:6-10).

Lemma 3.2. If the lines $a_i x + b_i y + c_i = 0$, $\mathrm{i} = 1,2,3$ are not concurrent and two of them are nonparallel, the determinant

$$\begin{vmatrix} a_1 & b_1 & c_1 \\ a_2 & b_2 & c_2 \\ a_3 & b_3 & c_3 \end{vmatrix}$$

is nonzero, (Ekmekçi,2001:6-10).

.

Theorem 3.3. In the taxicab plane, the taxicab midset of two distinct lines consists of one or two lines.

Proof. Let l_1 and l_2 be two different lines with equations $a_1 x + b_1 y + c_1 = 0$ and $a_2 x + b_2 y + c_2 = 0$, respectively. If the lines l_1 and l_2 are parallel, the points $X = (x, y)$ in the taxicab midset of the lines l_1 and l_2 that satisfy the equation

$$d_T(X,l_1) = d_T(X,l_2) \qquad (3.1)$$

form the line with the equation

$$a_1 x + b_1 y + \frac{c_1 + c_2}{2} = 0 \cdot$$

If the lines l_1 and l_2 are not parallel, the taxicab midset of them consists of two lines. The lines in the taxicab midset are as follows according to the types of the lines l_1 and l_2:

1) In the case that the lines l_1 and l_2 are the steep lines, then $a_1 \neq 0$ and $a_2 \neq 0$. From equation (3.1), the taxicab midset of lines l_1 and l_2 consists of the line $l_1^{'}$ with equation

$$(b_2 a_1 - b_1 a_2) y - (c_2 a_1 - c_1 a_2) = 0$$

and the line $l_2^{'}$ with equation

$$2a_1 a_2 x + (b_2 a_1 + b_1 a_2) y + (c_2 a_1 + c_1 a_2) = 0 .$$

Since $|b_2 a_1 + b_1 a_2| < 2|a_1 a_2|$, $l_2^{'}$ is a steep line. Thus, it is evident that the taxicab midset of two steep lines is made up of a steep line and a horizontal

line. In particular, if the intersection of lines is the origin, one of the lines in the midset is the x-axis.

2) If l_1 is a steep line and l_2 is a gradual line, then $a_1 \neq 0$ and $b_2 \neq 0$. From equation (3.1), the taxicab midset of lines l_1 and l_2 consists of the line $l_1^{'}$ with equation

$$(1+\frac{a_2}{b_2})x+(1+\frac{b_1}{a_1})y+\frac{c_1}{a_1}+\frac{c_2}{b_2}=0$$

and the line $l_2^{'}$ with equation

$$(1-\frac{a_2}{b_2})x+(-1+\frac{b_1}{a_1})y+\frac{c_1}{a_1}-\frac{c_2}{b_2}=0.$$

Depending on the values of a_1, b_1, a_2 and b_2, one of these lines is a gradual line and the other is a steep line. In particular, when the lines l_1 and l_2 are the y-axis and x-axis, respectively, the taxicab midset consists of the separator lines passing through the origin.

3) In the case that the lines l_1 and l_2 are the gradual lines, then $b_1 \neq 0$ and $b_2 \neq 0$. From equation (3.1), the taxicab midset of lines l_1 and l_2 consists of the line $l_1^{'}$ with equation

$$(a_1b_2+a_2b_1)x+2b_1b_2y+(c_1b_2+c_2b_1)=0$$

and the line $l_2^{'}$ with equation

$$(a_1b_2-a_2b_1)x+(c_1b_2-c_2b_1)=0.$$

Since $|a_1b_2+a_2b_1|<2|b_1b_2|$, $l_1^{'}$ is a gradual line. So, it is seen that the taxicab midset of two gradual lines occurs a gradual line and a vertical line.

Corollary 3.4. In the taxicab plane, if two given lines are parallel, the taxicab midset of these lines is a line parallel to both lines. If the lines are not parallel, the taxicab midset is two lines, one of which is a gradual line and the other a steep line, passing through the intersection of the given lines.

THE TAXICAB CIRCLES TANGENT TO A TRIANGLE

In Euclidean geometry, the incircle of a triangle is the circle that is tangent to all three sides of the triangle and has its center located inside the triangle. The center of this circle, called the incenter, is the point where the angle bisectors of the triangle's interior angles intersect. The incircle is equidistant from each side of the triangle, and this distance is the radius of the circle. The excircles of a triangle are circles that are tangent to the sides of the triangle but have their centers located outside the triangle. Each

triangle has three excircles, one associated with each side. The centers of these excircles are found at the intersection of an interior angle bisector and the bisectors of the exterior angles of the other two sides.

In this section, it is explored that the taxicab circles are tangent to all sides of a triangle in the taxicab plane. To determine these taxicab circles, instead of using the angle bisectors of the triangle, the taxicab midsets of the sides are used.

Definition 4.1. A taxicab incircle is a taxicab circle located inside a triangle that is tangent to all three sides (excluding their extensions). The center of the taxicab incircle, called the incenter, is the point where the three internal taxicab midsets of the triangle's sides intersect. The radius of the taxicab incircle is the taxicab distance from the incenter to any side of the triangle.

Definition 4.2. A taxicab excircle is a taxicab circle located outside a triangle that is tangent to one side of the triangle and to the extensions of the other two sides. Its center, named as the excenter, is determined by the intersection of one internal taxicab midset and two external taxicab midsets. The radius of the taxicab excircle is the taxicab distance from the excenter to the side and the extended line of the triangle.

A line can be tangent to a taxicab circle in two cases: the line is *tangent at a vertex* to the circle, or the line is *tangent along a side* to the circle, (Ekmekçi,2001:19) (Ekmekçi,2024:144-158). Therefore, a taxicab circle that is tangent to all sides of a triangle can be as follows:

i) If each side of a triangle (or the extended line of the side) is tangent at vertex to the taxicab circle, then the circle is said to be *tangent at vertex* to the triangle, (Fig. 1)

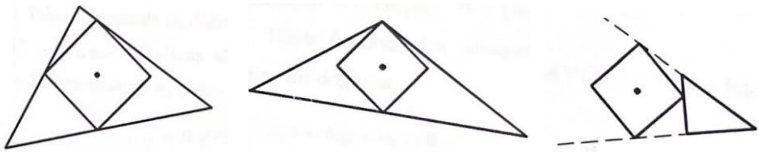

Figure 1

ii) If at least one side (or the extended line of the side) of a triangle (or the extended line of the side) is tangent along side to the taxicab circle and the remaining side(s) are tangent at vertex to it, then the taxicab circle is said to be both *tangent along side and tangent at vertex* to the triangle, , (Fig. 2)

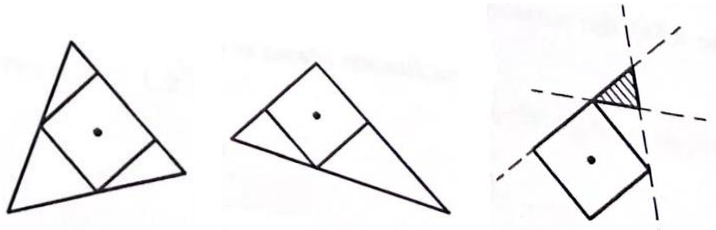

Figure 2

Theorem 4.3. Let all sides of a triangle in the taxicab plane lie on gradual lines. Then there are three taxicab circles tangent at vertex to the triangle. One of these is the taxicab incircle, while the other two are taxicab excircles.

Proof. Suppose that ABC is a triangle in taxicab plane. Let the extended lines of the sides *AB, AC, BC* of the triangle *ABC* be denoted by l_1, l_2, l_3 respectively where the line l_i has the equation $a_i x + b_i y + c_i = 0$, $i = 1,2,3$. Since l_1, l_2 and l_3 are the gradual lines, the absolute values of the slopes of the lines l_i are less than 1. Also, since they are neither concurrent nor parallel, the determinant

$$\begin{vmatrix} a_1 & b_1 & c_1 \\ a_2 & b_2 & c_2 \\ a_3 & b_3 & c_3 \end{vmatrix} \tag{4.1}$$

is nonzero. The taxicab midset of lines l_1 and l_2 are the line

$$(m_1 - m_2)x = k_2 - k_1 \tag{4.2}$$

and the line $l_2^{'}$

$$\frac{1}{2}(m_1 + m_2)x + y + \frac{1}{2}(k_1 + k_2) = 0 \tag{4.3}$$

where $\frac{c_i}{b_i} = k_i$, $\frac{a_i}{b_i} = m_i$ and $b_i \neq 0$, $i = 1,2,3$. Similarly, the taxicab midset of lines l_1 and l_3 are the line $l_3^{'}$

$$(m_1 - m_3)x = k_3 - k_1 \tag{4.4}$$

and the line $l_4^{'}$

$$\frac{1}{2}(m_1 + m_3)x + y + \frac{1}{2}(k_1 + k_3) = 0 \cdot \tag{4.5}$$

And, the taxicab midset of lines l_2 and l_3 occurs the line $l_5^{'}$

$$(m_2 - m_3)x = k_3 - k_2 \tag{4.6}$$

and the line $l_6^{'}$

$$\frac{1}{2}(m_2+m_3)x+y+\frac{1}{2}(k_2+k_3)=0. \tag{4.7}$$

The determinant in (1) is written as follows

$$\Delta=\begin{vmatrix} m_1 & 1 & k_1 \\ m_2 & 1 & k_2 \\ m_3 & 1 & k_3 \end{vmatrix}\neq 0.$$

Since translations preserve the taxicab distance, placing the vertex *A* of the triangle at the origin will not affect the generality and will facilitate our analysis.

It is assumed that the side *AB* of the triangle lies in the first quadrant and the side *AC* lies in the second quadrant. Then, the lines $l_1^{'}$, $l_4^{'}$ and $l_6^{'}$ are the three internal taxicab midsets of the sides in the triangle *ABC*. The incenter which is the intersection point of these lines is

$$M_1=(\frac{k_2-k_1}{m_1-m_2},\frac{k_1(m_2+m_3)-k_2(m_1+m_3)+k_3(-m_1+m_2)}{2(m_1-m_2)}). \tag{4.8}$$

The taxicab distances from point M_1 to lines l_1, l_2 and l_3 are equal and this distance is

$$r_1=\left|\frac{k_1(m_3-m_2)+k_2(m_1-m_3)+k_3(-m_1+m_2)}{2(m_1-m_2)}\right|=\left|\frac{\Delta}{2(m_1-m_2)}\right|. \tag{4.9}$$

Thus, the points on the taxicab incircle C_1 with the incenter M_1 and the radius r_1 satisfy the equation

$$\left|x-\frac{k_2-k_1}{m_1-m_2}\right|+\left|y-\frac{k_1(m_2+m_3)-k_2(m_1+m_3)+k_3(-m_1+m_2)}{2(m_1-m_2)}\right|=r_1. \tag{4.10}$$

It is immediately seen that the vertices of the taxicab circle C_1 are A_1, A_2, A_3 and A_4 as follows:

$$A_1=\left(\frac{k_1(m_3-m_2-2)+k_2(m_1-m_3+2)+k_3(-m_1+m_2)}{2(m_1-m_2)},\frac{k_1(m_3+m_2)+k_2(-m_1-m_3)+k_3(-m_1+m_2)}{2(m_1-m_2)}\right),$$

$$A_2=\left(\frac{k_2-k_1}{m_1-m_2},m_3\frac{k_1-k_2}{m_1-m_2}-k_3\right),$$

$$A_3=\left(\frac{k_1(-m_3+m_2-2)+k_2(-m_1+m_3+2)+k_3(m_1-m_2)}{2(m_1-m_2)},\frac{k_1(m_3+m_2)+k_2(-m_1-m_3)+k_3(-m_1+m_2)}{2(m_1-m_2)}\right),$$

$$A_4=\left(\frac{k_2-k_1}{m_1-m_2},\frac{k_1m_2-k_2m_1}{m_1-m_2}\right).$$

Upon substituting the values of k_i and m_i in the points, it becomes evident that point A_4 is equivalent to the point *A*. Consequently, at the point *A*, the taxicab incircle C_1 is tangent at the vertex to the triangle's sides *AB* and *AC*. Additionally, the triangle's side *BC* contains only the circle's vertex A_2, and

at the point A_2, C_1 is tangent at vertex to the side *BC*. Since the sides of the triangle are on gradual lines, C_1 is inside the triangle and is the incircle of the triangle *ABC*.

The lines $l_2^{'}$ and $l_3^{'}$ are the external taxicab midset of the triangle, while the line $l_6^{'}$ is the internal taxicab midset. The excenter which is the intersection point of these lines is

$$M_2 = (\frac{k_3 - k_1}{m_1 - m_3}, \frac{k_1(m_2 + m_3) + k_2(m_3 - m_1) - k_3(m_1 + m_2)}{2(m_1 - m_3)}). \quad (4.11)$$

The taxicab distances from point M_2 to lines l_1, l_2 and l_3 are equal and this distance is

$$r_2 = \left| \frac{\Delta}{2(m_1 - m_3)} \right|. \quad (4.12)$$

Thus, the points on the taxicab excircle C_2 with the excenter M_2 and the radius r_2 satisfy the equation

$$\left| x - \frac{k_3 - k_1}{m_1 - m_3} \right| + \left| y - \frac{k_1(m_2 + m_3) + k_2(m_3 - m_1) - k_3(m_1 + m_2)}{2(m_1 - m_3)} \right| = r_2. \quad (4.13)$$

It is immediately seen that the vertices of the taxicab excircle C_2 are as follows:

$$A_1 = \left(\frac{k_1(m_3 - m_2 - 2) + k_2(m_1 - m_3) + k_3(-m_1 + m_2 + 2)}{2(m_1 - m_3)}, \frac{k_1(m_3 + m_2) + k_2(-m_1 + m_3) + k_3(-m_1 - m_2)}{2(m_1 - m_3)} \right),$$

$$A_2 = \left(\frac{k_3 - k_1}{m_1 - m_3}, \frac{k_1 m_3 - k_3 m_1}{m_1 - m_3} \right),$$

$$A_3 = \left(\frac{k_1(-m_3 + m_2 - 2) + k_2(-m_1 + m_3) + k_3(m_1 - m_2 + 2)}{2(m_1 - m_3)}, \frac{k_1(m_3 + m_2) + k_2(-m_1 + m_3) + k_3(-m_1 - m_2)}{2(m_1 - m_3)} \right),$$

$$A_2 = \left(\frac{k_3 - k_1}{m_1 - m_3}, m_3 \frac{k_1 - k_3}{m_1 - m_3} - k_2 \right).$$

It obtained that the point A_2 coincides with the point *B*. Consequently, at the point *B*, the triangle's sides *AB* and *BC* is tangent at the vertex to the taxicab circle C_2. Also, the triangle's side *BC* is tangent at vertex to C_2 at the point A_2. Since the sides of the triangle are on gradual lines, it is not possible for C_2 to intersect the triangle at any point other than these points. C_2 is the excircle of the triangle *ABC*.

The lines $l_2^{'}$ and $l_5^{'}$ are the external taxicab midset of the triangle, while the line $l_4^{'}$ is the internal taxicab midset. Other excenter which is the intersection point of these lines is

$$M_3=(\frac{k_3-k_2}{m_2-m_3},\frac{k_1(-m_2+m_3)+k_2(m_3+m_1)-k_3(m_1+m_2)}{2(m_2-m_3)})\cdot \qquad (4.14)$$

The taxicab distances from point M_3 to lines l_1, l_2 and l_3 are equal and this distance is

$$r_3=\left|\frac{\Delta}{2(m_2-m_3)}\right|\cdot \qquad (4.15)$$

Thus, the the taxicab excircle C_3 with the excenter M_3 and the radius r_3 is

$$\left|x-\frac{k_3-k_2}{m_2-m_3}\right|+\left|y-\frac{k_1(-m_2+m_3)+k_2(m_3+m_1)-k_3(m_1+m_2)}{2(m_2-m_3)}\right|=r_3\cdot \qquad (4.16)$$

It is immediately seen that the vertices of the taxicab excircle C_3 are as follows:

$$A_1=\left(\frac{k_1(-m_3+m_2)+k_2(-m_1+m_3-2)+k_3(m_1-m_2+2)}{2(m_2-m_3)},\frac{k_1(m_3-m_2)+k_2(m_1+m_3)+k_3(-m_1-m_2)}{2(m_2-m_3)}\right),$$

$$A_2=\left(\frac{k_3-k_2}{m_2-m_3},\frac{k_2m_3-k_3m_2}{m_2-m_3}\right),$$

$$A_3=\left(\frac{k_1(m_3-m_2)+k_2(m_1-m_3-2)+k_3(-m_1+m_2+2)}{2(m_2-m_3)},\frac{k_1(m_3-m_2)+k_2(m_1+m_3)+k_3(-m_1-m_2)}{2(m_2-m_3)}\right),$$

$$A_4=\left(\frac{k_3-k_2}{m_2-m_3},m_1\frac{k_2-k_3}{m_2-m_3}-k_1\right)\cdot$$

It obtained that the point A_2 coincides with the point *C*. Consequently, at the point *C*, the triangle's sides *AC* and *BC* is tangent at the vertex to the taxicab circle C_3. Also, the triangle's side *AB* is tangent at vertex to C_3 at the point A_4. Since the sides of the triangle are on gradual lines, it is not possible for C_3 to intersect the triangle at any point other than these points. and is the taxicab excircle of the triangle *ABC*, (Fig.3).

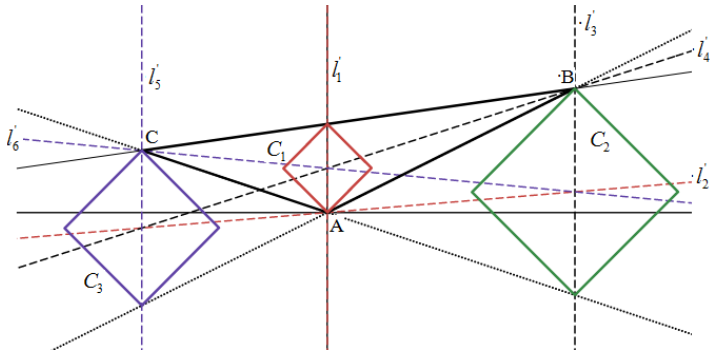

Figure 3

Since the position of the taxicab midsets formed by the sides of the triangle will be the same when the slope of the side *BC* is positive or negative, the incircle and excircles of the triangle do not change for this case.

Now, it is assumed that all sides of the triangle lies in the first quadrant. Let the slope of the side *AC* be greater than the slope of the side *AB*. If the slope of the side *BC* is negative, the lines $l_2^{'}$, $l_4^{'}$ and $l_5^{'}$ are the internal taxicab midset of the triangle and the taxicab circle C_3 in (4.16) is the taxicab incircle of the triangle. The triangle is tangent at vertex to C_3. Also, the circle C_1 in (4.10) and the circle C_2 in (4.13) are the excircles of the triangle *ABC*.

If the slope of the side *BC* is positive, the lines $l_2^{'}$, $l_3^{'}$ and $l_6^{'}$ are the internal taxicab midset of the triangle and the taxicab circle C_2 in (4.13) is the taxicab incircle of the triangle. The triangle is tangent at vertex to C_2. Also, the circle C_1 in (4.10) and the circle C_3 in (4.16) are the excircles of the triangle *ABC*.

Let the slope of the side *AB* be greater than the slope of the side *AC*. If the slope of the side *BC* is negative, the lines $l_2^{'}$, $l_3^{'}$ and $l_6^{'}$ are the internal taxicab midset of the triangle and the taxicab circle C_2 in (13) is the taxicab incircle of the triangle. The other two circles are the taxicab excircles of the triangle. If the slope of the side *BC* is positive, the lines $l_2^{'}$, $l_4^{'}$ and $l_5^{'}$ are the internal taxicab midset of the triangle. The taxicab circle C_3 in (16) is the taxicab incircle of the triangle while C_1 and C_2 are the taxicab excircles of *ABC*, (Fig.4).

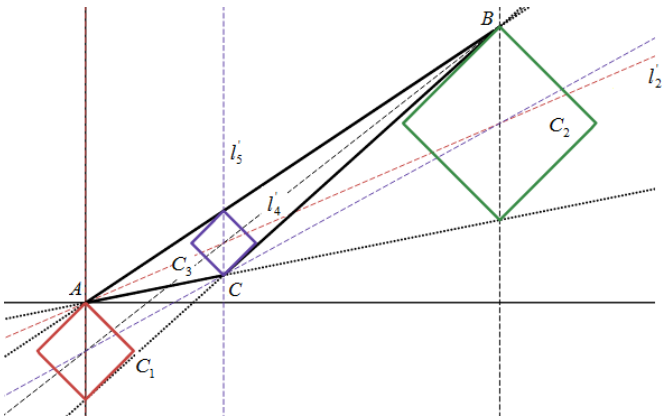

Figure 4

In the case that the sides *AB* and *AC* are in the first and third regions respectively, the lines $l_1^{'}$, $l_4^{'}$ and $l_6^{'}$ are the internal taxicab midsets. Therefore, for triangle *ABC*, C_1 is the taxicab incircle, while C_2 and C_3 are the taxicab excircles.

In the case that the sides *AB* and *AC* are in the first and fourth regions, respectively, the positions of the taxicab midsets change depending on whether the slope of the side *BC* is positive or negative. If the slope of the side *BC* is negative, the taxicab circle C_2 in (4.13) is the taxicab incircle of the triangle and ,the circle C_1 in (4.10) and the circle C_3 in (4.16) are the excircles of the triangle *ABC*. The taxicab circle C_2 in (4.13) is the triangle's taxicab incircle if the side *BC* slope is negative, and the triangle *ABC*'s taxicab excircles are the circles C_1 in (4.10) and C_3 in (4.16). If the side *BC* has a positive slope, the taxicab circle C_3 in (4.16) is the triangle's taxicab incircle, and the triangle ABC's taxicab excircles are the circles C_1 in (4.10) and C_2 in (4.13).

Thus, when all the sides of the triangle lie on gradual lines, the triangle has one taxicab incircle and two taxicab excircles.

Theorem 4.4. Let all sides of a triangle in the taxicab plane lie on steep lines. Then there are three taxicab circles tangent at vertex to the triangle. One of these is the taxicab incircle, while the other two are taxicab excircles.

Proof. Suppose that ABC is a triangle in taxicab plane. Let the extended lines of the sides *AB, AC, BC* of the triangle *ABC* be denoted by l_1, l_2, l_3 respectively where the line l_i has the equation $a_i x + b_i y + c_i = 0$, $i = 1,2,3$. Since l_1, l_2 and l_3 are the steep lines, the absolute values of the slopes of the lines l_i are greater than 1. Also, since they are neither concurrent nor parallel, the determinant in (4.1) is nonzero.

The taxicab midset of the lines l_1 and l_2 consists of the line $l_1^{'}$ with the equation

$$l_1^{'} : (m_1 - m_2) y = k_2 - k_1 \tag{4.17}$$

and the line $l_2^{'}$ with the equation

$$l_2^{'} : x + \frac{1}{2}(m_1 + m_2) y + \frac{1}{2}(k_1 + k_2) = 0 \tag{4.18}$$

where $\frac{c_i}{a_i} = k_i$, $\frac{b_i}{a_i} = m_i$ and $a_i \neq 0$, $i = 1,2,3$. Similarly, the taxicab midset of lines l_1 and l_3 consists of the line $l_3^{'}$ with the equation

$$(m_1 - m_3)y = k_3 - k_1 \tag{4.19}$$

and the line $l_4^{'}$ with the equation

$$x + \frac{1}{2}(m_1 + m_3)y + \frac{1}{2}(k_1 + k_3) = 0 \cdot \tag{4.20}$$

And, the taxicab midset of the lines l_2 and l_3 occurs the line $l_5^{'}$ with the equation

$$(m_2 - m_3)y = k_3 - k_2 \tag{4.21}$$

and the line $l_6^{'}$ with the equation

$$x + \frac{1}{2}(m_2 + m_3)y + \frac{1}{2}(k_2 + k_3) = 0 \cdot \tag{4.22}$$

The determinant in (1) is written as follows

$$\Delta = \begin{vmatrix} 1 & m_1 & k_1 \\ 1 & m_2 & k_2 \\ 1 & m_3 & k_3 \end{vmatrix} \neq 0 \cdot$$

As in Theorem 4.3, the situations will be examined by taking the vertex *A* of triangle as the origin. The triangle's side *AB* is thought to be in the first quadrant, while the side *AC* is thought to be in the third. The three internal taxicab midsets of the sides in the triangle *ABC* are therefore the lines $l_1^{'}$, $l_4^{'}$ and $l_6^{'}$. They intersect at the incenter

$$M_1 = (\frac{k_1(m_2 + m_3) - k_2(m_1 + m_3) + k_3(-m_1 + m_2)}{2(m_1 - m_2)}, \frac{k_2 - k_1}{m_1 - m_2}) . \tag{4.23}$$

From the point M_1 to the lines l_1, l_2 and l_3, the taxicab distances equal r_1 in (4.9). The equation

$$\left| x - \frac{k_1(m_2 + m_3) - k_2(m_1 + m_3) + k_3(-m_1 + m_2)}{2(m_1 - m_2)} \right| + \left| y - \frac{k_2 - k_1}{m_1 - m_2} \right| = r_1 \tag{4.24}$$

is thus satisfied by the points on the taxicab incircle C_1 with the center M_1 and the radius r_1. Similar to Theorem 4.3, the vertices of taxicab circle C_1 are simply obtained. The sides *AB* and *AC* of the triangle are tangent at the vertex *A* to the taxicab circle C_1. The side *BC* is also tangent to C_1 at the antipodal vertex of the point *A* where the coordinates of the antipodal point

are $\left(m_3 \frac{k_1 - k_2}{m_1 - m_2} - k_3, \frac{k_2 - k_1}{m_1 - m_2} \right)$. The sides of the taxicab circle C_1 lie on the separator lines passing through the point *A* and its antipodal point. Since all sides of the triangle are steep lines, it is not possible for C_1 to intersect the triangle at any point other than these points and C_1 is the taxicab incircle of the triangle *ABC*, (Fig. 5).

The triangle's external taxicab midsets are the lines $l_2^{'}$ and $l_3^{'}$, while the internal taxicab midset is line $l_6^{'}$. An excenter which is the intersection point of these lines is

$$M_2 = (\frac{k_1(m_2 + m_3) + k_2(m_3 - m_1) - k_3(m_1 + m_2)}{2(m_1 - m_3)}, \frac{k_3 - k_1}{m_1 - m_3}) . \qquad (4.25)$$

The taxicab distances from point M_2 to the sides of the triangle are equal to r_2 found in (4.12). Thus, the points on the taxicab circle C_2 with the center M_2 and the radius r_2 satisfy the equation

$$\left| x - \frac{k_1(m_2 + m_3) + k_2(m_3 - m_1) - k_3(m_1 + m_2)}{2(m_1 - m_3)} \right| + \left| y - \frac{k_3 - k_1}{m_1 - m_3} \right| = r_2 . \qquad (4.26)$$

The sides *AB* and *BC* of the triangle are tangent at vertex to the taxicab circle C_2 at point *B*. The extended line of side *AC* is also tangent to C_2 at the antipodal point of *B* where the coordinates of the antipodal point are $\left(m_2 \frac{k_1 - k_3}{m_1 - m_3} - k_2, \frac{k_3 - k_1}{m_1 - m_3} \right)$. Since the sides of C_2 lie on the separator lines passing through the point *B* and its antipodal point, the three steep lines containing the triangle's sides do not intersect C_2 at any point other than *B* and its antipodal. Thus, C_2 is a taxicab excircle of triangle *ABC*, (Fig. 5).

The external taxicab midsets $l_2^{'}$ and $l_5^{'}$ and the internal taxicab midset $l_4^{'}$ is concurrent at the point

$$M_3 = (\frac{k_1(-m_2 + m_3) + k_2(m_3 + m_1) - k_3(m_1 + m_2)}{2(m_2 - m_3)}, \frac{k_3 - k_2}{m_2 - m_3}) . \qquad (4.27)$$

The taxicab distances from the excenter M_3 to the sides of the triangle are equal to r_3 found in (4.15). And, the taxicab excircle C_3 with the excenter M_3 and the radius r_3 has the equation

$$\left|x-\frac{k_1(-m_2+m_3)+k_2(m_3+m_1)-k_3(m_1+m_2)}{2(m_2-m_3)}\right|+\left|y-\frac{k_3-k_2}{m_2-m_3}\right|=r_3. \qquad (4.28)$$

The sides *AC* and *BC* of the triangle are tangent at vertex to the taxicab circle C_3 at the point *C*. The extended line of side *AB* is also tangent to C_3 at the antipodal point of *C* where the antipodal point is $\left(m_1\frac{k_3-k_2}{m_3-m_2}-k_1,\frac{k_3-k_2}{m_2-m_3}\right)$. Since the sides of C_3 lie on the separator lines passing through the point *C* and its antipodal point, the three steep lines containing the triangle's sides cannot intersect C_3 at any point other than *C* and its antipodal. And, C_3 is a taxicab excircle of triangle *ABC*, (Fig. 5).

In this case, whether the slope of the side *AB* is greater or less than the slope of the side *AC* will not change the result for this case.

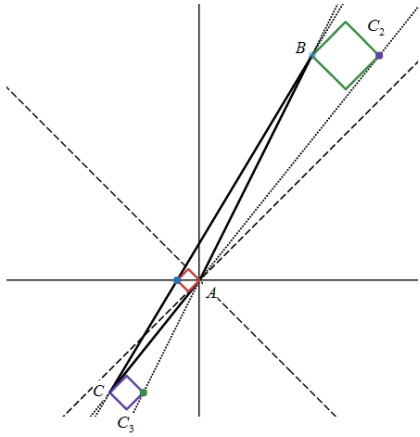

Figure 5

Now suppose that the sides *AB* and *AC* of the triangle are in the first and second quadrants respectively. If the side *BC* has a positive slope, the interior of the triangle is determined by the inequalities $x+m_1y+k_1\le 0$, $x+m_2y+k_2\ge 0$ and $x+m_3y+k_3\ge 0$. Then, the three internal taxicab midsets of the sides in the triangle ABC are the lines $l_2^{'}$, $l_4^{'}$ and $l_5^{'}$. They intersect at the incenter M_3 given in (4.27). The taxicab distances from point M_3 to the sides of the triangle are equal to r_3 in (4.15). The sides *AC* and *BC* of the

triangle are tangent at vertex to the taxicab circle C_3 in (4.28) (with the center M_3 and the radius r_3) at the point *C*. The side *AB* is tangent to C_3 at the antipodal point of *C*. So, C_3 is the taxicab incircle of the triangle *ABC*.

The exterior region containing the side *BC* is determined by the inequalities $x+m_1y+k_1 \le 0$, $x+m_2y+k_2 \ge 0$ and $x+m_3y+k_3 \le 0$. Then, the internal taxicab midset $l_6^{'}$ and the external taxicab midsets $l_2^{'}$ and $l_3^{'}$ in this region intersect at the excenter M_2 obtained in (4.25) and $d_T(M_2,l_1)=d_T(M_2,l_2)=d_T(M_2,l_3)=r_2$ where the value r_2 is as found in (4.12). The sides *AB* and *BC* are tangent at vertex to the taxicab circle C_2 in (4.26) (with the center M_2 and the radius r_2) at the point *B*. The line l_2 (the extended of the side *AC*) is tangent to C_2 at the antipodal point of *B* where the antipodal point is $\left(m_2\frac{k_1-k_3}{m_1-m_3}-k_2,\frac{k_3-k_1}{m_1-m_3}\right)$. So, C_2 is the taxicab excircle of the triangle *ABC*.

The another exterior region containing the side *AC* is determined by the inequalities $x+m_1y+k_1 \le 0$, $x+m_2y+k_2 \le 0$ and $x+m_3y+k_3 \ge 0$. Then, the internal taxicab midset $l_4^{'}$ and the external taxicab midsets $l_1^{'}$ and $l_6^{'}$ in this region intersect at the excenter M_1 obtained in (4.24) and $d_T(M_1,l_1)=d_T(M_1,l_2)=d_T(M_1,l_3)=r_1$ where the value r_1 is as found in (4.9). The sides *AC* and *AB*, and the line l_3 are respectively tangent at vertex to C_1 (with the center M_1 and the radius r_1 in (24)) at the points *A* and antipodal of *A* where the antipodal point is $\left(m_3\frac{k_1-k_2}{m_1-m_2}-k_3,\frac{k_2-k_1}{m_1-m_2}\right)$. Since all sides of C_1 are on the separator lines passing through the points *A* and antipodal of *A*, C_1 cannot intersect the lines l_1, l_2 and l_3 at any point other than these two points. Accordingly, C_1 is the triangle *ABC*'s taxicab excircle. The last exterior region containing the side *AB* is determined by the inequalities $x+m_1y+k_1 \ge 0$, $x+m_2y+k_2 \ge 0$ and $x+m_3y+k_3 \ge 0$. The taxicab midsets in

this region are the lines $l_1^{'}, l_3^{'}$ and $l_5^{'}$ such that $l_5^{'}$ is the internal midset and the others are the external midsets. In this region, there isn't a taxicab excircle since the lines $l_1^{'}, l_3^{'}$ and $l_5^{'}$ are parallel.

If the slope of the side *BC* is negative, the interior of the triangle is determined by the inequalities $x + m_1 y + k_1 \le 0$, $x + m_2 y + k_2 \ge 0$ and $x + m_3 y + k_3 \le 0$. Then the internal taxicab midsets are the the lines $l_2^{'}, l_3^{'}$ and $l_6^{'}$ while the external taxicab midsets are the lines $l_1^{'}, l_4^{'}$ and $l_5^{'}$. Three internal taxicab midsets intersect at the incenter M_2 in the interior of the triangle and $d_T(M_2, l_1) = d_T(M_2, l_2) = d_T(M_2, l_3) = r_2$. The taxicab incircle C_2 with the center M_2 and the radius r_2 has the equation in (4.26). While the sides *AB* and *BC* are tangent to taxicab circle C_2 at the point *B*, the side *AC* is tangent to it at the antipodal point of *B*. Since the taxicab midsets $l_1^{'}, l_3^{'}$ and $l_5^{'}$ in the exterior region that includes the side *AC* and the extended lines l_1 and l_3 are parallel, they don't meet. Therefore, a taxicab excircle does not occur in this region. The taxicab midsets $l_1^{'}, l_4^{'}$ and $l_6^{'}$ in the exterior region containing the side *AB* intersect at the point M_1 and $d_T(M_1, l_1) = d_T(M_1, l_2) = d_T(M_1, l_3) = r_1$. The taxicab excircle C_1 with the center M_1 and the radius r_1 has the equation in (4.24). While the sides *AB* and *AC* are tangent to taxicab circle C_1 at the point *A*, the side *BC* is tangent to it at the antipodal point of *A*. The taxicab midsets $l_1^{'}, l_4^{'}$ and $l_6^{'}$ in the exterior region containing the side *BC* intersect at the point M_3 and $d_T(M_3, l_1) = d_T(M_3, l_2) = d_T(M_3, l_3) = r_3$. The taxicab excircle C_3 with the center M_3 and the radius r_3 has the equation in (4.28). While the sides *BC* and *AC* are tangent to taxicab excircle C_3 at the point *C*, the side *AB* is tangent to it at the antipodal point of *C*.

When similar analyses are conducted based on the positions of the triangle's sides, in the following cases, the taxicab circle C_2 obtained in (4.26) is the

taxicab incircle of the given triangle *ABC*, while the taxicab circles C_1 and C_3 found in (4.24) and (4.28) are its taxicab excircles:

- When the sides *AB* and *AC* are in the first quadrant such that the slope of the side *AC* is greater than the slope of the side *AB*, with the slope of *BC* being negative.
- When the sides *AB* and *AC* are in the first quadrant such that the slope of the side *AB* is greater than the slope of the side *AC*, with the slope of *BC* being positive.
- When the sides *AB* and *AC* are respectively in the first and second quadrants such that the slope of side *BC* is negative.
- When the sides *AB* and *AC* are respectively in the third and fourth quadrants such that the slope of side *BC* is negative.

In the following cases, the taxicab circle C_1 obtained in (4.24) is the taxicab incircle of the given triangle *ABC*, while the taxicab circles C_2 and C_3 found in (4.26) and (4.28) are its taxicab excircles:

- When the sides *AB* and *AC* are respectively in the first and second quadrants,
- When the sides *AB* and *AC* are respectively in the first and fourth quadrants,
- When the sides *AB* and *AC* are respectively in the second and third quadrants.
- When the sides *AB* and *AC* are respectively in the second and fourth quadrants.

In the following cases, the taxicab circle C_3 obtained in (4.28) is the taxicab incircle of the given triangle *ABC*, while the taxicab circles C_1 and C_2 found in (4.24) and (4.26) are its taxicab excircles:

- When the sides *AB* and *AC* are in the first quadrant such that the slope of the side *AC* is greater than the slope of the side *AB*, with the slope of *BC* being positive.
- When the sides *AB* and *AC* are in the first quadrant such that the slope of the side *AB* is greater than the slope of the side *AC*, with the slope of *BC* being negative.

- When the sides *AB* and *AC* are respectively in the first and second quadrants such that the slope of side *BC* is positive.
- When the sides *AB* and *AC* are respectively in the third and fourth quadrants such that the slope of side *BC* is positive.

Theorem 4.5. Let two sides of a triangle in the taxicab plane lie on gradual lines and the other side be on the steep line. Then there are four taxicab circles tangent at vertex to the triangle. One of these is the taxicab incircle, and the other are taxicab excircles.

Proof. Suppose that *ABC* is a triangle in taxicab plane. Let the extended lines of the sides *AB, AC, BC* of the triangle *ABC* be denoted by l_1, l_2, l_3 respectively where the line l_i has the equation $a_i x + b_i y + c_i = 0$, $i = 1,2,3$.

Assume that the sides *AB* and *AC* are on gradual lines, and the side *BC* is on a steep line. Then, while the absolute values of the slopes of lines l_1 and l_2 are less than 1, the slope of line l_3 is greater than 1 in absolute value. Also, since they are neither concurrent nor parallel, the determinant in (4.1) is nonzero. The taxicab midsets of the lines l_1 and l_2 are the lines l_1' and l_2' obtained in (4.2) and (4.3), respectively. The taxicab midset of lines l_1 and l_3 consists of the line l_3' with the equation

$$(1-m_1)x + (m_3' - 1)y + (k_3' - k_1) = 0 \tag{4.29}$$

where $\frac{c_3}{a_3} = k_3'$, $\frac{b_3}{a_3} = m_3'$, $a_3 \neq 0$, $\frac{c_i}{b_i} = k_i$, $\frac{a_i}{b_i} = m_i$, $b_i \neq 0$, $i = 1,2$ and the line l_4' with the equation

$$(1+m_1)x + (m_3' + 1)y + (k_3' + k_1) = 0. \tag{4.30}$$

And, the taxicab midset of the lines l_2 and l_3 occurs the line l_5' with the equation

$$(1-m_2)x + (m_3' - 1)y + (k_3' - k_2) = 0 \tag{4.31}$$

and the line l_6' with the equation

$$(1+m_2)x + (m_3' + 1)y + (k_3' + k_2) = 0. \tag{4.32}$$

Since $b_1 \neq 0$, $b_2 \neq 0$, and $a_3 \neq 0$, it follows from the determinant in (1) that

$$\Delta = \begin{vmatrix} m_1 & 1 & k_1 \\ m_2 & 1 & k_2 \\ 1 & m_3' & k_3' \end{vmatrix} \neq 0.$$

As in Theorem 4.3 and Theorem 4.4, the cases will be examined by taking the vertex *A* of triangle as the origin. It is assumed that all sides of the triangle are in the first quadrant. If the side *BC* has a positive slope, the interior of the triangle is determined by the inequalities $m_1x + y + k_1 \leq 0$, $m_2x + y + k_2 \geq 0$ and $x + m_3'y + k_3' \leq 0$. Then, while three internal taxicab midsets of the triangle *ABC* are the lines l_2', l_3' and l_6', its external taxicab midsets are the lines l_1', l_4' and l_5'. Three internal taxicab midsets are concurrent and intersect at the point

$$M_1 = \left(\frac{k_1(1+m_3') + k_2(-1+m_3') - 2k_3'}{2(1-m_1) + (m_1+m_2)(1-m_3')}, \frac{k_1(-1-m_2) + k_2(-1+m_1) + k_3'(m_1+m_2)}{2(1-m_1) + (m_1+m_2)(1-m_3')} \right). \quad (4.33)$$

The taxicab distances from the incenter M_1 to the sides of the triangle are equal and this distance is

$$r_1 = \left| \frac{\Delta}{2(1-m_1) + (m_1+m_2)(1-m_3')} \right| \quad (4.34)$$

where $\Delta = k_1(-1+m_2m_3') + k_2(1-m_1m_3') + k_3'(m_1-m_2).$

Thus, the taxicab incircle C_1 with the incenter M_1 and the radius r_1 is

$$|x-c_1| + |y-c_2| = r_1 \quad (4.35)$$

where

$$c_1 = \frac{k_1(1+m_3') + k_2(-1+m_3') - 2k_3'}{2(1-m_1) + (m_1+m_2)(1-m_3')}$$

and

$$c_2 = \frac{k_1(-1-m_2) + k_2(-1+m_1) + k_3'(m_1+m_2)}{2(1-m_1) + (m_1+m_2)(1-m_3')}.$$

The sides *AB*, *AC*, and *BC* of the triangle are tangent to the C_1 taxicab circle at the vertices $(c_1, c_2 + r_1)$, $(c_1, c_2 - r_1)$, and $(c_1 + r_1, c_2)$, respectively, such that $(c_1, c_2 + r_1)$ and $(c_1, c_2 - r_1)$ are antipodal points. Since all sides of C_1 are on the separator lines passing through the points $(c_1, c_2 + r_1)$ and

$(c_1, c_2 - r_1)$, C_1 can not intersect the triangle at any point other than these three points. So, C_1 is the taxicab incircle of the triangle *ABC*.

The exterior region containing the side *AB* is determined by the inequalities $m_1x + y + k_1 \geq 0$, $m_2x + y + k_2 \geq 0$ and $x + m_3^{'}y + k_3^{'} \leq 0$. The taxicab midsets in this region are the lines $l_1^{'}, l_4^{'}$ and $l_6^{'}$ such that $l_6^{'}$ is the internal midset and the others are the external midsets. These taxicab midsets are concurrent and intersect at the excenter

$$M_2 = \left(\frac{k_2 - k_1}{m_1 - m_2}, \frac{k_1(-1 - m_2) + k_2(1 + m_1) + k_3^{'}(m_1 - m_2)}{(m_1 - m_2)(1 + m_3^{'})} \right) \tag{4.36}$$

and

$$d_T(M_2, l_1) = d_T(M_2, l_2) = d_T(M_2, l_3) = r_2 = \left| \frac{\Delta}{(m_2 - m_1)(1 + m_3^{'})} \right| \quad \ldots(4.37)$$

Thus, the taxicab excircle C_2 with the excenter M_2 and the radius r_2 is

$$\left| x - \frac{k_2 - k_1}{m_1 - m_2} \right| + \left| y - \frac{k_1(-1 - m_2) + k_2(1 + m_1) + k_3^{'}(m_1 - m_2)}{(m_1 - m_2)(1 + m_3^{'})} \right| = r_2. \tag{4.38}$$

While the sides *AB* and *AC* of the triangle are tangent to the taxicab circle C_2 at the point $(\frac{k_2 - k_1}{m_1 - m_2}, \frac{k_1(-1 - m_2) + k_2(1 + m_1) + k_3^{'}(m_1 - m_2)}{(m_1 - m_2)(1 + m_3^{'})} - r_2) = A$, and the extended lines l_3 of the side *BC* is tangent to it at the vertex $(\frac{k_2 - k_1}{m_1 - m_2} + r_2, \frac{k_1(-1 - m_2) + k_2(1 + m_1) + k_3^{'}(m_1 - m_2)}{(m_1 - m_2)(1 + m_3^{'})})$. C_2 does not meet the triangle at any other point than these two point because all of its sides are on the separator lines. As a result, one of the taxicab excircles of the triangle *ABC* is C_2.

The another exterior region containing the side *AC* is determined by the inequalities $m_1x + y + k_1 \leq 0$, $m_2x + y + k_2 \leq 0$ and $x + m_3^{'}y + k_3^{'} \leq 0$. Then, the internal taxicab midset $l_3^{'}$ and the external taxicab midsets $l_1^{'}$ and $l_5^{'}$ in this region intersect at the excenter

$$M_3 = \left(\frac{k_2 - k_1}{m_1 - m_2}, \frac{k_1(1 - m_2) + k_2(-1 + m_1) + k_3^{'}(-m_1 + m_2)}{(m_1 - m_2)(-1 + m_3^{'})} \right) \tag{4.39}$$

and

$$d_T(M_3, l_1) = d_T(M_3, l_2) = d_T(M_3, l_3) = r_3$$

where the value r_3 is equal to

$$\left| \frac{\Delta}{(m_1 - m_2)(-1 + m_3')} \right|. \tag{4.40}$$

As in the taxicab excircle C_2, the sides *AB* and *AC* are tangent to the excircle C_3 (with the excenter M_3 and the radius r_3) at point *A*, while the extended line l_3 is tangent to the point $\left(\frac{k_2 - k_1}{m_1 - m_2} + r_3, \frac{k_1(1 - m_2) + k_2(-1 + m_1) + k_3'(-m_1 + m_2)}{(m_1 - m_2)(-1 + m_3')} \right)$. Thus C_3 is another one of the taxicab excircles of the triangle *ABC*.

The exterior region containing the side *BC* is determined by the inequalities $m_1 x + y + k_1 \le 0$, $m_2 x + y + k_2 \ge 0$ and $x + m_3' y + k_3' \ge 0$. Then, the internal taxicab midset l_2' and the external taxicab midsets l_4' and l_5' in this region intersect at the excenter

$$M_4 = \left(\frac{k_1(-1 + m_3') + k_2(1 + m_3') - 2k_3'}{2(1 + m_1) - (m_1 + m_2)(1 + m_3')}, \frac{k_1(-1 + m_2) + k_2(-1 - m_1) + k_3'(m_1 + m_2)}{2(1 + m_1) - (m_1 + m_2)(1 + m_3')} \right) \tag{4.41}$$

and

$$d_T(M_4, l_1) = d_T(M_4, l_2) = d_T(M_4, l_3) = r_4$$

where the value r_4 is equal to

$$\left| \frac{\Delta}{2(1 + m_1) - (m_1 + m_2)(1 + m_3')} \right|. \tag{4.42}$$

The side *BC*, the lines l_1 and l_2 are tangent to the taxicab excircle C_4 with the excenter M_4 and the radius r_4 at the vertices

$$\left(\frac{k_1(-1 + m_3') + k_2(1 + m_3') - 2k_3'}{2(1 + m_1) - (m_1 + m_2)(1 + m_3')} - r_4, \frac{k_1(-1 + m_2) + k_2(-1 - m_1) + k_3'(m_1 + m_2)}{2(1 + m_1) - (m_1 + m_2)(1 + m_3')} \right),$$

$$\left(\frac{k_1(-1 + m_3') + k_2(1 + m_3') - 2k_3'}{2(1 + m_1) - (m_1 + m_2)(1 + m_3')}, \frac{k_1(-1 + m_2) + k_2(-1 - m_1) + k_3'(m_1 + m_2)}{2(1 + m_1) - (m_1 + m_2)(1 + m_3')} + r_4 \right), \quad \text{and}$$

$$\left(\frac{k_1(-1 + m_3') + k_2(1 + m_3') - 2k_3'}{2(1 + m_1) - (m_1 + m_2)(1 + m_3')}, \frac{k_1(-1 + m_2) + k_2(-1 - m_1) + k_3'(m_1 + m_2)}{2(1 + m_1) - (m_1 + m_2)(1 + m_3')} - r_4 \right), \quad \text{respectively.}$$

The triangle can only meet the taxicab excircle C_4 at these vertices because

all sides of C_4 are on the separator lines that go through them. Another taxicab excircle of the triangle *ABC* is therefore C_4. For this case, the fact that the slope of side *BC* on the steep line is negative does not affect the result.

Let the sides *AB* and *AC* on the gradual line be in the first and fourth quadrants, respectively, and let the side *BC* be on the steep line in the triangle *ABC*. The taxicab incircle of the triangle is the taxicab circle C_1, while C_2, C_3, and C_4 are the taxicab excircles in the exterior regions of the triangle including the sides *AB*, *AC*, and *BC*, respectively. The triangle is tangent to the circles C_2 and C_3 at vertex *A*, which is the intersection of the gradual sides.

For the triangle *ABC*, if the side *AB* on the gradual line is in the first quadrant, the side *AC* on the steep line is in the second quadrant, and the side *BC* is on the gradual line. The centers and the radii of the taxicab incircle C_1 and the taxicab excircles C_2, C_3, and C_4 in the triangle can be directly obtained from (33) and (34); (36) and (37); (41) and (42); (39) and (40), respectively, by substituting $m_3^{'}$ and $k_3^{'}$ with $m_2^{'}$ and $k_2^{'}$, and m_2 and k_2 with m_3 and k_3.

For other cases, the results can be immediately obtained using the isometry group of the taxicab plane.

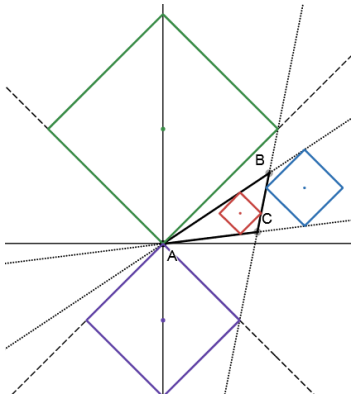

Figure 6

Theorem 4.6. Let two sides of a triangle in the taxicab plane lie on steep lines and the other side be on the gradual. Then there are four taxicab circles

tangent at vertex to the triangle. One of these is the taxicab incircle, and the other are taxicab excircles.

Proof. Suppose that *ABC* is a triangle in taxicab plane. Let the extended lines of the sides *AB, AC, BC* of the triangle *ABC* be denoted by l_1, l_2, l_3 respectively where the line l_i has the equation $a_i x + b_i y + c_i = 0$, $i = 1,2,3$. Assume that the sides *AB* and *AC* are on steep lines, and the side *BC* is on a gradual line. Then, while the absolute values of the slopes of lines l_1 and l_2 are greater than 1, the slope of line l_3 is less than 1 in absolute value. Also, since they are neither concurrent nor parallel, the determinant in (4.1) is nonzero. From (4.17) and (4.18), the taxicab midset of the lines l_1 and l_2 are

$$l_1^{'} : (m_1^{'} - m_2^{'}) y = k_2^{'} - k_1^{'}$$

and the line

$$l_2^{'} : x + \frac{1}{2}(m_1^{'} + m_2^{'}) y + \frac{1}{2}(k_1^{'} + k_2^{'}) = 0$$

where $\frac{c_i}{a_i} = k_i^{'}$, $\frac{b_i}{a_i} = m_i^{'}$ and $a_i \neq 0$, $i = 1,2$.

The taxicab midset of lines l_1 and l_3 are the lines

$$l_3^{'} : (1 - m_3) x + (m_1^{'} - 1) y + (k_1^{'} - k_3) = 0$$

and

$$l_4^{'} : (1 + m_3) x + (m_1^{'} + 1) y + (k_1^{'} + k_3) = 0$$

where $\frac{c_3}{b_3} = k_3$, $\frac{a_3}{b_3} = m_3$ and $b_3 \neq 0$. And, the taxicab midset of the lines l_2 and l_3 are the lines

$$l_5^{'} : (1 - m_3) x + (m_2^{'} - 1) y + (k_2^{'} - k_3) = 0$$

and

$$l_6^{'} : (1 + m_3) x + (m_2^{'} + 1) y + (k_2^{'} + k_3) = 0 .$$

Since $a_1 \neq 0$, $a_2 \neq 0$, and $b_3 \neq 0$, it is obtained from the determinant in (1) that

$$\Delta = \begin{vmatrix} 1 & m_1^{'} & k_1^{'} \\ 1 & m_2^{'} & k_2^{'} \\ m_3 & 1 & k_3 \end{vmatrix} \neq 0 \text{ ..}$$

As in Theorem 4.3, Theorem 4.4 and Theorem 4.5, the cases will be examined by taking the vertex *A* of triangle as the origin. All of the triangle's sides are presumed to be in the first quadrant. If the side *BC* has a positive slope, the interior of the triangle is determined by the inequalities $x+m_1'y+k_1' \le 0$, $x+m_2'y+k_2' \ge 0$ and $m_3x+y+k_3 \ge 0$. Then, while three internal taxicab midsets of the triangle *ABC* are the lines l_2', l_3' and l_6', its external taxicab midsets are the lines l_1', l_4' and l_5'. Three internal taxicab midsets are concurrent and intersect at the incenter

$$M_1 = \left(\frac{k_1'(1+m_2') + k_2'(1+m_1') - k_3(m_1'+m_2')}{2(-1+m_1') + (m_1'+m_2')(-1+m_3)}, \frac{(k_1'+k_2')(1-m_3) + 2(k_3-k_1')}{2(-1+m_1') + (m_1'+m_2')(-1+m_3)} \right).$$

From the point M_1, the taxicab distances to the triangle's sides are equal, and this distance is

$$r_1 = \left| \frac{\Delta}{2(-1+m_1') + (m_1'+m_2')(-1+m_3)} \right|$$

where $\Delta = k_1'(1-m_3m_2') + k_2'(-1+m_3m_1') + k_3(m_2'-m_1').$ The sides *AB*, *AC*, and *BC* of the triangle are tangent at vertex to the taxicab circle C_1 with the center M_1 and the radius r_1, and C_1 is the taxicab incircle of the triangle *ABC*. The internal taxicab midset l_6' and the external taxicab midsets l_1' and l_4' in the exterior region containing the side *AB* intersect at the excenter

$$M_2 = \left(-\frac{k_1'(-1+m_2') + k_2'(1+m_1') + k_3(m_1'-m_2')}{(m_1'-m_2')(1+m_3')}, \frac{k_2'-k_1'}{m_1'-m_2'} \right)$$

and

$$d_T(M_2, l_1) = d_T(M_2, l_2) = d_T(M_2, l_3) = r_2$$

where the value r_2 is

$$\left| \frac{\Delta}{(m_1'-m_2')(1+m_3)} \right|.$$

The side *AB*, the lines l_2 and l_3 are tangent at vertex to the taxicab circle C_2 with the center M_2 and the radius r_2, and C_2 is a taxicab excircle of the triangle *ABC*. The internal taxicab midset l_2' and the external taxicab midsets

$l_4^{'}$ and $l_5^{'}$ in the exterior region containing the side *BC* intersect at the excenter

$$M_3 = \left(\frac{k_1^{'}(-1+m_2^{'}) + k_2^{'}(-1-m_1^{'}) + k_3(m_1^{'}+m_2^{'})}{2(1+m_1^{'}) - (m_1^{'}+m_2^{'})(1+m_3)}, \frac{k_1^{'}(-1+m_3) + k_2^{'}(1+m_3) - 2k_3}{2(1+m_1^{'}) - (m_1^{'}+m_2^{'})(1+m_3)} \right)$$

and

$$d_T(M_3, l_1) = d_T(M_3, l_2) = d_T(M_3, l_3) = r_3$$

where the value r_3 is equal to

$$\left| \frac{\Delta}{2(1+m_1^{'}) - (m_1^{'}+m_2^{'})(1+m_3)} \right|.$$

The side *BC*, the lines l_1 and l_2 are tangent at vertex to the taxicab circle C_3 with the center M_3 and the radius r_3, and C_3 is another taxicab excircle of the triangle *ABC*. The internal taxicab midset $l_2^{'}$ and the external taxicab midsets $l_4^{'}$ and $l_5^{'}$ in the exterior region containing the side *AC* and the extended lines l_1 and l_3 intersect at the excenter

$$M_4 = \left(-\frac{k_1^{'}(-1+m_2^{'}) + k_2^{'}(1-m_1^{'}) + k_3(m_1^{'}-m_2^{'})}{(m_2^{'}-m_1^{'})(1-m_3^{'})}, \frac{k_1^{'}-k_2^{'}}{m_2^{'}-m_1^{'}} \right)$$

and

$$d_T(M_4, l_1) = d_T(M_4, l_2) = d_T(M_4, l_3) = r_4$$

where the value r_4 is equal to

$$\left| \frac{\Delta}{(m_2^{'}-m_1^{'})(1-m_3)} \right|.$$

The side *AC*, the lines l_1 and l_3 are tangent at vertex to the taxicab circle C_4 with the center M_4 and the radius r_4, and C_4 is the last taxicab excircle of the triangle *ABC*.

For other cases, the results can be immediately obtained using the isometry group of the taxicab plane.

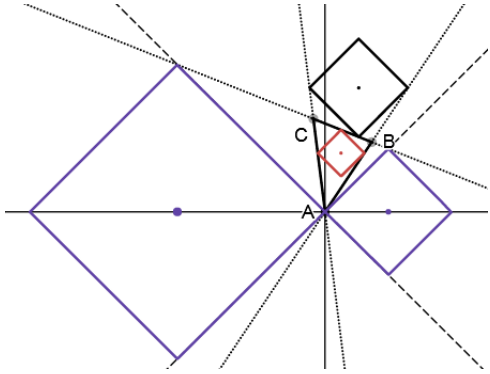

Figure 7

Corollary 4.7. In the taxicab plane, if one of the sides of a triangle lies on a separator line, there are at least three and at most four taxicab circles tangent to the triangle. These taxicab circles are tangent along a side to the side on the separator line, while being tangent at vertex to the other sides.

Corollary 4.8. In the taxicab plane, if two of the sides of a triangle lies on the separator lines, there are three taxicab circles tangent to the triangle. These taxicab circles are tangent along a side to the sides on the separator line, while being tangent at vertex to the other, (Fig.8).

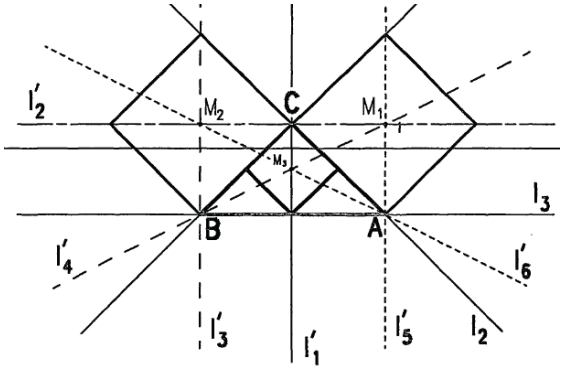

Figure 8

REFERENCES

Akça, Z. and Çalış, C. (2021). Voronoi diyagramı ve Taksi düzlemi üzerine. Erzincan Üniversitesi Fen Bilimleri Enstitüsü Dergisi, 14(1), 175–181.

Akça, Z. and Kaya, R. (2004). On the distance formulae in three dimensional taxicab space. Hadronic J., 27(5), 521–532.

Akça, Z. and Kaya, R. (1997). On the taxicab trigonometry. J. of Inst. Math. Comput. Sci. Math. Ser., 10(3), 151–159.

Akça, Z. and Kaya, R. (2004). On the norm in higher dimensional taxicab spaces. Hadronic J. Suppl, 19(4), 491–501.

Bayar, A. and Ekmekçi, S. (2015). On complex numbers and taxicab plane. Mathematical Sciences and Applications E-Notes, 3(1), 58–64.

Bayar, A. and Ekmekçi, S. (2014). On circular inversions in taxicab plane. Journal of Advanced Research in Pure Mathematics, 6(4), 33–39.

Bayar, A., and Kaya, R. (2005). On the taxicab distance on a sphere. Missouri Journal of Mathematical Sciences, 17(1), 41–51.

Bayar, A., Ekmekçi, S. and Özcan, M. (2009). On trigonometric functions and cosine and sine rules in taxicab plane. International Electronic Journal Of Geometry, 2(1), 17–24.

Ekmekçi, S. (2001). The properties related to the taxicab circles. Doctoral dissertation, Eskişehir Osmangazi University, Institute of Science and Technology, Turkey.

Ekmekçi, S. (2024). A Note on the Tangents and Chords of Taxicab Circles, New Trends and Frontiers in Natural Science and Mathematics, All Sciences Academy.
Eskişehir Osmangazi University, Institute of Science and Technology, Turkey.

Kaya, R., Akça, Z., Özcan, M. and Günaltılı, İ. (2000). General equation for taxicab conics and their classification. Mitt. Math. Ges. Hamburg , 19(0), 135–148.

Krause, E. F. (1975). Taxicab geometry. Menlo Park, California: Addison –Wesley Publishing Company.

Özcan, M., Ekmekçi, S. and Bayar, A. (2002). A note on the variation of the taxicab lengths under rotations. The Pi Mu Epsilon Journal, 11(7), 381–384.

On Truncated Simplicial Commutative Algebras

İbrahim İlker AKÇA[1]
Ummahan EGE ARSLAN[2]

1- Prof. Dr.; Eskişehir Osmangazi University, Department of Mathematics and Computer Sciences, Faculty of Science, iakca@ogu.edu.tr,ORCID No:0000-0003-4269-498X
2- Prof. Dr.; Eskişehir Osmangazi University, Department of Mathematics and Computer Sciences, Faculty of Science, uege@ogu.edu.tr ORCID No:0000-0002-2995-0718

ABSTRACT

In this paper we give an encoding method that crossed modules and 2-crossed modules are equivalent to truncated simplicial commutative algebras.

Keywords – Simplicial Algebra, Peiffer Elements, 2-Crossed Modules, Face And Degeneracy Maps.

INTRODUCTION

In their paper, Z. Arvasi and T. Porter established notable equivalences within algebraic categories. Specifically, they demonstrated that the category of simplicial algebras aligns with both the category of crossed modules of algebras and the category of 2-crossed modules of algebras. Furthermore, they elucidated that the equivalence extends to more specific structures: the category of crossed modules of algebras corresponds to simplicial algebras equipped with Moore complexes of length 1, while the category of 2-crossed modules of algebras corresponds to those with Moore complexes of length 2. Building upon these insights, this paper introduces an encoding method that further solidifies the equivalence between crossed modules and 2-crossed modules with truncated simplicial commutative algebras. This encoding method promises to streamline the study and application of these algebraic structures, offering a unified framework for understanding their interrelations and properties.

1-Review of simplicial algebras

All algebras will be commutative and will be over the same fixed but unspecified ground ring.
A simplicial (commutative) algebra **E** consists of a family of algebras $\{E_n\}$ together with face and degeneracy maps

$$d_i = d_i^n : \quad E_n \to E_{n-1}, \quad 0 \leqslant i \leqslant n \quad (n \neq 0)$$
$$s_i = s_i^n : \quad E_n \to E_{n+1}, \quad 0 \leqslant i \leqslant n.$$

satisfying the usual simplicial identities given in Andre [1] or [8], for example. It can be completely described as a functor $\mathbf{E}: \boldsymbol{\Delta}^{op} \to \boldsymbol{CommAlg_k}$ where $\boldsymbol{\Delta}$ is the category of finite ordinals $[n] = \{0 < 1 < \cdots < n\}$ and increasing maps.

Elements $x \in E_n$ are called *n-dimensional simplices*. A simplex *x* is called *degenerate* if $x = s_i(y)$ for some *y*.

A simplicial map $f: \mathbf{E} \to \mathbf{E}'$ is a family of homomorphisms $f: E_n \to E'_n$ commuting with the d_i and s_i. We let **Simp.Alg.** denote the category of simplicial algebras.

An essential reference from our point of view is Carrasco's thesis, [**5**], where many of the basic techniques used here were developed systematically for the first time and the notion of hypercrossed complex was defined (although in a different context).

The following notation and terminology is derived from the analogous group theoretic case treated in [5], [6]. For the ordered set $[n] = \{0 < 1 < \cdots < n\}$, let $\alpha_i^n: [n+1] \to [n]$ be the increasing surjective map given by

$$\alpha_i^n(j) = \begin{cases} j & \text{if } j \leqslant i \\ j-1 & \text{if } j > i. \end{cases}$$

Let *S*(*n*, *n*-*r*) be the set of all monotone increasing surjective maps from [*n*] to [*n*-*r*]. This can be generated from the various α_i^n by composition. The composition of these generating maps is subject to the following rule $\alpha_j \alpha_i = \alpha_{i-1} \alpha_j$, $j < i$. This implies that every element $\alpha \in S(n, n-r)$ has a unique expression as $\alpha = \alpha_{i_1} \circ \alpha_{i_2} \circ \cdots \circ \alpha_{i_r}$ with $0 \leq i_1 < i_2 \cdots < i_r \leq n-1$, where the indices i_k are the elements of [*n*] such that $\{i_1, \cdots, i_r\} = \{i: \alpha(i) = \alpha(i+1)\}$. We thus can identify *S*(*n*, *n*-*r*) with the set $\{(i_r, \cdots, i_1): 0 \leq i_1 < i_2 \cdots < i_r \leq n-1\}$. In particular, the single element of *S*(*n*,*n*), defined by the identity map on [*n*], corresponds to the empty 0-tuple ( ) denoted by $\emptyset_n$. Similarly the only element of *S*(*n*,0) is (*n* – 1, *n*- 2,…, 0). For all n ≥ 0, let $S(n) = \bigcup_{0 \leq r \leq n} S(n, n-r)$.

We say that $\alpha = (i_r, \cdots, i_1) < \beta = (j_s, \cdots, j_1)$ in *S*(*n*)

$$\begin{array}{ll} \text{if} & i_1 = j_1, \ldots, i_k = j_k \quad \text{but} \quad i_{k+1} > j_{k+1} \quad (k \geqslant 0) \text{ or} \\ \text{if} & i_1 = j_1, \ldots, i_r = j_r \quad \text{and} \quad r < s. \end{array}$$

This makes *S*(*n*) an ordered set. For instance, the orders in *S*(2) and in *S*(3) are respectively:

$$\begin{array}{rcl} S(2) & = & \{\emptyset_2 < (1) < (0) < (1,0)\}; \\ S(3) & = & \{\emptyset_3 < (2) < (1) < (2,1) < (0) < (2,0) < (1,0) < (2,1,0)\}. \end{array}$$

We also define $\alpha \cap \beta$ as the set of indices which belong to both α *and* β.

The Moore complex

The Moore complex **NE** of a simplicial algebra **E** is the complex

$$\mathbf{NE}: \quad \cdots \to NE_n \xrightarrow{\partial_n} NE_{n-1} \to \cdots \to NE_1 \xrightarrow{\partial_1} NE_0 \xrightarrow{\partial_0} 0$$

where

$$NE_0 = E_0, \qquad NE_n = \bigcap_{i=0}^{n-1} \mathrm{Ker} d_i, \qquad \partial_n = d_n \text{ (restricted to } NE_n).$$

We say that the Moore complex **NE** of a simplicial algebra is of length k if $NEn = 0$ for all $n \geq k + 1$ so that a Moore complex is of length r for $r \geq k$.

The n^{th} homotopy module $\pi_n(\mathbf{E})$ of **E** is the n^{th} homology of the Moore complex is **E,** i.e.,

$$\begin{aligned} \pi_n(\mathbf{E}) &\cong H_n(\mathbf{NE}) \\ &= \bigcap_{i=0}^{n} \mathrm{Ker} d_i^n / d_{n+1}^{n+1} (\bigcap_{i=0}^{n-1} \mathrm{Ker} d_i^{n+1}) \end{aligned}$$

If **A** is a simplicial module **NA** is a chain complex in the usual sense and **N** gives a functor from **SimpMod,** the category of simplicial modules to **ChMod** the category of (non-negatively graded) chain complexes of modules.

We will need to make use of the semidirect product decomposition several times. The basic result is the following:

Proposition: *If **E** is a simplicial algebra, then for any* $n \geq 0$

$$\begin{aligned} E_n \cong\ & (\ldots (NE_n \rtimes s_{n-1} NE_{n-1}) \rtimes \ldots \rtimes s_{n-2} \ldots s_0 NE_1) \rtimes \\ & (\ldots (s_{n-2} NE_{n-1} \rtimes s_{n-1} s_{n-2} NE_{n-2}) \rtimes \ldots \rtimes s_{n-1} s_{n-2} \ldots s_0 NE_0). \end{aligned}$$

Proof: This is by repeated use of the following lemma.

Lemma: *Let **E** be a simplicial algebra. Then En can be decomposed as a semidirect product:*

$$E_n \cong \mathrm{Ker} d_n^n \rtimes s_{n-1}^{n-1}(E_{n-1}).$$

Proof: The isomorphism is defined as follows:

$$\begin{aligned} \theta : \ E_n &\longrightarrow \mathrm{Ker} d_n^n \rtimes s_{n-1}^{n-1}(E_{n-1}) \\ e &\longmapsto (e - s_{n-1} d_n e, s_{n-1} d_n e). \end{aligned}$$

2-Truncations

By an *ideal chain complex* of algebras, (X, d), we mean one in which each Imd_{i+1} is an ideal of X_i. Given any ideal chain complex (X, d) of algebras and an integer n, the truncation $t_{n|}X$ of X at level n will be defined by

$$(t_{n|}X)_i \;=\; \begin{cases} X_i & \text{if } \; i < n \\ X_i/Imd_{n+1} & \text{if } \; i = n \\ 0 & \text{if } \; i > n. \end{cases}$$

The differential d of $t_{n|}X$ is that of X for $i > n$, d_n is induced from the n^{th} differential of X and all other are zero. (for more information see Illusie [8]). Truncation is of course functorial.

Proposition: *There is a truncation functor* $t_{n|}X: \boldsymbol{SimpAlg} \to \boldsymbol{SimpAlg}$ *such that there is a natural isomorphism*

$$t_{n|}N \cong Nt_{n|},$$

where N is the Moore complex functor from ***SimpAlg*** *to the category of chain complexes of algebras.*

Proof: We first note that $d_{n+1}^{n+1}(NEn+1)$ is contained in E_n as an ideal and that all face maps of **E** vanish on it. We can thus take

$$t_{n|}\mathbf{E} = \begin{cases} E_i & \text{for all } i < n \\ E_n/d_{n+1}^{n+1}(NE_{n+1}) & \text{for } i = n \end{cases}$$

and for $i > n$ we take the semidirect decomposition of E_i given by Proposition 1.1, delete all occurrences of NE_k for $k > n$ and replace any NE_n by $NE_n/d_{n+1}^{n+1}(NE_{n+1})$. The definition of face and degeneracy is easy as is the verification that $t_{n|}$N and $Nt_{n|}$ are the same.

This truncation functor has nice properties. (In the chain complex case, these are discussed in Illusie [8]).

Proposition: *Let* $T_{n|}$ *be the full subcategory of* ***SimpAlg*** *defined by the simplicial algebras whose Moore complex is trivial in dimensions greater than n and let* $i_n : T_{n|} \to$ **SimpAlg** *be the inclusion functor.*

(a) The functor $t_{n|}$ *is left adjoint to* i_n*. (We will usually drop the* i_n *and so also write* $t_{n|}$ *for the composite functor.)*

(b) The natural transformation η*, the co-unit of the adjunction, is a natural epimorphism which induces an isomorphism on* π_i *for* $i \leq n$*.*

(c) For any simplicial algebra $\boldsymbol{E}$*,* $\pi(t_{n|}\ \mathbf{E}\ ) = 0$ *if* $i > n$*.*

(d) To the inclusion $T_{n|} \to T_{n+1|}$*, there corresponds a natural epimorphism* η_n *from* $t_{n+1|}$ to $t_{n|}$*. If* $\boldsymbol{E}$ *is simplicial algebra,* the kernel of η_n (**E**) is a $K(\pi_{n+1}($ **E** $), n+1)$, i.e. has a single non-zero homotopy module in dimension $n+1$, that being $\pi_{n+1}(\boldsymbol{E})$.

As each statement is readily verified using the Moore complex and the semidirect product decomposition, the proof of the above will be left out.

A comparison of these properties with those of the coskeleta functors (cf. Artin and Mazur [4]) is worth making. Recall that given any integer $k \geq 0$, there is a functor $cosk_n$ defined on the category of simplicial sets, which is the composite of a truncation functor (differently defined) and its right adjoint. The n-simplicies of $cosk_k\mathbf{X}$ are given by Hom(sk $_k$ $\Delta[n], \mathbf{X}$) the set of simplicial maps from the k -skeleton of the n -simplex $\Delta[n]$ to simplicial set $\mathbf{X}$. There is a canonical map from $\mathbf{X}$ to $cosk_k\boldsymbol{X}$ whose homotopy fibre an Eilenberg-Maclane space of type $(\pi_k(\mathbf{X}), k)$. This k-skeleton is constructed using finite limits and there is an analogue in any category of simplicial objects in a category $\mathbf{C}$ provided that $\mathbf{C}$ has finite limits, thus in particular in **SimpAlg.** Z. Arvasi and T. Porter (cf.[2]) have calculated the Moore complex of $cosk_k\boldsymbol{E}$ for a simplicial algebra $\mathbf{E}$ using a construction described in Duskin's Memoir [7]. Their results gives

$$N(\cos k_k\mathbf{E})_l = 0 \text{ if } l > k+1$$

$$N(\cos k_k\mathbf{E})_{k+1} = Ker(\partial_k : NE_k \to NE_{k-1})$$

$$N((\cos k_k\mathbf{E})_l) = NE_l \text{ if } l \leq k.$$

There is a natural epimorphism from $\cos k_{k+1}\mathbf{E}$ to $t_{k|}\mathbf{E}$ which on passing to Moore complexes gives

$$\begin{array}{ccccccccc} 0 & \longrightarrow & Ker\partial_{k+1} & \longrightarrow & NE_{k+1} & \longrightarrow & NE_k & \xrightarrow{\partial_k} & NE_{k-1} \\ & & \downarrow & & \downarrow & & \downarrow & & \downarrow \\ 0 & \longrightarrow & 0 & \longrightarrow & 0 & \longrightarrow & NE_k/Im\partial_{k+1} & \longrightarrow & NE_{k-1} \end{array}$$

This epimorphism of chain complexes thus has an acyclic kernel. The epimorphism therefore induces an isomorphism on all homotopy modules and hence is a weak homotopy equivalence. We may thus use either $t_{k|}\mathbf{E}$ or $\cos k_{k+1}\mathbf{E}$ as a model for *k*-type of simplicial algebra **E**.

Truncated simplicial algebras

It is well known that the category of simplicial algebras is equivalent to the category of crossed modules of algebra and category of 2-crossed modules of algebras. In [2], Z. Arvasi and T. Porter proved that the category of crossed modules of algebras is equivalent to the category of simplicial algebras with Moore complex of length 1 and that the category of 2-crossed modules of algebras is equivalent to the category of simplicial algebras with Moore complex of length 2. In this section we will give slight reformulations of this results by means of the truncated simplicial algebras.

As a first step to understanding truncated simplicial algebras a bit more, we will give a variant of an argument. We will look at a 1-truncated simplicial algebra.

Proposition: *(c.f [3]) Let* I_2 *be the ideal of* E_2 *generated by elements of the form*

$$C_{(1)(0)}(x \otimes y) = s_1(x)(s_1(y) - s_0(y)).$$

The image of I_2 by ∂_2 is known to be $\ker d_0 \ker d_1$ by direct calculation.

The form of this element $C_{(1)(0)}(x \otimes y)$, is obtained by taking the two elements, x and y , of degree 1 in the Moore complex of a simplicial algebra, $\mathbf{E}$, mappling them up to degree 2 by complementary degeneracies, and then looking at the component of the result that is in the Moore complex term, NE_2. (It is easy to show that E_2 is a semidirect product of NE_2 and degenerate copies of lower degree Moore complex terms.) The idea behind this pairing can be extended to higher dimensions. It gives the Peiffer pairings $C_{\alpha,\beta} : NE_p \times NE_q \to NE_{p+q}$.

In general, these take $x \in NE_p$ and $y \in NE_q$ and (α, β) a complimentary pair of index strings (of suitable lengths), and sends (x, y) to the component in NE_{p+q} of $s_\alpha(x)s_\beta(y)$; see the paper [3].

Crossed Modules of Algebras

J.H.C. Whitehead (1949) [10] described crossed modules in various contexts especially in his investigation into the algebraic structure of relative homotopy groups. We recall the definition of crossed modules of commutative algebras given by T.Porter, [9].

Definition: Let R be a $k-$algebra with identity. A pre-crossed module of commutative algebras is an R-algebra C together with a commutative action of R on C and a morphism

$\partial : C \to R$

such that for all $c \in C$, $r \in R$

$CM1)\ \partial(r \cdot c) = r\partial(c)$

This is a crossed R -module if in addition,

$CM2)\ \partial c \cdot c' = cc'$

for all $c, c' \in C$. The last condition is called the Peiffer identity. We denote such a crossed

module by (C, R, ∂) . A map of crossed modules

$(\partial : C \to R) \to (\partial' : C' \to R')$
is a pair of homomorphisms $f_0 : R \to R'$, $f_1 : C \to C'$ such that $f_0\partial = \partial' f_1$ and $f_1(r \cdot c) = f_0(r) \cdot f_1(c)$ for all $c \in C$, $r \in R$.

1- and 2-truncated Simplicial Algebras

Suppose that $\mathbf{E}$ is a simplicial algebra and that $NE_i = 0$ for $i \geq 2$. This leaves us just with
$\partial : NE_1 \to NE_0$.
We make $NE_0 = E_0$ act on NE_1 by multiplication via s_0
$g \cdot c = s_0(g)c$ for $g \in E_0$, $c \in NE_1$,
and
$\partial(g \cdot c) = g\partial(c)$.
Thus the first crossed module axiom is satisfied. For the other one, we note that $C_{(1)(0)}(c_1 \otimes c_2) \in NE_2$, which is trivial, so

$$\begin{aligned} 0 &= d_2(s_1c_1(s_1c_2 - s_0c_2)) \\ &= c_1(c_2 - s_0d_1c_2) \\ &= c_1c_2 - c_1s_0d_1c_2 \\ &= c_2c_1 - s_0d_1(c_2)c_1 \\ &= c_2c_1 - d_1(c_2) \cdot c_1, \end{aligned}$$

so the Peiffer identity holds as well. Thus $\partial : NE_1 \to NE_0$ is a crossed module. Thus we have the following slight reformulation of results in [2].

Proposition: *The category of crossed modules of algebras is equivalent to the subcategory T*1] *of 1-truncated simplicial algebras.*

The main reason for restating and proving this result in this form is that we can glean more information from the proof for examining the next level, 2-truncated simplicial algebras.
If we replace our 1-truncated simplicial algebra by an arbitrary one, then we have already introduced the idea of a Peiffer commutator of two elements, and there we used the term Peiffer lifting without specifying what particular interest the construction had. We recall that here: Given a simplicial algebra, **E**, and two elements $c_1, c_2 \in NE_1$ as above, then the Peiffer commutator of c_1 and c_2 is defined by
$\langle c_1, c_2 \rangle = c_2c_1 - \partial(c_2) \cdot c_1$.

We met earlier, $C_{(1)(0)}$, which gives the Peiffer lifting denoted

$\{-,-\} : NE_1 \otimes NE_1 \to NE_2$

where

$\{c_1 \otimes c_2\} = s_1(c_1)(s_1(c_2) - s_0(c_2))$

and we noted

$\partial_2\{c_1 \otimes c_2\} = \langle c_1, c_2 \rangle.$

These structures come into their own for a 2-truncated simplicial algebra. Suppose that **E** is now a simplicial algebra, which is 2-truncated, so its Moore complex looks like:

$$\ldots 0 \longrightarrow NE_2 \xrightarrow{\partial_2} NE_1 \xrightarrow{\partial_1} NE_0.$$

For the moment, we will concentrate our attention on the morphism ∂_2.
The commutative algebra NE_1 acts on NE_2 by multiplication via s_1 s_0 that if $g \in NE_1$ and $c \in NE_2$,

$$g \cdot c = s_1(g)c$$

It is clear that $\partial_2(g \cdot c) = \partial_2(s_1(g)c) = g\partial_2(c)$ and as before, we consider for $c_1, c_2 \in NE_2$ this time, the Peiffer pairing given by

$s_2(c_1)(s_2(c_2) - s_1(c_2))$

which is in NE_3. However that latter algebra is trivial, so this element is trivial, and hence, so is its image in NE_2 . The same calculation as before shows that, with this s_1 -based action of NE_1 on NE_2 , (NE_2, NE_1, ∂_2) is a crossed module.

We also know that there is a Peiffer lifting

$\{- \otimes -\} : NE_1 \otimes NE_1 \to NE_2,$

which measures the obstruction to $NE_1 \to NE_0$ being a crossed module, since $\partial\{- \otimes -\}$ is the Peiffer commutator, whose vanishing is equivalent to $NE_1 \to NE_0$ being a crossed module. We do not have yet in our investigation a detailed knowledge of how the two structures interact, nor any other distinguishing properties of $\{- \otimes -\}$. We will not give such a detailed derivation here, but from it we can obtain the following:

Proposition: *Let* **E** *be a 2-truncated simplicial algebra. The Peiffer lifting*

$\{- \otimes -\} : NE_1 \otimes NE_1 \to NE_2,$

has the following properties:

(i) it is a map such that if $c_1, c_2 \in NE_1$

$\partial_2\{c_1 \otimes c_2\} = c_2c_1 - \partial_1(c_2)\cdot c_1,$

(ii) if $l_0, l_1 \in NE_2$

$\{\partial_2(l_0) \otimes \partial_2(l_1)\} = l_0l_1,$

(iii) if $c_1, c_2, c_3 \in NE_1$

$$\{c_1 \otimes c_2c_3\} = \{c_1c_2 \otimes c_3\} + \partial_1(c_3)\cdot\{c_1 \otimes c_2\},$$

(iv) if $l \in NE_2$ and $c \in NE_1$

$$\{c \otimes \partial_2(l)\} + \{\partial_2(l) \otimes c\} = \partial_1(c)\cdot l,$$

(v) if $c_1, c_2 \in NE_1$ *and* $n \in NE_0$

$$n\cdot\{c_1 \otimes c_2\} = \{n\cdot c_1 \otimes c_2\} + \{c_1 \otimes n\cdot c_2\},$$

The above can be encoded in the definition of a 2-crossed module of *k*-algebras.

Definition: A 2-crossed module of k -algebras consists of a complex of C_0 -algebras

$C_2 \overset{\partial_2}{\to} C_1 \overset{\partial_1}{\to} C_0$

with ∂_2, ∂_1 morphisms of C_0 -algebras, where the algebra C_0 acts on itself by multiplication, further there is a C_0 -bilinear function giving

$\{-\otimes-\} : C_1 \otimes C_1 \to C_2,$

which satisfies the following axioms: for all $x, x_1, x_2 \in C_2, y, y_0, y_1, y_2 \in C_1$ and $z \in C_0$

1: $\partial_2\{y_0 \otimes y_1\} = y_0y_1 - \partial_1(y_1)\cdot y_0,$

2: $\{\partial_2(x_1) \otimes \partial_2(x_2)\} = x_1x_2,$

3: $\{y_0 \otimes y_1y_2\} = \{y_0y_1 \otimes y_2\} + \partial_1(y_2)\cdot\{y_0 \otimes y_1\},$

4: $\{y \otimes \partial_2(x)\} + \{\partial_2(x) \otimes y\} = \partial_1(y)\cdot x,$

5: $z\cdot\{y_0 \otimes y_1\} = \{z\cdot y_0 \otimes y_1\} = \{y_0 \otimes z\cdot y_1\}.$

The pairing $\{-\otimes-\}: C_1 \otimes C_1 \to C_2$ is often called the *Peiffer lifting* of the 2-crossed module. Note that we have not specified that C_1 acts on C_2. We colud done that as follows: if y$\in C_1$ *and* $x \in C_2$ define

$$y\cdot x = \{y \otimes \partial_2(x)\}.$$

Therefore with this action

$$\partial_2: C_2 \to C_1$$

is a crossed module of *k*-algebras.

We denote such a 2-crossed module by $\{C_2, C_1, C_0, \partial_2, \partial_1\}$. *A morphism of 2-crossed modules is given by a diagram*

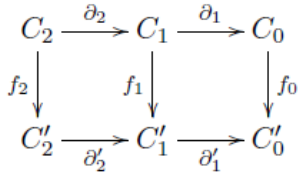

where

$$f_0\partial_1 = \partial_1' f_1, f_1\partial_2 = \partial_2' f_2,$$

$$f_1(z \cdot y) = f_0(z) \cdot f_1(y),\ f_2(z \cdot x) = f_0(z) \cdot f_2(x),$$

and

$$\{- \otimes -\}(f_1 \times f_1) = f_2\{- \otimes -\},$$

for all $x \in C_2, y \in C_1, z \in C_0$.

These compose a category which we will denote by 2 -*CMod*. The following should be clear.

Theorem: *The Moore complex of a 2-truncated simplicial algebra is a 2-crossed module of k-algebras. The assignment is functorial.*

We will denote this functor by $\lambda: T_{2]} \to 2 - CMod$. It is an equivalence of categories.

REFERENCES

[1] Andre, M. (1974). Homologie des algebres commutatives, *Grundlehren Band*, 206, Springer, Verlag, Berlin.

[2] Arvasi, Z. and Porter, T. (1998). Freeness conditions of 2-crossed modules of commutative algebras, *Applied Categorical Structures*, 6: 455-471.

[3] Arvasi, Z. and Porter, T. (1997). Higher dimensional Peiffer elements in simplicial commutative algebras, *Theory and Applications of Categories*, Vol.3, No. 1 pp. 1-23.

[4] M.Artin and Mazur, B. (1968). Etale homotopy. *Lecture Notes in Maths*, **100**, Springer Verlag.

[5] Carrasco,P. (1987). Complejos hipercruzados: cohomología y extensiones. *Ph.D. Thesis*, Univ. de Granada.

[6] Carrasco, P. and Cegarra, A. M. (1991). Group-theoretic algebraic models for homotopy types. *Journal Pure Appl. Algebra*, **75 ,** 195-235.

[7] Duskin, J. Simplicial methods and the interpretation of triple cohomology. *Mem. Amer. Math. Soc.*, **163** (1970), 117-136.

[8] Illusie, L. (1971), (1972). Complexe cotangent et deformations I, II. *Springe Lecture Notes in Maths*, I **239**, II **283.**

[9] Porter, T. (1987). Homology of commutative algebras and an invariant of Simis and Vasconceles. *J.Algebra.* 109, 458-465.

[10] Whitehead, J.H.C. (1949). Combinatorial Homotopy I and II, *Bull. Amer. Math. Soc.*, 55, 231-245 and 453-456.

On 2-Algebras and Cat-1 Algebras

Ummahan EGE ARSLAN

Prof. Dr.; Eskişehir Osmangazi University, Department of Mathematics and Computer Sciences, Faculty of Science, uege@ogu.edu.tr ORCID No:0000-0002-2995-0718

ABSTRACT

In [1] it was defined the notion of 2-algebra as a categorification of algebras, and shown that the category of strict 2-algebras is equivalent to the category of crossed modules in commutative algebras. In this paper we show that the category of strict 2-algebras is equivalent to the category of cat^1-algebras.

Keywords –Cat^1-algebra, 2-Algebra, Crossed Module.

INTRODUCTION

A 2-group is a categorified version of a group. Internal categories in the category of groups are exactly the same as 2-groups. The Brown-Spencer theorem [7] thus constructs the associated 2-group of a crossed module given by Whitehead [13] to define an algebraic model for a (connected) homotopy 2-type. The fact that the composition in the internal category must be a group homomorphism implies that the interchange law must hold. This equation is in fact equivalent via the Brown-Spencer result to the Peiffer identity.

To obtain analogous results in (commutative) algebras, we use Porter's works [11] which gave some categorical results in the theory of crossed modules in commutative algebras. He also stated that there is an equivalence of categories between the internal category in the category of k-algebras and the crossed module of commutative algebras.

Given a group G , it is known that automorphisms of G yield a 2 -group. An analogous result in algebras, multiplications of C yield a strict 2 -algebra where C is an algebra.

In [9] Loday reformulated the notion of a crossed module as a cat^1-group, namely a group G with a pair of endomorphisms $t, h : G \to R$ having a common image R and satisfying certain axioms. A description of cat^1-algebras and their equivalence to crossed modules of algebras appears in Shammu's Ph.D. thesis [12] and is implicit in more general expositions of cat^1-objects by Ellis [8] and Porter [11]. A cat^1-algebra denoted by $\mathbf{C} = (e; t, h, G, R)$ has source algebra G, range algebra R and two surjections $t, h : G \to R$ and an embedding $e : R \to G$ satisfying

CAT1) $te = he = id_R$,

CAT2) Ker t Ker $h = 0$.

In [4] it was introduced cat^1-R-algebroids, as a generalization of cat^1-algebras, and proven the equivalence between the categories of cat^1-R-algebroids and crossed modules of R-algebroids.

In [1] it was defined the notion of 2-algebra as a categorification of algebras,

and shown that the category of strict 2-algebras is equivalent to the category of crossed modules in commutative algebras and in [2] it was defined the notion of homotopy of 2-algebras and it was explored the relation of crossed module homotopy and 2-algebra homotopy. In addition, the notion of homotopy of Lie crossed module morphisms and homotopies of crossed complex morphisms of associative R-algebras was examined respectively, in [5] and [3]. It also appears a presentation of 2-crossed modules, which is closely related to cat^2 groups in [10]. In this paper we show that the category of strict 2-algebras is equivalent to the category of cat^1 algebras.

Preliminaries

In [1] it is defined the notion of 2-algebra as a categorification of algebras, and shown that the category of strict 2-algebras is equivalent to the category of crossed modules of commutative algebras.

2-algebras

Definition: A weak 2-algebra consists of

■ a 2-module A, [6], equipped with a functor $\bullet: A\times A\to A$, which is defined by $(x,y)\mapsto x\bullet y$ and bilinear on objects and defined by $(f,g)\mapsto f\bullet g$ on morphisms satisfying the interchange law, i.e.,

$(f_1\bullet g_1)\circ(f_2\bullet g_2)=(f_1\circ f_2)\bullet(g_1\circ g_2)$

and

■ k-bilinear natural isomorphisms

$\alpha_{x,y,z}:(x\bullet y)\bullet z\to x\bullet(y\bullet z)$

$l_x: 1\bullet x\to x$

$r_x: x\bullet 1\to x$

such that the following diagrams commute for all objects $w,x,y,z\in A_0$

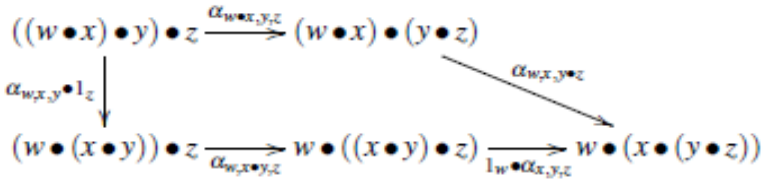

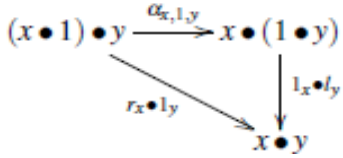

A strict 2-algebra is the special case where $\alpha_{x,y,z}$, l_x , and r_x are all identity morphisms. In this case we have

$(x \bullet y) \bullet z = x \bullet (y \bullet z)$

$1 \bullet x = x, x \bullet 1 = x.$

Strict 2-algebra is called commutative strict 2-algebra if $x \bullet y = y \bullet x$ for all objects $x, y \in A_0$ and $f \bullet g = g \bullet f$ for all morphisms $f, g \in A_1$.

In the rest of this paper, the term 2-algebra will always refer to a commutative strict 2-algebra. A homomorphism between 2-algebras should preserve both the 2-module structure and the $\bullet$ functor.

Definition: Given 2-algebras A and A' , a homomorphism

$F : A \to A'$

consists of

■ a linear functor F from the underlying 2-module of A to that of A' , and

■ a bilinear natural transformation

$F_2(x, y) : F_0(x) \bullet F_0(y) \to F_0(x \bullet y)$

■ an isomorphism $F : 1' \to F_0(1)$ where 1 is the identity object of A and $1'$ is the identity object of A' .

2-algebras and homomorphisms between them give the category of 2-algebras denoted by **2Alg** .

Therefore, if $A = (A_0, A_1, s, t, e, \circ, \bullet)$ is a 2-algebra, A_0 and A_1 are algebras with $\bullet$ bilinear functor. Thus we can take that 2-algebra is a 2-category with a single object say $*$, and A_0 collections of its 1-morphisms and A_1 collections of its 2-morphisms are algebras with identity.

Cat^1 – Algebras

A description of cat^1-algebras and their equivalence to crossed modules of algebras appears in Shammu's Ph.D. thesis [12] and is implicit in more general expositions of cat^1-objects by Ellis [8] and Porter [11].

Definition: A cat^1-algebra, (G,C,s,t,e), consists of k-algebra C and G, two surjections $s,t : G \to C$ and an embedding $e : C \to G$ satisfying;

CAT1) $te = se = id_C$,

CAT2) Ker t Ker $s = 0$.

A morphism $(G,C,s,t,e) \to (G',C',s',t',e')$ of cat^1-algebras is a pair (γ,ρ) where $\gamma : G \to G', \rho : C \to C'$ are homomorphisms satisfying

$$s'\gamma = \rho s, \qquad t' = \rho t, \quad e'\rho = \gamma e$$

Thus, one can define the category of cat^1-algebras, which will be denoted by $\boldsymbol{Cat^1}$.

In this part we show that the category of strict 2-algebras is equivalent to the category of cat^1-algebras.

Theorem The category of cat^1-algebras **Cat** ^{1} is equivalent to the category of 2 -algebras, **2Alg**.

Proof: Let $A = (A_0, A_1, s, t, e, \circ, \bullet)$ be a 2-algebra consisting of a single object, say $*$, and an algebra A_0 of 1-morphisms and an algebra A_1 of 2-morphisms. For $x, y \in A_0$ and $f : x \to y \in A_1$, we get the following diagram:

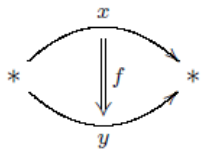

We define morphisms $s : A_1 \to A_0, s(f) = x, t : A_1 \to A_0, t(f) = y$ and morphism $e : A_0 \to A_1$, $e(x) : x \to x \in A_1$ for $x \in A_0$.

The s,t and e morphisms are algebra morphisms, and we have

$$se(x) = s(e(x)) = x = Id_{A_0}(x)$$

$$te(x) = t(e(x)) = x = Id_{A_0}(x).$$

We define an algebra homomorphism $t|_H : H \to A_0, t|_H(h) = t(h)$ where $H = \text{Ker}s = \{f \in A_1 \mid s(f) = Id_{A_0}\}$. We have semidirect product

$$\text{Ker } s \rtimes A_0 = \{(h,x) \mid h \in \text{Ker}s, x \in A_0\}$$

with the multiplication

$$(h,x)\bullet(h',x') = (x \blacktriangleright h' + x' \blacktriangleright h + h' \bullet h, x \bullet x')$$

where the action of A_0 on Ker s is defined by $x \blacktriangleright h = e(x) \bullet h$. For each $f \in A_1$, we can write $f = n + e(x)$ where $n = f - es(f) \in$ Ker s and $x = s(f)$. Suppose $f' = n' + e(x')$. Then

$$\begin{aligned} f \bullet f' &= (n + e(x)) \bullet (n' + e(x')) \\ &= n \bullet n' + n \bullet e(x') + e(x) \bullet n' + e(x) \bullet e(x') \\ &= e(x') \bullet n + e(x) \bullet n' + n \bullet n' + e(x \bullet x') \\ &= x' \blacktriangleright n + x \blacktriangleright n' + n \bullet n' + e(x \bullet x'). \end{aligned}$$

There is a homomorphism

$$\begin{array}{rccc} \phi: & A_1 & \longrightarrow & \mathrm{Ker}s \rtimes A_0 \\ & n + e(x) & \longmapsto & \phi(n + e(x)) = (n, x). \end{array}$$

because of

$$\begin{aligned} \phi(f \bullet f') &= \phi(x' \blacktriangleright n + x \blacktriangleright n' + n \bullet n' + e(x \bullet x')) \\ &= (x' \blacktriangleright n + x \blacktriangleright n' + n \bullet n', x \bullet x') \\ &= (n, x) \bullet (n', x') \\ &= \phi(f) \bullet \phi(f') \end{aligned}$$

Also, there is an obvious inverse

$$\begin{array}{rccc} \phi^{-1}: & \mathrm{Ker}s \rtimes A_0 & \longrightarrow & A_1 \\ & (n, x) & \longmapsto & \phi^{-1}(n, x) = n + e(x) \end{array}$$

which is also a homomorphism. Hence ϕ is an isomorphism and we have established that

$$\mathrm{Ker}\, s \rtimes A_0 \simeq A_1.$$

Since A is a 2-algebra and $\mathrm{Ker}\, s \rtimes A_0 \simeq A_1$, we can define following algebra morphisms:

$$\begin{array}{rccc} s: & \mathrm{Ker}s \rtimes A_0 & \longrightarrow & A_0 \\ & (h, x) & \longmapsto & s(h, x) = x \end{array} \qquad \begin{array}{rccc} t: & \mathrm{Ker}s \rtimes A_0 & \longrightarrow & A_0 \\ & (h, x) & \longmapsto & t(h, x) = t\,|_H\,(h) + x \end{array}$$

and

$$\begin{array}{rccc} e: & A_0 & \longrightarrow & \mathrm{Ker}s \rtimes A_0 \\ & x & \longmapsto & e(x) = (0, x) \end{array}$$

We also define

$$\begin{array}{rccl} \circ: & \mathrm{Ker}s \rtimes A_0 \ {}_t\times_s \ \mathrm{Ker}s \rtimes A_0 & \longrightarrow & \mathrm{Ker}s \rtimes A_0 \\ & ((h,x),(h',t\mid_H (h)+x)) & \longmapsto & (h'+h,x) \end{array}$$

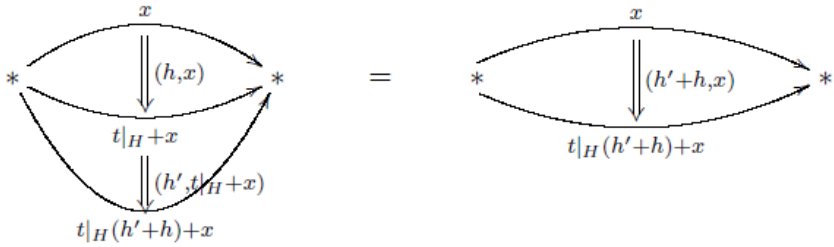

which is vertical composition;
$(h,x)\circ(h',t\mid_H (h)+x)=(h'+h,x)$,

for pairs (h,x) *and* $(h',t\mid_H (h)+x)$ satisfying $t(h,x)=s(h',t\mid_H (h)+x)=t\mid_H (h)+x$.

For $(h,x),(g,y)\in \mathrm{Ker}s\rtimes A_0$, horizontal composition is defined by

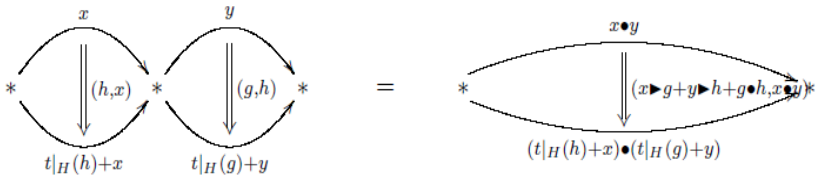

$$\begin{array}{rcl} (h,x)\bullet(g,y) & = & (x\blacktriangleright g+y\blacktriangleright h+g\bullet h, x\bullet y) \\ & = & (e(x)\bullet g+e(y)\bullet h+g\bullet h, x\bullet y). \end{array}$$

Thus we have

$se(x)=s((0,x))=x=Id_{A_0}(x)$

$te(x)=t((0,x))=x+t\mid_H (0)=x=Id_{A_0}(x).$

By the interchange law, we have

$$\begin{array}{rcl} (h,x)\bullet(h',x') & = & (h,0)\bullet(h',-t\mid_H (h')) \\ & = & (0\blacktriangleright h'-t\mid_H (h')\blacktriangleright h+h'\bullet h, 0\bullet(-t\mid_H (h')) \\ & = & (0,0) \end{array}$$

and so we get $t\,|_H\,(h') \blacktriangleright h = h' \bullet h.$ Then,

$$\begin{aligned}(h,x)\bullet(h',x') &= (h,0)\bullet(h',-t\,|_H\,(h')) \\ &= (0\blacktriangleright h' - t\,|_H\,(h')\blacktriangleright h + h'\bullet h, 0\bullet(-t\,|_H\,(h')) \\ &= (0,0)\end{aligned}$$

for (h,x) $\in$ Kers={(h,0) $|h \in H\}$ and $(h', x') \in Kert = \{(h,-t\,|_H\,(h)) \mid h \in H\}$.

Hence $(\mathrm{Ker}s \rtimes A_0, A_0, s, t, e)$ is a cat^1-algebra. Then we have a functor Λ : **2Alg** $\rightarrow$ **Cat**^{1}.

Conversely, let (G,C,s,t,e) be a cat^1-algebra. Therefore there are two epimorphisms $s,t : G \rightarrow C$ and a morphism $e : C \rightarrow G$ satisfying:

CAT1) $te = se = id_C$,

CAT2) Ker t Ker $s = 0$.

We define an algebra homomorphism $t\,|_H : H \rightarrow C$ by $t\,|_H\,(h) = t(h)$ where

H = Ker $s = \{g \in G \mid s(g) = 0\}$.

We have semidirect product

$$\mathrm{Ker}\ s \rtimes C = \{(h,x) \mid h \in \mathrm{Ker}s, x \in C\}$$

with multiplication

$$(h,x)(h',x') = (x \blacktriangleright h' + x' \blacktriangleright h + h'h, xx')$$

where the action of C on Ker s is defined by $C \times \mathrm{Ker}s \longrightarrow \mathrm{Ker}s, (x,h) \mapsto x \blacktriangleright h = e(x)h.$

It is known that $\mathrm{Ker}\ s \rtimes C$ is isomorphic to G. So $(\mathrm{Ker}s \rtimes C, C, s, t, e)$ is also a cat^1-algebra which $s,t : \mathrm{Ker}s \rtimes C \rightarrow C$ and $e : C \rightarrow \mathrm{Ker}s \rtimes C$ are given by $s(h,c) = c$, $t(h,c) = t\,|_H\,(h) + c$ and $e(c) = (0,c)$. Since

$$(0,0) = (h,x)(h',x') = (h,0)(h',-t\,|_H\,(h')) = (0\blacktriangleright h' - t\,|_H\,(h')\blacktriangleright h + hh', 0)$$

for $(h,x) \in$ Ker $s = \{(h,0) \mid h \in H\}$ and

$(h', x') \in Ker\ t = \left\{\left(\mathrm{h}, -t\,|_H\,(\mathrm{h})\right) | \mathrm{h} \in \mathrm{H}\right\}$, we get $t\,|_H\,(h') \blacktriangleright h = h'h.$

Take a single object as $*$, $A_0 = C$ and $A_1 = \mathrm{Kers} \rtimes C.$

We define two different compositions for elements in $\mathrm{Kers} \rtimes C.$
One of them is called by vertical composition;

$(h, c) \circ (h', t\,|_H\,(h) + c) = (h + h', c)$

for $(h, c), (h', t\,|_H\,(h) + c) \in \mathrm{Kers} \rtimes C.$

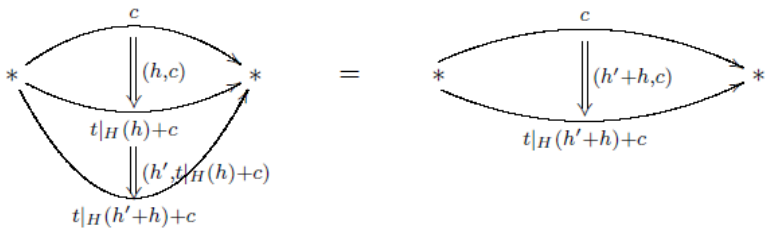

Other composition is called by horizontal composition;

$$(h, c) \bullet (g, c') = (c \blacktriangleright g + c' \blacktriangleright h + gh, cc')$$

for $(h,c),(g,c') \in \mathrm{Kers} \rtimes C.$

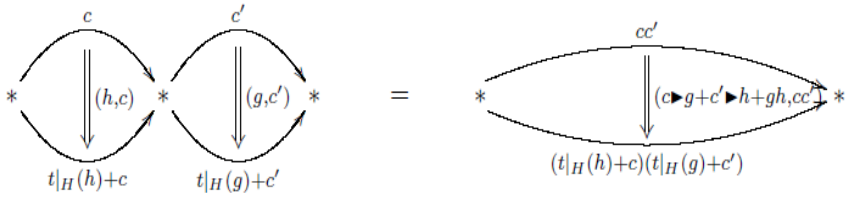

Since $c = Id_C(c) = te(c) = t\,|_H\,\mathrm{e(c)}$, we get

$$\begin{aligned}
(t\,|_H\,(h) + c)(t\,|_H\,(g) + c') &= t\,|_H\,(h)t\,|_H\,(g) + t\,|_H\,(h)c' + ct\,|_H\,(g) + cc' \\
&= t\,|_H\,(hg) + c't\,|_H\,(h) + ct\,|_H\,(g) + cc' \\
&= t\,|_H\,(hg) + t\,|_H\,e(c')\,t\,|_H\,(h) + t\,|_H\,e(c)\,t\,|_H\,(g) + cc' \\
&= t\,|_H\,(hg) + t\,|_H\,(e(c')\,h) + t\,|_H\,(e(c)\,g) + cc' \\
&= t\,|_H\,(hg + e(c')\,h + e(c)\,g) + cc' \\
&= t\,|_H\,(hg + c' \blacktriangleright h + c \blacktriangleright g) + cc' \\
&= t(c \blacktriangleright g + c' \blacktriangleright h + gh, cc').
\end{aligned}$$

It is easy to see that the interchange law is satisfied for these compositions, because of $t \mid_H (h') \blacktriangleright h = h'h.$ Therefore we have constructed a 2 -algebra A consists of a single object $*$, k -algebra A_0 of 1-morphisms and k -algebra A_1 of 2-morphisms. So there is a functor $\Lambda : \mathbf{Cat}^1 \to \mathbf{2Alg}$.

REFERENCES

[1] Akça İ. İ., Ege Arslan U. (2023). Categorification of Algebras:2-Algebras, Ikonion Journal of Mathematics, Vol. 5. (1) , 1-19.

[2] Akça İ. İ.,Ege Arslan U. (2022). Homotopies of 2-Algebra morphisms, Communications in Advanced Mathematical Sciences, Vol. 5 (4), 170-179.

[3] Akça İ. İ., Avcıoğlu O. (2021). Homotopies of crossed complex morphisms of associative R-algebras, Georgian Mathematical Journal, 28 (2), 163-173.

[4] Akça İ. İ., Avcıoğlu O. (2022). Equivalence between (pre) cat^1- R-algebroids and (pre) crossed modules of R-algebroids, Bull. Math. Soc. Math. Raumanie Teme (110) No. 3, 267-288.

[5] Akça İ.İ., Sıdal Y. (2018). Homotopies of crossed modules of Lie algebras, Konuralp Journal of Mathematics, 6. (2), 259-263.

[6] Baez J.C., Crans A.S. (2004). Higher Dimensional Algebra VI: Lie 2 -Algebras, Theory and Applications of Categories, 12: (15), 492-538.

[7] Brown R. Spencer C. (1976). G-groupoids, Crossed modules and the fundamental groupoid of a topological group, Proc. Kon. Ned. Akad.v. Wet, 79: 296-302.

[8] Ellis G. J. (1988). Higher dimensional crossed modules of algebras, Jour. of Pure and Appl. Alg. 52, 277-282.

[9] Loday J. L. (1982). Spaces with finitely many non-trivial homotopy groups, Jour. of Pure and Appl. Alg. 24; 179-202.

[10] Özel E., Ege Arslan U., Akça İ. İ. (2024). A higher-dimensional categorical perspective on 2-crossed modules, Demonstratio Mathematica,57,1,1-36.

[11] Porter T. (1987). Some categorical results in the theory of crossed modules in commutative algebras, Journal of Algebra, 109; 415-429.

[12] Shammu N.M. ,(1992). Algebraic and an Categorical Structure of Category of Algebras, Ph.D.Thesis, U.C.N.W.

[13] Whitehead, J.H.C. (1949). Combinatorial homotopy I and II, *Bull. Amer. Math. Soc.*, 55, 231-245 and 453-456.

Substrate Preferences of Liverworts (Marchantiophyta) in Yenice District, Çanakkale

Özcan ŞİMŞEK[1]

1- Dr.Öğr.Üyesi.; Çanakkale Onsekiz Mart Üniversitesi Yenice MYO Ormancılık Bölümü. ozcan.simsek@gmail.com ORCID No: 0000-0002-3210-7641

ABSTRACT

Liverworts, recognized as the oldest terrestrial plants, exhibit a broad global distribution, although their spread is constrained by their reproductive dependence on water. These plants inhabit diverse environments and display varying substrate preferences, commonly found on trees, soil, or rocks. Factors such as pH, substrate physical properties, temperature, aspect, and humidity significantly influence liverwort substrate preferences. Additionally, the type of liverwort plays a crucial role in determining substrate preference.

The Yenice district of Çanakkale, notable for its extensive forested areas and abundant natural landscapes, is situated in the northern part of the Kaz Mountains (Mount Ida). This region provides ideal habitats for liverworts due to its rich forests and natural areas. This study analyzed the substrate preferences of liverwort samples collected from the Yenice district. The findings revealed that 69.05% of the liverworts were epiphytic, 21% were epigeic and 10% were epilithic. Among leafy liverworts, the proportion of epiphytic samples increased to 84%, whereas thalloid liverworts predominantly preferred the epigeic substrate type, with a rate of 49%. This research underscores the significance of forests and natural areas in shaping the distribution and substrate preferences of liverworts.

Keywords – Liverworts, Marchantiophyta, Yenice, Çanakkale, Substrate

INTRODUCTION

Liverworts (Marchantiophyta), which are relatively unknown and often mistaken for mosses, are elegant and fascinating plants that are widely distributed in nature. The origin of the term "liverwort" is rooted in the "doctrine of signatures," which posits that plants resembling specific parts of the body may be used to treat ailments in those corresponding parts. Due to the thallus liverworts' vague resemblance to the human liver, the name was derived from the Greek and Latin word for liver, *Hepatica*, and has been adapted into various languages (e.g., liverwort in English, *leberkraut* in German, *hépatique* in French, *fegatella* in Italian, and Azez alsacher in Arabic) (Bowman, 2016).

Although Fry and Fry (1911) claimed that the term "liverwort" was first introduced by the Italian botanist Micheli in the early 18th century, Fuchs provided the first definitive description of *Marchantia polymorpha* (female) in printed literature in his work *De Historia Stirpium*, published in 1542. He criticized earlier authors for using the term *hepatica* instead of *lichen* for this plant and noted that he found no reference to its use for liver ailments in ancient Greek texts (Bowman, 2016). This evidence suggests that the term "liverwort" was in use much earlier than previously thought.

Although humanity's relationship with plants dates back to its very existence, even predating the cognitive revolution, the foundations of scientific research on plants were laid by Greek philosophers in the 6th to 4th centuries BC, as they sought to understand the natural world. Early studies primarily focused on compiling lists of plants and describing their uses. One of the earliest known lists, attributed to Diocles of Carystos around 350 BC, is believed to have included simple descriptions of plants, their habitats, and their medicinal properties. While the original versions of these early texts have not survived, their format—resembling plant catalogs—was adopted and perpetuated by writers from ancient Greece to the Renaissance (Şimşek, 2023a).

Although liverworts appear in vague descriptions and illustrations in works spanning from antiquity to the Dark Ages, the first detailed and realistic definitions and drawings of liverworts emerged during the Renaissance. These depictions predominantly focused on plants belonging to the genus *Marchantia*, though some other liverwort taxa were also documented (Bowman, 2016).

Liverworts, the modern representatives of the planet's earliest terrestrial plants, have fossil records dating back to the Middle Devonian period. *Metzgeriothallus sharonae*, identified through its well-preserved thallus fossils, is recorded as the oldest known liverwort. Additionally, liverwort spore fossils from even earlier periods have been discovered (Şimşek et al., 2016). Consequently, it is unsurprising that liverworts, which have persisted on Earth since ancient times, have been utilized by humans for various purposes throughout history (Şimşek, 2023a).

Söderström et al. (2015) reported that the global diversity of liverworts and hornworts comprises 7,486 species, distributed across 92 families and 398 genera. Of these, only 215 species are hornworts, while the remainder represent liverwort taxa.

Many liverworts exhibit remarkable tolerance to repeated cycles of wetting and drying, a trait that contributes to their success as epiphytes, enabling them to thrive on other plants. Similar to many mosses, the leaves of leafy liverworts are typically only one cell thick. To maintain water balance, they have evolved intricate and often specialized structures. For instance, the complexly lobed leaves observed in genera such as Radula, Frullania, and Scapania are distinctive to leafy liverworts (Şimşek, 2023b).

Bryophytes, including liverworts, are primitive plants that play a crucial role in initiating ecological succession on land and contributing to the development of biological diversity on Earth. These plants are widely distributed, from the poles to the equator, and typically grow on various substrates such as rock (*epilithic*), soil (*epigeic*), submerged surfaces, and wood (*epiphytic*) within their habitats (Ezer et al., 2013). The type of substrate significantly influences the distribution and habitat preferences of liverworts, as it varies in pH, temperature, organic and inorganic composition, and

physical structure. This study investigates the substrate preferences of liverwort species identified in the Yenice district of Çanakkale.

The requirement for water during reproduction is a significant factor limiting the distribution of liverworts. Despite their sensitivity to moisture and shade, liverworts exhibit a remarkable diversity, with species adapted to various habitat types. They are commonly found in humid environments, including peat bogs, forests and under-forest habitats, as well as along the edges of streams, lakes, and marshes. Additionally, liverworts inhabit water-seeping rocks, soil, aquatic surfaces, organic materials such as decaying logs, and the trunks and branches of trees (Keçeli, 2004).

MATERIAL AND METHOD

Research Area

The Yenice District, selected as the research area, is located in Türkiye's Marmara Region, and according to Henderson's (1961) grid system, it falls within the B6 grid (Figure 1).

Based on these characteristics, it is believed that the Yenice district of Çanakkale provides an exceptionally suitable geography for the habitat formation of liverworts. Yenice District is located in the southern Marmara region of the Marmara region, in the inland areas of the Biga Peninsula. It is situated in the southeast of Çanakkale province. With a surface area of 1367 km², Yenice is the largest district in Çanakkale. It is bordered by Balıkesir to the east and south, Bayramiç to the southwest, Çan to the west and northwest, and Biga to the north (Figure 2) (Şimşek, 2024).

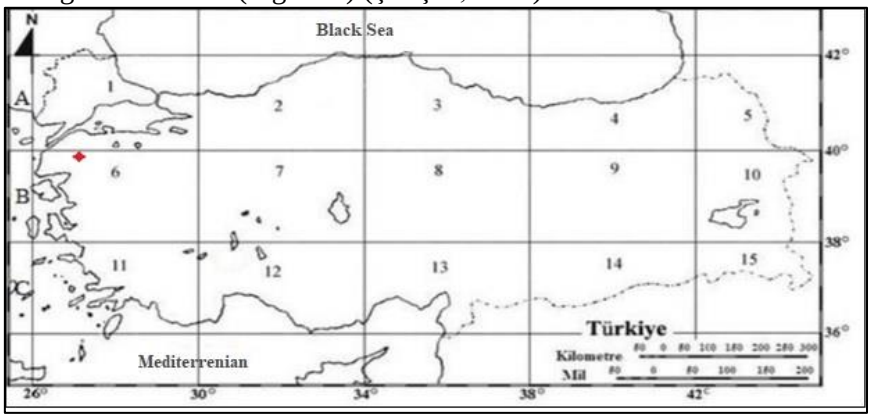

Figure 1 Henderson (1961) grid system and location of the research area (Şimşek, 2024)

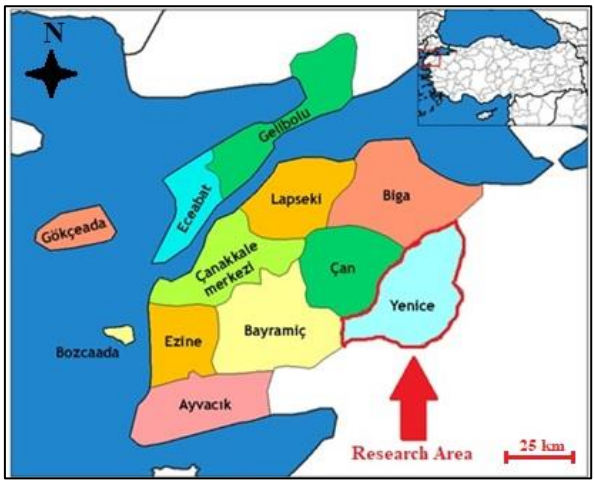

Figure 2 Location of Yenice District (Adopted from URL 2)

One of the most notable features of the Yenice district is its vegetation and land use (Figure 3). Forest areas cover 90,628 ha of the district's land, accounting for 66.2%. Consequently, forests are closely tied to the livelihoods of many local settlements, providing partial economic support. There are two Forest Management Directorates within the district. Due to the influence of elevation and thus varying microclimatic and growth conditions, different tree species and mixed forest communities can be found in the forested areas. In some parts of the forests, single-species communities dominate (such as *Abies nordmanniana* subsp. *equi-trojani* (Asch. & Sint. ex Boiss.) Coode & Cullen) and *Pinus nigra* J.F.Arnold communities), while in other areas, mixed forests of broad-leaved and coniferous species are common (Şimşek, 2024).

The region's forests contain species typical of the Mediterranean, Black Sea and continental climates. The main tree species in the district's forests are:

Turkish pine (*Pinus brutia* Ten.), black pine (*Pinus nigra* J.F.Arnold), oak species (*Quercus cerris* L., *Q. petraea* (Matt.) Liebl., *Q. frainetto* Ten.), chestnut (*Castanea sativa* Mill.), Kazdağı fir (*Abies nordmanniana* subsp. *equi-trojani* (Asch. & Sint. ex Boiss.) Coode & Cullen), hornbeam (*Carpinus betulus* L.), oriental beech (*Fagus orientalis* Lipsky), oriental plane (*Platanus orientalis* L.), alder (*Alnus glutinosa* (L.) Gaertn.), elm (*Ulmus minor* Mill.), ash (*Fraxinus excelsior* L.), silver linden (*Tilia tomentosa* Moench), hazel (*Corylus avellena* L. and *C. maxima* Mill.), strawberry tree (*Arbutus unedo* L.), Grecian strawberry tree (*Arbutus andrachne* L.), tree heath (*Erica arborea* L. and *E. manipuliflora* Salisb.), cornelian cherry (*Cornus mas* L.), laurel (*Laurus nobilis* L.), rockrose (*Cistus creticus* L. and *C. salviifolius* L.), dog rose (*Rosa canina* L.), spring clematis (*Clematis cirrhosa* L.), English ivy (*Hedera helix* L.), blackberry (*Rubus canescens* DC. and *R. caesius* L.) and stinging nettle (*Urtica dioica* L.) (Şimşek, 2024).

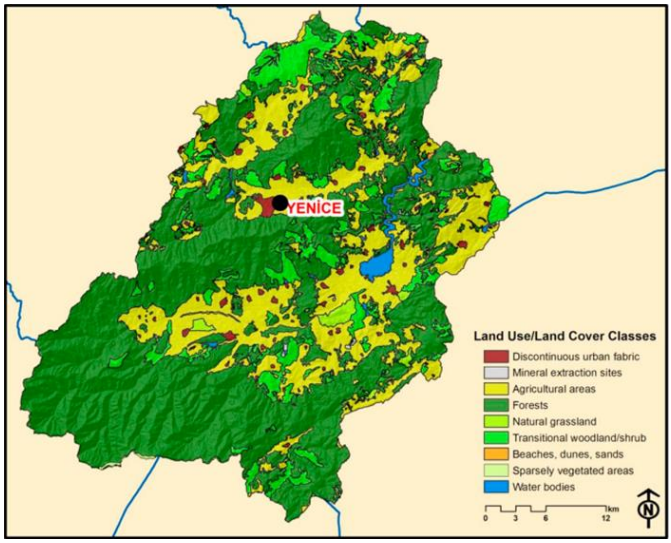

Figure 3 Land use map of Yenice district (Ayhan et.al 2020)

Research Material

The material of the research consists of 294 liverwort samples belonging to the liverwort flora of Yenice district (Çanakkale/Türkiye). The liverwort samples collected from designated stations in the Yenice District spanning February 2021 and February 2023, during various periods characterized by varying vegetation and climatic conditions. As a result of the identification process, 29 liverwort taxa belonging to 17 families were identified from the area. Of the liverwort species, 19 are leafy liverwort taxa, while 10 are thalloid liverwort taxa. The substrate types of the samples collected and identified in this study were recorded and categorized. In total, samples were obtained from seven distinct substrate types: T (tree), S (soil), R (rock), L (log), WS (wet soil), WR (wet rock), and WL (wet decaying log). (Şimşek, 2024).

In this study, statistical analyses were conducted to evaluate the substrate preferences of liverwort samples collected from the Yenice district. Additionally, the substrates were categorized into three groups—epilithic, epigeic, and epiphytic—and statistical data were analyzed based on this classification.

RESULTS

The research revealed that liverwort samples collected from Yenice showed a strong preference for tree (T) as a substrate, with 189 samples, while wet decaying logs (WL) were the least preferred, with only one sample recorded. The results are presented in Table 1, Table 2 and Graph 1.

Table 1 Substrates of liverwort samples

FAMILY	SPECIES	T	S	R	L	WS	WR	WL
Aneuraceae	*Aneura pinguis* (L.) Dumort.	0	1	0	0	3	0	0
Aytoniaceae	*Mannia gracilis* (F. Weber) D.B. Schill & D.G. Long *(Syn: Asterella gracilis (F.Weber) Underw.*	1	0	0	0	0	1	0
	Reboulia hemisphaerica (L.) Raddi	0	2	0	1	0	0	0
Conocephalaceae	*Conocephalum conicum* (L.) Dumort.	0	2	2	0	3	2	0
Fossombroniaceae	*Fossombronia pusilla* (L.) Nees	0	4	0	1	1	0	0
Frullaniaceae	*Frullania dilatata* (L.) Dumort.	95	0	3	3	0	0	1
	Frullania teneriffae (F.Weber) Nees	2	0	0	0	0	0	0
Jungermanniaceae	*Mesoptychia turbinata* (Raddi) L. Söderstr. & Váňa	0	1	0	0	0	0	0
Lejeuneaceae	*Lejeunea cavifolia* (Ehrh.) Lindb.	1	0	2	2	1	0	0
	Lejeunea lamacerina (Steph.) Schiffn.	7	1	2	1	0	0	0
Lophocoleaceae	*Chiloscyphus polyanthos* (L.) Corda	0	1	0	0	1	0	0
	Lophocolea heterophylla (Schrad.) Dumort.	1	0	0	0	0	0	0
	Lophocolea bidentata (L.) Dumort.	0	1	0	0	0	0	0
Lunulariaceae	*Lunularia cruciata* (L.) Dumort. ex Lindb.	0	8	4	0	7	0	0
Marchantiaceae	*Marchantia polymorphya* L.	0	1	0	0	1	1	0
Metzgeriaceae	*Metzgeria furcata* (L.) Corda	32	1	0	1	0	0	0

FAMILY	SPECIES	T	S	R	L	WS	WR	WL
Pallaviciniaceae	*Pallavicinia lylellii* (Hook.) Gray	0	0	0	0	3	0	0
Pelliaceae	*Pellia epiphylla* (L.) Corda	0	6	1	0	4	2	0
Plagiochilaceae	*Plagiochila porelloides* (Torr. ex Nees) Lindenb.	0	1	0	0	0	0	0
Porellaceae	*Porella arboris-vitae* (With.) Grolle	1	0	1	0	0	0	0
	Porella cordeana (Huebener) Moore	1	0	1	0	0	0	0
	Porella pinnata L.	1	1	2	0	0	0	0
	Porella plathyphylla (L.) Pfeiff.	4	0	1	1	0	0	0
Radulaceae	*Radula complanata* (L.) Dumort.	42	1	2	2	0	0	0
	Radula lindenbergiana Gottsche ex C.Hartm.	1	0	0	1	0	0	0
Scapaniaceae	*Diplophyllum albicans* (L.) Dumort.	0	2	1	0	0	0	0
	Scapania compacta (Roth) Dumort.	0	0	1	0	1	0	0
	Scapania irrigua (Nees) Nees	0	0	1	0	0	0	0
	Scapania undulata (L.) Dumort.	0	2	0	0	0	0	0
	TOTAL:	**189**	**36**	**24**	**13**	**25**	**6**	**1**

Table 2 Counts of liverwort samples by substrate type

T	S	R	L	WS	WR	WL
189	36	24	13	25	6	1

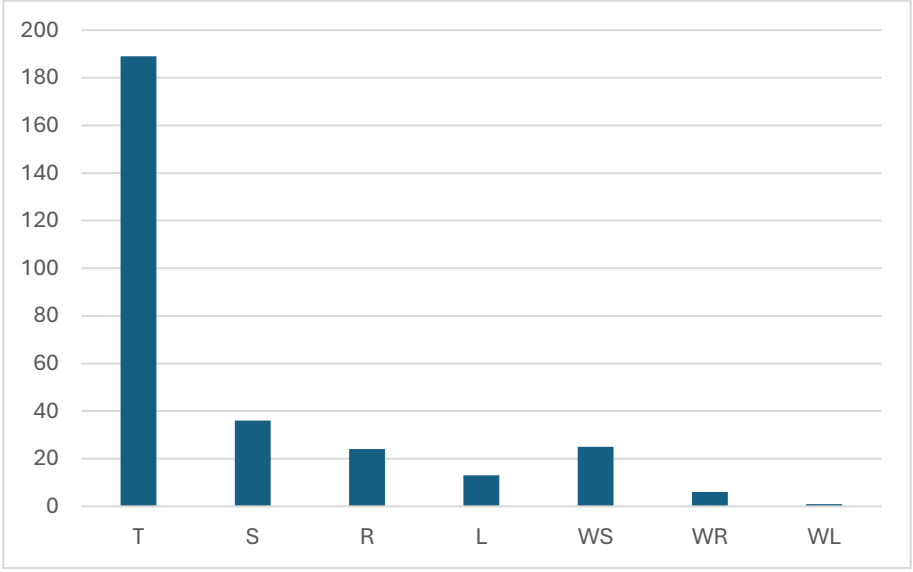

Graph 1 Counts of liverwort samples by substrate type

The proportions of substrate types were calculated and are presented in Graph 2.

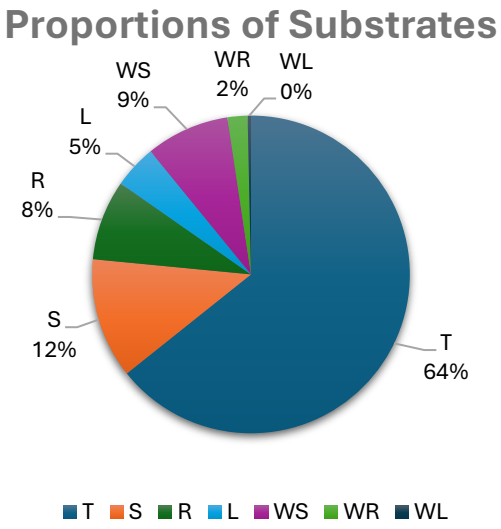

Graph 2 Proportions of liverwort samples by substrate type

When thalloid and leafy liverworts are evaluated separately, it is observed that thalloid liverworts are most frequently found on trees (T) with 33 samples, followed by soil (S) with 25 samples and wet soil (WS) with 22 samples. The counts and proportions of substrates containing thallus liverwort samples are presented in Table 3, Graph 3, and Graph 4.

Table 3 Counts of thalloid liverwort samples by substrate type

T	S	R	L	WS	WR	WL
33	25	7	3	22	6	0

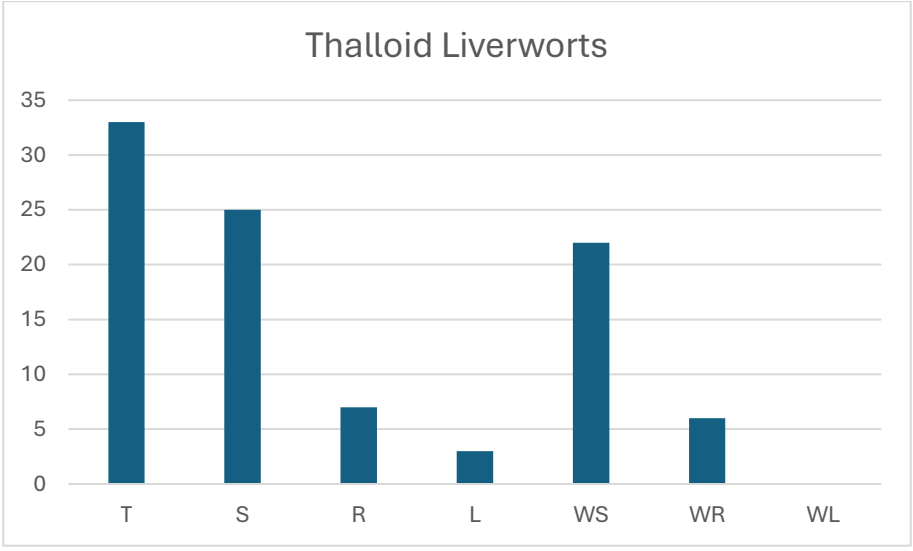

Graph 3 Counts of thalloid liverwort samples by substrate type

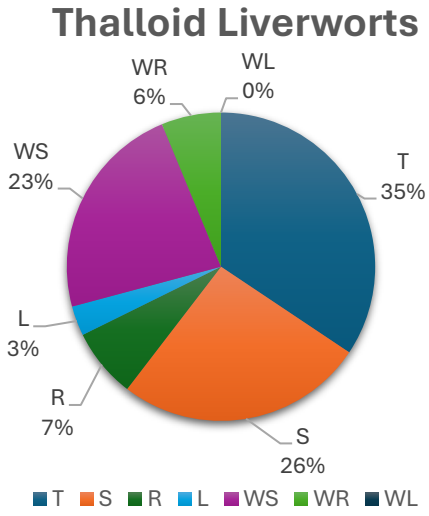

Graph 4 Proportions of thalloid liverwort samples by substrate type

When thalloid and leafy liverworts are evaluated separately, it is observed that leafy liverworts are most frequently found on trees (T) with 156 samples, followed by rock (R) with 17 samples. The counts and proportions of substrates containing thallus liverwort samples are presented in Table 4, Graph 5, and Graph 6.

Table 4 Counts of leafy liverwort samples by substrate type

T	S	R	L	WS	WR	WL
156	11	17	10	3	0	1

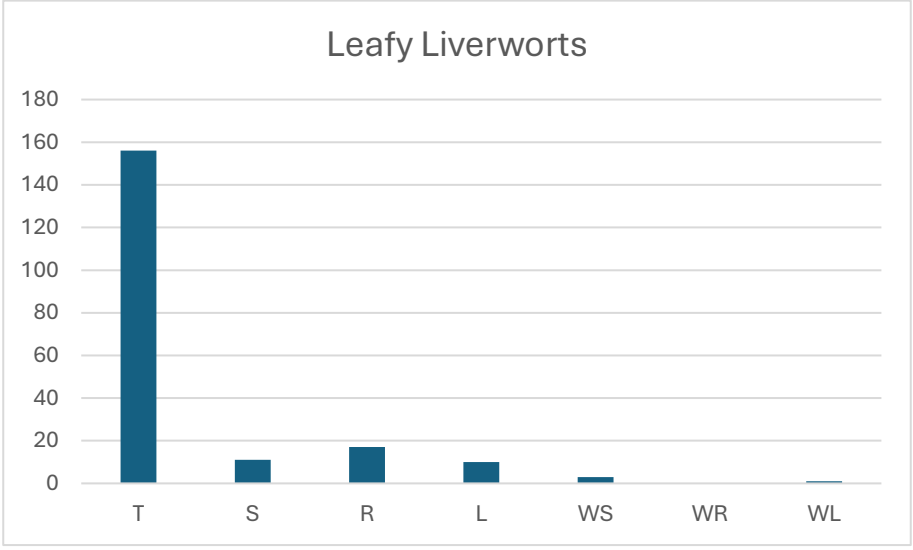

Graph 5 Counts of leafy liverwort samples by substrate type

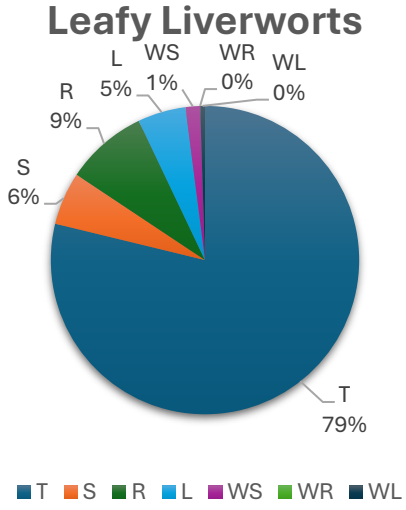

Graph 6 Proportions of leafy liverwort samples by substrate type

Additionally, the substrates were categorized into three groups—epilithic, epigeic, and epiphytic—and statistical data were analyzed based on this classification. Counts and proportions of substrates liverwort samples by substrate are given in Table 5, Graph 7 and Graph 8. It is observed that liverwort samples are most frequently found epiphytic with 203 samples (%60,05), followed epigeic with 61 samples (%20,75) while least frequently found with 30 samples (%10,2).

Table 5 Counts and proportions of liverwort samples by substrate

	Epiphytic	**Epigeic**	**Epilithic**
Counts	203	61	30
Proportions	%69,05	%20,75	%10,2

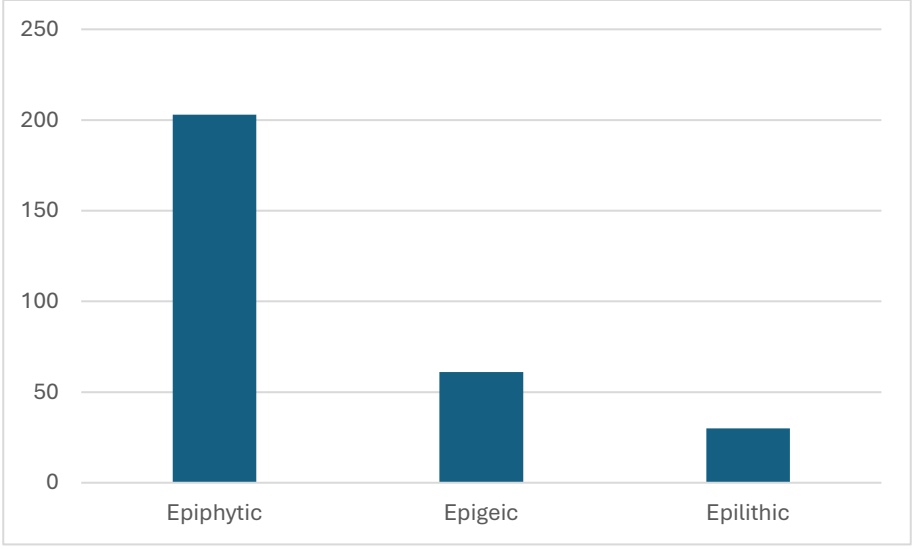

Graph 7 Liverwort samples by substrate type

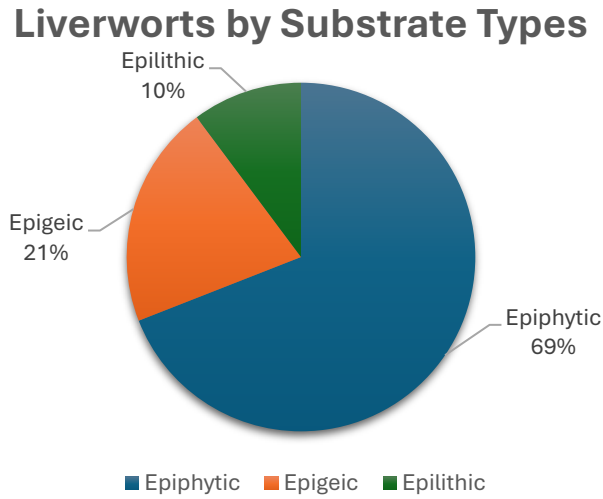

Graph 8 Proportions of liverwort samples by substrate type

When thalloid and leafy liverworts are analyzed separately, it is observed that thalloid liverworts are predominantly epigeic, whereas leafy liverworts are primarily epiphytic. The corresponding results are presented in Table 6 and Graphs 9, 10, 11, and 12.

Table 6 Counts and proportions of thalloid and leafy liverworts samples by substrate

	Epiphytic	**Epigeic**	**Epilithic**
Thalloid	36	47	13
Leafy	167	14	17

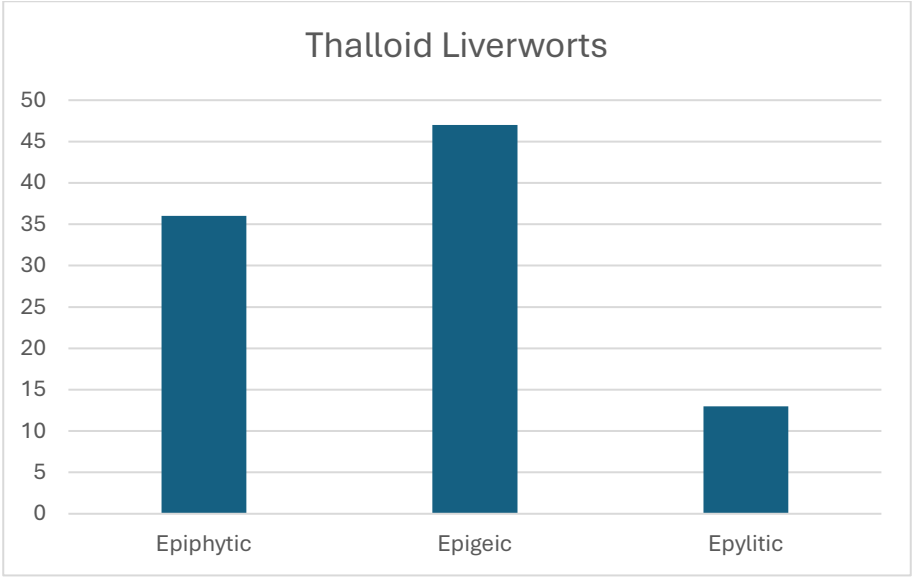

Graph 9 Thalloid liverwort samples by substrate type

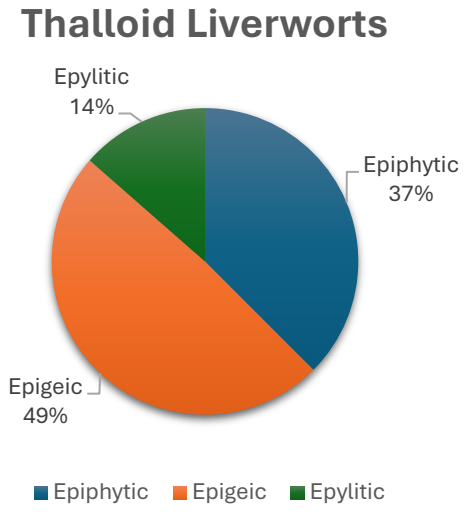

Graph 10 Proportions of thalloid liverwort samples by substrate type

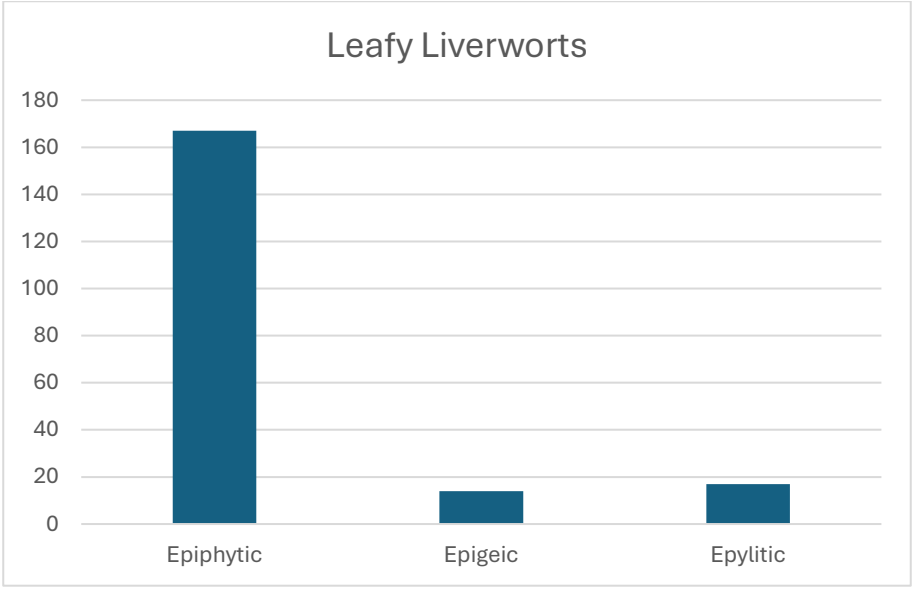

Graph 11 Leafy liverwort samples by substrate type

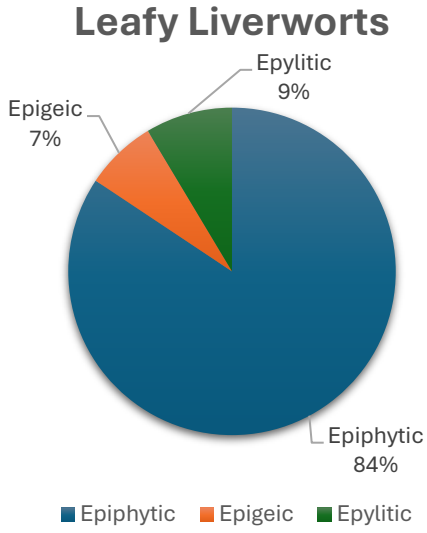

Graph 12 Proportions of leafy liverwort samples by substrate type

The sample counts of epiphytic, epigeic, and epilithic liverwort species and families are presented in Table 7, Table 8 and Graph 13.

Table 7 Substrate distributions of samples belonging to liverwort species

Family	Species	Epiphytic	Epigeic	Epilithic
Aneuraceae	*Aneura pinguis* (L.) Dumort.	0	4	0
Aytoniaceae	*Mannia gracilis* (F. Weber) D.B. Schill & D.G. Long *(Syn: Asterella gracilis (F.Weber) Underw.*	1	0	1
	Reboulia hemisphaerica (L.) Raddi	1	2	0
Conocephalaceae	*Conocephalum conicum* (L.) Dumort.	0	5	4
Fossombroniaceae	*Fossombronia pusilla* (L.) Nees	1	5	0
Frullaniaceae	*Frullania dilatata* (L.) Dumort.	99	0	3
	Frullania teneriffae (F.Weber) Nees	2	0	0
Jungermanniaceae	*Mesoptychia turbinata* (Raddi) L. Söderstr. & Váňa	0	1	0
Lejeuneaceae	*Lejeunea cavifolia* (Ehrh.) Lindb.	3	1	2
	Lejeunea lamacerina (Steph.) Schiffn.	8	1	2
Lophocoleaceae	*Chiloscyphus polyanthos* (L.) Corda	0	2	0
	Lophocolea heterophylla (Schrad.) Dumort.	1	0	0
	Lophocolea bidentata (L.) Dumort.	0	1	0
Lunulariaceae	*Lunularia cruciata* (L.) Dumort. ex Lindb.	0	15	4
Marchantiaceae	*Marchantia polymorphya* L.	0	2	1
Metzgeriaceae	*Metzgeria furcata* (L.) Corda	33	1	0
Pallaviciniaceae	*Pallavicinia lylellii* (Hook.) Gray	0	3	0
Pelliaceae	*Pellia epiphylla* (L.) Corda	0	10	3
Plagiochilaceae	*Plagiochila porelloides* (Torr. ex Nees) Lindenb.	0	1	0
Porellaceae	*Porella arboris-vitae* (With.) Grolle	1	0	1
	Porella cordeana (Huebener) Moore	1	0	1
	Porella pinnata L.	1	1	2
	Porella plathyphylla (L.) Pfeiff.	5	0	1
Radulaceae	*Radula complanata* (L.) Dumort.	44	1	2
	Radula lindenbergiana Gottsche ex C.Hartm.	2	0	0
Scapaniaceae	*Diplophyllum albicans* (L.) Dumort.	0	2	1
	Scapania compacta (Roth) Dumort.	0	1	1
	Scapania irrigua (Nees) Nees	0	0	1
	Scapania undulata (L.) Dumort.	0	2	0
	TOTAL:	**203**	**61**	**30**

Table 8 Substrate distributions of samples belonging to liverwort families

Family	Epiphytic	Epigeic	Epilithic
Aneuraceae	0	4	0
Aytoniaceae	2	2	1
Conocephalaceae	0	5	4
Fossombroniaceae	1	5	0
Frullaniaceae	101	0	3
Jungermanniaceae	0	1	0
Lejeuneaceae	11	2	4
Lophocoleaceae	1	3	0
Lunulariaceae	0	15	4
Marchantiaceae	0	2	1
Metzgeriaceae	33	1	0
Pallaviciniaceae	0	3	0
Pelliaceae	0	10	3
Plagiochilaceae	0	1	0
Porellaceae	8	1	5
Radulaceae	46	1	2
Scapaniaceae	0	5	3
TOTAL:	**203**	**61**	**30**

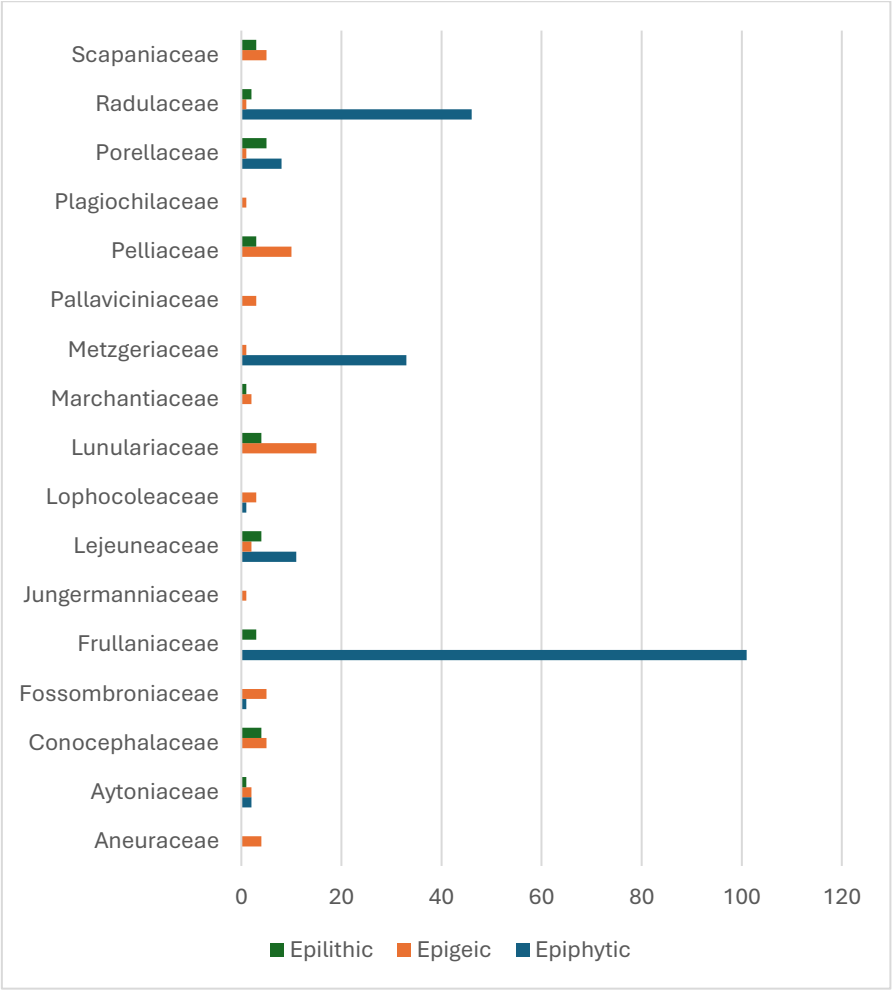

Graph 13 Substrate distributions of samples belonging to liverwort families

DISCUSSION

Liverworts are non-vascular plants that require water for reproduction, which restricts their distribution to moist and shaded habitats. Despite this limitation, they are among the oldest terrestrial plants, having successfully persisted on Earth for over 400 million years. Unlike vascular plants, liverworts lack true roots but possess rhizoids that enable them to attach to substrates. They inhabit a variety of substrates, with their preferences influenced by factors such as pH, surface physical properties, and temperature. Additionally, substrate preferences may vary depending on the specific characteristics of each species.

In this study, the substrate preferences of 294 plant samples representing 29 liverwort species identified in the Yenice district of Çanakkale were analyzed based on various parameters. The objective was to determine which substrate types are preferred by liverworts in the Yenice district. Liverworts were classified as epiphytic, epigeic, or epilithic according to their substrate preferences.

The study revealed that among the 294 liverwort samples collected from the Yenice district, the majority were epiphytic (69.05%), followed by epigeic (21%), and the least were epilithic (10%).

Thalloid and leafy liverworts were also analyzed separately. In thalloid liverworts, the highest proportion was observed in epigeic substrates (49%), followed by epiphytic (37%) and epilithic (14%). Conversely, in leafy liverworts, the highest proportion was recorded in epiphytic substrates (84%), followed by epilithic (9%) and epigeic (7%).

An analysis of the liverwort families revealed that the Frullaniaceae family is highly widespread, with the highest number of samples, a significant portion of which are epiphytic. This abundance contributes to the high proportion of epiphytic liverworts overall. While thalloid species are more frequently associated with the epigeic category, the Metzgeriaceae family exhibits a notable preference for epiphytic substrates, differing from other families.The Yenice district of Çanakkale, the study area, provides suitable habitats for epiphytic liverworts due to its extensive forest cover. Approximately 66% of the district's surface area is composed of forests, a factor that significantly contributes to the abundance of epiphytic liverworts in the region.

Considering these findings, it has been determined that epiphytic liverworts exhibit a wide distribution in the Yenice district, where forested areas are abundant, whereas epigeic species are more prevalent among thalloid liverworts. These results underscore the critical role of natural habitats, particularly forests, in shaping the substrate preferences and distribution patterns of liverworts.

FUNDING

This work was supported by Çanakkale Onsekiz Mart University The Scientific Research Coordination Unit, Project number: FBA-2020-3430

REFERENCES

Ayhan, Ç. K., Taşlı, T. C., Özkök, F. and Tatlı, H. (2020). Land use suitability analysis of rural tourism activities: Yenice, Turkey. *Tourism Management*, *76*, 103949.

Bowman, J. L. (2016). A brief history of Marchantia from Greece to genomics. Plant and Cell Physiology, 57(2), 210-229.

Ezer, T., Seyli, T., Bozdoğan, Ş. G., & Kara, R. (2013). Epifitik Bryofitlerin Ağaç Tercihine Göre Dağılımı. Türk Bilimsel Derlemeler Dergisi, (1), 188-191.

Fry, E., & Fry, A. (1911). The Liverworts, British and Foreign. Witherby & Company.

Keçeli, T. (2004). Batı Karadeniz Bölgesi (Bolu-Zonguldak-Bartın-Kastamonu) Ciğerotları Florası. Ankara Üniversitesi Fen Bilimleri Enstitüsü Biyoloji Ana Bilim Dalı, Doktora Tezi, Ankara.

Şimşek, Ö., (2023a). Ciğerotları, Etnobriyoloji ve Türkiye'de Bulunan Bazı Ciğerotlarının Etnobriyolojik Özellikleri. Matematik ve Fen Bilimleri Üzerine Araştırmalar (pp.153-169), Özgür Yayınları.

Şimşek, Ö., (2023b). Yeşil Sentez İle Nanopartikül Sentezinde Briyofitler. Scıence And Mathematıcs In A Globalızıng World (pp.99-108), Duvar Yayınları.

Şimşek, Ö., (2024). Liverwort (Marchantiophyta) and Hornwort (Anthocerotophyta) Flora of Yenice District (Çanakkale): New Floristic Findings from the Northern Part of Mount Ida (Kaz Dağı). Anatolian Bryology, vol.10, no.2, 95-109.

Şimşek, Ö., Canlı, K., & Gürsu, G. (2016). Karasal Yaşamın Başlangıcında Briyofitler, 2(1-2), 70-74. https://doi.org/10.26672/anatolianbryology.267213

Söderström L, Hagborg A, von Konrat M, Bartholomew-Began S, Bell D, Briscoe L, Brown E, Cargill DC, Costa DP, Crandall-Stotler BJ, Cooper ED, Dauphin G, Engel JJ, Feldberg K, Glenny D, Gradstein SR, He X, Heinrichs J, Hentschel J, Ilkiu-Borges AL, Katagiri T, Konstantinova NA, Larraín J, Long DG, Nebel M, Pócs T, Felisa Puche F, Reiner-Drehwald E, Renner MAM, Sass-Gyarmati A, Schäfer-Verwimp A, Moragues JGS, Stotler RE, Sukkharak P, Thiers BM, Uribe J, Váňa J, Villarreal JC, Wigginton M, Zhang L, Zhu R-L (2015) World checklist of hornworts and liverworts. PhytoKeys 59: 1–828. doi: 10.3897/phytokeys.59.6261

Molecularly Imprinted Conductive Polymer-Based Sensors: Recent Advances

Songül ŞEN GÜRSOY

1- Prof. Dr.; Burdur Mehmet Akif Ersoy Üniversitesi Fen-Edebiyat Fakültesi Kimya Bölümü. ssen@mehmetakif.edu.tr ORCID No: 0000-0002-9506-9822

ABSTRACT

Molecularly imprinted polymers are receiving increasing attention from researchers as sensing materials in sensor design. They have advantages over other biosensor techniques due to their chemical and physical stability, low cost, relatively easy production, reusability and high selectivity. In recent years, they have also proven useful as receptor materials and have been reported for a wide variety of applications. Molecularly imprinted conductive polymers, which provide easy connection to commercially available sensing platforms compared to other sensing methods, have a great application potential with the influence of digitalization. In this study, the situation was determined by presenting conductive polymer-based (polypyrrole, polyaniline and polythiophene) molecular imprinted sensor applications published in the last few years for different analytes. Finally, a vision of the contributions that promising sensor technology will make to the evolution of sensors is shared.

Keywords – molecularly imprinted conducting polymers; polypyrrole; polyaniline; polythiophene

INTRODUCTION

Sensors can be defined as functionalized tools that convert chemical or physical events occurring on a specific surface into understandable signals. Molecularly imprinted polymer (MIP) sensors, which have surfaces coated with a polymer layer containing cavities specific to target molecules, stand out due to their performance in analyte recognition. MIP-based sensors have quite a lot attention in recent years because their robust structure, ease of template removal, simple refilling of cavities, and the ability to tailor these cavities to the molecular structure and geometry of the target analyte. Molecularly imprinted polymers are synthetic materials which mimic the behavior of receptor molecules towards their substrates. Unlike biomolecules, MIPs offer several advantages, including greater stability in various solvent environments, better storage, and reusability due to their resistance to a wider range of temperatures and pH values.

Different methods such as fluorescence (Li et al., 2023:6553), Raman scattering (Yeganegi et al., 2023:125271), surface plasmon resonance (Torrini et al., 2024:116133), and electrochemical techniques (Al Faysal, 2024:126791) combined with MIP sensors are used for the detection of a lot of analytes. Moreover, sensors incorporating a MIP component are effectively utilized for the determination biomarkers, hormones, various chemicals, proteins, and pharmaceuticals, with remarkable detection capabilities (Anirudhan et al., 2018:942; Li et al., 2019:77; Xing et al., 2022:16668).

However, challenges remain in the practical implementation of sensor technology. (Newman and Turner, 2005:2435). Even with these sensors, measurement results and repeatability are affected by storage conditions (Wang et al., 2013:161). Although selectivity can be relatively low for the detection of complex biological compounds, the sensitivity of sensors can be developed by adding modifiers like metal, carbon nanoparticles, and metal oxides to the sensing component.

Initial studies on MIPs were conducted with insulating polymers. MIP research began in the 1970s with silica gel (Polyakov et al, 1937:100; Dickey 1949:227), and continued with extensive research using a wide variety of organic polymers (Wulff, 2013:1359). To date, vinyl and acrylate, based polymers are among the most commonly used (Sajini and Mathew, 2021:100072). The discovery of conducting polymers and their combination with various materials has led to their use in MIPs. Fundamentally, the interplay between the molecule and the template, in terms of the MIP's working mechanism, is especially the similiar for both conducting polymers and insulating. However, using conducting polymers as MIPs offers the advantage of a direct electrical response upon analyte binding.

Combining the electrical conductivity of conducting polymers with the selective recognition properties of molecularly imprinted polymers (MIPs) brings together the advantages of both techniques. This synergistic effect enables the fabrication of sensing devices not possible with insulating polymers (Anantha-Iyengar et al., 2019:1). In MIPs prepared with conducting polymers, the electrical properties at the binding sites change after interaction with the analyte, enabling direct detection. These specific binding sites enhance the affinity of the electrochemical sensor towards the target analyte. Conducting polymers, acting as both receptor and transducer, can also reduce interference from similar compounds. This is because these compounds differ not only in their interactions at the binding sites but also in the resulting electrochemical signals (Blanco-López et al., 2004:1922). Furthermore, they retain all the advantages offered by insulating polymers.

A crucial step in achieving optimal selectivity, sensitivity, stability, and rebinding capacity in conductive polymer-based molecularly imprinted polymers (MIPs) is the choice of a monomer that can provide optimal interactions with the template. Conductive polymers are intrinsically electrically conductive and possess high electrical capacitance (Zao et al, 2018:30; Wang et al, 2019: 989). They also adhere strongly to electrode surfaces, forming mechanically stable layers (Ratautaite et al, 2013:16). Conductive polymers are highly efficient at transferring electrical charges. Due to these properties, they are utilized for electron transfer from certain redox proteins and other biological structures (Oztekin et al, 2011:2541). They are also used with various transducers, sometimes as a layer and sometimes as the transducer itself.

Conductive polymers not only provide electrical conductivity but can also serve as matrices for the immobilization of biomaterials (DNA, enzymes, antibodies, antigens, receptors, etc.) that specifically bind to target analytes. Although biomolecules offer specific selectivity for target analytes, their lack of robustness against varying pH and temperature conditions and their high cost necessitate an alternative approach. Molecular imprinted polymer matices have appeared as a viable alternative, serving as synthetic receptors, with conductive polymers finding significant applicability in this area. The most studied conductive polymers in MIP sensor systems are polyaniline (PANI), polypyrrole (PPy), and polythiophene (PTH). (Holguín et al, 2019:29; Kumar et al, 2020:115938; Tekbaşoğlu et al, 2017:81).

2.1. Polypyrrole based MIP sensors

Polypyrrole, a conducting polymer, is widely used in chemical sensors and biosensors. It offers numerous advantages, including facile preparation via electropolymerization, good redox properties, high environmental stability, favorable electrical characteristics, and notably, biocompatibility. As an intrinsicly conductive polymer, polypyrrole (PPy) does not require any additives to enhance conductivity. Therefore, it is commonly employed in the synthesis of molecularly imprinted polymers (MIPs) for different kind of analits, including chemical species and biomolecules. PPy-MIP based sensors enable rapid, sensitive, and selective determination of bacteria, drugs, toxins, pesticides, dyes, ions, and various protein-based compounds.

In a study conducted by Liustrovaite et al., a sensor based on molecularly imprinted polymers (MIPs) was studied for the determination of Listeria monocytogenes. The sensor utilized platinum and screen-printed carbon electrodes (SPCE) that were modified with a polypyrrole layer created from a polymerization solution containing pyrrole and Listeria monocytogenes bacteria suspended in phosphate buffer (PBS) at neutral pH. The bacteria embedded in the imprinted cavities were extracted using trypsin and L-lysine enzymes, and these methods were compared to more traditional extraction techniques involving sulfuric acid and acetic acid. The findings indicated that the limit of detection (LOD) for the trypsin-prepared MIP-Ppy/SPCE was 70 CFU/mL, within a linear detection range of 300 to 6700 CFU/mL (Liustrovaite et al., 2023:1597).

In another study that employed polypyrrole, a new molecularly imprinted sensor was developed for detection of ethanethiol in wine. The MIP sensor was constructed on the glassy carbon electrode (GCE) using electrochemical methods. The addition of gold nanoparticles (AuNPs) significantly improved the sensor's sensitivity by enhancing its conductivity and increasing the effective surface area. The linear working range for ethanethiol was established to be between 0.3 and 3.1 mg L^{-1} and detection limit was 0.4 mg L^{-1}. The ethanethiol sensor, named AuNP/MIP/GCE, was

successfully utilized for analyzing wine samples, achieving recovery rates between 99% and 107% (Asunción Alonso-Lomillo et al., 2023:123936).

Elamin and his team utilized a molecularly imprinted polymer (MIP) sensor that incorporates copper nanoparticles for the detection of sulfadiazine, an important antibacterial compound. The sensor demonstrated excellent stability and reproducibility, with a working range from 10^{-9} to 10^{-5} mol L^{-1} and 3.1×10^{-10} mol L^{-1} detection limit. This sensor tested on real milk samples and it allowed for the sensitive detection of sulfadiazine. This novel approach achieved the lowest detection limit reported to date compared to other electrochemical sensors for sulfadiazine (Elamin et al., 2023:1270).

Due to their damaging effects on both environment and human health, dyes have attracted the attention of researchers, and suitable methods for their detection have been developed. Boguzaite et al. (2023) focused on developing molecularly imprinted polypyrrole based sensor for the recognition of methylene blue (MB) among these dyes. The MIP was directly deposited onto the ITO coated glass electrode. Changes in optical absorbance were used to evaluate the MB adsorption capacity of the polypyrrole-based MIP layer. A linear working range was detected in the working concentration range from 0.1 μM to 10 mM. As a result of this study the methylene blue retained its native (unpolymerized) form during the deposition of the MIP (Boguzaite et al., 2023:549).

PPy-based MIP sensors are also used for ion determination. In one study, a polypyrrole-based molecularly imprinted polypyrrole sensor for the detection of phosphate ion was successfully synthesized and characterized. The phosphate-imprinted MIP synthesis was performed by depositing polypyrrole on a gold wire electrode surface using cyclic voltammetry. The phosphate ion imprinted electrode's response investigated potentiometrically. It exhibited an excellent linear response with good sensitivity in the working range of 1×10^{-7} to 0.1 M. It also demonstrated high selectivity for phosphate ions in the presence of interfering anions (Cl^-, NO_3^-, and SO_4^{2-}) (Hikmat and Tasfiyati, 2023:117).

The determination of components found in blood is the most common studies in the sensor field. Dopamine is one of these components. Dopamine is an important component working as neurotransmitter in the central nervous system of mammalian. Therefore, due to its various pathophysiological and physiological effects, dopamin's detection is important for clinical diagnosis and following the pharmacological treatment. A molecularly imprinted polymer modified screen-printed electrode was developed for dopamine detection in this study. Comparison of polypyrrole based molecular imprinted sensor with non-imprinted based screen printed electrodes indicated that high selectivity, sensitivity and reproducibility of the MIP based dopamine electrode. The sensitivity was calculated as 0.078 μA μM^{-1}. The detection limit was 0.8 μM. The linear

concentration range was detected between 0.8 and 45 μM, and a dynamic range up to 350 μM were achieved. The sensor was successfully tested on real human samples to evaluate its potential as a screening method for biochemical analysis (Merli et al., 2024:2528).

The SARS-CoV-2 glycoprotein was employed as the template molecule, while polypyrrole (Ppy), a conductive polymer generated through electrochemical methods, used as the matrix for creating molecular imprints. PPy layers were electrochemically accumulated onto platinum disc platinum electrode in two different modes. The first one is molecularly imprinted and the second one is non-imprinted polypyrrole. The performance of these two form of electrodes was tested using pulsed amperometric detection (PAD). The integrated Cottrell equation (Anson plot) was utilized to calculate the charge that flowed through the MIP and NIP layers during the evaluation of the PAD measurement results. The reaction between polypyrrole based MIP and SARS-CoV-2 spike glycoproteins was analyzed using Anson plot-based calculations, which revealed that SARS-CoV-2-S glycoproteins interacted more strongly with MIP-Ppy than with NIP-Ppy (Ratautaite et al., 2023:123981).

2.2. Polyaniline based MIP sensors

Polyaniline (PANI), though not as widely used as PPy, is similarly popular and preferred in sensor applications. PANI has some remarkable properties, such as its reversible dopability, good pH and environmental stability, and superior electrical conductivity (Kang et al., 1998:277). PANI generally possesses modifiable properties. PANI is also becoming advantageous in various applications by forming nanofibers because of its high surface area to its volume (Long et al., 2011:1415). When using the aniline monomer, as it is a toxic compound that causes methemoglobinemia and splenic toxicity (Iwersen-Bergmann et al., 2000:171). Examples of some MIP sensors designed in recent years using polyaniline are presented.

The phenylalanine (Phe) sensing performance of polyaniline (PANI)-based molecularly imprinted polymers (MIPs) was investigated using both glassy carbon (GC) and indium tin oxide (ITO) electrodes. PANI-MIP/ITO exhibited clearer and more distinct redox responses for Phe detection compared to PANI-MIP/GCE. The interaction mechanism between PANI and Phe was also explored through molecular computations. The specificity of PANI-MIP for Phe detection was studied in the presence of similar amino acids and organic molecules such as ascorbic acid, allantoin, sucrose, and urea. The sensor showed 4.88 μM a detection limit, which is similar with previously reported values. This study demonstrates the promise of MIP-based electrochemical sensing (Sarangi et al, 2024:10258).

The early, efficient, and accurate identification of hypothyroidism and hyperthyroidism is vital for timely intervention. A MIP sensor based on

polyaniline (PANI) was developed for the detection of thyroxine (T4), a key biomarker in this context, by imprinting T4 onto a PANI matrix immobilized on ITO electrodes. The MIP sensor was characterized with spectroscopic, chromatographic, and electrochemical methods. It exhibited a linear working range between 5 and 50 pg mL^{-1} and a detection limit of 6.16 pg mL^{-1}. Recovery values from saliva samples ranged from 96% to 115.2%. The developed PANI based MIP sensor demonstrated high selectivity against various interfering substances, indicating its significant potential for future point-of-care applications (Singh et al., 2024:147).

In recent years, a molecularly imprinted gas sensor has been developed to detect the smell of strawberries. Furaneol, known as 2,5-dimethyl-4-hydroxy-3(2H)-furanone, is identified as a key biomarker for strawberry aroma. However, measuring the concentration of furaneol poses challenges due to its weak adsorption characteristics, polarity, and non-reactive nature. This study introduced a polyaniline-based molecularly imprinted polymer (MIP). The MIP-PANI gas sensor successfully achieved sensitive and selective detection of furaneol gas at room temperature and under varying humidity levels. The studies about PANI based molecular imprinted and non-imprinted sensors indicated that MIP sensor has stronger interaction with furaneol than that of NIP sensor. Additionally, the MIP-PANI sensor was compared to a commercial electronic nose system for real strawberries. These results indicate that MIP-PANI has promising potential for cheap, rapid and specific detection of furaneol (Kim et al., 2023:1542).

The COVID-19 pandemic began in 2019 and continued for several years, has prompted researchers to develop rapid, econamic, basic, and widely available virus sensors. In this way, viral outbreaks and economic losses caused by outbreak-related closures can be prevented. To this end, a virus sensor was created using molecular imprinting technology with polyaniline (PANI) polymer that is in shape of wearable paper for the detection of lentivirus as a proof of concept. This sensor was capable of detecting lentivirus in liquid with a 4181 TU/mL detection limit and in aerosols with a detection activity of 0.33% to 2.90% at gaps from 30 cm to 60 cm.

The sensor was fabricated by co-polymerizing a solution of aniline monomer and the virus onto polyethylene terephthalate (PET) paper substrate. An interesting dry measurement method was developed, enabling aerosol virus detection within 1.5 hours after the virus was aerosolized onto the MIP sensor. This technique was based on a mechanism that affected the conductivity of the PANI film through the interaction of the aerosolized virus with the molecularly imprinted virus templates on the PANI. The designed virus sensor was used to create a paper-based face mask for detecting viruses in aerosols. This biosensor shows excellent stability over long periods under dry medium, offering an alternative technique for detecting viral infections (Batra et al., 2023:861).

2.3. Polythiophene based MIP sensors

Studies on MIP sensors prepared using polythiophene are relatively fewer compared to those using polypyrrole and polyaniline, which were mentioned previously. Thiophene-based MIP sensors are more commonly based on thiophene derivatives rather than polythiophene itself. Creatinine concentration in human saliva serves as an important biomarker for kidney disease. Monitoring creatinine levels is vital, especially for dialysis patients and those with kidney disorders. This study presents a disposable sensor developed for rapid detection of creatinine. Besides this sensor offers continuous determinatin of even small quantities of creatinine. The fabricated sensor features a polythiophene matrix integrated with creatinine-imprinted niobium oxide nanoparticles. The developed sensor demonstrated a high sensitivity (4.614 mA cm^{-2} nM^{-1}), very low detection limit (34 pM), and effective selectivity for creatinine determination in the presence of other analytes that may be found in human saliva. These molecules are tyrosine, glucose, urea, and glutamine. The developed sensor was tested for genuine saliva samples, and demonstrated significant potential for real-time monitoring of creatinine levels in patients with muscle and kidney-related disorders (Saddique et al., 2024:3644).

In recent years, another study on polythiophene-based MIP sensors presented an enzyme-free electrochemical sensor design for the selective detection and monitoring of uric acid. Gouty arthritis, which occurs with the accumulation of uric acid (UA) crystals in arthrosis, is a painful disease and effective and accessible diagnostic methods need to be developed. The developed sensor is disposable. Some electrochemical measurement methods were used for the study. The sensor exhibits excellent UA detection performance with a wide working range (1–500 μM), a sensitivity of 2.91 μA cm−2·μM−1, a detection limit of 354 nM, and significant selectivity against common interfering substances. It was also tested in real saliva samples in this study and showed a recovery of 90.4%. As a result, the sensor is sensitive and cost-effective (Shahzad et al, 2023: 097505).

MIP sensors prepared using polythiophene are being tested for the determination of antibiotic residues. In one such study, a protocol was proposed for in situ monitoring of azithromycin (AZN) leaching into source waters, utilizing a novel functional monomer containing a phenyl group, a stronger electron donor, to compete for electropolymerization. Various monomers were investigated in this study, and the performance of the resulting sensors was compared. A monothiophene with a moderate initiation potential was also employed as a linker to overcome steric hindrance. The resulting AZN sensor showed high selectivity and good performance for various macrolide antibiotics with a low detection limit (0.120 μM) (Pan et al, 2021: 117670).

Polythiophene-based MIP sensors are also encountered in analyses conducted for food safety. Chlorpyrifos is a pesticide often used in agriculture, particularly in vegetable cultivation, to control pests and increase crop yields. While chlorpyrifos is moderately toxic, its widespread usage caused the accumulation of residues or derivatives in soil and water. In a 2022 study, molecular imprinting was employed using multi-walled carbon nanotubes and thiophene derivative monomers to design a novel electrochemical sensor for chlorpyrifos detection in vegetable samples. For this purpose, a copolymer of 3-thiopheneacetic acid and 3,4-ethylenedioxythiophene was synthesized on carbon nanotubes. A glassy carbon electrode was coated via drop-casting for chlorpyrifos detection. Under optimized conditions, the resulting sensor exhibited a limit of detection (LOD) of 4.0×10^{-12} M for chlorpyrifos. Its high repeatability and reusability make this sensor a promising material for pesticide monitoring in vegetable samples (Anirudhan et al, 2022:132010).

3. CONCLUSIONS

Insulating polymers used in non-conductive polymer-based molecularly imprinted sensors are insufficient for the chemical detection of target analytes. Furthermore, electron transfer during the interacting of the molecule to the matrix and subsequent transduction cannot be achieved with insulating polymers. From these two perspectives, conductive polymer-based molecularly imprinted sensors enable selective and highly sensitive recognition of the analyte. The incorporation of additives into conductive polymers and the implementation of surface imprinting strategies enhance the conductivity while also improving the binding kinetics.

The purpose of this review is to put forth an overview of conductively-based molecularly imprinted sensors and their applications designed in the last few years. Conductive polymer-based molecularly imprinted sensors have attracted interest due to their simplicity and applicability for the recognition of a wide range of analytes, such as bacteria, viruses, antibiotics, ions, hormones, and aroma compounds. When considering the limited number of publications in this area, it can be safely asserted that interest in this field will increase strongly.

REFERENCES

Al Faysal, A., Cetinkaya, A., Erdoğan, T., Ozkan, S.A., Gölcü, A. (2025). Comparative study of two MIP-based electrochemical sensors for selective detection and quantification of the antiretroviral drug lopinavir in human serum. *Talanta*, 281, 126791.

Alonso-Lomillo, M.A and Domínguez-Renedo, O. (2023). Molecularly imprinted polypyrrole based electrochemical sensor for selective determination of ethanethiol, *Talanta*, 253, 123936.

Anantha-Iyengar, G., Shanmugasundaram, K., Nallal, M., Lee, K.-P., Whitcombe, M.J., Lakshmi, D., Sai-Anand, G. (2019). Functionalized conjugated polymers for sensing and molecular imprinting applications. *Prog. Polym. Sci.* 88, 1-129.

Anirudhan, T., Deepa, J. (2018). Electrochemical sensing of cholesterol by molecularly imprinted polymer of silylated graphene oxide and chemically modified nanocellulose polymer *Mater. Sci. Eng.* C, 92, 942-956.

Anirudhan, T.S., Athira, V.S., Nair, S.S. (2022). Detection of chlorpyrifos based on molecular imprinting with a conducting polythiophene copolymer loaded on multi-walled carbon nanotubes, *Food Chemistry*, 381, 132010.

Batra, J. S., Chi, T. -Y., Huang, M. -F., Zhu, D., Chen, Z., Lee, D. -F., & Kameoka, J. (2023). Wearable Biosensor with Molecularly Imprinted Conductive Polymer Structure to Detect Lentivirus in Aerosol. Biosensors, 13(9), 861.

Blanco-López, M.C., Gutiérrez-Fernández, S., Lobo-Castañón, M.J., Miranda-Ordieres, A.J., Tuñón-Blanco, P. (2004). Electrochemical sensing with electrodes modified with molecularly imprinted polymer films. Anal. Bioanal. Chem. 378, 1922-1928.

Boguzaite, R., Pilvenyte, G., Ratautaite, V., Brazys, E., Ramanaviciene, A., Ramanavicius, A. (2023). Towards Molecularly Imprinted Polypyrrole-Based Sensor for the Detection of Methylene Blue. *Chemosensors*, 11, 549.

Dickey, F.H. (1949). The Preparation of Specific Adsorbents. 35, (pp. 227-229). Proc. Natl. Acad. Sci. USA

Drobysh, M., Ramanavicius, A., Baradoke, A. (2023). Polyaniline-based electrochemical immunosensor for the determination of antibodies against SARS-CoV-2 spike protein, *Science of The Total Environment*, 862, 160700.

Elamin, M.B., Ali, S.M.A., Essousi, H., Chrouda, A., Alhaidari, L.M., Jaffrezic-Renault, N., Barhoumi, H. (2023). An Electrochemical Sensor for Sulfadiazine Determination Based on a Copper Nanoparticles/Molecularly Imprinted Overoxidized Polypyrrole Composite. *Sensors*, 23, 1270.

Hikmat, H. and Tasfiyati, A.N. (2023). Synthesis and Characterization of a Polypyrrole-Based Molecularly Imprinted Polymer Electrochemical Sensor for the Selective Detection of Phosphate Ion, *Journal of Analytical Chemistry*, 78(1), 117-124.

Holguín, M., Rojas Álvarez, O.E., Arizabaleta, C.A., Torres, W. (2019). Molecular dynamics of the interaction of l-tryptophan with polypyrrole oligomers. *Comput. Theor. Chem*, 1147, 29-34.

Iwersen-Bergmann, S., Schmoldt, A. (2000). Acute intoxication with aniline: Detection of acetaminophen as aniline metabolite. *Int. J. Leg. Med.* 113, 171-174.

Kang, E.-T., Neoh, K.G., Tan, K.L. (1998). Polyaniline: A polymer with many interesting intrinsic redox states. *Prog. Polym. Sci.* 23, 277-324.

Kim, W., Lee, D., Wu, G., Cha, Y.L., Md. M, Shakir., Cho, S., Kim, D.-J. (2023). Molecularly Imprinted Chemiresistive Sensor for Specific Recognition of Furaneol as a Biomarker of Strawberry Flavor Conditions, *ACS Sens.* 8(4), 1542-1549.

Kumar, V., Mirzaei, A., Bonyani, M., Kim, K.-H., Kim, H.W., Kim, S.S. (2020). Advances in electrospun nanofiber fabrication for polyaniline (PANI)-based chemoresistive sensors for gaseous ammonia. *TrAC Trends Anal. Chem*, 129, 115938.

Li, B., Tan, H., Anastasova, S., Power, M., Seichepine, F., Yang, G.-Z. (2019). A bio-inspired 3D micro-structure for graphene-based bacteria sensing, *Biosens. Bioelectron*, 123, 77-84.

Li, B., Qi, J., Liu, F. *et al.* (2023). Molecular imprinting-based indirect fluorescence detection strategy implemented on paper chip for non-fluorescent microcystin. *Nat Commun* 14, 6553.

Liustrovaite, V., Pogorielov, M., Boguzaite, R., Ratautaite, V., Ramanaviciene, A., Pilvenyte, G., Holubnycha, V., Korniienko, V., Diedkova, K., Viter, R., & Ramanavicius, A. (2023). Towards Electrochemical Sensor Based on Molecularly Imprinted Polypyrrole for the Detection of Bacteria—*Listeria monocytogenes*. Polymers, 15(7), 1597.

Long, Y.-Z., Li, M.-M., Gu, C., Wan, M., Duvail, J.-L., Liu, Z., Fan, Z. (2011). Recent advances in synthesis, physical properties and applications of conducting polymer nanotubes and nanofibers. *Prog. Polym. Sci.* 36, 1415-1442.

Merli, D., Cutaia, A., Hallulli, I., Bonanni, A., & Alberti, G. (2024). Molecularly Imprinted Polypyrrole-Modified Screen-Printed Electrode for Dopamine Determination. Polymers, 16(17), 2528.

Newman, J.D., Turner, A.P. (2005). Home blood glucose biosensors: a commercial perspective *Biosens. Bioelectron*, 20 (12), 2435-2453.

Sajini, T., Mathew, B. (2021). A brief overview of molecularly imprinted polymers: Highlighting computational design, nano and photo-responsive imprinting. *Talanta Open*, 4, 100072.

Oztekin, Y., Ramanaviciene, A., Yazicigil, Z., Solak, A.O., Ramanavicius, A. (2011). Direct electron transfer from glucose oxidase immobilized on polyphenanthroline-modified glassy carbon electrode. *Biosens. Bioelectron*, 26, 2541-2546.

Pan, Y., Shan, D., Ding, L., Yang, X., Xu, K., Huang, H., Wang, J., Ren, H. (2021). Developing a generally applicable electrochemical sensor for detecting macrolides in water with thiophene-based molecularly imprinted polymers, *Water Research*, 205, 117670.

Polyakov, M.V., Kuleshina, L., Neimark, I. (1937). On the Dependence of Silica Gel Adsorption Properties on the Character of Its Porosity. 10, (pp. 100-112) *Zhurnal Fizieskoj Khimii/Akad. SSSR*.

Ratautaite, V., Boguzaite, R., Brazys, E., Plausinaitis, D., Ramanavicius, S., Samukaite-Bubniene, U., Bechelany, M., Ramanavicius, A. (2023). Evaluation of the interaction between SARS-CoV-2 spike glycoproteins and the molecularly imprinted polypyrrole, *Talanta*, 253, 123981.

Ratautaite, V., Ramanaviciene, A., Oztekin, Y., Voronovic, J., Balevicius, Z., Mikoliunaite, L., Ramanavicius, A. (2013). Electrochemical stability and repulsion of polypyrrole film. *Colloids Surf. A Physicochem. Eng. Asp.* 418, 16-21.

Saddique, Z., Saeed, M., Faheem, M., Bajwa, S.Z., Mujahid, A. and Afzal, A. (2024). Core-shell niobium(V) oxide@molecularly imprinted polythiophene nanoreceptors for transformative, real-time creatinine analysis, *Nanoscale Adv*,6, 3644-3654.

Sarangi, S., Srivastava, R. Gogoi-Tiwari, J., Kar, R.K. (2024). Electrochemical Sensing of Phenylalanine using Polyaniline-Based Molecularly Imprinted Polymers, *J. Phys. Chem. B.* 128(41),10258-10271.

Shahzad, N., Ajmal R. and Afzal, A. (2023). Non-Enzymatic Electrochemical Sensors for Accurate and Accessible Uric Acid Detection *Journal of The Electrochemical Society, J. Electrochem. Soc.* 170, 097505.

Singh, D., Roy, S., Mahindroo, N., Mathur, A. (2024). Design and development of an electroanalytical sensor based on molecularly imprinted polyaniline for the detection of thyroxine, *Journal of Applied Electrochemistry*, 54, 147-161.

Tekbaşoğlu, T.Y., Soğanci, T., Ak, M., Koca, A., ¸Sener, M.K. (2017). Enhancing biosensor properties of conducting polymers via copolymerization: Synthesis of EDOT-substituted bis(2-pyridylimino)isoindolato-palladium complex and electrochemical sensing of glucose by its copolymerized film. *Biosens. Bioelectron*, 87, 81-88.

Torrini, F., Ferraro, G., Fratini, E., Palladino, P., Scarano, S., Minunni, M. (2024). Toward nano-sized imprinted norepinephrine-derived biopolymer as artificial receptors for detecting IgG1 by surface plasmon resonance. *Biosensors and Bioelectronics*, 252, 116133.

Yeganegi, A., Fardindoost, S., Tasnim, N., Hoorfar, M. (2024). Molecularly imprinted polymers (MIP) combined with Raman spectroscopy for selective detection of Δ^9-tetrahydrocannabinol (THC). *Talanta*, 267, 125271.

Wang, G., He, X., Wang, L., Gu, A., Huang, Y., Fang, B., Geng, B., Zhang, X. (2013). Non-enzymatic electrochemical sensing of glucose *Microchim. Acta*, 180, 161-186.

Wang, Y., Chen, Y., Liu, Y., Liu, W., Zhao, P., Li, Y., Dong, Y., Wang, H., Yang, J. (2019). Urchin-like Ni1/3Co2/3(CO3)0.5OH_0.11H2O anchoring on polypyrrole nanotubes for supercapacitor electrodes. *Electrochim. Acta*, 295, 989-996.

Wulff, G. (2013). Fourty years of molecular imprinting in synthetic polymers: Origin, features and perspectives. *Microchim. Acta*, 180, 1359-1370.

Xing, G., Wang, C., Liu, K., Luo, B., Hou, P., Wang, X., Dong, H., Wang, J., Li, A. (2022). A probe-free electrochemical immunosensor for methyl jasmonate based on a Cu-MOF–carboxylated graphene oxide platform *RSC Adv*, 12 (26), 16688-16695.

Zhao, Z.; Yu, T.; Miao, Y.; Zhao, X. Chloride ion-doped polyaniline/carbon nanotube nanocomposite materials as new cathodes for chloride ion battery. Electrochim. Acta 2018, 270, 30-36.

On Inversions in Generalized Taxicab Space

Ayşe BAYAR [1]

Ziya AKÇA [2]

1- Prof. Dr.; Eskişehir Osmangazi University, Department of Mathematics and Computer Science, Faculty of Science,. akormaz@ogu.edu.tr ORCID No: 0000-0002-2210-5423
2- Prof. Dr.; Eskişehir Osmangazi University, Department of Mathematics and Computer Science, Faculty of Science,. zakca@ogu.edu.tr ORCID No: 0000-0001-6379-0546

ABSTRACT

This study delves into the concept of inversion within the three-dimensional generalized taxicab geometry, a field that adapts classical geometric transformations to non-Euclidean metric spaces. In traditional geometry, circular inversion is a transformation mapping points in analytical space to one another, with profound implications for solving geometric problems. This concept has been extended to three-dimensional spaces by replacing the circle of inversion with a sphere, allowing for transformations that interchange the interior and exterior of the sphere. Generalized forms of such transformations exhibit distinct properties in non-Euclidean metric geometries, such as those using the taxicab distance.

Building upon this foundation, the study explores inversion within the generalized taxicab sphere, defining its core properties and analyzing the images of points under these transformations. By introducing the directed generalized taxicab length for line segments, it establishes the groundwork for defining critical geometric constructs: the generalized taxicab cross-ratio and harmonic conjugates. These constructs, integral to classical inversion theory, are reinterpreted and examined in the context of the generalized taxicab space.

Key findings of this research include the interplay between inversion, cross-ratios, and harmonic conjugates, shedding light on the unique geometric relationships in this non-Euclidean setting. By advancing the understanding of spherical inversions in generalized taxicab geometry, this work opens avenues for further exploration and application in broader mathematical contexts.

Keywords – Generalized taxicab geometry, cross-ratio, spherical inversions, distance, harmonic conjugates

INTRODUCTION

Inversion in a circle is a fundamental geometric transformation that maps one point in an analytical space to another. This transformation plays a significant role in geometry, serving as a powerful tool for analyzing and solving a wide range of problems and theorems. In recent years, metric geometries based on various distance functions have been extensively studied and developed. For more information on this subject, see the studies (Akça and Kaya, 2004:591), (Çolakoğlu, 2018:83), (Çolakoğlu, 2019:1359), (Ekmekçi et al., 2015:159), (Ekmekçi et al., 2015:27), (Gelisgen and Kaya, 2008:187), (Krause, 1975), (Menger, 1952), (Minkowski, 1967). Circular inversion maps have also been explored using different distance functions, such as the taxicab distance, maximum distance, and Chinese Checkers

distance (Bayar and Ekmekçi, 2014:33), (Ekmekçi, 2023:1), (Ekmekçi and.Bilgin, 2023:50), (Pekzorlu and Bayar, 2022:28), (Yüca and Can, 2020:26).

The concept of circular inversion has been extended to three-dimensional spaces by replacing the circle of inversion with a sphere (Ramirez and Rubiano, 2016:132). In this generalized form, inversion with respect to a sphere is a transformation that interchanges the interior and exterior of the sphere. Specifically, points outside the sphere are mapped to corresponding points inside it, while points inside the sphere are mapped to the exterior.

This concept has also been extended to certain three-dimensional non-Euclidean spaces, where inversions with respect to spheres exhibit distinct properties not seen in Euclidean geometry. In these non-Euclidean settings, the behavior of the transformation varies, resulting in new and unique geometric relationships. Several key characteristics of spherical inversion in these spaces have been thoroughly explored and analyzed, which has contributed to a deeper understanding of the transformation and broadened its range of potential applications (Can, 2022:100), (Cırık and Ekmekçi, 2022:360), (Pekzorlu and Bayar, 2020:1498), (Pekzorlu and Bayar, 2020:45).

In this article, we focus on developing the concept of spherical inversion within the framework of generalized taxicab geometry. Specifically, we define the inversion process with respect to a sphere in this metric space and establish several important properties of this newly formulated transformation. In addition to defining spherical inversion, we introduce key related constructs such as inverse points, the cross ratio, and harmonic conjugates, as they apply to generalized taxicab space.

PRELIMINARIES

The Euclidean space $\mathbf{R}^3$ and the taxicab space $\mathbf{R}_T^3$ share many similarities. Although the distance function in (Akça and Kaya, 2004:591) differs, the points, lines, and angle measurements remain consistent. In the three-dimensional taxicab space, the inversion is defined with respect to a taxicab sphere, and its properties are detailed in (Pekzorlu and Bayar, 2020:45). In (Gelisgen and Kaya, 2008:187), the isometries that preserve the taxicab metric in $\mathbf{R}_T^3$ are identified. Then, In (Çolakoğlu, 2019:1359) and (Çolakoğlu, 2018:83), Euclidean isometries preserving the generalized taxicab metric are determined. These findings are specified for the generalized taxicab distance function in three dimensions, which encompasses the taxicab distance function as a special case.

Definition 1. The generalized taxicab distance between locations $P_1 = (x_1, y_1, z_1)$ and $P_2 = (x_2, y_2, z_2)$ in $\mathbf{R}^3$ is defined as follows. For any positive real numbers $a, b,$ and $c,$ the function

$$d_{Tg} : \mathbf{R}^3 \times \mathbf{R}^3 \to [0, \infty)$$

is given by

$$d_{Tg}(P_1, P_2) = a\,|x_2 - x_1| + b\,|y_2 - y_1| + c\,|z_2 - z_1|,$$

which is called generalized taxicab distance function in $\mathbf{R}^3$. Here, the real numbers $a, b,$ and c are all positive. The space endowed with the generalized taxicab metric d_{Tg} is denoted by $\mathbf{R}^3_{T_g}$.

This is known as the generalized taxicab distance function in $\mathbf{R}^3$. In this case, the numbers $a, b,$ and c are positive real numbers. $\mathbf{R}^3_{T_g}$ is the space provided with the generalized taxicab metric d_{Tg}.

The generalized taxicab distance d_{Tg} between locations $P_1 = (x_1, y_1, z_1)$ and $P_2 = (x_2, y_2, z_2)$ is a family of distance functions, dependent on the positive values of numbers $a, b,$ and c, as the definition implies. When $a = b = c = 1$, the generalized taxicab distance reduces to the standard taxicab distance in $\mathbf{R}^3$, representing a specific instance.

Definition 2. The set of points (x, y, z) in the space that satisfy the equation

$$a\,|x| + b\,|y| + c\,|z| = 1$$

is the unit generalized taxicab sphere in $\mathbf{R}^3_{T_g}$. Its vertices are $A_1 = (\frac{1}{a}, 0, 0), A_2 = (-\frac{1}{a}, 0, 0), A_3 = (0, \frac{1}{b}, 0), A_4 = (0, -\frac{1}{b}, 0), A_5 = (0, 0, \frac{1}{c}),$ $A_6 = (0, 0, -\frac{1}{c})$, and it forms an octahedron (see Figure 1). The unit generalized taxicab sphere transforms into a regular octahedron if $a = b = c$. Specifically, when $a = b = c = 1$ the unit taxicab sphere is obtained. In this case, the unit taxicab sphere in $\mathbf{R}^3$ corresponds to the set of points satisfying the equation $|x| + |y| + |z| = 1$, which also forms an octahedron with vertices at (±1,0,0), (0,±1,0),(0,±1,0), and (0,0,±1).

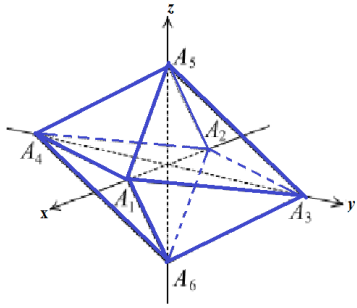

Figure 1

TAXICAB SPHERICAL INVERSIONS

The concept of spherical inversion in the generalized taxicab space $\mathbf{R}^3_{T_g}$ is inspired by the analogous notion in the traditional taxicab space $\mathbf{R}^3_T$. In both cases, inversion serves as a transformation that maps points in the space in such a way that their distances from a fixed center are related in a reciprocal manner. The following definitions, lemmas, and theorems outline the properties and behavior of this inversion within the framework of generalized taxicab geometry.

Definition 3. Let C_{T_g} be a generalized taxicab sphere centered at a point O with radius r in $\mathbf{R}^3_{T_g}$. The inversion with respect to the generalized taxicab sphere C_{T_g}, denoted by $I_{T_g(O,r)}$, is a function defined as follows:

$$I_{T_g(O,r)} : \mathbf{R}^3_{T_g} - \{0\} \to \mathbf{R}^3_{T_g} - \{0\}$$

This function takes a point P and maps it to a point P' on the line joining O and P, such that the taxicab distance between O and P, denoted by $d_{T_g}(O,P)$, satisfies:

$$d_{T_g}(O,P) \cdot d_{T_g}(O,P') = r^2.$$

The point P' is said to be the generalized taxicab spherical inverse of P with respect to the sphere C_{T_g}. The sphere C_{T_g} is referred to as the sphere of inversion, O is called the center of inversion in $\mathbf{R}^3_{T_g}$.

Similar to reflections, generalized taxicab spherical inversions are involutions, meaning that applying the inversion twice yields in the identity transformation. The fixed points of $I_{T_g(O,r)}$ are precisely the points that lie on the generalized taxicab sphere C_{T_g} with center O and the radius r.

Lemma 4. Let C_{T_g} be a generalized taxicab sphere with the center O and the radius r in $\mathbf{R}^3_{T_g}$. Let $I_{T_g(O,r)}$ be a generalized taxicab spherical inversion with respect to C_{T_g}. If the point P lies outside C_{T_g}, then its inverse point P', will be inside C_{T_g}, and vice versa.

Proof. Assuming that point P is outside of C_{T_g}, then $d_{Tg}(O,P) > r$. $d_{Tg}(O,P) \cdot d_{T_g}(O,P') = r^2$ if $P' = I_{T_g(O,r)}(P)$. Thus, $d_{Tg}(O,P') < r$ and $r^2 = d_{T_g}(O,P) \cdot d_{T_g}(O,P') > r \cdot d_{Tg}(O,P')$.

At the point O, the inversion $I_{T_g(O,r)}$ is not defined. However, the inversion $I_{T_g(O,r)}$ becomes a one-to-one map on the extended generalized taxicab sphere by adding a point at infinity, represented by O_∞, to the generalized taxicab space. This point is the inverse of the center O of the generalized taxicab inversion sphere C_{T_g}.

Theorem 5. Let C_{T_g} be a generalized taxicab sphere centered at $O=(0,0,0)$ and with the radius r in $\mathbf{R}^3_{T_g}$. If $P=(x,y,z)$ and $P'=(x',y',z')$ are inverse points with respect to the taxicab spherical inversion $I_{T_g(O,r)}$, then

$$\begin{cases} x' = \frac{r^2 x}{\left(a|x|+b|y|+c|z|\right)^2} \\ y' = \frac{r^2 y}{\left(a|x|+b|y|+c|z|\right)^2} \\ z' = \frac{r^2 z}{\left(a|x|+b|y|+c|z|\right)^2} \end{cases}.$$

Proof. Assume that, with regard to the generalized taxicab spherical inversion $I_{T_g(O,r)}$, $P=(x,y,z)$ and $P'=(x',y',z')$ are inverse points. Since the rays OP and OP' are pointing in the same direction and the points P and P' are collinear are collinear with the center O,

$$OP' = k.OP,\ k \in \mathbf{R}^+$$
$$(x',y',z') = (kx,ky,kz)$$

According to $d_{Tg}(O,P).d_{Tg}(O,P') = r^2$,

$$k = \frac{r^2}{(a|x|+b|y|+c|z|)^2}.$$

To derive the equations of x', y' and z', substitute the value of k into $(x',y',z') = (kx,ky,kz)$.

Corollary 6. Let C_{T_g} be a generalized taxicab sphere with the center $O=(x_0,y_0,z_0)$ and the radius r in $\mathbf{R}^3_{T_g}$. If $P=(x,y,z)$ and $P'=(x',y',z')$ are inverse points with respect to the generalized taxicab spherical inversion $I_{T_g(O,r)}$, then x', y' and z' are obtained as

$$\begin{cases} x' = x_0 + \frac{r^2(x-x_0)}{\left(a|x-x_0|+b|y-y_0|+c|z-z_0|\right)^2} \\ y' = y_0 + \frac{r^2(y-y_0)}{\left(a|x-x_0|+b|y-y_0|+c|z-z_0|\right)^2} \\ z' = z_0 + \frac{r^2(z-c)}{\left(a|x-x_0|+b|y-y_0|+c|z-z_0|\right)^2} \end{cases}.$$

Proof. The inversion center can be translated from the origin from $(0,0,0)$ to (x_0, y_0, z_0) as the translation preserves distances in the generalized taxicab space $\mathbf{R}^3_{T_g}$. By applying this translation, one may readily obtain the values of x', y', and z'.

Theorem 7. Let P be between O and Q in $\mathbf{R}^3_{T_g}$, and let Q, O, and P be any three collinear points. If P and Q are mapped to P' and Q', respectively, by the generalized taxicab spherical inversion $I_{T_g(O,r)}$, then

$$d_{Tg}(P',Q') = \frac{r^2 \cdot d_{Tg}(P,Q)}{d_{Tg}(O,P) \cdot d_{Tg}(O,Q)}.$$

Proof. First, assume that O, P, and Q are collinear. We deduce from Definition 3 that

$$d_{Tg}(O,P) \cdot d_{T_g}(O,P') = r^2 = d_{Tg}(O,Q) \cdot d_{Tg}(O,Q').$$

Since the generalized taxicab and Euclidean distance ratios along a line are equal,

$$\begin{aligned} d_{Tg}(P',Q') &= \left| d_{Tg}(O,P') - d_{Tg}(O,Q') \right| \\ &= \left| \frac{r^2}{d_{Tg}(O,P)} - \frac{r^2}{d_{Tg}(O,Q)} \right| \\ &= \frac{r^2 \cdot d_{Tg}(P,Q)}{d_{Tg}(O,P) \cdot d_{Tg}(O,Q)} \end{aligned}$$

is reached.

In the generalized taxicab space $\mathbf{R}^3_{T_g}$, this theorem is invalid when O, P, and Q are not collinear. For example, for $O=(0,0,0)$, $P=(1,0,0)$, $Q=(1,1,1)$ and $r=2$, the inversion $I_{T_g(O,r)}$ with $a=b=c=9$, then transform P and Q into $P'=(\frac{4}{81},0,0)$ and $Q'=(\frac{4}{81},\frac{4}{81},\frac{4}{81})$. Also,

$d_{T_g}(P,Q)=18$, $d_{T_g}(P',Q')=\frac{8}{9}$, $d_{T_g}(O,P)=9$ and $d_{T_g}(O,Q)=27$. Using these values, it is observed that theorem is not satisfied.

Theorem 8. Assume that $a=b=c$. Let P,Q and O be any three non-collinear points in $\mathbf{R}^3_{T_g}$ and $I_{T_g(O,r)}$ be the inversion in the generalized taxicab circle centered at the point O with the radius r such that maps P and Q into P' and Q', respectively. If the direction of the rays OP and OQ belong to one of the sets D_i, $i=1,2,3$, then

$$d_{T_g}(P',Q')=\frac{r^2\cdot d_{T_g}(P,Q)}{d_{T_g}(O,P)\cdot d_{T_g}(O,Q)},$$

where

$$D_1=\{(1,0,0),(0,1,0),(0,0,1)\},$$
$$D_2=\{(1,1,1),(-1,1,1),(1,-1,1),(1,1,-1)\},$$
$$D_3=\{(1,1,0),(1,0,1),(0,1,1),(1,-1,0),(1,0,-1),(0,1,-1)\}.$$

Proof. Since translations preserve the generalized taxicab distances, the center O of the generalized inversion sphere as the origin can be taken without loss of generality. Consider the case that the directions of the rays OP and OQ belong to the set D_1. Then the inverse points of $P=(p,0,0)$ and $Q=(0,q,0)$ under $I_{T_g(O,r)}$ are $P'=(\frac{r^2}{a^2p},0,0)$ and $Q'=(0,\frac{r^2}{a^2q},0)$. The generalized taxicab distances from the inversion center to the points P and Q are $a|p|$, and $a|q|$, respectively. Also, the generalized taxicab distance between the points P' and Q'

$$d_{T_g}(P',Q')=\frac{r^2}{a|p|}+\frac{r^2}{a|q|}=\frac{r^2(a|p|+a|q|)}{(a|p|)(a|q|)}.$$

Since the generalized taxicab distance between the points P and Q is $a|p|+b|q|$, the equality

$$d_{T_g}(P',Q')=\frac{r^2\cdot d_{T_g}(P,Q)}{d_{T_g}(O,P)\cdot d_{T_g}(O,Q)}$$

is satisfied. Similarly, the validity of the equality for the other forms of P and Q in D_1 can be seen easily.

Suppose that the directions of the rays OP and OQ belong to the set D_2. Then the invers points of the choosen points $P=(p,p,p)$ and

$Q=(-q,q,q)$ respect to $I_{Tg(O,r)}$ in D_2 are $P'=\left(\frac{r^2}{9a^2p},\frac{r^2}{9a^2p},\frac{r^2}{9a^2p}\right)$ and $Q'=\left(-\frac{r^2}{9a^2q},\frac{r^2}{9a^2q},\frac{r^2}{9a^2q}\right)$. The generalized taxicab distance between the points P' and Q' is found as

$$d_{Tg}(P',Q')=a\left|\frac{r^2}{9a^2p}+\frac{r^2}{9a^2q}\right|+2a\left|\frac{r^2}{9a^2p}-\frac{r^2}{9a^2q}\right|$$
$$=r^2\frac{a|p+q|+2a|q-p|}{9a^2|p||q|}.$$

Also, the generalized taxicab distances from the inversion center to the points P and Q are $d_{T_g}(O,P)=3a|p|$, $d_{T_g}(O,Q)=3a|q|$, and the generalized taxicab distance between P and Q is $a|p+q|+2a|q-p|$. If we use these in the equality (1), we obtain

$$d_{T_g}(P',Q')=\frac{r^2\cdot d_{T_g}(P,Q)}{d_{T_g}(O,P)\cdot d_{T_g}(O,Q)}.$$

Similarly, the validity of the equality for the other forms of the rays OP and OQ in D_2 can be proved easily.

Suppose that the directions of the rays OP and OQ belong to the set D_3. Then the invers of the chosen points $P=(ap,bp,0)$ and $Q=(0,bq,-cq)$ respect to $I_{T_g(O,r)}$ in D_3 are $P'=\left(\frac{r^2}{4a^2p},\frac{r^2}{4a^2p},0\right)$ and $Q'=\left(0,\frac{r^2}{4a^2q},-\frac{r^2}{4a^2q}\right)$. The generalized taxicab distance between the points P' and Q' is found as Then the invers points of $P=(p,p,0)$ and $Q=(0,q,-q)$ respect to $I_{T_g(O,r)}$ in D_3 are $P'=\left(\frac{r^2}{4a^2p},\frac{r^2}{4a^2p},0\right)$ and $Q'=\left(0,\frac{r^2}{4a^2q},-\frac{r^2}{4a^2q}\right)$. The generalized taxicab distance between the points P' and Q' is found as

$$d_{Tg}(P',Q')=a\left|\frac{r^2}{4a^2p}\right|+a\left|\frac{r^2}{4a^2p}-\frac{r^2}{4a^2q}\right|+a\left|\frac{r^2}{4a^2q}\right|$$
$$=r^2\frac{a|p|+a|q-p|+a|q|}{4a^2|p||q|}.$$

In this equality, the value $a|p|+a|q-p|+a|q|$ is the generalized taxicab distance between P and Q, and the value $4a^2|p||q|$ is the product of $2a|p|$ and $2a|q|$ which are the generalized taxicab distances from the inversion center to the points P and Q. So, the equality is valid. Similarly, the proof can be done for the other forms of the rays OP and OQ in D_3.

Theorem 9. Let P,Q and O be any three non-collinear points in $\mathbf{R}^3_{T_g}$ and $I_{T_g(O,r)}$ be the inversion in the generalized taxicab circle centered at the point O with the radius r such that maps P and Q into P' and Q', respectively. If the direction lines of the rays OP and OQ belong to one of the sets $D_i, i=1,2,3$, then

$$d_{T_g}(P',Q')=\frac{r^2\cdot d_{T_g}(P,Q)}{d_{T_g}(O,P)\cdot d_{T_g}(O,Q)},$$

where

$$D_1=\{(1,0,0),(0,1,0),(0,0,1)\},$$
$$D_2=\{(a,b,c),(-a,b,c),(a,-b,c),(a,b,-c)\},$$
$$D_3=\{(a,b,0),(a,0,c),(0,b,c),(a,-b,0),(a,0,-c),(0,b,-c)\}.$$

Proof. Since translations preserve the generalized taxicab distances, it is enough to consider the center O of the generalized inversion sphere as the origin. Consider the case that the directions of the rays OP and OQ belong to the set D_1. Then the inverse points of $P=(p,0,0)$ and $Q=(0,q,0)$ under $I_{T_g(O,r)}$ are $P'=(\frac{r^2}{a^2p},0,0)$ and $Q'=(0,\frac{r^2}{b^2q},0)$. The generalized taxicab distances from the inversion center to the points P and Q are $a|p|$, and $b|q|$, respectively. Also, the generalized taxicab distance between the points P' and Q' The generalized taxicab distance between the points P' and Q' is calculated as

$$d_T(P',Q')=\frac{r^2}{a|p|}+\frac{r^2}{b|q|}=\frac{r^2(a|p|+b|q|)}{(a|p|)(b|q|)}=\frac{r^2\cdot d_{T_g}(P,Q)}{d_{Tg}(O,P)\cdot d_{T_g}(O,Q)}.$$

Similarly, the validity of the equality for the other forms of P and Q in D_1 can be seen easily.

Suppose that the directions of the rays OP and OQ belong to the set D_2. If the points P and Q are choosen as (pa, pb, pc) and $(-aq, bq, cq)$, the images of P and Q respect to $I_{(O,r)}$ are

$$P' = \left(\frac{r^2 a}{(a^2+b^2+c^2)^2 p}, \frac{r^2 b}{(a^2+b^2+c^2)^2 p}, \frac{r^2 c}{(a^2+b^2+c^2)^2 p} \right)$$

and

$$Q' = \left(-\frac{r^2 a}{(a^2+b^2+c^2)^2 q}, \frac{r^2 b}{(a^2+b^2+c^2)^2 q}, \frac{r^2 c}{(a^2+b^2+c^2)^2 q} \right)$$

The generalized taxicab distance between the points P' and Q' is found as

$$d_{Tg}(P', Q') = a^2 \frac{r^2 |q+p|}{(a^2+b^2+c^2)^2 |p||q|} + (b^2+c^2) \frac{r^2 |q-p|}{(a^2+b^2+c^2)^2 |p||q|}$$

$$= r^2 \frac{a^2 |p+q| + (b^2+c^2)|q-p|}{(a^2+b^2+c^2)^2 |p||q|}.$$

The generalized taxicab distances from the inversion center to the points P and Q are found $(a^2+b^2+c^2)|p|$, and $(a^2+b^2+c^2)|q|$, respectively. The generalized taxicab distance between P and Q is

$$a^2 |p+q| + (b^2+c^2)|q-p|.$$

If we use these, we obtain

$$d_{T_g}(P', Q') = \frac{r^2 \cdot d_{T_g}(P, Q)}{d_{T_g}(O, P) \cdot d_{T_g}(O, Q)}.$$

Similarly, the validity of the equality for the other forms of OP and OQ for D_2 can be seen easily.

Now, let P, Q be the points in $\mathbf{R}^3_{T_g}$ such that the directions of the rays OP and OQ belong to the set D_3. If $P = (ap, bp, 0)$ and $Q = (aq, 0, cq)$, then the inverses of P and Q respect to $\mathbf{R}^3_{T_g}$ calculated as $P' = \left(\frac{r^2 a}{(a^2+b^2)^2 p}, \frac{r^2 b}{(a^2+b^2)^2 p}, 0 \right)$ and $Q' = \left(\frac{r^2 a}{(a^2+c^2)^2 q}, 0, \frac{r^2 c}{(a^2+c^2)^2 q} \right)$. The generalized taxicab distance between the points P' and Q' is calculated as

$$d_T(P',Q') = a\left|\frac{ar^2}{(a^2+b^2)^2 p} - \frac{ar^2}{(a^2+c^2)^2 q}\right| + b\frac{br^2}{(a^2+b^2)^2|p|} + c\frac{cr^2}{(a+c)^2|q|}$$
$$= r^2\frac{a^2|q-p| + b^2|q| + c^2|p|}{(a^2+b^2)^2|p||q|}.$$

In this equality, since

$$a^2|q-p| + b^2|q| + c^2|p| = d_{T_g}(P,Q)$$

and

$$(a^2+b^2)^2|p||q| = d_{T_g}(O,P).d_{T_g}(O,P),$$

the proof is complited. Similarly, the validity of the equality for the other forms of the directions OP and OQ in D_2 can be seen easily.

CROSS RATIO AND HARMONIC CONJUGATES

In the generalized taxicab space, the inversion in a generalized taxicab circle does not preserve distances. In this section, we will show that the cross-ratio remains invariant under generalized spherical inversion in the generalized taxicab plane, and we will examine harmonic conjugates under inversion in a generalized taxicab circle.

$d_{Tg}[AB]$ is the generalized taxicab directed distance between points A and B along a line l in $\mathbf{R}^3_{T_g}$. $d_{Tg}[AB] = d_{T_g}(A,B)$ if the ray that begins at A and travels through B has a positive orientation. $d_{Tg}[AB] = -d_{T_g}(A,B)$ if the beam is pointing in the opposite direction. The inversion in the taxicab circle in the taxicab plane and space keeps the taxicab cross ratio (Bayar and Ekmekçi, 2014:33), (Pekzorlu and Bayar, 2022:28). Now, we will examine the properties related to the cross ratio and harmonic conjugates in $\mathbf{R}^3_{T_g}$

Definition 10. Let A, B, C and D be four distinct points on a directed line in $\mathbf{R}^3_{T_g}$. The generalized taxicab cross ratio of the points A, B, C, D is denoted as $(AB,CD)_{T_g}$, and defined by

$$(AB,CD)_{T_g} = \frac{d_{T_g}[AC]}{d_{T_g}[AD]}.\frac{d_{T_g}[BD]}{d_{T_g}[BC]}.$$

Proposition 11. Let A, B, C and D be four distinct points on a directed line in $\mathbf{R}^3_{T_g}$. Then the generalized taxicab cross-ratio the generalized taxicab cross-ratio $(AB,CD)_{T_g}$ is positive, if both C and D are between A and B or not.

Proof. Suppose that both points C and D are between the points A and B. For the array $ACDB$, since $d_{T_g}[BD] = -d_{T_g}(B,D)$, the generalized taxicab cross-ratio $(AB,CD)_{T_g}$ is obtained as

$$\begin{aligned}(AB,CD)_{T_g} &= \frac{d_{T_g}[AC]}{d_{T_g}[AD]}.\frac{d_{T_g}[BD]}{d_{T_g}[BC]} \\ &= \frac{d_{T_g}(A,C)}{d_{T_g}(A,D)}.\frac{-d_{T_g}(B,D)}{-d_{T_g}(B,C)} \\ &= \frac{d_{T_g}(A,C)}{d_{T_g}(A,D)}.\frac{d_{T_g}(B,D)}{d_{T_g}(B,C)}\end{aligned}$$

and is positive. For the arrays $ACDB$, $ADCB$, $BCDA$ or $BCDA$, the proof can be made similarly. Now, suppose that neither C nor D be between A and B. For the array $CABD$, since $d_{T_g}[AC] = -d_{T_g}(A,C)$ and $d_{T_g}[BC] = -d_{T_g}(B,C)$, $(AB,CD)_{T_g}$ are positive. For the arrays $ACDB$, $BCDA$ or $BCDA$, the proof is similar.

Proposition 12. Let C and D be four distinct points on a directed line in $\mathbf{R}^3_{T_g}$. If the pairs $\{A,B\}$ and $\{C,D\}$ separate each other, the generalized taxicab cross-ratio is negative.

Proof. Suppose that the pairs the pairs $\{A,B\}$ and $\{C,D\}$ separate each other. For the array $CADB$, since $d_{T_g}[AC] = -d_{T_g}(A,C)$, $d_{T_g}[BC] = -d_{T_g}(B,C)d_{T_g}$, and $d_{T_g}[BD] = -d_{T_g}(B,D)$, the generalized taxicab cross ratio $(AB,CD)_{T_g}$ is obtained as

$$\begin{aligned}(AB,CD)_{T_g} &= \frac{d_{T_g}[AC]}{d_{T_g}[AD]}.\frac{d_{T_g}[BD]}{d_{T_g}[BC]} \\ &= \frac{-d_{T_g}(A,C)}{d_{T_g}(A,D)}.\frac{-d_{T_g}(B,D)}{-d_{T_g}(B,C)} \\ &= -\frac{d_{T_g}(A,C)}{d_{T_g}(A,D)}.\frac{d_{T_g}(B,D)}{d_{T_g}(B,C)}\end{aligned}$$

and negative. For the arrays $DACB$, $CBDA$, or $DBCA$, the proof is similar.

It is well known that the cross ratio of four diffrent collinear points differently from the inversion center is invariant under the inversion in a

Euclidean sphere (Ramirez and Rubiano, 2016:132). The following theorem proves that this property is also valid for the inversion in a generalized taxicab sphere.

Theorem 13. The generalized taxicab cross-ratio of four distinct points on a directed line passing through the inversion center is invariant under inversion in a generalized taxicab sphere in $\mathbf{R}^3_{T_g}$.

Proof. Let A, B, C and D be four collinear locations in $\mathbf{R}^3_{T_g}$, where O is the center of the inversion $I_{T_g(O,r)}$. Let A, B, C and D be transformed into A', B', C', and D', respectively, by $I_{T_g(O,r)}$. The generalized taxicab spherical inversion maintains the separation or non-separation of the pair A, B and C, D while reversing the taxicab directed distance from the point A to the point B along a line l in $\mathbf{R}^3_{T_g}$ to the taxicab directed distance from the point B' to the point A'. Therefore, it is sufficient to demonstrate that. If $\left|(A'B', C'D')_{T_g}\right| = \left|(AB, CD)_{T_g}\right|$. This is in accordance with Lemma 4

$$\left|(A'B', C'D')_{T_g}\right| = \left|\frac{d_{T_g}\left[A'C'\right]}{d_T\left[A'D'\right]} \cdot \frac{d_{T_g}\left[B'D'\right]}{d_{Tg}\left[B'C'\right]}\right|$$

$$= \left|\frac{d_{T_g}\left(A', C'\right)}{d_{Tg}\left(A', D'\right)} \cdot \frac{d_{Tg}\left(B', D'\right)}{d_{T_g}\left(B', C'\right)}\right|$$

$$= \left|\frac{\left(\frac{r^2 \cdot d_{T_g}(A,C)}{d_{Tg}(O,A) \cdot d_{Tg}(O,C)}\right)}{\left(\frac{r^2 \cdot d_{T_g}(A,D)}{d_{Tg}(O,A) \cdot d_{Tg}(O,D)}\right)} \cdot \frac{\left(\frac{r^2 \cdot d_{T_g}(B,D)}{d_{T_g}(O,B) \cdot d_{Tg}(O,D)}\right)}{\left(\frac{r^2 \cdot d_T(B,C)}{d_{T_g}(O,B) \cdot d_{Tg}(O,C)}\right)}\right|$$

$$= \left|\frac{d_{Tg}\left(A,C\right)}{d_{T_g}\left(A,D\right)} \cdot \frac{d_{T_g}\left(B,D\right)}{d_{T_g}\left(B,C\right)}\right|$$

$$= \left|\frac{d_{T_g}\left[AC\right]}{d_{Tg}\left[AD\right]} \cdot \frac{d_{T_g}\left[B,D\right]}{d_{T_g}\left[B,C\right]}\right| = \left|(AB, CD)_{T_g}\right|.$$

Consider that the points A, B, C, D are given on the directed line. If point C is between points A and B, the line segment AB is internally divided by point C. Otherwise, it is externally divided. In the case of internal division, the ratio $\frac{d_{T_g}[AC]}{d_{T_g}[CB]}$ of the resulting directed generalized taxicab lengths is positive, and it is negative in the case of external division.

Definition 14. Let A, B, C and D be fourth points on a line l in $\mathbf{R}^3_{T_g}$. If the cross-ratio $(AB,CD)_{T_g} = -1,$ then the points C and D is said to be harmonically divided by A and B. The taxicab harmonic set of points is represented as $H(AB,CD)_{T_g}$, and the points C and D are referred to as generalized taxicab harmonic conjugates with regard to A and B.

Corollary 15. Two distinct points C and D are generalized taxicab harmonic conjugates with respect to the points A and B if and only if $(AB,CD)_T = -1.$

Proof. C and D be generalized taxicab harmonic conjugates with respect to A and B then $(CD,AB)_{T_g} = -1$. By using the definition $(CD,AB)_{T_g}$,

$$\begin{aligned}(CD,AB)_{T_g} &= \frac{d_{T_g}[CA]}{d_{Tg}[CB]}\frac{d_{T_g}[DB]}{d_{Tg}[DA]}\\ &= \frac{d_{T_g}[AC]}{d_{Tg}[BC]}\frac{d_{T_g}[BD]}{d_{Tg}[AD]}\\ &= \frac{d_{Tg}[AC]}{d_{Tg}[AD]}\frac{d_{T_g}[BD]}{d_{Tg}[BC]} = (AB,CD)_{T_g}\end{aligned}$$

From the last equality, $(AB,CD)_T = -1$ is obtained.

Theorem 16. The line segment $[AB]$ has a diameter of S in $\mathbf{R}^3_{T_g}$, and let S be a generalized taxicab sphere with a center of O. Let P and P' be different points on the ray OA that serve as internal and external divisions of the segment $[AB]$. If P and P' are inverse points with respect to the generalized taxicab spherical inversion $I_{T_g(O,r)}$, then P and P' are taxicab harmonic conjugates with respect to A and B.

Proof. Suppose that, with regard to A and B, P and P' are generalized taxicab harmonic conjugates. Consequently,

$$(AB,PP')_{Tg} = -1$$

$$\frac{d_{T_g}[AP]}{d_{T_g}[AP']}\cdot\frac{d_{T_g}[BP']}{d_{T_g}[BP]} = -1.$$

Given that P is on the ray OB and internally divides the line segment $[AB]$

$$d_{T_g}(P,B) = r - d_{Tg}(O,P) \text{ and } d_{Tg}(A,P) = r + d_{T_g}(O,P).$$

As P' is on the ray OB and externally divides the line segment $[AB]$, similarly,

$$d_{Tg}(A,P') = d_{T_g}(O,P') + r \text{ and } d_{Tg}(B,P') = d_{T_g}(O,P') - r.$$

If these equalities are used in the equalty

$$\frac{d_{T_g}[AP]}{d_{T_g}[AP']} \cdot \frac{d_{T_g}[BP']}{d_{T_g}[BP]} = -1,$$

$$\frac{d_{Tg}(O,P)+r}{d_{T_g}(O,P')+r} \cdot \frac{d_{T_g}(O,P')-r}{d_{T_g}(O,P)-r} = -1$$

and the result is

$$\left(r + d_{T_g}(O,P)\right) \cdot \left(d_{Tg}(O,P') - r\right) = \left(d_{T_g}(O,P') + r\right) \cdot \left(r - d_{T_g}(O,P)\right).$$

The last equivalence can be simplified to $d_{T_g}(O,P) \cdot d_{Tg}(O,P') = r^2$. Thus, with relation to the generalized taxicab spherical inversion $I_{g(O,r)}$, P and P' are generalized taxicab inverse points.

On the other hand, $d_{T_g}(O,P) \cdot d_{Tg}(O,P') = r^2$ if P and P' are generalized taxicab inverse points with regard to the taxicab spherical inversion $I_{g(O,r)}$. From the cross-ratio

$$\frac{d_{T_g}[AP]}{d_{T_g}[AP']} \cdot \frac{d_{T_g}[BP']}{d_{T_g}[BP]},$$

we can write the equality

$$\frac{d_{Tg}(A,P)}{d_{T_g}(A,P')} \cdot \frac{d_{T_g}(B,P')}{d_{T_g}(B,P)} = \frac{d_{Tg}(O,P)+r}{d_{T_g}(O,P')+r} \cdot \frac{d_{T_g}(O,P')-r}{d_{T_g}(O,P)-r}$$

$$= \frac{d_{Tg}(O,P)d_{T_g}(O,P') - rd_{Tg}(O,P) + rd_{T_g}(O,P') - r^2}{d_{T_g}(O,P)d_{T_g}(O,P') - rd_{Tg}(O,P') + rd_{T_g}(O,P) - r^2}.$$

The last equality can be simplified by utilizing $d_{T_g}(O,P) \cdot d_{Tg}(O,P') = r^2$,

$$\frac{d_{T_g}[AP]}{d_{T_g}[AP']} \cdot \frac{d_{T_g}[BP']}{d_{T_g}[BP]} = -1.$$

Thus, P and P' are generalized taxicab harmonic conjugates with respect to the points A and B.

RESULTS AND DISCUSSION

In this study, investigates the concept of inversion within generalized taxicab geometry, providing a thorough examination through precise

definitions, theorems, and proofs. Formulas have been developed to determine the coordinates of inverse points using generalized taxicab circle inversion, illustrating the relationships between the inversion center, the radius, and the positions of points in this geometric space.

The research also explores how certain geometric properties, such as cross-ratios and harmonic conjugates, are preserved under inversion. A significant finding is the introduction and analysis of the generalized taxicab cross-ratio, a fundamental concept in this context. It is shown that, much like in Euclidean geometry, the cross-ratio remains invariant under generalized taxicab circle inversion, confirming a core geometric principle in this non-Euclidean setting.

Additionally, the study introduces the notion of harmonic division in the generalized taxicab space, defines harmonic conjugates, and establishes the relationship between harmonic division and inversion.

In conclusion, this research offers important insights into the behavior of circle inversions in generalized taxicab geometry, contributing to a deeper understanding of non-Euclidean planes and opening new avenues for future exploration in this field.

REFERENCES

Akça, Z., and Kaya R. (2004). On the distance formulae in three dimensional taxicab space. Hadronic Journal, 27(5), 521-532.

Bayar A., and Ekmekçi S. (2014). On circular inversions in taxicab plane. Journal of Advanced Research in Pure Mathematics,6(4), 33-39.

Can, Z. (2022). On spherical inversions in three dimensional Tetrakis Hexahedron space. Erciyes Üniversitesi Fen Bilimleri Enstitüsü Dergisi, 38(1), 100-108.

Cırık, Y., and Ekmekçi, S. (2022). On the maksimum spherical inversions. Erzincan University Journal of Science and Technology, 15(1), 360-371.

Çolakoğlu, H. B. (2019). On Generalized Taxicab Metric in Three Dimensional Space, Commun. Fac. Sci. Univ. Ank. Ser. A1 Math. Stat. Volume 68, Number 2, Pages 1359-1369.

Çolakoğlu, H. B. (2018). The generalized taxicab group. International Electronic Journal of Geometry, 11(2), 83-89

Ekmekçi, S., Bayar, A., and Altıntaş, A. (2015). On the group of isometries of the generalized taxicab plane. International Journal of Contemporary Mathematical Sciences, 10(4), 159-166.

Ekmekçi, S., Akça, Z., and Altıntaş, K. (2015). On trigonometric functions and norm in the generalized taxicab metric. Mathematical Sciences and Applications E-Notes, 3(2), 27-33.

Ekmekçi, S. (2023). A note on the maximum circle inverses of lines in the maximum plane. Ikonion Journal of Mathematics, 5(2),1-9.

Ekmekçi, S., and Bilgin, Y. (2023). On the Inversion in a Generalized Taxicab Circle, Hagia Sophia Journal of Geometry, 2(5), 50-58.

Gelişgen, Ö., and Kaya, R. (2008). The Taxicab Space Group, Acta Mathematica Hungarica, 122(1), 187-200.

Krause, E. F. (1975). Taxicab geometry. Addison-Wesley Publishing Company, Menlo Park, California, USA.

Menger, K. (1952). You Will Like Geometry, Guildbook of Illinois Institute of Technology Geometry Exhibit, Museum of Science & Industry,Chicago, Illinois.

Minkowski, H. (1967). Gasammelte Abhandlungen, Chelsea Publishing Co., New York.

Ramirez, L., and Rubiano, G. N. (2016). A generalization of the spherical inversion, International Journal of Mathematical Education in Science and Technology, 48(1), 132-149.

Pekzorlu, A., and Bayar, A. (2020). On the Chinese Checkers spherical inversions in three dimensional Chinese Checkers space. Communications Faculty of Sciences University of Ankara Series A1: Mathematics and Statistics, 69(2), 1498-1507.

Pekzorlu, A., and Bayar, A. (2020). Taxicab spherical inversions in taxicab space. Journal of Mahani Mathematical Research Center, 9(1), 45-54.

Pekzorlu, A., and Bayar, A. (2022). On the Chinese Checkers circular inversions in the Chinese Checkers plane. Hagia Sophia Journal of Geometry, 4(2), 28-34.

Yüca, G., and Can, Z. (2020). On the circular inversion in Maximum plane. Ikonion Journal of Mathematics, 2(2), 26-34.

Exploring Stellar Interactions: The Case of LN Cyg in Binary Star Evolution

Neslihan ALAN[1]

1- Dr.; İstanbul University, Faculty of Science, Department of Astronomy and Space Sciences. neslihan.alan@gmail.com ORCID No: 0000- 0001- 9809- 7493

ABSTRACT

Eclipsing binary stars are rare objects for which the fundamental parameters of the components, such as mass and radii, can be calculated directly. Such stars play a critical role in better understanding stellar evolution because they appear all over the H-R diagram. The investigation of stellar interactions in binary stars is crucial for understanding the physical processes and testing theoretical models. Such interactions are most common in binary systems in the close-contact and early-contact phases, which show light variations of the Beta Lyrae and W Ursae Majoris types. Therefore, LN Cyg, a binary star in the early contact phase, was selected for this study. The high-resolution *TESS* light curves of the system, combined with ground-based multi-color photometric data, were solved for the first time in this research and the fundamental parameters of the components were precisely determined. The analysis revealed that the system is in the early-contact phase and has a high-temperature difference between the components. The massive component of the system is 1.83±0.26 $M_{\odot}$, while the low-mass component is 1.24±0.19 $M_{\odot}$. The system hosts stars in the intermediate mass range. The radii of the components were calculated to be 1.64±0.08 $R_{\odot}$ and 1.37±0.07 $R_{\odot}$ for the massive and low-mass components, respectively. The distance of LN Cyg was found as 1150±308 pc. LN Cyg is a large mass-ratio binary star in the early contact phase and requires more investigation to better understand the mass transfer processes, and detailed research using high-resolution spectra is needed to reveal these processes.

Keywords – Binaries: eclipsing - Contact binary stars - Fundamental parameters of stars - Astronomy data analysis – Light Curve Analayis

INTRODUCTION

Binary stars are the systems of two stars that are gravitationally bounded by each other in orbit around a common center of mass. These, in astronomy, are called physical binaries. If two stars appear to be close together in the sky yet are not gravitationally related, they are called optical binaries. Gravitationally bound binary star systems orbit according to Kepler's laws. The term "binary star" was first used by William Herschel in 1802 (Chen et al. 2024). If this system contains more than two stars, it is referred to as a "multiple systems".

Observational surveys indicate that a significant fraction of the stars in the Universe are members of binary or multiple systems. Approximately 50% to 70% of stars are part of such systems, though this percentage varies depending on stellar mass and type. Massive stars exhibit a higher probability of forming binaries compared to low-mass stars (Raghavan et al., 2010). Also according to Heintz (1969), 85% of all stars are binary systems.

Binary stars are of great importance in astronomy, playing a critical role in understanding the structure and evolution of stars. They represent a unique tool for the determination of fundamental stellar parameters such as mass, radii, luminosity, and age. By applying Kepler's laws to these systems, astronomers can derive the masses of individual stars with high precision (Moe and Di Stefano, 2017). Moreover, binary systems allow tracing the process of galaxy formation and evolution. Close binary systems are particularly significant as they can lead to high-energy phenomena such as supernova explosions or black hole formation (Sana et al., 2012).

Eclipsing binaries are systems in which the plane of the stars' orbits is aligned along the observer's line of sight. This alignment results in one star periodically passing in front of the other and thus causing observable decreases in magnitude. These allow astronomers to derive accurate measurements of stellar sizes and separations. The classification of eclipsing binary stars is often dependent on the shapes of light curves and the interaction of stars within their Roche lobes.

The Roche lobe is one of the most significant concepts in binary star research and in celestial mechanics. It is that volume around a star in a binary system inside which material orbiting that star will be gravitationally bound to that star. In fact, the Roche lobe is determined by the equipotential surface at which the gravitational forces of the two stars and the centrifugal force due to rotation around the system are in balance.

Material within the Roche lobe is bound to the star, but material moving beyond the lobe may overflow onto the companion star or indeed leave the system altogether. Where the Roche lobes of the two stars touch is termed the Lagrange point L_1 and provides a means of mass transfer between the two stars if one star fills or overflows its Roche lobe. This is a very important phenomenon in the evolution of binary systems, influencing the processes of accretion, the formation of an accretion disk, and the dynamics of stellar interaction. Figure 1 displays a 3D visualization of the dimensionless Roche potential in a co-rotating frame for a binary system with a mass ratio q=2 (Postnov and Yungelson, 2014).

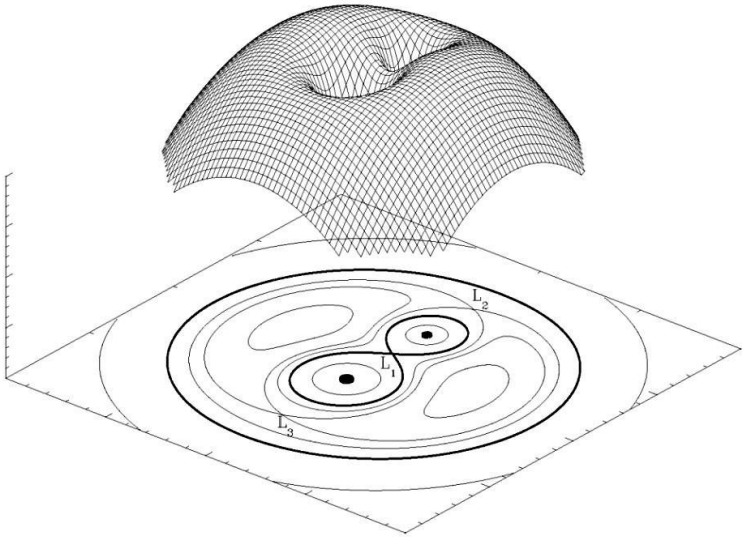

Figure 1: A three-dimensional visualization of the dimensionless Roche potential in a co-rotating reference frame for a binary system with a component mass ratio of q = 2 (Postnov and Yungelson, 2014). L_1, L_2, and L_3 are the Lagrangian points where the forces, as perceived in the rotating reference frame, are in equilibrium.

Eclipsing Eclipsing binary stars are classified into three types according to Roche geometry; detached, semi-detached, and contact systems. Detached systems consist of stars within their individual Roche lobes and present an eclipse light curve with brightness between eclipses remaining steady. Such systems, therefore, have minimal interaction, allowing both stars to evolve independently (Wilson and Devinney, 1971). The category of semi-detached systems includes those in which one star completely fills its Roche lobe, accreting material from its companion. This will lead to those beautifully regarded light curves that change continuously in brightness and give some idea of the mass transfer and orbital evolution (Pringle, 1981). Then we have a contact system in which both stars exceed their Roche lobes, sharing a common envelope. These systems have wave-like light curves that are smooth because of very intense interactions and tidal forces (Lucy, 1968). Roche lobe size is critical in the binary system type and is calculated using Eggleton's (1983) formula. This formula provides an accurate approximation of the effective size of the Roche lobe with respect to the mass ratio of the two stars, further contributing to a clearer picture of the mass transfer process and configurations existent between stars.

Additional refinement is offered by the peculiar patterns of their light curves. Algol-type binaries (EA) consist of rather sharp eclipses and even smoother intervals, which are features typical of detached systems. Binaries of the Beta Lyrae type (EB), on the contrary, show continuous brightness variations, associated most commonly with semi-detached configurations.

Nearly sinusoidal light curves are shown by W Ursae Majoris type binaries (EW), which are contact systems. Such light curves are the result of the sharing of a common envelope and, consequently, similar surface conditions. For this traditional classification, the light curves of the eclipsing binaries are as shown in Figure 2.

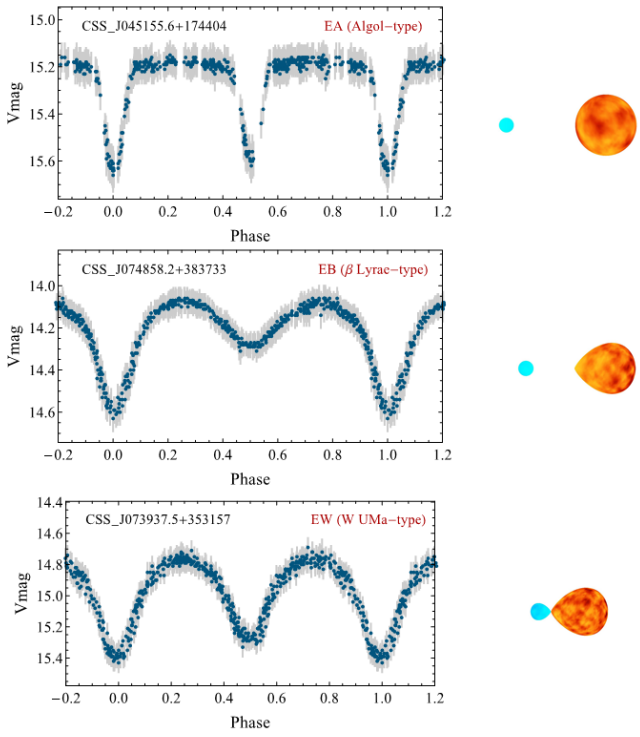

Figure 2: The left panels illustrate different types of eclipsing binary light curves, while the right panels depict the corresponding binary system configurations for each light curve type (Fu et al., 2020).

Among all the different classifications, semi-detached and contact binary systems hold a special place due to the mass transfer phenomenon that occurs among them. Their photometric studies provide critical information about stellar astrophysics. Such systems as exceptional tools to determine fundamental stellar parameters including mass, luminosity, and radii, examine stellar evolution, and investigate complex interactions going on in configurations of a close binary nature. In this context, the study of stars in the near contact and early contact phases is very important for a better understanding of the physical phenomena during the transition to the detached, semi-detached, and contact phases. In this research, LN Cyg, which is reported to be in the early contact phase in the literature, has been

selected to be analyzed and its astrophysical parameters determined together with high sensitivity *TESS* and ground-based observational data.

LN CYG SYSTEM

The LN Cyg system was first identified as a variable star by Ross in 1928. Decades later, Margoni et al. (1989) performed a comprehensive study at Asiago, analyzing the photometric properties of 36 variable stars, including LN Cyg. Their research focused on magnitude variations in colors *B* and *V* and revealed remarkable differences. The magnitude ranges for LN Cyg were determined to be $14^m.1$–$14^m.8$ in B and $13^m.3$–$14^m.5$ in *V*, with $(B\text{-}V)_{min}$ and $(B\text{-}V)_{max}$ values calculated as +0.3 and +0.8, respectively. Furthermore, Brancewicz and Dworak (1980) conducted a statistical analysis using an iterative method based on fundamental astronomical principles. This approach provided the geometric and physical parameters of 1048 binary stars, including LN Cyg. Some information from the GCVS catalog and the findings of Brancewicz and Dworak (1980) for LN Cyg are summarized in Tables 1 and 2. It has been reported that the parallax of the system as 0.6625±0.0122 mas in the *Gaia* DR3 catalog (*Gaia* collaboration, 2023). Moreover, Khalatyan et al. (2024) used *Gaia* DR3 data (most notably the low-resolution XP spectra) to determine the atmosphere parameters and masses of 217 million stars. The logT_{eff}, log$g$, mass, and metallicity determined as mean for the LN Cyg are 3.877 ± 0.024 *K*, 3.888 ± 0.207 cgs, 1.705 ± 0.262 $M_\odot$, and -0.198± 0.391, respectively.

Table 1: Some information about the LN Cyg from AAVSO VSX Search.

Other Names	ASASSN-V J205730.93+331438.4, SV* R 286
Variability Type	EB/SD
Mag. Range (B_{max}-B_{min}) (mag)	14.0 - 15.1
Spectral Type	A2:
Epoch	2433237.347
Period (day)	0.523945

Table 2: Findings of Brancewicz and Dworak (1980).

R_1, R_2 ($R_\odot$)	1.40, 1.64
RL_1, RL_2 (%)	73, 100
L_1, L_2 (Solar unit)	7.56, 1.85
T_1, T_2 (K)	8120, 5290
M_1+M_2 ($M_\odot$)	4.99
q (M_2/M_1)	0.70
Type	β Lyr
Spectral Type	A2:+

OBSERVATIONAL DATA

The Observations of eclipsing binary systems hold immense value in astrophysics and offer unparalleled opportunities to directly measure fundamental stellar parameters. These systems allow for highly accurate determinations of masses, radii, and orbital inclinations. By combining data from high-precision space missions such as the Transiting Exoplanet Survey Satellite (*TESS*) with ground-based multicolor photometric observations, astronomers can further refine these measurements. In this research, *TESS* data were combined with CCD observations obtained by Alan (2010) in Johnson *VRI* filters using the Apogee ALTA U47 CCD camera attached to the 40 cm Cassegrain Telescope at the Ankara University Kreiken Observatory to perform a photometric analysis of the LN Cyg eclipsing binary system.

The reduction for ground-based observations was performed using the IRAF program. GSC 2692 1470 was chosen as the comparison star, while GSC 2692 1394 served as the check star. The catalog information of LN Cyg with the comparison and check stars are given in Table 3. Light curves were generated by averaging the differential magnitude values over 0.001 phase intervals. In this way, 534, 536, and 568 observation data were obtained for the *V*, *R* and *I* filters, respectively. Nightly extinction coefficients were calculated using observations of the comparison star. The estimated uncertainty for an observation point is of the order of $\pm 0^m.007$ for the *V* and *I* filters and $\pm 0^m.006$ for the *R* filter. Besides the ground-based multicolor observations, the light curve solution incorporates from *TESS* data which observes the sky in 27.4-day sectors. *TESS* collects broadband photometric data in a wavelength range of 600–1000 nm (Ricker et al., 2015). For LN Cyg, the *TESS* observations were conducted during Sector 15 with a cadence of 1800 seconds, spanning August 15 to September 10, 2019. These data were retrieved from the Mikulski Archive for Space Telescopes (MAST) database (https://archive.stsci.edu/). The analysis utilized the Pre-search Data Conditioning Simple Aperture Photometry (PDC-SAP) light curves, as outlined by Ricker et al. (2015). The mean photometric uncertainty associated with these data is approximately 0.1%.

Table 3: SIMBAD/CDS catalog information of LN Cyg, comparison, and check stars.

	LN Cyg	**GSC 2692 1470**	**GSC 2692 1394**
α (2000) (^{h} ^{m} ^{s})	20 57 30.86	20 57 26.25	20 57 43.88
δ (2000) (° ' ")	+33 14 38.82	+33 11 48.70	+33 17 24.28
Magnitude (*B, V*) (mag)	14.15-13.47*	13.03, 11.38	11.82, 11.09

Note: * refers to data taken from the AAVSO VSX search.

PHOTOMETRIC ANALYSIS

A detailed photometric analysis of the LN Cyg system's light curve was performed using the normalized ground-based *VRI* observations and *TESS* data simultaneously. In the analysis, the Wilson-Devinney (W-D) method (Wilson and Devinney, 1971) was used and the uncertainties in the derived parameters were investigated through Monte Carlo simulations (Zola, 2004; Zola, 2010). Spectroscopic radial velocity measurements were not available for the LN Cyg system; therefore, the mass ratio (q) was determined using the q-search (Terrell and Wilson 2005) technique based on light curve modeling. This method, often referred to as the photometric mass ratio test, identifies the most possible q value by minimizing the χ^2 statistic through iterative calculations. During the q-search process, all parameters were kept free, while q was incrementally fixed at steps of 0.01 within the range of 0 to 1. As a result of the analysis, the minimum χ^2 value obtained for the system corresponds to around q=0.68. Figure 3 presents the results of q-search for the system. LN Cyg, which was identified as an EB type eclipsing binary system in previous studies (Brancewicz and Dworak, 1980), was later found to be of EW type (Alan 2010; Heinze et al., 2018). Therefore, the solution was applied with MOD 6 (contact binary) where both components fill the Roche lobe. The W-D code analysis was performed using a combination of parameters that were fixed based on literature studies and theoretical models, along with parameters that were continuously adjusted and improved through multiple iterations. The fixed and adjustable parameters are outlined below. The primary component's effective temperature was fixed at 7447 *K* by given Khalatyan et. al. (2024) using *Gaia* DR3 data. The root-mean-square limb darkening law was applied in the analysis, with coefficients of limb darkening obtained from the tables given by van Hamme (1993), considering the temperatures of the LN Cyg components and the filter wavelengths. For the primary component, characterized by a radiative atmosphere ($T_{\rm eff}$ > 7200 *K*), the bolometric gravity-darkening exponent was fixed at 1, following (Lucy, 1967), while the bolometric albedo was fixed at 1 in agreement with Rucinski, 1969. In contrast, for the secondary component with a convective atmosphere ($T_{\rm eff}$ > 7200 *K*), the bolometric gravity-darkening exponent was set to 0.32, based on (Lucy, 1967), and the bolometric albedo was kept at 0.5, in accordance with (Rucinski, 1969). It was assumed that both components were in synchronous rotation, with rotational parameters set to F_1=F_2=1. During the analysis, orbital eccentricity e was held at 0. In the analysis, the orbital inclination (i), the mass ratio (q), the secondary component's effective temperature ($T_{2,\rm eff}$), phase shift, and the primary component's fractional luminosity (L_1) were treated as free parameters. To assess the potential influence of a third body, the third light contribution (l_3) was included as a free parameter. However, no evidence of a third light was found for LN Cyg.

The derived model parameters are presented in Table 4, while Figure 4 illustrates a comparison between the theoretical and observed light curves. Morever, Figure 5 shows the Roche geometry of LN Cyg.

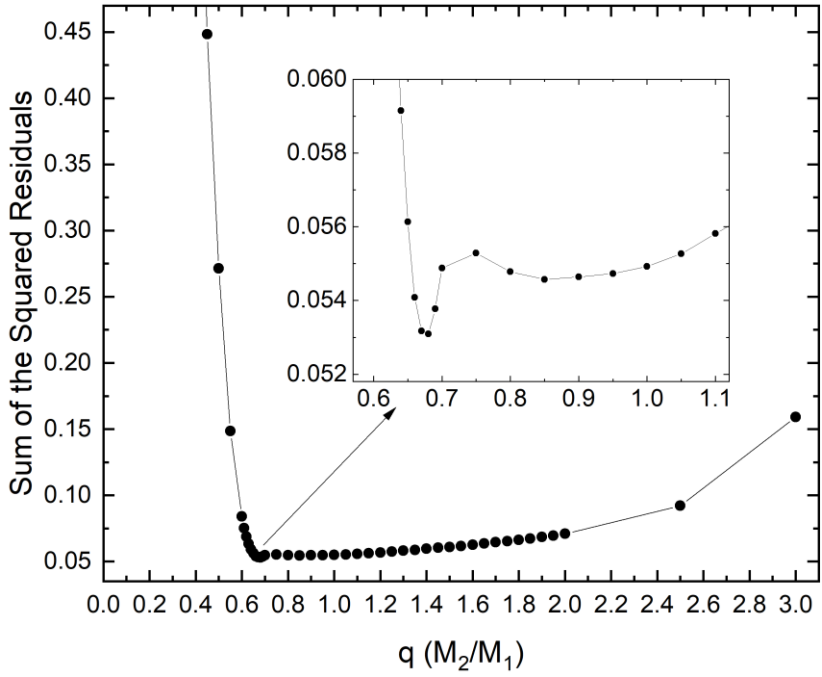

Figure 3: A visual depiction of *q*-search results for LN Cyg.

Table 4: The findings from the light curve analysis of LN Cyg. Numerical subscripts 1 designate the primary component, 2 the secondary component, and 3 the third component. The asterisk (*) refers to parameters that remain fixed during the analysis. The fractional radii r_1 and r_2 were determined using the geometric mean approach.

Parameter	**Value**
T_0 (HJD)	2455426.3225
Orbital Period (day)	0.52394278
i (°)	89.55 ± 0.15
T_1 (K)*	7447
T_2 (K)	5482 ± 18
Ω_1	3.2001 ± 0.0005
Ω_2	3.2001 ± 0.0005
q (=M_2/M_1)	0.676 ± 0.008
r_1 (mean)	0.4129 ± 0.0004
r_2 (mean)	0.3439 ± 0.0003
$l_1/(l_1+l_2)$ *TESS*	0.777 ± 0.001
$l_2/(l_1+l_2)$ *TESS*	0.223 ± 0.001
l_3/l_T (%) *TESS*	0.00
$l_1/(l_1+l_2)$ *V*	0.828 ± 0.003
$l_2/(l_1+l_2)$ *V*	0.172 ± 0.001
$l_1/(l_1+l_2)$ *R*	0.798 ± 0.003
$l_2/(l_1+l_2)$ *R*	0.202± 0.001
$l_1/(l_1+l_2)$ *I*	0.777 ± 0.003
$l_2/(l_1+l_2)$ *I*	0.223 ± 0.001

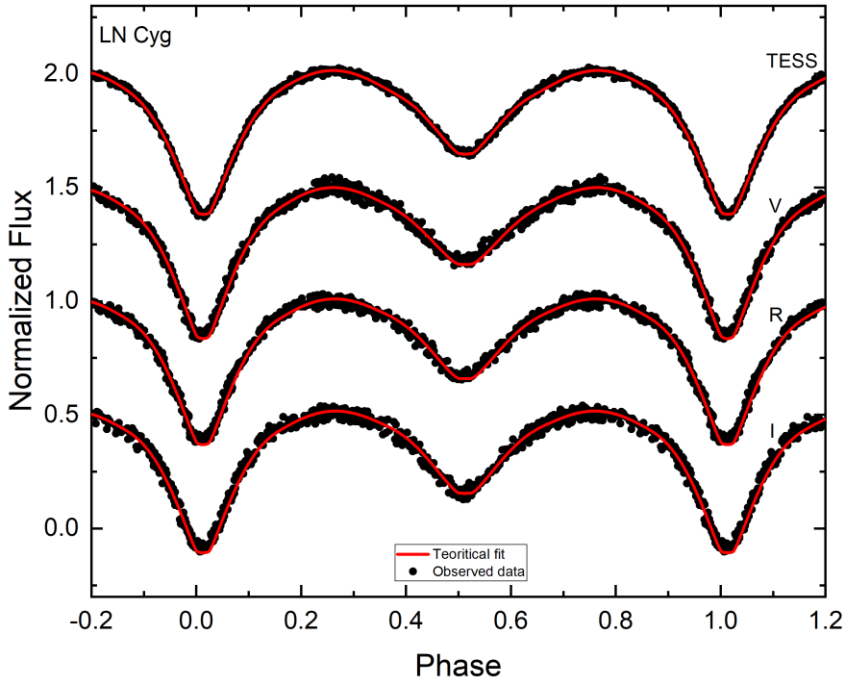

Figure 4: Theoretical light curves (depicted by the red line) are compared with observational data (represented by black dots) for LN Cyg.

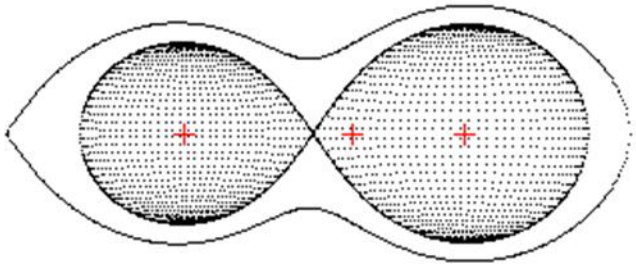

Figure 5: The Roche geometry for LN Cyg was constructed based on the parameters obtained from the best-fitting light curve model.

FUNDAMENTAL PARAMETERS OF LN CYG

The analysis of the light curve data allowed for the estimation of the fundamental parameters of the LN Cyg binary system's components. The primary component's effective temperature and mass were assumed to be at $T_{1,\mathrm{eff}}$ = 7447 *K* and M_1=1.83 $M_\odot$, values determined by Khalatyan et. al. (2024) using *Gaia* DR3 data. These parameters served as the starting point for further calculations. The secondary component's mass was subsequently calculated using the mass ratio derived through detailed photometric analysis of the system. To compute the radii of both stars, the semi-major axis was first calculated by applying Kepler's third law, while the fractional radii values were taken directly from Table 4. The luminosities and the bolometric magnitudes were obtained by using the solar values of $T_{\mathrm{eff},\odot}$= 5777 *K*, $M_{\mathrm{bol},\odot}$= 4.74 mag, along with the bolometric corrections provided by Eker et al. (2020). The primary and secondary components' surface gravity values were computed as $\log g_1$= 4.27 ±0.02 and $\log g_2$= 4.26 ± 0.04 in cgs units, respectively. A detailed summary of the estimated fundamental parameters can be found in Table 5.

The distance to LN Cyg was determined to be 1050±308 pc, using an interstellar extinction value of A_V=0.80 provided by Khalatyan et. al. (2024), the component light ratios detailed in Table 4, the system's apparent magnitude, and bolometric corrections calculated as BC_1= 0.064 mag and BC_2= -0.087 mag following Eker et. al. (2020).

Table 5. The fundamental stellar parameters estimated for the LN Cyg system.

Parameter	**Value**
a ($R_\odot$)	3.97 ± 0.19
M_1 ($M_\odot$)	1.83 ± 0.26
M_2 ($M_\odot$)	1.24 ± 0.19
R_1 ($R_\odot$)	1.64 ± 0.08
R_2 ($R_\odot$)	1.37 ± 0.07
log (L_1 /L_t)	0.87 ± 0.13
log (L_2 /L_t)	0.18 ± 0.06
log g_1 (cgs)	4.27 ± 0.02
log g_2 (cgs)	4.26 ± 0.02
M_{bol1} (mag)	2.56 ± 0.34
M_{bol2} (mag)	4.29 ± 0.35
d (pc)	1150 ± 308

RESULTS AND DISCUSSION

Contact binary stars show a wide range of ages, from one billion years old to ten billion years old. This is important for studying the evolution of binary stars of various masses. These types of systems are crucial for understanding the effects of different physical processes such as magnetic activity, microscale changes, fundamental parameters, and the effects of the interactions between the component stars on these processes. In this research, the first simultaneous solution of *TESS* observational data obtained at high sensitivity with ground-based multicolor photometric observations of the LN Cyg binary system in the early contact phase has been performed. As a result of the solutions, it was found that the temperature difference between the components is high and the components are in the early contact phase, similar to the previous findings of Alan (2010). The analysis has led to a detailed determination of the fundamental parameters of the components of the LN Cyg binary system, which is very significant in terms of stellar astrophysics. The calculations revealed masses of M_1=1.83±0.26 $M_\odot$ for the primary component and M_2=1.24 ± 0.19 $M_\odot$ for the secondary component. The radii of the components were obtained as R_1=1.64 ± 0.08 $R_\odot$ and R_2=1.37±0.07 $R_\odot$ for the primary and secondary components, respectively. The mass found for the primary component is considerably smaller than the value given by Dworak as M_1=2.92 $M_\odot$. Drowak reported the Roche lobe filling factors of the components of the system as RL_1=100% and RL_2=70% and suggested that LN Cyg is a semi-detached system. Analyses performed by Alan 2010 using ground-based multicolor photometric data revealed that both components of the system fill the Roche lobes. In the catalog of about 350,000 eclipsing binaries published by Chen (2020), the type of the system is listed as EW. The analysis in this research, which combines high-resolution *TESS* data with ground-based data, confirms that the system is a contact binary.

After the fundamental parameters of the components were established, the distance of LN Cyg to our solar system was calculated to be 1150 ± 308 pc. This distance is slightly closer than the distance of 1509 pc given in *Gaia* DR3. The binary star nature of the system may cause deviations in the *Gaia* distances. For a better understanding of the nature of the system and a detailed evolutionary study, precise spectral data should be obtained.

REFERENCE

Alan, N., 2010, LN Cyg Sisteminin İlk Işık Eğrisi Analizi, XVII. UAK, 88-96.

Brancewicz, H. K., and Dworak, T. Z., 1980, A Catalogue of Parameters for Eclipsing Binaries, *Acta Astronomica*, 30, 501–524.

Chen X., Wang S., Deng L., de Grijs R., Yang M., Tian H., 2020, The Zwicky Transient Facility Catalog of Periodic Variable Stars, *Astrophysical Journal Supplement*, 249, 1, 18.

Chen, X., Liu, Z., Han, Z., 2024, Binary stars in the new millennium, *Progress in Particle and Nuclear Physics*, Volume 134, 2024, 104083.

Eggleton, P. P., 1983, Approximations to the radii of Roche lobes, *Astrophysical Journal*, 268, 368-369.

Eker Z., Soydugan F., Bilir S., Bakış V., Aliçavuş F., Özer S., Aslan S., Alpsoy S., Köse Y., 2020, Empirical bolometric correction coefficients for nearby main-sequence stars in the Gaia era, *Monthly Notices of the Royal Astronomical Society*, Volume 496, Issue 3, Pages 3887–3905.

Fu, J-B., He, X., Yi, T., 2020, Deep Learning Techniques for Eclipsing Binary Light Curves Classification, *Physics, Computer Science*, Corpus ID: 247022238.

Gaia Collaboration, Vallenari, A., Brown, A. G. A., Prusti, T., et al., 2023. Gaia Data Release 3. Summary of the content and survey properties, *Astronomy and Astrophysics*, 674, A1.

Heintz, W. D., 1969, A Statistical Study of Binary Stars, *Journal of the Royal Astronomical Society of Canada*, 63, 275-298.

Khalatyan, A., Anders, F., Chiappini, C., et al., 2024, Transferring spectroscopic stellar labels to 217 million Gaia DR3 XP stars with SHBoost, *Astronomy and Astrophysics*, 691, A98.

Lucy, L. B., 1968, The structure of contact binaries, *Astrophysical Journal*, 151, 1123.

Lucy, L. B., 1967, Gravity-Darkening for Stars with Convective Envelopes, *Zeitschrift für Astrophysik*, 65, 89–92.

Margoni, R., Stagni, R., Munari, U., and Marton, S., 1989, 36 Revisited Variable Stars Around Nova Cygni 1970, *Astronomy and Astrophysics Supplement Series*, 81, 393–399.

Moe M., Di Stefano R., 2017, Mind Your Ps and Qs: The Interrelation between Period (P) and Mass-ratio (Q) Distributions of Binary Stars, *The Astrophysical Journal Supplement Series*, 230, 15.

Postnov, Konstantin and Yungelson, L., 2014, The Evolution of Compact Binary Star Systems, *Living Reviews in Relativity*. 17. 10.12942/lrr-2014-3.

Pringle, J. E., 1981, Accretion discs in astrophysics, *Annual Review of Astronomy and Astrophysics*, 19, 137-162.

Raghavan, D., McAlister, H. A., Henry, T. J., et al., 2010, A survey of stellar families: Multiplicity of nearby solar-type stars, *The Astrophysical Journal Supplement Series*, 190, 1-42.

Ricker, G. R., Winn, J. N., Vanderspek, R., et al., 2015, Transiting Exoplanet Survey Satellite (TESS), *Journal of Astronomical Telescopes, Instruments, and Systems*, 1, 014003.

Ross, V. E., 1928, New Variable Stars (sixth list), *Astronomical Journal*, 38, 99–100.

Rucinski, S. M., 1969, The Proximity Effects in Close Binary II. The Bolometric Reflection Effect for Stars with Deep Convective Envelopes, *Acta Astronomica*, 19, 245.

Sana H., de Mink S. E., de Koter A., et al., 2012, Binary Interaction Dominates the Evolution of Massive Stars, *Science*, 337, 444.

Terrell D., Wilson R. E., 2005, Photometric Mass Ratios of Eclipsing Binary Stars, *Astrophysics and Space Science*, 296, 221.
Wilson, R. E., and Devinney, E. J., 1971, Realization of accurate close-binary light curves: Application to MR Cygni, *Astrophysical Journal*, 166, 605.

From 2-Crossed Modules of R-Algebroids to Simplicial R-Algebroids

Işınsu YALĞIN[1]

1- Dr.; Eskişehir Osmangazi Üniversitesi Fen-Edebiyat Fakültesi Matematik-Bilgisayar Bölümü. isinsudoganay@gmail.com ORCID No:0000-0001-8723-8799

ABSTRACT

As a generalization of the 2-crossed module of commutative algebras, we present the 2-crossed module of R-algebroids in this work. Next, we construct a functor from the category of 2-crossed modules of R-algebroids to the category of simplicial R-algebroids with Moore complex of length two.

Keywords - R-algebroids, Simplicial R-algebroids, Crossed modules, 2-crossed modules, Equivalence of categories

INTRODUCTION

Whitehead introduced crossed modules of groups for the first time in (1941:409-428), (1946:806-810). Group crossed modules are equivalent to simplicial groups with Moore complex of length one (Conduche, 1984:155-178) and similarly for groupoid crossed modules (Mutlu ve Porter, 1998:174-194). Conduche addressed the idea of a group 2-crossed module and shown in (1984:155-178) that the category of group 2-crossed modules is equal to the category of simplicial groups with a two-length Moore complex. Arvasi and Ulualan investigated the relationships between simplicial groups with a length of two Moore complex, crossed squares, quadratic modules, and 2-crossed modules in (2006:1-27). The definitions of algebra crossed and 2-crossed modules (Arvasi and Porter, 1996:426-448), (Porter, 1986:458-465) are similar to those of the group case, actions by the automorphisms is replaced by the actions by the multipliers. Algebra 2-crossed modules and simplicial algebras are closely related, just like in the group case (Conduche, 1984:155-178), (Mutlu and Porter, 1998:174-194), (Mutlu and Porter, 1998:48-173). A 2-crossed module can be obtained from a simplicial algebra if it has a Moore complex of length two. Equivalence from category of simplicial algebra with a two-length Moore complex to category algebra crossed module is given in (Porter, 1986:458-465), (Arvasi, 1997:160-181), (Grandjean and Vale, 1986). Also in (2010:475-488), (2022:326-331) Akca and Pak worked on the pseudo simplicial groups. Moreover in (Akca and Arvasi, 2002:43-57), the higher order Peiffer elements in simplicial Lie algebras are examined. The homotopy theory of 2 -crossed modules of commutative algebras studied in (Akca ve Emir, 2016:99-128). Then in (Akca and Emir, 2019:289-311), the concept of a 2 -fold homotopy between a pair of 1 -fold homotopies connecting 2 -crossed module morphisims was defined. As a more broadly, Mitchell in (1972:1-161), (1985:333, 96) and Amgott in (1986:1-14) specifically studied R-algebroids, where R is a commutative ring. R-algebroids were defined categorically by Mitchell. Later, Mosa introduced crossed modules of R-algebroids as a generalization of crossed modules of associative R-algebras and demonstrated in his thesis (Mosa, 1986) that they are equivalent to special double R-algebroids with connections. Additionally, it was mentioned in

(Gurmen and Ulualan, 2020:113-121) that there was a close relationship between the category of simplicial R-algebroids with the length one Moore complex and the internal categories in the category of R-algebroids. Subsequent investigations by Akca and Avcıoglu (2017:37-48), (2018:2863-2875), (2017:148-155), (2017:225-242), (2022:267-288) delve deeper into crossed modules of R-algebroids, unraveling intricate connections and properties. Also in (Arslan, Akca, Irmak and Avcıoglu, 2019:5293-5304) and (Ozel, Arslan and Akca, 2024:1-36), it is examined the some properties of 2-crossed modules. As a generalization of the 2-crossed module of commutative algebras, we present the 2-crossed module of R-algebroids in this work. Next, we derive an equivalence of categories between the category of 2-crossed modules of R-algebroids and the category of simplicial R-algebroids with Moore complex of length two.

PRELİMİNARİES

Definition: Let R be a commutative ring. An R-category is a category in which composition is R-bilinear and all homsets have R-module structures.

In such a category, for any two objects A and B, the homset Hom(A, B) is an R-module, denoted as $\mathrm{Hom}_R(A, B)$, and for any morphisms f Hom(A, B) and g Hom(B, C), the composition gf is an R-bilinear map.

This structure allows for the study of categorical concepts and constructions within the context of R-modules, providing a rich framework for algebraic and categorical investigations.

Definition: An R-algebroid is a small R-category. R- algebroids can be non identity. A set of functions s, t : Mor(U) → Ob(U), the source and target functions, respectively, and an object set Ob(U) = U_o, a morphism set Mor(U), are included with an R-algebroid U. A single object R-algebroid corresponds to an associative R-algebra.

Let U and V be R-algebroids and $U_0 = V_0$, if the family of maps

$$\begin{array}{rcl} V(a,b) \times U(b,c) & \to & V(a,c) \\ (v,u) & \mapsto & v^u \end{array}$$

satisfies the following conditions

1) $v^{u_1+u_2} = v^{u_1} + v^{u_2}$
2) $(v_1 + v_2)^u = v_1^u + v_2^u$
3) $(v^u)^{u'} = v^{uu'}$
4) $(v'v)^u = v'v^u$
5) $r \cdot v^u = (r \cdot v)^u = v^{r \cdot u}$
6) $v^{1_{t_v}} = v$

for all a, b, c in U_0 and u, u′, u_1, u_2 Mor(U),v, v′, v1, v2 in Mor(V) such that t(v′) = s(v), t(u) = s(u′),t(v) = t(v_1) = t(v_2) = s(u) = s(u_1) = s(u_2), r in R it is called the right action of U on V . The left action of U on V is similarly defined. U exhibits both right and left actions on V under the condition (uv)u′ = u(vu′) is satisfied for all a, b, c in U_0, v in V (a, b), u 2 in U(d, a) and u′ in U(b, c) then U has an associative action on V .

Definition: An R-functor is an R-linear functor between two R-categories, and an R-algebroid morphism is an R-functor between two R-algebroids.

In category Alg(R), all R-algebroids and their morphisms are included.

Definition: Let R is an commutative ring U and V be two R-algebroids of the same object set U_o and V has an associative action on U . For the set U ⋊ V = {(u, v)|u ∈ U, v ∈ V }, if the following conditions are satisfied

1) $(u, v) + (u', v') = (u + u', v + v')$
2) $R \times (U \rtimes V) \to U \rtimes V$
   $(r, (u, v)) \quad {}^r(u, v) = ({}^r u, {}^r v)$
3) $((u, v), (u'', v'')) = (uu'' + u^{v''} + {}^v u'', vv'')$

U ⋉ V is an R-algebroid. This R-algebroid is called the semi-direct product R-algebroid of U and V .

Definition: A simplicial R-algebroid is a sequence of R-algebroids E ={E_0,E_1, ...,En, ...} together with homomorphisms d_n^i : $E_n \to E_{n-1}$ ($0 \le i \le n \ne 0$) and s_n^j : $E_n \to E_{n+1}$ ($0 \le j \le n \ne 0$) such that identity on object set, this homomorphisms are requared to satisfy the simplicial identities

$$
\begin{aligned}
&1)\quad d_i^{n-1}d_j^n = d_{j-1}^{n-1}d_j^n \quad , \quad 0 \le i < j \le n \\
&2)\quad s_i^{n+1}s_j^n = s_{j+1}^{n+1}s_i^n \quad , \quad 0 \le i \le j \le n \\
&3)\quad d_i^{n+1}s_j^n = s_{j-1}^{n-1}d_i^n \quad , \quad 0 \le i < j \le n \\
&4)\quad d_i^{n+1}s_j^n = Id \quad , \quad i = j \; or \; i = j+1 \\
&5)\quad d_i^{n+1}s_j^n = s_j^{n-1}d_{i-1}^n \quad , \quad 0 \le j < i-1 \le n
\end{aligned}
$$

We denote this simplicial R-algebroid with E = (E_n,d_n^i ,s_n^j).

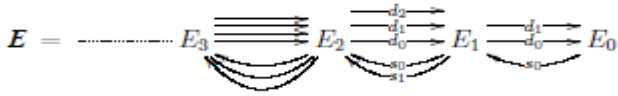

Let E = (E_n,d_n^i ,s_n^j) and F = (F_n,δ_n^i ,σ_n^j) be R-algebroids. A simplicial map f ={f_n : n in N} : E → F is a family of homomorphisms. We have thus defined category of simplicial R-algebroids, which we will denote by Simp.R-Alg..

Let E be a simplicial R-algebroid. The Moore complex (NE, ∂) of E is the chain complex defined by $NE_n = \bigcap_{i=0}^{n-1} kerd_n^i$ with $\partial n : NE_n \to NE_{n-1}$ induced from d_n^n by restriction.

$$
\ldots \to NE_2 \xrightarrow{d_2^2} NE_1 \xrightarrow{d_1^1} E_0 = E_0
$$

We say that the Moore complex (NE, ∂) of E is of length k if $NE_n = 0$ for all $n \le k+1$. We denote category of simplicial R-algebroids with Moore complex of lenght k by Simp.R-Alg.$_{\le k}$.

Definition: A 2-crossed module of R-algebroids (J,K,L,∂_1,∂_2,{.}$_{1,2}$) is given by a chain complex of R-algebroids with same object set U_0 together with associative actions of L on K and J such that ∂_1 and ∂_2 R-algebroid morphisms such that identity on U_0, where L act on itself by composition. We also have an R-bilinear functions (the Peiffer liftings)

$$
\{.\}_1 : K \times K \to J
$$

$$
\{.\}_2 : K \times K \to J
$$

satisfying the following axioms provided that target source compatibility is ensured

$$
\begin{array}{lll}
CM1) & \partial_2\{k,k'\}_1 & = kk' - k^{\partial_1(k')}, \\
 & \partial_2\{k,k'\}_2 & = kk' - {}^{\partial_1(k)}k', \\
CM2) & \{\partial_2(j),\partial_2(j')\}_{1,2} & = jj', \\
CM3) & \{k,k'k''\}_1 & = \{kk',k''\}_1 + \{k,k'\}_1^{\partial_1(k'')}, \\
 & \{k,k'k''\}_2 & = \{kk',k''\}_2 - {}^{\partial_1(k)}\{k',k''\}_2, \\
CM4) & \{\partial_2(j),k'\}_1 & = j^{k'} - j^{\partial_1(k')}, \\
 & \{\partial_2(j),k'\}_2 & = j^{k'}, \\
CM5) & \{k,\partial_2(j')\}_1 & = {}^{k}j' \\
 & \{k,\partial_2(j')\}_2 & = {}^{k}j' - {}^{\partial_1(k)}j' \\
CM6) & {}^{l}\{k',k''\}_{1,2} & = \{{}^{l}k',k''\}_{1,2} \\
 & \{k',k''\}_{1,2}^{p} & = \{k',k^{''p}\}_{1,2}
\end{array}
$$

Note that $\partial_2 : J \to K$ is a crossed module with action of K on J.

Definition: Let C = (J,K,L,∂_1,∂_2,{.}$_{1,2}$) and C' = (J',K',L',∂_1' ,∂_2' ,{.}) be 2-crossed modules, a 2-crossed module map f = (f_2, f_1, f_0) : C → C′ consists of algebroid maps $f_0 : L \to L'$, $f_1 : K \to K'$ and $f_2 : J \to J'$ making the diagram

$$
\begin{array}{ccccc}
J & \xrightarrow{\partial_2} & K & \xrightarrow{\partial_1} & L \\
\downarrow{\scriptstyle f_2} & & \downarrow{\scriptstyle f_1} & & \downarrow{\scriptstyle f_0} \\
J' & \xrightarrow{\partial_2'} & K' & \xrightarrow{\partial_1'} & L'
\end{array}
$$

commutative and preserving all actions and Peiffer liftings

$$
\begin{array}{lll}
1) & f_1({}^{l}k) & = {}^{f_0(l)}f_1(k) \\
 & f_1(k^{l'}) & = f_1(k)^{f_0(l')} \\
2) & f_2({}^{l}j) & = {}^{f_0(l)}f_2(j) \\
 & f_2(j^{l'}) & = f_2(j)^{f_0(l')} \\
3) & f_2\{k,k'\}_{1,2} & = \{f_1(k),f_1(k')\}_{1,2}
\end{array}
$$

From the definition, it's notable that if f = (f_2, f_1, f_0) represents a 2-crossed module morphism, then f_2, f_1, and f_0 are equal to each other on the set of objects.

As a result, all R-algebroid 2-crossed modules and their morphisms collectively constitute a category denoted by 2XMod.

FROM 2XMOD TO SİMP.R-ALG.$\leq_2$

We construct a functor from 2XMod to Simp.R-Alg.$_{\leq 2}$ in this section.

Proposition: Given a 2-crossed module of R-algebroids

$$\boldsymbol{C} = J \xrightarrow{\partial_2} K \xrightarrow{\partial_1} L,$$

We obtain a simplicial R-algebroid with Moore complex of lenght 2.

Proof: Let C be a 2-crossed module of R-algebroids. Then L act on J and K. Also K act on J. Starting from here, let E_0, E_1, E_2 and E_3 defined respectively and the morphisms be defined in such a way that they provide simplicial identities as a following,

1) Set $E_0 = L$.

2) We can form the semi-direct product $E_1 = K \rtimes L$. There are R-algebroid morphisms by using the action of L on K ;

- $d_0^1 : K \rtimes L \to L \quad , \quad d_0^1(k,l) = l$
- $d_1^1 : K \rtimes L \to L \quad , \quad d_1^1(k,l) = \partial_1(k) + l$
- $s_0^0 : L \to K \rtimes L \quad , \quad s_0^0(l) = (0,l)$

3) k, k′ in K act on j in J from right and left

$$\bullet\ K \times J \to J \qquad (k,j) \mapsto {}^k j = \{k, \partial_2(j)\}_1$$

$$\bullet\ J \times K \to J \qquad (j,k') \mapsto j^{k'} = \{\partial_2(j), k'\}_2$$

using this actions we can form the semi-direct product $J \rtimes K$. (k′, l), (m′, q) in $K \rtimes L$ act on (h,m), (j, k) in $J \ltimes K$ from right and left

$$\bullet\ (K \rtimes L) \times (J \rtimes K) \to (J \rtimes K)$$
$$((k',l),(h,m)) \mapsto {}^{(k',l)}(h,m) = \left({}^{\partial_1(k')}h + {}^{l}h - \{k',m\}_2, {}^{l}m + k'k\right)$$

$$\bullet\ (J \rtimes K) \times (K \rtimes L) \to (J \rtimes K)$$
$$((j,k),(m',q)) \mapsto (j,k)^{(m',q)} = \left(j^{\partial_1(m')} + j^{lq} - \{k,m'\}_1, k^q + km'\right)$$

using this actions we form the semi-direct product E2 = $(J \rtimes K) \rtimes (K \rtimes L)$. There are R-algebroid morphisms ;

- $d_0^2 : (J \rtimes K) \rtimes (K \rtimes L) \to K \rtimes L \quad , \quad d_0^2(j,k,k',l) = (k',l)$
- $d_1^2 : (J \rtimes K) \rtimes (K \rtimes L) \to K \rtimes L \quad , \quad d_1^2(j,k,k',l) = (k+k',l)$
- $d_2^2 : (J \rtimes K) \rtimes (K \rtimes L) \to K \rtimes L \quad , \quad d_2^2(j,k,k',l) = (\partial_2(j)+k, \partial_1(k')+l)$
- $s_0^1 : K \rtimes L \to (J \rtimes K) \rtimes (K \rtimes L) \quad , \quad s_0^1(k,l) = (0,0,k,l)$
- $s_1^1 : K \rtimes L \to (J \rtimes K) \rtimes (K \rtimes L) \quad , \quad s_1^1(k,l) = (0,k,0,l)$

for t(k) = s(j), t(j) = s(k′), t(k′, l) = s(h,m), t(j, k) = s(m′, q).

4) There are actions of (j, k), (j′, k′) in J o K on j, j′ in J given by

- $(J \rtimes K) \times J \to J \qquad ((j,k),j') \mapsto {}^{(j,k)}j' = (jj', kj')$
- $J \times (J \rtimes K) \to J \qquad (j,(j',k')) \mapsto j^{(j',k')} = (jj', j^{k'})$

using this we form semi-direct product J ⋊ (J ⋊ K). There are actions of ((j″, k′), (k″, l)), ((h″,m′), (m″, q)) in ((J ⋊ K) ⋊ (K ⋊ L)) on (h, (h′,m)), (j, (j′k)) in (J ⋊ (J ⋊ K)) given by

- $(((J \rtimes K) \rtimes (K \rtimes L)) \times (J \rtimes (J \rtimes K)) \to (J \rtimes (J \rtimes K))$
  $((j'',k'),(k'',l)),(h,(h'm)) \mapsto {}^{((j'',k'),(k'',l))}(h,(h',m))$

- $((J \rtimes (J \rtimes K)) \times ((J \rtimes K) \rtimes (K \rtimes L)) \to (J \rtimes (J \rtimes K)$
  $(j,(j',k)),((h'',m'),(m'',q)) \mapsto (j,(j'k))^{((h'',m'),(m'',q))}$

$$
\begin{aligned}
&{}^{((j'',k'),(k'',l))}(h,(h',m)) = \\
&\big({}^{\partial_1(k')}h + {}^{\partial_1(k')}h' + {}^{\partial_1(k'')}h + {}^{l}h - \{k',m\}_2 - \{k',\partial_2(h')\}_1 - l''h' - \{\partial_2(l''),m\}_2, \\
&{}^{\partial_1(k'')}h' + {}^{l}h' - \{k'',m\}_2 + \{k',\partial_2(h')\}_1 + \{\partial_2(l''),m\}_2 + l''h', k'm + k''m + {}^{l}m\big)
\end{aligned}
$$

$$
\begin{aligned}
&(j,(j'k))^{((h'',m'),(m'',q))} = \\
&\big(j^{\partial_1(m')} + m^{\prime\partial_1(m')} + j^{\partial_1(m'')} + j^{q} - \{k,m'\}_1 - \{k,\partial_2(h'')\}_1 - \{\partial_2(j'),m'\}_2 - j'h'', \\
&j^{\prime\partial_1(m'')} + j^{\prime q} - \{k,m''\}_1 + \{k,\partial_2(h'')\}_1 + \{\partial_2(j'),m'\}_2 + j'h'', km' + km'' + k^{q}\big)
\end{aligned}
$$

using this actions we form E_3 = (J ⋊ (J ⋊ K)) ⋊ ((J ⋊ K) ⋊ (K ⋊ L)). There are R-algebroid morphisms ;

- $d_0^3 : E_3 \to E_2 \quad , \quad d_0^3((j,(j'k)),((j'',k'),(k'',l))) = (j'',k',k'',l)$
- $d_1^3 : E_3 \to E_2 \quad , \quad d_1^3((j,(j'k)),((j'',k'),(k'',l))) = (j'+j'',k+k',k'',l)$
- $d_2^3 : E_3 \to E_2 \quad , \quad d_2^3((j,(j'k)),((j'',k'),(k'',l))) = (j+j',k,k'+k'',l)$
- $d_3^3 : E_3 \to E_2 \quad , \quad d_3^3((j,(j'k)),((j'',k'),(k'',l))) = (j,\partial_2(j')+j,\partial_2(j'')+k',\partial_1(k'')+l)$
- $s_0^2 : E_2 \to E_3 \quad , \quad s_0^2(j,k,j',l) = (0,0,0,j,k,k',l)$
- $s_1^2 : E_2 \to E_3 \quad , \quad s_1^2(j,k,j',l) = (0,j,k,0,0,k',l)$
- $s_2^2 : E_2 \to E_3 \quad , \quad s_2^2(j,k,j',l) = (j,0,k,0,0,k',l)$

for t(j, k) = s(j′), t(j) = s(j′, k′), t((j″, k′), (k″, l)) = s(h,(h′,m)) t(j, (j′k)) = s((h ″,m′), (m″, q). Also

$$\begin{aligned} ker d_0^3 &= \{((j,(j'k)),((0,0),(0,0))\} \\ ker d_1^3 &= \{((j,(0,k)),((0,k'),(0,0))\} \\ ker d_2^3 &= \{((0,(0,0)),((j'',0),(0,0))\} \\ ker d_0^3 \cap ker d_1^3 \cap ker d_2^3 &= \{(0,0,0,0,0,0,0)\} = NE_3 \end{aligned}$$

Thus G_C = (E_n, d_n^i , s_n^j) is a simplicial R-algebroid with Moore complex of lenght 2.

Proposition: Let C = (J,K,L,∂_1,∂_2,$\{.\}_{1,2}$) and C’ = (J’,K’,L’,∂_1' ,∂_2' ,$\{.\}_{1,2}'$) be 2-crossed modules of R-algebroids.

$$\begin{array}{ccccc} J & \xrightarrow{d_2} & K & \xrightarrow{d_1} & L \\ \downarrow{\scriptstyle f_2} & & \downarrow{\scriptstyle f_1} & & \downarrow{\scriptstyle f_0} \\ J' & \xrightarrow{d_2'} & K' & \xrightarrow{d_1'} & L' \end{array}$$

Also let (f_2, f_1, f_0) be a 2-crossed module morphism from C to C′. If G_C and $G_{C'}$ are simplicial R-algebroids then we obtain a simplicial R-algebroid morphisms from G_C = E to $G_{C'}$ = E’ by using (f_2, f_1, f_0).

Proof: Let be

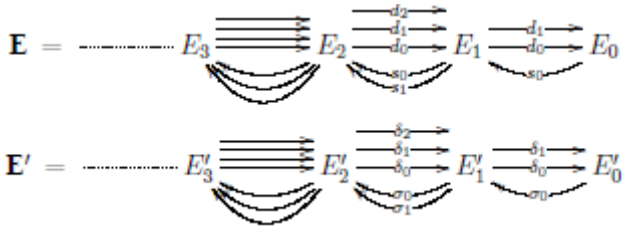

Thus

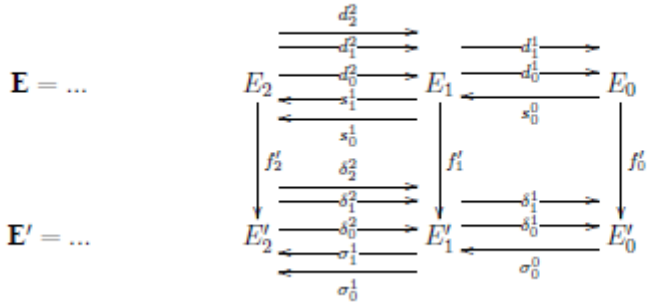

we set $f'_0 = (f_0)$, $f'_1 = (f_1, f_0)$, $f'_2 = (f_2, f_1, f_1, f_0)$. Therefore $f = (..., f'_2, f'_1, f'_0)$ is an simplicial R-algebroid morphism.

Then, a calculation proves to following proposition:

Proposition: The assignment G : 2XMod ⟶ Simp.R-Alg.$_{\leq 2}$ defined by G(C) = G_C on objects and by $G(f_2, f_1, f_0) = f$ on morphisms is a functor.

REFERENCES

Akca I.I., Pak S. (2010). Pseudo simplicial groups and crossed modules. Turkish Journal of Mathematics ; 34 (4): 18 475-488.

Akca I.I., Pak S. (2022). Pseudo Simplicial Algebras, Crossed Modules and 2-Crossed Modules. Konuralp Journal of Mathematics 10 (2) 326-331.

Akca I.I, Arvasi Z. (2002). Simplicial and crossed Lie algebras. Homology, Homotopy and Applications ; 4 (1): 43-57.

Aḳca I.I, Emir K., Martins JF. (2016). Pointed homotopy of maps between 2 -crossed modules of commutative algebras. Homology, Homotopy and Applications ; 18 (1): 99-128.

Aḳca I.I, Emir K, Martins J. (2019). Two-fold homotopy of 2 -crossed module maps of commutative algebras. Communations in Algebra ; 47 (1): 289-311.

Akca I.I., Avcıoglu O. (2022). Equivalence between (pre)cat1-R-algebroids and (pre) crossed modules of R- algebroids, Bull. Math. Soc. Sci. Math. Roumanie Teme (110) No-3, 267-288.

Amgott S. M. (1986). Separable algebroids, Journal of Pure and Applied Algebra, 40, 1-14.

Arslan Ege U., Akca I.I., Onarli Irmak G., Avcioglu O. (2019). Fibrations of 2-crossed Modules, Mathematical Methods in the Applied Sciences 42 (16), 5293-5304.

Arvasi Z., Porter T. (1996). Simplicial and crossed resolutions of commutative algebras, Journal of Algebra, 181(2), 426-448.

Arvasi Z., Porter T. (1998). Freeness conditions for 2-crossed modules of commutative algebras, Application Category Structure, 6(4), 455-471.

Arvasi Z. (1997). Crossed squares and 2-crossed modules of commutative algebras, Theory Applications Categories, 3, 160-181.
Arvasi Z., Ulualan E. (2006). On algebroic models for homotopy 3-types, Journal of homotopy and related structures, 1(1), 1-27.
Avcıoglu O., Akca I.I. (2017). Coproduct of Crossed A-Modules of R-algebroids, Topological Algebra and its Applications, 5, 37-48.
Avcıoglu O., Akca I.I. (2018). Free modules and crossed modules of R-algebroids, Turkish Journal of Mathematics, 42: 2863-2875.
Avcıoglu O., Akca I.I. (2017). On generators of Peiffer ideal of a pre-R-algebroid in a precrossed module and applications, NTMSCI 5, No. 4, 148-155 .
Avcıoglu O., Akca I.I. (2017). On Pullback and Induced Crossed Modules of R-Algebroids, Com- mun.Fac.Sci.Univ.Ank.Series A1, Volume 66, Number 2, Pages 225-242.
Conduche D. (1984). Modules croises generalises de longueur 2, Journal of Pure and Applied Algebra, 34, 155-178.
Doncel J.L., Grandjean A.R., Vale, M. J. (1992). On the homology of commutative algebras, Journal of Pure and Applied Algebra, 79(2), 131-157.
Grandjean A.R., Vale M.J. (1986). 2-Modulos Cruzados En La Cohomologıa De Andre- Quillen, (Madrid: Real Academia de Ciencias Exactas, Fısicas y Naturales de Madrid).
Gurmen O., Ulualan E. (2020). Simplicial algenroids and internal categories within R- algebroids, Tbilisi Math. J., 13(1), 113-121.
Mitchell B. (1972). Rings with several object, Advances in Mathematics, 8(1), 1-161.
Mitchell B. (1978). Some applications of module theory to functor categories, Bull. Amer. Math. Soc., 84, 867-885.
Mitchell B. (1985). Separable algebroids, Mem. Amer. Math. Soc., 57, 333, 96.
Mosa G.H. (1986). PhD Thesis, University College of North Wales, (Bangor).
Mutlu A., Porter T. (1998), Freeness conditions for 2-crossed modules and complexes, Theory Applications Categories, 4, 174-194.
Mutlu A., Porter T. (1998). Applications of peiffer pairings in the moore complex of a simplicial group, Theory Applications Categories, 4, 148-173.
Ozel E., Arslan Ege U., Akca I.I. (2024). A Higher Dimensional Categorical Perspective on 2-crossed Modules. 57, 20240061, 1-06.
Porter T. (1986). Homology of commutative algebras and an invariant of simis and vasconcelos, Journal of Algebra, 99(2), 458-465.
Whitehead J. H. C. (1941). On adding relations to homotopy groups, Annals of Mathematics, 42(2), 409-428.
Whitehead J. H. C. (1946). Note on a previous paper entitled “On adding relations to homotopy groups”, Annals of Mathematics , 47(4), 806-810.

Fibonacci Sequence

Murat CANDAN[1]

1- Prof. Dr.; İnönü Üniversitesi Fen Edebiyat Fakültesi Matematik Bölümü. murat.candan@inonu.edu.tr ORCID No: 0000-0002-1941-7442

ABSTRACT

The Fibonacci sequence is a mathematical series defined as:

$F_n=F_{n-1}+F_{n-2}$, with initial terms $F_0=0$ and $F_1=1$.

This sequence is integral to various fields of mathematics, nature, and applied sciences. Each number in the series represents the sum of the two preceding numbers, and as the sequence progresses, the ratio between consecutive terms approaches the golden ratio ($\phi\approx1.618\phi\approx1.618$). The Fibonacci sequence is known for its appearances in diverse natural phenomena, such as the arrangement of leaves, the spirals of shells, and even the breeding patterns of animals.

Mathematical Properties of Fibonacci Sequence

The Fibonacci sequence exhibits fascinating mathematical properties. For instance:

1. **Recursive Relation:** The sequence is defined recursively, making it a foundational example in algorithmic and computational studies.
2. **Golden Ratio Connection:** The ratio $Fn+1/Fn$ converges to the golden ratio as $n\rightarrow\infty$.
3. **Matrix Representation:** Fibonacci numbers can be derived using matrix exponentiation, showcasing their linear algebraic significance.
4. **Binet's Formula:** The n-th Fibonacci number can be calculated directly using Binet's closed-form formula:

$F_n=\phi_n-(1-\phi)_n, 5F_n=5\phi_n-(1-\phi)_n$.

Fibonacci Sequence in Nature

The sequence is observed extensively in the natural world, demonstrating its role in the optimization and efficiency of biological systems:

- **Phyllotaxis:** Leaves, seeds, and petals in plants often follow Fibonacci numbers to maximize sunlight absorption and space utilization.
- **Animal Kingdom:** Patterns in the population growth of rabbits (a classical Fibonacci example), the structure of pine cones, and the spirals in shells follow Fibonacci principles.

Fibonacci Sequence in Dizi (Sequence) Spaces

In mathematical analysis, Fibonacci numbers have inspired advancements in sequence spaces. Sequence spaces are topological vector spaces consisting of real or complex-valued sequences. Prof. Dr. Murat Candan has notably contributed to defining new sequence spaces using generalized Fibonacci sequences and matrices. His work focuses on:

- **Topological Properties:** Exploring norm, completeness, and compactness in Fibonacci-based sequence spaces.
- **Geometric Characteristics:** Studying convexity, reflexivity, and super-reflexivity within these spaces.
- **Matrix Transformations:** Investigating the behavior of Fibonacci-based sequence spaces under matrix transformations, particularly with Nörlund and generalized Fibonacci matrices.

Broader Applications

The Fibonacci sequence is not limited to mathematics and nature; it also finds applications in technology, art, and engineering:

- **Algorithm Design:** Fibonacci-based algorithms are used in computer science for tasks like searching and sorting.
- **Architecture and Art:** The golden ratio derived from the Fibonacci sequence is a principle of aesthetics in design.
- **Financial Markets:** Traders use Fibonacci retracement levels for predicting support and resistance in price movements.

The Fibonacci sequence is a profound intersection of mathematics, nature, and applied sciences. Its recursive structure and connection to the golden ratio make it a cornerstone in understanding patterns, growth, and optimization. The mathematical exploration of Fibonacci-based sequence spaces, as conducted by Prof. Dr. Murat Candan and others, highlights the sequence's theoretical significance and practical applications. This growing body of research continues to unveil the sequence's potential for solving complex problems across disciplines, from biology to computational sciences.

Keywords – Fibonacci Sequences

Reflections of Fibonacci Sequences in Nature

The Fibonacci sequence takes its place in the history of science as a striking sequence known for its mathematical aesthetics and its impact on nature. This sequence is formed by a simple rule: Each term is equal to the sum of the two preceding terms. This mathematical principle has reflections in every aspect of nature, from plants to animals, from galaxies to the human body. The influence of the Fibonacci sequence goes beyond our understanding of biological structures in nature, revealing fundamental principles of design and organisation.

After briefly explaining the mathematical foundations of the Fibonacci sequence, this chapter will examine its different reflections in nature. A variety of scientific observations and research will be used to detail the effects of the Fibonacci sequence in areas as diverse as plant organisation, animal behaviour, cosmic structures and human biology.

Mathematical Structure of the Fibonacci Sequence

The Fibonacci sequence is one of the most important sequences in the history of mathematics, representing the harmony between aesthetics and functionality. Although this sequence is based on a simple addition rule, it has a wide range of effects from mathematics to biology, engineering to art. Understanding the mathematical foundations of the Fibonacci sequence helps us to grasp why this sequence appears so widely in nature and in man-made systems.

In this chapter, the mathematical structure of Fibonacci sequence will be analysed in detail, properties of the sequence, related concepts and applications will be discussed with examples.

Definition of Fibonacci Sequence

The Fibonacci sequence is mathematically defined as follows:

This definition states that each term of the Fibonacci sequence is the sum of the two preceding terms. The Fibonacci sequence begins as follows:

One of the main properties of this sequence is that its ratio approaches the golden ratio. When approaching infinity, the ratio of two consecutive terms of the sequence approaches the golden ratio (φ), defined by the expression.

This connection plays a critical role in the various reflections of the Fibonacci sequence in geometry, art and nature.

Mathematical Properties of Fibonacci Sequence

Recursive Definition and Closed Formula

Although the Fibonacci sequence is based on a recursive definition, it can also be expressed explicitly, i.e. by a closed formula. This formula is known as the Binet formula and is as follows:

This formula makes it possible to calculate any term of the Fibonacci sequence without knowing the previous terms of the sequence. Binet's formula explains the connection of Fibonacci numbers with the golden ratio in a mathematical way.

Modular Arithmetic and Fibonacci Sequence

The Fibonacci sequence also shows interesting properties in its modular arithmetic. For example, the ratio between two consecutive terms of the Fibonacci sequence has a repeating pattern according to a given module. This property has important applications in computer science and cryptography.

Prime Numbers in Fibonacci Sequence

The primes in the Fibonacci sequence are a separate area of research in mathematics. Fibonacci primes refer only to the prime terms of the Fibonacci sequence. The arrangement of these numbers has a complex structure and is linked to prime number theory.

Pisano Loops

The Fibonacci sequence has a repeating cycle in its modular arithmetic. These cycles are called Pisano cycles and refer to the repeating patterns of the Fibonacci sequence with respect to a given module. Pisano cycles allow us to understand the regular structure of the sequence and the length of these cycles varies depending on the module.

Fibonacci Sequence and Golden Ratio

The mathematical structure of the Fibonacci sequence is very closely related to the golden ratio (φ). The ratio of the two consecutive terms of the sequence approaches the golden ratio as you progress through the sequence. This can be expressed by a limit as follows:

The golden ratio is a critical concept for understanding the applications of the Fibonacci sequence in nature, as it has both a geometric and numerical structure.

Geometric Representations of the Fibonacci Sequence

The Fibonacci sequence can also be represented geometrically. For example, the Fibonacci spiral is constructed using a series of squares and quarter circles. This geometric representation allows us to understand spiral structures in nature.

Fibonacci Squares and Spirals

A Fibonacci spiral is constructed using Fibonacci squares. The side length of each square is equal to the consecutive Fibonacci numbers in the sequence. The quarter circles drawn on each of these squares form the Fibonacci spiral. This spiral is found in many structures in nature, such as shells, galaxies and plant structures.

Logarithmic Spirals

The Fibonacci spiral is in reality a logarithmic spiral approximation. Logarithmic spirals have a mathematical form based on the golden ratio. These spirals optimise the size and shape variations of biological structures.

Applications of Fibonacci Sequence

The mathematical properties of the Fibonacci sequence find many applications in different disciplines. These applications range from biology to economics.

Computer Science and Algorithms

The Fibonacci sequence is used in various algorithms in computer science. For example, the Fibonacci search algorithm is an effective search method in data structures. Also, data structures such as Fibonacci stacks are useful in complex calculations.

Finance and Economics

The Fibonacci sequence is used in technical analysis in financial markets. Fibonacci retracement levels are used to analyse price movements and predict future turning points. These levels play an important role in understanding psychological behaviour in the markets.

Despite its mathematical simplicity, the Fibonacci sequence has an extraordinary richness. It's recursive structure, closed formula and geometric representations reveal the connection between mathematical aesthetics and the real world. Understanding the mathematical structure of the Fibonacci sequence provides a foundation for a deeper study of its effects in nature and in man-made systems.

Fibonacci Sequence in the Plant Kingdom

The Fibonacci sequence reveals a hidden order among numbers that offers a profound insight into mathematical and biological phenomena. Introduced by Leonardo Fibonacci, it is an arithmetic sequence in which each number is the sum of two preceding numbers. The formula of the sequence is expressed mathematically as follows:

$$F(n)=F(n-1)+F(n-2),(n \geq 2, F(0) = 0, F(1) = 1).$$

The reflection of this sequence in plants draws attention as an indicator of aesthetic order and biological activity in nature. In the plant kingdom, we can see the traces of the Fibonacci sequence in the examination of a wide variety of morphological structures, from the arrangement of flower petals to the spiral arrangement of seeds.

This study aims to detail the patterns, biological mechanisms and evolutionary advantages of the Fibonacci sequence in plants.

2. Fundamentals and Mathematical Properties of Fibonacci Sequence

The Fibonacci sequence is not just a sequence of numbers, but reflects a fundamental principle underlying many phenomena and structures in nature. There is a ratio of approximately 1.618 between each consecutive number of the sequence, and this ratio is known as the "golden ratio" (φ). Mathematically

$$\phi=1+52.\ \phi=21+5.$$

The golden ratio plays a decisive role in the growth patterns of plants. Thanks to this ratio, energy efficiency and space optimisation are achieved in plants.

3. Fibonacci sequence in plants

In the plant kingdom, reflections of the Fibonacci sequence are observed in various morphological features:

3.1. Arrangement of flower petals

The number of petals of many flowers is equal to a number in the Fibonacci sequence. For example:

- Three petals on the lily,
- 5 petals on the primrose,
- The daisy usually has 34 or 55 petals.

These numbers are associated with the genetically encoded growth mechanisms of plants and provide an advantage in the evolutionary process.

3.2. Spiral arrangement of seeds

In plants such as sunflowers and pine cones, the seeds and scales are arranged in a geometry called the golden spiral. The number of these spirals corresponds to two consecutive numbers in the Fibonacci sequence (e.g. 21 and 34). This arrangement ensures that the seeds cover the optimum area and utilise sunlight with maximum efficiency.

3.3. Leaf Arrangement (Phyllotaxy)

Phyllotaxy is the arrangement of leaves attached to a plant stem. In most plants, the leaves are arranged at an angle related to the Fibonacci sequence. These angles are usually measured at 137.5°, which is the golden angle. This arrangement ensures that the leaves do not overshadow each other and ensure maximum light intake for photosynthesis.

4. Biological Mechanisms of Fibonacci Sequence

The biological processes that explain the formation of the Fibonacci sequence in plants are as follows:

4.1. Effect of Meristematic Cells

Plant growth originates from cells called meristems. The rate at which these cells divide and differentiate is regulated in accordance with the Fibonacci sequence.

4.2. Role of Hormones

Plant hormones, especially auxin, play an important role in the organisation of leaves and flowers. Auxin accumulates at the growth points and ensures that the cells are organised in a Fibonacci sequence.

4.3. Genetic Control

Growth regulation in plants is a genetically controlled process. An order in accordance with the Fibonacci sequence is associated with gene expression.

5. Evolutionary Advantages

The advantages of Fibonacci sequence in plants can be listed as follows:

5.1. Area Optimisation

The Fibonacci arrangement maximises the surface area of the plants so that they benefit more from sunlight.

5.2. Energy Efficiency

The spiral layout saves energy during growth. This allows the plant to produce more biomass with fewer resources.

5.3. Competitive Advantage

Growth in accordance with the Fibonacci sequence allows plants to better adapt to environmental conditions, which makes them more advantageous in ecological competition.

6. Biomimicry and Technological Applications of Fibonacci Sequence

The Fibonacci sequence in plants has also been a source of inspiration in engineering and design. In particular

- Layout of solar panels,

- Optimum storage systems,
- Efficient water transport systems are inspired by Fibonacci patterns.

The Fibonacci sequence is an expression of order and harmony in the plant kingdom. This pattern, which is seen in many morphological structures from flower petals to seed sequences, shows how biology is intertwined with mathematics. This order provides both evolutionary advantages and has been a source of inspiration for humanity in design and engineering. Understanding the Fibonacci sequence in the plant kingdom helps us understand not only biology, but also mathematics and the aesthetics of nature in a deeper way.

This topic encourages an interdisciplinary approach, as a common research area for both biologists and mathematicians.

In nature, the most striking reflections of the Fibonacci sequence are seen in plants. Phyllotaxy, the arrangement of leaves, branches or seeds, represents a form of the Fibonacci sequence. Plants are in an interaction that makes it possible for them to survive against external factors, and this interaction can be explained by the effects of the Fibonacci sequence.

Leaf Arrangements

In plants, the arrangement of the leaves often corresponds to the Fibonacci sequence. For example, in a rose petal or a sunflower, the arrangement of the leaves on the stem can be related to consecutive Fibonacci numbers. This structure is optimised so that the plant can receive the maximum amount of shade or sunlight it can see.

Seed and Flower Arrangements

The arrangement of seeds in plants such as sunflowers, daisies and pineapples is in accordance with the Fibonacci sequence. This arrangement forms a spiral pattern, allowing the seeds to settle in the most efficient way possible. In a sunflower, for example, the clockwise and anti-clockwise spirals of the seed arrangement usually correspond to consecutive Fibonacci numbers.

Fibonacci Sequence in the Animal Kingdom

The Fibonacci sequence is an important concept that provides a mathematical explanation of the order and structure in biological systems. It is a sequence of numbers in which each term is the sum of two preceding terms. It is mathematically defined as follows:

$$F(n)=F(n-1)+F(n-2),(n \geq 2, F(0) = 0, F(1) = 1).$$

The observation of the Fibonacci sequence and the related golden ratio in various organisms in nature is not limited to plants; the effects of this sequence in the animal kingdom are also remarkable. A wide range of biological features such as the body structure, behaviour and population dynamics of animals can be associated with the Fibonacci sequence.

This study aims to address how the Fibonacci sequence manifests in the animal kingdom, the underlying biological mechanisms and the evolutionary advantages of this order.

2. Fundamentals and Mathematical Properties of Fibonacci Sequence

The Fibonacci sequence is considered a mathematical model of self-repeating and growth-expressing processes in nature. The ratio between consecutive numbers in the sequence approaches the golden ratio ($\phi\phi$). The golden ratio has approximately the following value:

$$\phi=1+52\approx1.618.$$

This ratio is observed in animal body proportions, behavioural patterns and population growth rates. The Fibonacci sequence is a fundamental principle in the organisation of complex biological systems.

3. Fibonacci Sequence in the Animal Kingdom

3.1. Body Proportions in Animals

The ratio of animal body parts to each other can be related to the Fibonacci sequence and the golden ratio. For example:

- **Shellfish (Nautilus):** The spiral shell structure coincides with the Fibonacci spiral. This spiral ensures energy efficiency during growth and increases the durability of the shell.
- **Body proportions of insects:** The antennal lengths or segments of most insects increase in accordance with the Fibonacci sequence.

3.2. Animal Behaviour and Movement Models

The Fibonacci sequence is also observed in the movement and behaviour patterns of animals. For example:

- **Bees** The population ratios of male and female bees follow the Fibonacci sequence. Drones come from only one parent (the female bee), whereas female bees come from two parents (one female and one male). This genetic structure leads to population proportions that conform to the Fibonacci sequence.
- **Predator and prey relationships:** In some population models, the balance between prey and predator can be explained by the Fibonacci sequence and the golden ratio.

3.3. Spiral Structures and Organisation

Spiral structures are often seen in the bodies of animals and are related to the Fibonacci spiral:

- **Sea stars** The arms of sea stars are often associated with numbers in the Fibonacci sequence (such as 5 or 8).
- **Snails** Snail shells follow a growth pattern similar to a golden spiral. This spiral structure expands outwards depending on the growth of the animal.

4. Behavioural and Ecological Mechanisms of the Fibonacci Sequence

4.1. Population Dynamics

The growth rate and population dynamics of animal communities reflect the effects of the Fibonacci sequence:

- **Bee colonies:** As already mentioned, the genetic structure of male and female bees conforms to the Fibonacci sequence. This ensures balance in the growth and development of the colony.
- **Rabbit Population:** The classic example of the Fibonacci sequence, the rabbit population model shows how the population grows if a pair of rabbits breed under ideal conditions.

4.2. Movement Mechanisms of Animals

The paths and strategies that animals follow when moving can be related to the Fibonacci sequence. For example:

- **Strategies of predators to track their prey:** Some predators follow a Fibonacci sequence to predict the movements of their prey.
- **Schools of fish:** The distances and movement patterns between individuals in schools of fish may be related to the Fibonacci spiral.

4.3. Genetic and Evolutionary Basis

The genetic structure and evolutionary processes of animals can be explained by the Fibonacci sequence:

- **DNA helix:** The helical structure of DNA has a geometry associated with the golden ratio and the Fibonacci spiral.
- **Evolutionary advantages:** The Fibonacci order allows animals to save energy and better adapt to environmental changes.

5. Evolutionary Advantages of Fibonacci Sequence

The evolutionary advantages of the Fibonacci sequence in the animal kingdom can be summarised as follows:

5.1. Energy Efficiency

Growth and movement in accordance with the Fibonacci sequence allows animals to optimise energy consumption. For example, spiral shells and body structures facilitate growth.

5.2. Area Optimisation

The spiral organisation allows the animals' bodies to occupy less space and make better use of environmental conditions.

5.3. Genetic Advantages

When population dynamics and genetic arrangements conform to the Fibonacci sequence, animals have a better chance of survival.

6. Applications and Inspirations of Fibonacci Sequence in the Animal Kingdom

The Fibonacci sequence has been used in many technological and engineering applications inspired by animals:

- **Movement strategies of robotics:** Inspired by the movement patterns in schools of fish, robotic systems have been developed.

- **Biomimicry:** Energy efficient designs inspired by the spiral structure and movements of animals.

The existence of the Fibonacci sequence in the animal kingdom shows that the order and aesthetics in nature are based on a mathematical foundation. This order, which is observed in many biological systems from seashells to bee colonies, provides both evolutionary advantages and is an important source of inspiration for science and engineering. The Fibonacci sequence contributes to the understanding of patterns in nature by combining biology with mathematics.

Research in this area encourages a deeper study of the Fibonacci sequence in animals and the transformation of this order into new applications for humanity.

The animal kingdom also shows the effects of the Fibonacci sequence. Physical structures such as shells, body proportions and movement patterns show the effects of the Fibonacci sequence.

Sea Shells and Spiral Forms

Marine creatures such as the nautilus shell develop shells in the form of logarithmic spirals, a geometric reflection of the Fibonacci sequence. This spiral form optimises the structural strength of the creature and the increase in size.

Bee Hives

The family trees of male and female individuals in bee colonies can be directly related to the Fibonacci sequence. While male bees have only one parent (the female bee), female bees have two parents. This lineage structure shows that Fibonacci order is also reflected in animal behaviour.

Cosmological Reflections

The Fibonacci sequence is found not only in biological structures but also in cosmological patterns in the universe. Spiral structures in galaxies follow the logarithmic spirals of the Fibonacci sequence.

Galaxy Structures

Many galaxies, such as the Milky Way galaxy, have spiral arms. These arms are arranged in a geometry based on the golden ratio. The reflection of the

Fibonacci sequence on these vast diameters offers a striking insight into the fundamental order of the universe.

DNA and Molecular

DNA has a complex structure that carries the genetic information of a living being. The DNA molecule reflects the golden ratio in the arrangement of sugar and phosphate chains. This biological structure reveals the effects of the Fibonacci sequence at the micro level.

Reflections of Fibonacci Sequence in Art and Architecture

The Fibonacci sequence was also used in art and architecture by people inspired by nature. During the Renaissance period, Leonardo da Vinci's works and structures such as the Parthenon draw attention with their designs based on the golden ratio.

Painting and Sculpture

Leonardo da Vinci associated the proportions of the human body with the golden ratio in works such as "Vitruvian Man". This inspired the works of other artists and led to the adoption of the Fibonacci sequence as an aesthetic criterion.

Architecture

The proportions of historical buildings such as the Parthenon are based on the geometric principles of the Fibonacci sequence. These structures improve people's aesthetic perception by combining the harmony found in nature with an architectural order

The Fibonacci sequence is a fundamental mathematical structure that helps us understand the diversity and order observed in nature. This sequence, which manifests itself in a wide range of from plants to animals, from galaxies to the human body, allows us to comprehend the aesthetic and functional harmony of the universe. More in-depth research on the Fibonacci sequence can offer new perspectives in both scientific and artistic fields.

Investigation of Prof. Dr. Murat Candan's Academic Studies on Fibonacci Sequence Spaces

The Fibonacci sequence has an important place in mathematical analysis and applied mathematics. The properties and generalisations of this sequence have

been studied in depth, especially in the theory of sequence spaces. Prof. Dr. Murat Candan is an academic known for his work in this field. In this article, Prof. Candan's academic studies on Fibonacci sequence spaces will be examined and the place of these studies in mathematical analysis will be evaluated.

Fibonacci Sequence and Sequence Spaces

The Fibonacci sequence is a sequence in which each term is the sum of the two preceding terms. It is mathematically defined as follows:

$$F_n=F_{n-1}+F_{n-2} \; ; \; n\geq 2 \; (F_0=0, \; F_1=1)$$

Generalisations of this sequence and its relation to different sequence spaces is an important research topic in mathematical analysis. Sequence spaces are linear subspaces of ω, the set of all real-valued sequences, and can be equipped with different norms to form Banach spaces.

Prof. Dr Murat Candan's Works

Prof. Dr. Murat Candan has defined new sequence spaces using Fibonacci and generalised Fibonacci sequences and studied their topological and geometric properties. In particular, he has worked on bounded and convergent sequence spaces obtained with generalised Fibonacci and Nörlund matrices. These studies reveal the relation of sequence spaces with matrix transformations and operator theory.

Topological and Geometric Properties of Sequence Spaces

Topological properties of sequence spaces are examined with concepts such as norm, convergence and completeness. Geometric properties include concepts such as uniform convexity, strict convexity and superreflexivity. Prof. Candan's work investigates these properties of sequence spaces defined using Fibonacci and generalised Fibonacci sequences.

Matrix Transformations and Sequence Spaces

Matrix transformations are used to define linear operators between sequence spaces. In particular, regular matrices and their domains are important tools for defining new sequence spaces. Prof. Dr. Candan defined new sequence

spaces using generalised Fibonacci and Nörlund matrices and studied their behaviour under matrix transformations.

Prof. Dr. Murat Candan's work on Fibonacci sequence spaces makes important contributions to mathematical analysis and the theory of sequence spaces. These studies help to understand the topological and geometric properties of sequence spaces and deepen the relationship between matrix transformations and sequence spaces. In the future, further extension of the work in this area and the study of different array spaces will open new horizons in mathematical analysis.

References:

Candan M, (2022). Some Characteristics of Matrix Operators on Generalized Fibonacci Weighted Difference Sequence Space, Symmetry, 14:7, 1283 doi.org/10.3390/sym14071283.

Candan M, (2015). A New Approach on the Spaces of Generalized Fibonacci Difference Null and Convergent Sequences, Mathematica Aeterna, 5:191 – 210

A Numerical Method for Solving a Class of Fractional Differential Equations with Proportional Caputo Derivative

Kenan Yildirim[1]

Sertan Alkan[2]

[1]Mus Alparslan University, Mus, Turkey
[2]Iskenderun Technical University, Hatay, Turkey
Emails: k.yildirim@alparslan.edu.tr[1], sertan.alkan@iste.edu.tr[2]

ABSTRACT

In this paper, a numerical solution method to solve fractional differential equations with proportional Caputo derivative is introduced. Fibonacci collocation method is applied to a class of fractional differential equations. In order to show the efficiency of the proposed method, two illustrative examples are presented by tables and graphical forms. After observation the tables and graphics, it is concluded that Fibonacci collocation method gives very good and robust approximation results for the class of investigated fractional differential equations.

Keywords: Fibonacci collocation method, initial value problems, proportional Caputo derivative.

1. INTRODUCTION

Over the last two decades several studies concerning both theoretical and physical applications of fractional calculus have been published related to various fields of science. Some of them this studies can be summarized as follows, but not limited to; (Akgül, Akgül & Yavuz, 2021; Hatipoglu, Alkan & Secer, 2017; Khan, Zarin, Akgül, Saeed & Gul, 2021; Alkan & Hatipoglu, 2017; Abro, Siyal & Atangana, 2021; Atangana, 2021; Bohner & Hatipoğlu, 2018; Hatipoğlu, 2019). Especially, In (Khalid, Abbas, Iqbal & Baleanu, 2020), authors study the computational research of the Caputo time fractional Allen–Cahn equation. In (Owolabi, 2018), Analysis and numerical simulation a multicomponent system with the Atangana–Baleanu fractional derivative by Owalabi. In (Akgül, 2018), Akgül has presented a novel method for a fractional derivative with non-local and non-singular kernel. In (Akgül, 2019), the solutions of differential equations with the generalized fractional derivatives are investigated and several numerical examples are presented. Atangana et al. (Atangana & Akgül, 2020) have studied some properties of fractal fractional derivation in detail. In (Fernandez, Baleanu & Srivastava, 2019), Fernandez and et. al. present the series representations for fractional-calculus operators involving generalized Mittag-Leffler functions. Wu et al. (Wu, Zeng & Baleanu, 2019) give the fractional impulsive differential equations including the, integral equations, short memory case and exact solutions. Recently an interesting new fractional operator namely, proportional Caputo hybrid operator is defined in (Baleanu, Fernandez & Akgül, 2020) by combining the proportional derivative and Caputo derivative. Hence, new hybrid fractional derivative has the properties of the both fractional derivatives and hence it is expected Caputo proportional derivative to have better modelling and analyzing results of engineering and applied sicences. In particular constant proportional Caputo derivative is introduced in the same paper as a special case of proportional Caputo hybrid operator. This relatively new fractional derivative definition and its properties could provide a variety among the fractional operators and a new tool for researchers. In (Akgül, Akgül & Baleanu, 2020) an application of constant proportional Caputo derivative to economic model that is based on market equilibrium is given. In (Sweilam, Al-Mekhlafi & Baleanu, 2021) the hybrid fractional order stochastic mathematical model of the Coronavirus (2019-nCov) is presented and found that the proportional Caputo hybrid operator has more suitable and generalized results for the Coronavirus model than the Caputo fractional derivative. Another biological mathematics application of constant proportional Caputo operator is

given by (Günerhan, Dutta, Dokuyucu & Adel, 2020) as a comparison of the solutions of the fractional HIV models constructed by using both operators. In (Ikram, Asjad, Akgül & Baleanu, 2021) generalization of Brinkman type fluid model by using constant proportional Caputo fractional operator is presented as an application for the thermo-physics. Due to the applicability of the proportional Caputo hybrid operator to broad range of science in this paper we propose the numerical solutions for a class of the equation (1) defined with the proportional Caputo hybrid operator.

$$Q_\alpha(x)u^{(\alpha)}(x) + \sum_{k=0}^{m} p_k\,(x)u^{(k)}(x) = g(x),\ \ 0 \le x \le 1,\ \ 0 < \alpha < 1 \qquad (1)$$

with the initial conditions

$$\sum_{k=0}^{m-1} [a_k u^{(k)}(0)\ +\ b_k u^{(k)}(0)] = \delta_k, \qquad (2)$$

where $u^{(0)}(x) = u(x)$ and $u(x)$ is an unknown functions. $P_k(x)$, $Q_\alpha(x)$ and g(x) are given continuous functions on the interval $[0,1]$, a_k, b_k and δ_k are suitable constants.

The equation (1) has a potential for modelling some phenomena in physics, biology. and engineering sciences. In this study the objective problem is solved by using Fibonacci collocation method due to its good approximation results. In (Kurt, Yalçinbas, & Sezer, 2013), Fibonacci collocation method is applied to linear differential-difference equations. Similarly, in (Kurt, Yalçinbas, & Sezer, 2013), the high-order linear Fredholm integro-differential-difference equations are used by using Fibonacci collocation method. In (Mirzaee & Hoseini, 2014), a class of systems of linear Fredholm integro-differential equations is studied by the method. The paper given by (Mirzaee & Hoseini, 2013) deals with that the application of Fibonacci collocation method to singularly perturbed differentialdifference equations. Also, in (Mirzaee & Hoseini, 2017), Fibonacci collocation method is used for approximately solving a class of systems of high-order linear Volterra integro-differential equations. Similarly, in (İbrahimoğlu, 2021), Mock-Chebyshev Polynomials are introduced. In this study, Fibonacci polynomials are employed due to having less computational process in the computation steps.

The aim of this study is to get the approximate solution as the truncated Fibonacci series defined by

$$u(x) = \sum_{n=1}^{N+1} c_n\, F_n(x) \qquad (3)$$

where $F_n(x)$ denotes the Fibonacci polynomials; c_n $(1 \le n \le N + 1)$ are unknown Fibonacci polynomial coefficients, and N is chosen as any positive integer such that $N \ge m$.

The paper consists of six sections. In Section 2, the basic properties of Fibonacci polynomials and the definition of the proportional Caputo derivative are presented. In Section 3, the fundamental matrix forms of Fibonacci collocation method by using fundamental relations of Fibonacci polynomials are constructed to obtain the approximate solutions for the given class of linear fractional differential equation. In section 4, the residual error function is formulated. In Section 5, two test problems are presented and the method are tested using the residual error function. Finally, conclusions are given in Section 6.

2. PRELIMINARIES

Large classes of polynomials can be defined by three-term recurrence relations. One of these polynomials, called the Fibonacci polynomials, were studied by Falcon and Plaza (Falcon & Plaza 2007; Falcon & Plaza 2009). The recurrence relation of those polynomials is defined by

$$F_n(x) = xF_{n-1}(x) + F_{n-2}(x)$$

where $F_1(x) = 1$, $F_2(x) = x$ and $n \geq 3$. The properties were further investigated by Falcon and Plaza in (Falcon & Plaza 2007; Falcon & Plaza 2009). The first few Fibonacci polynomials are

$$F_1 = 1,$$
$$F_2 = 1x,$$
$$F_3 = 1x^2 + 1,$$
$$F_4 = 1x^3 + 2x,$$
$$F_5 = 1x^4 + 3x^2 + 1,$$
$$F_6 = 1x^5 + 4x^3 + 3x,$$
$$F_7 = 1x^6 + 5x^4 + 6x^2 + 1,$$
$$F_8 = 1x^7 + 6x^5 + 10x^3 + 4x,$$
$$F_9 = 1x^8 + 7x^6 + 15x^4 + 10x^2 + 1,$$
$$F_{10} = 1x^9 + 8x^7 + 21x^5 + 20x^3 + 5x$$

Definition 1. (Baleanu, Fernandez & Akgül, 2020) The proportional-Caputo operator is defined by

$${}^{PC}_{0}D^{\alpha}_{x} f(x) = \frac{1}{\Gamma(1-\alpha)} \int_0^x \left(K_1(\alpha,t) f(t) + K_0(\alpha,t) f'(t)\right)(x-t)^{-\alpha} dt$$

where

$$K_0(\alpha, t) = \alpha t^{1-\alpha}$$

and

$$K_1(\alpha, t) = (1-\alpha)t^{\alpha}$$

specially.

3. FUNDAMENTAL RELATIONS

Let us assume that linear combination of Fibonacci polynomials Eq.(3) is an approximate solutions of Eq.(1). Our purpose is firstly to determine the matrix forms of Eq.(1) by using Eq.(3). Firstly, we can write Fibonacci polynomials in the matrix form

$$F(x) = T(x)M \tag{4}$$

where $F(x) = [F_1(x)\, F_2(x) \ldots F_{N+1}(x)]$, $T(x) = (1\ x\ \ x^2\ x^3\ \ldots . x^N)$, $C = \left(c_1\ c_2 \ldots\ c_{(N+1)}\right)^T$ and

$$M = \begin{bmatrix} 1 & 0 & 1 & 0 & 1 & 0 & 1 & 0 & 1 & 0 & \ldots \\ 0 & 1 & 0 & 2 & 0 & 3 & 0 & 4 & 0 & 5 & \ldots \\ 0 & 0 & 1 & 0 & 3 & 0 & 6 & 0 & 10 & 0 & \ldots \\ 0 & 0 & 0 & 1 & 0 & 4 & 0 & 10 & 0 & 20 & \ldots \\ 0 & 0 & 0 & 0 & 1 & 0 & 5 & 0 & 15 & 0 & \ldots \\ 0 & 0 & 0 & 0 & 0 & 1 & 0 & 6 & 0 & 21 & \ldots \\ 0 & 0 & 0 & 0 & 0 & 0 & 1 & 0 & 7 & 0 & \ldots \\ 0 & 0 & 0 & 0 & 0 & 0 & 0 & 1 & 0 & 8 & \ldots \\ 0 & 0 & 0 & 0 & 0 & 0 & 0 & 0 & 1 & 0 & \ldots \\ 0 & 0 & 0 & 0 & 0 & 0 & 0 & 0 & 0 & 1 & \ldots \\ \vdots & \vdots & \vdots & \vdots & \vdots & \vdots & \vdots & \vdots & \vdots & \vdots & \ddots \end{bmatrix}$$

Then we set the approximate solutions defined by a truncated Fibonacci series (3) in the matrix for

$$u(x) = F(x)C. \tag{5}$$

By using the relations Eq.(4) and Eq.(5), the matrix relation is expressed as

$$\begin{aligned} u(x) &\cong u_N(x) = F(x)C = T(x)MC \\ u'(x) &\cong u'_N(x) = T(x)BMC \\ u''(x) &\cong u''_N(x) = T(x)B^2MC \\ &\cdots \\ u^{(k)}(x) &\cong u_N^{(k)}(x) = T(x)B^kMC \end{aligned} \tag{6}$$

Also, the relations between the matrix $T(x)$ and its derivatives $T'(x), T''(x), \ldots, T^{(k)}(x)$ are

$$T'(x) = T(x)B, T''(x) = T(x)B^2$$
$$T'''(x) = T(x)B^3, \dots, T^k(x) = T(x)B^k \tag{7}$$

By substituting the Fibonacci collocation points defined by

$$x_i = \frac{i}{N}, i = 0,1, \dots N \tag{8}$$

into Eq.(6), we have

$$u^{(k)}(x_i) = T(x_i)B^k MC. \tag{9}$$

and the compact form of the relation (9) becomes

$$U^{(k)} = TB^k MC, \qquad k = 0,1,2, \tag{10}$$

where

$$U^{(k)} = \begin{bmatrix} u^{(k)}(x_0) \\ u^{(k)}(x_1) \\ \vdots \\ u^{(k)}(x_N) \end{bmatrix}$$

$$B = \begin{bmatrix} 0 & 1 & 0 & 0 & 0 & 0 & \cdots & 0 \\ 0 & 0 & 2 & 0 & 0 & 0 & \cdots & 0 \\ 0 & 0 & 0 & 3 & 0 & 0 & \cdots & 0 \\ 0 & 0 & 0 & 0 & 4 & 0 & \cdots & 0 \\ 0 & 0 & 0 & 0 & 0 & 5 & \cdots & 0 \\ 0 & 0 & 0 & 0 & 0 & 0 & \cdots & 0 \\ \vdots & \vdots & \vdots & \vdots & \vdots & \ddots & \ddots & N \\ 0 & 0 & 0 & 0 & 0 & 0 & \cdots & 0 \end{bmatrix},$$

$$B^0 = \begin{bmatrix} 1 & 0 & 0 & 0 & 0 & 0 & \cdots & 0 \\ 0 & 1 & 0 & 0 & 0 & 0 & \cdots & 0 \\ 0 & 0 & 1 & 0 & 0 & 0 & \cdots & 0 \\ 0 & 0 & 0 & 1 & 0 & 0 & \cdots & 0 \\ 0 & 0 & 0 & 0 & 1 & 0 & \cdots & 0 \\ 0 & 0 & 0 & 0 & 0 & 1 & \cdots & 0 \\ \vdots & \vdots & \vdots & \vdots & \vdots & \ddots & \ddots & 0 \\ 0 & 0 & 0 & 0 & 0 & 0 & \cdots & 1 \end{bmatrix} \tag{11}$$

$$T = \begin{bmatrix} T(x_0) \\ T(x_1) \\ \vdots \\ T(x_N) \end{bmatrix} = \begin{bmatrix} 1 & x_0 & \cdots & x_0^N \\ 1 & x_1 & \cdots & x_1^N \\ 1 & \vdots & \cdots & \cdots \\ 1 & x_N & \cdots & x_N^N \end{bmatrix}.$$

In addition, we can obtain the matrix forms $U^{(\alpha)}$ which appears in the fractional part of Eq. (1), by using Eq. (6) as

$$U^{(\alpha)} = TB^{\alpha}MC$$

By substituting the Fibonacci collocation points defined by

$$x_i = \frac{i}{N}, i = 0,1, \dots N$$

into Eq.(6), we have

$$U^{(\alpha)}(x_i) = T(x_i)B^{\alpha}(x_i)MC \tag{12}$$

In here, matrix form of B^{α}

$$B^{\alpha} = [(S_1X_1) + (X_2S_2S_3)], \tag{13}$$

where

$$B^{\alpha}(x_i) = [(S_1X_1(x_i)) + (X_2(x_i)S_2S_3)]$$

$$S_1 = diag[S_1\ [\alpha,N]\ S_1[\alpha,N]\ \cdots\ S_1[\alpha,N]\ ] \quad \text{where} \quad S_1[\alpha,N] = \frac{\alpha N\Gamma\,[N+1-\alpha]}{\Gamma[N+2-2\alpha]},$$

$$S_2 = diag[S_2\ [\alpha,N]\ S_2[\alpha,N]\ \cdots\ S_2[\alpha,N]\ ] \quad \text{where} \quad S_2[\alpha,N] = \frac{\Gamma[2-\alpha]}{\Gamma[1-\alpha]},$$

$$S_3 = diag[S_3\ [\alpha,N]\ S_3[\alpha,N]\ \cdots\ S_3[\alpha,N]\ ] \quad \text{where} \quad S_3[\alpha,N] = \frac{\Gamma\,[N+1+\alpha]}{\Gamma[N+2]},$$

$$X_1 = diag[X_1(x)\ X_1(x) \dots\ X_1(x)] \quad \text{where } X_1(x) = x^{1-2\alpha},$$

$$X_2 = diag[X_2(x)\ X_2(x) \dots\ X_2(x)] \quad \text{where } X_2(x) = x,$$

and

$$U^{(\alpha)} = \begin{bmatrix} U^{(\alpha)}(x_0) \\ U^{(\alpha)}(x_1) \\ \vdots \\ U^{(\alpha)}(x_N) \end{bmatrix}, \quad B^{(\alpha)} = \begin{bmatrix} B^{(\alpha)}(x_0) \\ B^{(\alpha)}(x_1) \\ \vdots \\ B^{(\alpha)}(x_N) \end{bmatrix}. \tag{14}$$

Substituting the collocation points ($x_i = {}^{i}/_{N}, i = 0,1, \dots, N$) into Eq. (1), gives the equation

$$Q_{\alpha}(x_i)u^{(\alpha)}(x_i) + \sum_{k=0}^{m} p_k\,(x_i)u^{(k)}(x_i) = g(x_i), \qquad 0 < \alpha < 1$$

which can be expressed with the aid of Eqs. (11) and (14) as

$$\left\{Q_\alpha U^{(\alpha)} + \sum_{k=0}^{m} P_k U^{(k)}\right\} C = G \tag{15}$$

where

$$P_k = diag[p_k(x_0)\ p_k(x_1)\ \ldots\ p_k(x_N)],$$

$$Q_\alpha = diag[Q_\alpha(x_0)\ Q_\alpha(x_1)\ \ldots\ Q_\alpha(x_N)]$$

and

$$G = [g(x_0)\ g(x_1)\ \ldots\ g(x_N)]^{\mathrm{T}}.$$

Substituting the relations (10) and (12) into Eq. (15), the fundamental matrix equation can be obtained as

$$\left\{Q_\alpha TB^\alpha M + \sum_{k=0}^{m} P_k TB_k M\right\} C = G \tag{16}$$

Briefly, Eq. (16) can also be written in the form,

$$WC = G \quad \text{or} \quad [W; G] \tag{17}$$

where

$$W = Q_\alpha TB^\alpha M + \sum_{k=0}^{m} P_k\, TB^k M$$

Here, Eq. (17) corresponds to a system of the $(N + 1)$ nonlinear algebraic equations with the unknown Fibonacci coefficients $c_n, n = 1, 2, \ldots, (N + 1)$.

Now, a matrix representation of the mixed conditions in Eq. (2) can be found. Using the relation in Eq. (6) at points a and b, the matrix representation of the mixed conditions in Eq. (2) that depends on the Fibonacci coefficients in matrix C becomes

$$\left\{\sum_{k=0}^{m-1} [a_k T(0) + b_k T(0)](B)^{(k)} M\right\} C = \delta_k,$$

or briefly

$$V_r C = [\delta_k] \quad \text{or} \quad [V_r; \delta_k]; \tag{18}$$

where

$$V_r = \sum_{k=0}^{m-1} [a_k T(0) + b_k T(0)](B)^{(k)} M = [v_0\ v_1\ v_2 \dots\ v_N].$$

Consequently, by replacing the row matrices in (18) by the m rows of the augmented matrix (17), the new augmented matrix becomes

$$\hat{\mathrm{W}} C = \hat{\mathrm{G}} \quad or \quad [\hat{\mathrm{W}}; \hat{\mathrm{G}}] \tag{19}$$

where

$$[\hat{\mathrm{W}}; \hat{\mathrm{G}}] = \begin{bmatrix} w_{00} & w_{01} & w_{02} & \cdots & w_{0N} & ; & g(x_0) \\ w_{10} & w_{11} & w_{12} & \cdots & w_{1N} & ; & g(x_1) \\ w_{20} & w_{21} & w_{22} & \cdots & w_{2N} & ; & g(x_2) \\ \vdots & \vdots & \vdots & \ddots & \vdots & ; & \vdots \\ w_{(N-m)0} & w_{(N-m)1} & w_{(N-m)2} & \cdots & w_{(N-m)N} & ; & g(x_{N-m}) \\ v_{00} & v_{01} & v_{02} & \cdots & v_{0N} & ; & \delta_0 \\ v_{10} & v_{11} & v_{12} & \cdots & v_{1N} & ; & \delta_1 \\ v_{20} & v_{21} & v_{22} & \cdots & v_{2N} & ; & \delta_2 \\ \vdots & \vdots & \vdots & \ddots & \vdots & ; & \vdots \\ v_{(m-1)0} & v_{(m-1)1} & v_{(m-1)2} & \cdots & v_{(m-1)N} & ; & \delta_{m-1} \end{bmatrix}$$

and

$$\hat{\mathrm{G}} = [g(x_0)\ \ g(x_1)\ \cdots g(x_{N+1-M})\ \ \delta_0\ \ \delta_1\ \delta_2\ \cdots\ \delta_{m-1}]^{\mathrm{T}}.$$

Thus, by solving the linear equation system in (19), the unknown Fibonacci coefficients $c_n, n = 1, 2, \dots, (N+1)$ are determined and substituted into (3), and the Fibonacci polynomial solutions is found.

4. SOLUTION ACCURACY

In this section, to test the accuracy of the proposed method, it is presented that the residual error function $\tilde{\mathrm{E}}_N(x)$. For $x_k \in [a, b]$, the function $\tilde{\mathrm{E}}_N(x)$ is given by

$$\tilde{\mathrm{E}}_N(x_k) = |L[u_N(x_k)] - g(x_k)| \cong 0 \tag{20}$$

and $\tilde{\mathrm{E}}_N \le 10^{-t_k}$ $(t_k\ any\ positive\ \ constant)$.

5. ILLUSTRATIVE EXAMPLES

In this section, two numerical examples are presented to illustrate the efficient of the proposed method. On these problems, the method is tested by using the residual error function given by (20). The obtained numerical results are presented with tables and graphics.

Example 1. Assume that the following differential equation

$$x^2u^{(\alpha)}(x) + (x+1)u(x) = 4x^4 + x^3; \quad u(0) = 0 \tag{21}$$

The exact solution of Eq.(21) for $\alpha = 1$ is given by $u(x) = x^3$. Table 1 presents the numerical results of the approximate solutions u at the different values of α when $N = 5$ for Eq.(21). In Table 2, it is shown that the numerical values of the residual error function $\tilde{E}_N$ for $N = 4, 7$ and 10 when $\alpha = 0.5$ for Eq.(21). Also, in Figure 1, it is presented that the graphics of the approximate solutions u at the different values of α when $N = 5$ for Eq.(21)

Example 2. Consider that the following differential equation

$$(x-2)u''(x) + e^x u^{(\alpha)}(x) + 2u(x) = xe^{-x} - 1; \; u(0) = 1, u'(0) = -1 \tag{22}$$

The exact solution of Eq.(22) for $\alpha = 1$ is given by $u(x) = e^{-x}$ .Table 3 presents the numerical results of the approximate solutions u at he different values of α when $N = 5$ for Eq.(22). In Table 4, it is shown that the numerical values of the residual error function $\tilde{E}_N$ for $N = 4,7$ and 10 when $\alpha = 0.5$ for Eq.(22). Also, in Figure 2, it is presented that the graphics of the approximate solutions u at the different values of α when $N = 5$ for Eq.(22).

Table 1. Numerical results of the approximate solutions u at the different values of α when N = 5 for Example 1

x	$\alpha = 0.1$	$\alpha = 0.5$	$\alpha = 0.9$	$\alpha = 1.0$
0.2	0.011970	0.011643	0.009223	0.008
0.4	0.116985	0.107224	0.074963	0.064
0.6	0.438696	0.375852	0.250710	0.216
0.8	1.089160	0.878579	0.584746	0.512
1.0	2.121030	1.616460	1.119660	1.000

Table 2. Numerical results of the residual error function $\tilde{E}_N$ at the different values of N when $\alpha = 0.5$ for Example 1

x	$\tilde{E}_4$	$\tilde{E}_7$	$\tilde{E}_{10}$
0.2	5.10632×10^{-4}	6.08867×10^{-7}	5.98885×10^{-12}
0.4	1.29941×10^{-3}	8.31422×10^{-7}	3.21218×10^{-12}
0.6	2.91073×10^{-3}	2.99808×10^{-6}	5.79559×10^{-12}
0.8	8.06119×10^{-3}	5.06281×10^{-5}	4.25020×10^{-11}
1.0	1.41281×10^{-1}	4.47786×10^{-3}	2.76943×10^{-4}

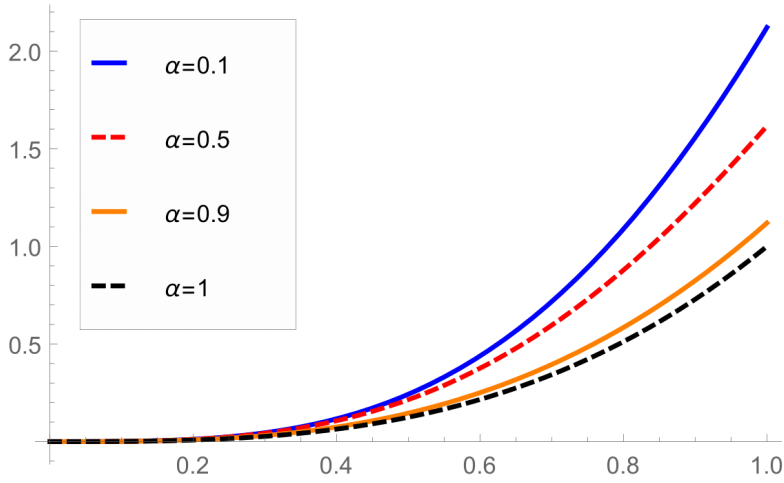

Figure 1. The graphical comparison of the approximate solutions u at the different values of α when $N = 5$ for Example 1

Table 3. Numerical results of the approximate solutions u at the different values of α when N = 5 for Example 2

x	$\alpha = 0.1$	$\alpha = 0.5$	$\alpha = 0.9$	$\alpha =$ 1.0
0.2	0.829771	0.829159	0.825633	0.818731
0.4	0.719578	0.714294	0.693733	0.670320
0.6	0.674665	0.655276	0.598893	0.548812
0.8	0.708683	0.658397	0.540202	0.449329
1.0	0.846672	0.738756	0.513879	0.367879

Table 4. Numerical results of the residual error function $\tilde{E}_N$ at the different values of N when $\alpha = 0.5$ for Example 2

x	$\tilde{E}_4$	$\tilde{E}_7$	$\tilde{E}_{10}$
0.2	4.92027×10^{-3}	9.87749×10^{-5}	1.85572×10^{-10}
0.4	1.10199×10^{-2}	4.34588×10^{-5}	5.70497×10^{-11}
0.6	4.34029×10^{-2}	1.21201×10^{-4}	9.78482×10^{-11}
0.8	3.09118×10^{-1}	5.20842×10^{-3}	1.41686×10^{-9}
1.0	1.00341×10^{0}	1.20548×10^{-1}	6.63552×10^{-3}

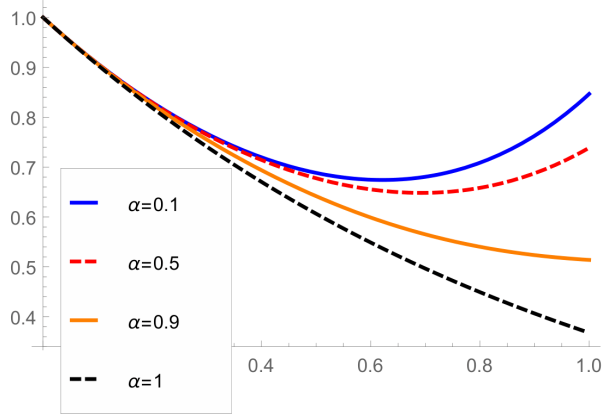

Figure 2. The graphical comparison of the approximate solutions u at the different of α when N = 5 for Example 2

6. CONCLUSIONS

In this research, Fibonacci collocation method is applied to obtain the approximate solutions of (1). This study has an importance by showing the applicability of the proposed method to the fractional differential equations constructed with proportional Caputo derivative. Illustrative examples given in the section 4 are demonstrate and support our findings. Regarding to the findings it can be said that Fibonacci collocation method is very efficient solution tool for the class of fractional differential equations (1). For future studies either the proposed method can be modified in order to have better results fort the class of fractional differential equations (1) or could be applied for various classes of fractional differential equations defined by proportional Caputo derivative.

REFERENCES

Abro, K. A., Siyal, A. & Atangana, A. (2021). Thermal stratification of rotational second-grade fluid through fractional differential operators. *Journal of Thermal Analysis and Calorimetry*, 143(5), 3667-3676. Doi: 10.1007/s10973-020-09312-8

Akgül, A. (2018). A novel method for a fractional derivative with non-local and non-singular kernel. Chaos, Solitons & Fractals, 114, 478–482. Doi: 10.1016/j.chaos.2018.07.032

Akgül, E. K., Akgül, A. & Baleanu, D. (2020). Laplace transform method for economic models with constant proportional Caputo derivative. *Fractal and Fractional*, 4(3), 30. Doi: 10.3390/fractalfract4030030

Akgül, E. K., Akgül, A., & Yavuz, M. (2021). New illustrative applications of integral transforms to financial models with different fractional derivatives. *Chaos, Solitons Fractals*, 146, 110877. Doi: 10.1016/j.chaos.2021.110877

Akgül, E.K. (2019). Solutions of the linear and nonlinear differential equations within the generalized fractional derivatives. Chaos, 29(2), 023108. Doi: 10.1063/1.5084035

Alkan, S., & Hatipoglu, V. F. (2017). Approximate solutions of Volterra-Fredholm integro-differential equations of fractional order. *Tbilisi Mathematical Journal*, 10(2), 1-13. Doi: 10.1515/tmj-2017-0021

Atangana, A. & Akgül, A. (2020). Analysis and Applications of the New Derivative, Chapter of Fractional Order Analysis: Theory, Methods and Applications, Wiley, New York. Doi: 10.1063/1.5084035

Atangana, A. (2021). A novel Covid-19 model with fractional differential operators with singular and nonsingular kernels: Analysis and numerical scheme based on Newton polynomial. *Alexandria Engineering Journal*, 60(4), 3781-3806. Doi: 10.1016/j.aej.2021.02.016

Baleanu, D., Fernandez, A. & Akgül, A. (2020). On a fractional operator combining proportional and classical differintegrals. *Mathematics*, 8(3), 360. Doi: 10.3390/math8030360

Bohner, M. & Hatipoğlu, V. F. (2018). Cobweb model with conformable fractional derivatives. *Mathematical Methods in the Applied Sciences*, 41(18), 9010-9017. Doi: 10.1002/mma.4846

Falcon, S. & Plaza, A. (2007). The k-Fibonacci sequence and the Pascal 2-triangle. *Chaos, Solitons & Fractals*, 33(1), 38-49. Doi: 10.1016/j.chaos.2006.10.022

Falcon, S. & Plaza, A. (2009). On k-Fibonacci sequences and polynomials and their derivatives. Chaos, Solitons & Fractals, 39(3), 1005-1019. Doi: 10.1016/j.chaos.2007.03.007

Fernandez, A., Baleanu, D. & Srivastava, H.M. (2019). Series representations for fractional-calculus operators involving generalised Mittag-Leffler functions. Commun. Nonlinear Sci. Numer. Simul., 67, 517–527. Doi: 10.1016/j.cnsns.2018.07.035

Günerhan, H., Dutta, H., Dokuyucu, M. A. & Adel, W. (2020). Analysis of a fractional HIV model with Caputo and constant proportional Caputo operators. *Chaos, Solitons & Fractals*, 139, 110053. Doi: 10.1016/j.chaos.2020.110053

Hatipoglu, V. F., Alkan, S. & Secer, A. (2017). An efficient scheme for solving a system of fractional differential equations with boundary conditions. *Advances in Difference Equations*, 2017(1), 1-13. Doi: 10.1186/s13662-017-1260-9

Hatipoğlu, V. F. (2019). A numerical algorithm for the solution of nonlinear fractional differential equations via beta-derivatives. *Mathematical Methods in the Applied Sciences*, 42(16), 5258-5265. Doi: 10.1002/mma.5305

Ikram, M. D., Asjad, M. I., Akgül, A. & Baleanu, D. (2021). Effects of hybrid nanofluid on novel fractional model of heat transfer flow between two parallel plates. *Alexandria Engineering Journal*, 60(4), 3593-3604. Doi: 10.1016/j.aej.2021.01.054

İbrahimoğlu, B. A. (2021). Mock-Chebyshev Polinom İnterpolasyonu. *Avrupa Bilim ve Teknoloji Dergisi*, (27), 858-865. Doi: 10.31590/ejosat.996547

Khalid, N., Abbas, M., Iqbal, M.K. & Baleanu, D. (2020). A numerical investigation of Caputo time fractional Allen–Cahn equation using redefined cubic B-spline functions. Adv. Differ. Equ. 2020, 158. Doi: 10.1186/s13662-020-02616-x

Khan, A., Zarin, R., Akgül, A., Saeed, A. & Gul, T. (2021). Fractional optimal control of COVID-19 pandemic model with generalized Mittag-Leffler function. *Advances in Difference Equations*, 2021(1), 1-22. Doi: 10.1186/s13662-021-03546-y

Kurt, A., Yalçinbas, S. & Sezer, M. (2013). Fibonacci collocation method for solving linear differential-difference equations. *Mathematical and Computational Applications*, (2013), 18(3), 448-458. Doi: 10.3390/mca18030448

Kurt, A., Yalçinbas, S. & Sezer, M. (2013). Fibonacci collocation method for solving high-order linear Fredholm integrodifferential-difference equations. *International Journal of Mathematics and Mathematical Sciences*, (2013), 2013. Doi: 10.1155/2013/486013

Mirzaee, F. & Hoseini, S. F. (2013). Solving singularly perturbed differential-difference equations arising in science and engineering with Fibonacci polynomials. *Results in Physics*, 3, 134-141. Doi: 10.1016/j.rinp.2013.08.001

Mirzaee, F. & Hoseini, S. F. (2014). Solving systems of linear Fredholm integro-differential equations with Fibonacci polynomials. *Ain Shams Engineering Journal*, 5(1), 271-283. Doi: 10.1016/j.asej.2013.09.002

Mirzaee, F. & Hoseini, S. F. (2017). A new collocation approach for solving systems of high-order linear Volterra integrodifferential equations with variable coefficients. *Applied Mathematics and Computation*, 311, 272-282. Doi: 10.1016/j.amc.2017.05.031

Owolabi, K.M. (2018). Analysis and numerical simulation of multicomponent system with Atangana–Baleanu fractional derivative. Chaos, Solitons & Fractals, 115, 127–134. Doi: 10.1016/j.chaos.2018.08.022

Sweilam, N. H., Al-Mekhlafi, S. M. & Baleanu, D. (2021). A hybrid stochastic fractional order Coronavirus (2019-nCov) mathematical model. *Chaos, Solitons & Fractals*, 145, 110762. Doi: 10.1016/j.chaos.2021.110762

Wu, G.C., Zeng, D.Q. & Baleanu, D. (2019). Fractional impulsive differential equations: exact solutions, integral equations and short memory case. Fract. Calc. Appl. Anal., 22, 180–192. Doi: 10.1515/fca-2019-0012